



HAL
open science

Signaux électromagnétiques dans les collisions hadroniques au LHC

Chi Linh Nguyen

► **To cite this version:**

Chi Linh Nguyen. Signaux électromagnétiques dans les collisions hadroniques au LHC. Autre [cond-mat.other]. Université de Grenoble, 2014. Français. NNT : 2014GRENY006 . tel-00986981

HAL Id: tel-00986981

<https://theses.hal.science/tel-00986981>

Submitted on 5 May 2014

HAL is a multi-disciplinary open access archive for the deposit and dissemination of scientific research documents, whether they are published or not. The documents may come from teaching and research institutions in France or abroad, or from public or private research centers.

L'archive ouverte pluridisciplinaire **HAL**, est destinée au dépôt et à la diffusion de documents scientifiques de niveau recherche, publiés ou non, émanant des établissements d'enseignement et de recherche français ou étrangers, des laboratoires publics ou privés.

THÈSE

Pour obtenir le grade de

DOCTEUR DE L'UNIVERSITÉ DE GRENOBLE

Spécialité : **Physique des Particules**

Arrêté ministériel : 7 août 2006

Présentée par

Chi Linh Nguyen

Thèse dirigée par **Jean-Philippe Guillet**
et codirigée par **François Arleo**

préparée au sein

Laboratoire d'Annecy-le-Vieux de Physique Théorique (LAPTh)
et de l'**École Doctorale de Physique de Grenoble**

Electromagnetic signals in hadronic collisions at the LHC

Thèse soutenue publiquement le **07/03/2014**,
devant le jury composé de :

M. Michel Fontannaz

LPT Orsay, Président

M. Matteo Cacciari

LPTHE, Rapporteur

M. David d'Enterria

CERN, Rapporteur

M. Michel Fontannaz

LPT Orsay, Examineur

M. Jean-Philippe Guillet

LAPTh, Directeur de thèse

M. François Arleo

LAPTh/LLR, Co-Directeur de thèse



Contents

Acknowledgements	iii
Introduction	1
1 Theoretical basic	5
1.1 The running coupling constant in QCD	6
1.2 Parton distribution functions	11
1.2.1 Deep inelastic electron-proton scattering	11
1.2.2 Naive parton model	13
1.2.3 QCD corrections	16
1.2.4 Altarelli-Parisi equation	22
1.2.5 PDF sets	24
1.3 Fragmentation Functions	29
1.3.1 Theoretical content	29
1.3.2 Fragmentation Functions sets	34
2 Aspects of jet production	39
2.1 Jet definition	40
2.1.1 Theoretical content	40
2.1.2 The k_t algorithm	41
2.1.3 The flavor- k_t algorithm	44
2.1.4 Jet phenomenology	48
2.2 JETPHOX overview	51
2.2.1 Theoretical content	51
2.2.2 Generation of events in JETPHOX with BASES-SPRING	56
2.2.3 Comparison between JETPHOX and the inclusive prompt photon data	61
3 Hadron jet correlations and constraints on FFs at LHC	67
3.1 Introduction	68
3.2 Framework	70
3.2.1 Fragmentation function sets	70
3.2.2 A quick look at LO calculation	70
3.2.3 The FF scale M_F issue	72
3.3 Same-side hadron-jet momentum correlations	75

3.3.1	Framework	75
3.3.2	Correlations with inclusive charged hadrons	77
3.3.3	Correlations with identified hadrons	80
3.4	Away-side hadron-jet momentum correlations	82
3.4.1	Framework	82
3.4.2	Correlations with inclusive charged hadrons	83
3.4.3	Correlations with identified hadrons	86
3.5	Conclusion	88
4	Photon Production in Association with Heavy-Flavor Jet	89
4.1	<code>bjETPHOX</code> : An upgrading from <code>JETPHOX</code>	92
4.1.1	Picking up sub-processes using random number generator	92
4.1.2	Select among flavor-contributions on <code>bjETPHOX</code>	99
4.1.3	Events with flavor selection	102
4.1.4	Analytical macros	104
4.2	The aspects of photon + heavy-quark jet production at LHC	105
4.2.1	The $Q\bar{Q}$ -pair invariant mass approach	105
4.2.2	The flavor- k_t algorithm approach	112
4.2.3	Charm meson FF approach	119
4.2.4	A look on bottom quark's distribution inside the proton	125
5	Conclusion	129
A	Analytical calculation	131
A.1	Invariant mass of two partons	132
A.2	The finite (factors)terms in parton differential cross section	134
B	Event analysis	137
B.1	List of channels <code>j0</code>	138
B.2	Demo loading <code>JETPHOX</code> events with <code>read_tree.C</code>	140
B.3	<code>HJETX</code> : an upgrading from <code>JETPHOX</code>	144
B.3.1	Usage	144
B.3.2	Demo analyse <code>HJETX</code> events with <code>ahjetx</code> class	144
B.4	Demo analyse <code>bjETPHOX</code> events with <code>ajetphox</code> class	147
	Bibliography	160

Acknowledgements

I express my very great appreciation to Jean-Philippe Guillet and François Arleo, my research supervisors, for their pedagogical training, patient guidance, enthusiastic encouragement, and useful critiques on my Ph.D. thesis project. I learnt from them a lot of excellent advice for dealing with physics problems.

I offer my special thanks to Patrick Aurenche for his guidance, support, pedagogical training, and many helpful suggestions in understanding physics.

I thank Michel Fontannaz, Matteo Cacciari, and David d'Enterria for accepting to be members of the jury, for careful reading the manuscript, and for giving very useful comments.

I wish to thank Cao Thi Truc Thanh for her help in the C++ programming. As a professional programmer, she gave me many helpful advice, especially when I started writing the codes used in my thesis. I would like to thank Mathieu Gauthier-Lafaye for his help and discussion in programming. I would like to thank Le Bao Tran, Tao Li, Maud Schwoererf, Dimitra Tsionou, Laurent Basara, Fabien Krayzel, and Guilhem Bernard for their sharing the experience of ROOT, statistics, and Latex.

My special thanks are extended to the warm support from LAPTh. I would like to thank Fawzi Boudjema for his support to Ph.D. students which encouraged me in completing the thesis. I also thank Luc Frappat for his advice in preparing the necessary activities for completing the requirements of the University of Grenoble - Alpes. I would like to thank members of the administrative staff of LAPTh: Dominique Turc, Véronique Jonnery, Virginie Malaval, Nathalie Perkins, for their professional and friendly help in dealing with the official documents and keeping my spirits up when dealing with the French bureaucracy.

I acknowledge the financial support from Ca Mau 120 - Mekong 1000 Project, Can Tho University, Vietnam, without which my thesis project could not have been carried out.

I owe a lot to my family, especially to my parents, for their support throughout my studies in Vietnam as well as in France. They always encouraged me to overcome the difficulties and made me confident in my work.

Introduction

One of the basic ingredients of the Standard Model of particle physics is Quantum Chromodynamics (QCD) which describes the interactions between the fundamental components of matter : the quark and the gluons. Since the Large Hadron Collider (LHC) at CERN¹ is probing a domain of energy much higher than what was accessible before with the Tevatron collider at Fermilab, QCD has to be tested under these new conditions. This is one of the purposes of the project which consists in developing theoretical tools which will allow, via a direct confrontation of theory with some sets of LHC experimental data, to study the quark and gluon composition of the proton and nuclei. The results of these studies are important as they are necessary ingredients to discover if new physics, beyond the Standard Model, will be uncovered at the LHC. Indeed they will allow to make very precise predictions for the Standard Model so that any deviation from it in the observables will be a signal for new physics.

The production of prompt photon² in hadron colliders provides clean experimental signatures because the pointlike electromagnetic coupling of photon to the quark constituents, leading to precise tests of perturbative QCD [1, 2]. In addition, the jet algorithms which can be defined both at theoretical and experimental level allow to better compare experimental measurements of jet production with theoretical predictions. On the experimental side, the LHC with p - p collisions operates at $\sqrt{s} = 8$ TeV, although this is still not the nominal energy, there is a significant increase of the center-of-mass energy comparing to previous collider experiments. It opens a new era for particle physics and in particular for QCD studies. Using data collected in 2010 and 2011, both ATLAS and CMS Collaborations have published the measurements of standard QCD cross sections: jets, $t\bar{t}$ +jets, γ +jets, $W(Z)$ +jets, etc... Among all these cross sections, there is a particular interest on cross sections involving prompt photons. The measurements of inclusive prompt-photon [3, 4, 5] and prompt-photon+jet [6, 7] productions ($\sqrt{s} = 7$ TeV), cover much larger kinematic regions than the previous measurements at Tevatron. In addition, the measurements performed in p - \bar{p} collisions at the Tevatron ($\sqrt{s} = 1.96$ TeV) become increasingly precise. Both D0 and CDF Collaborations have performed the measurements

1. <http://public.web.cern.ch/public/en/About/About-en.html>

2. Prompt photons are the photons which originate directly from the hard subprocess scattering and do not come from the decay of hadrons, such as π^0 , η , etc. They are produced with high transverse momentum.

of prompt photon in association with heavy-quark jet productions [8, 9]. Therefore, the measurements of prompt photon production at the Tevatron and the LHC experiments allow to put stronger constraints on QCD inputs such as parton distributions (PDFs) and fragmentation functions (FFs).

On the theoretical side, the NLO QCD prediction of the inclusive prompt-photon production and prompt-photon+jet production in hadron-hadron collisions agree with available experimental measurements up to highest transverse energy of photons. This confirms the current knowledge of NLO QCD formalism implemented in those reactions. For more specific processes, i.e. prompt-photon production in association with heavy-quark jet, theoretical predictions on $\gamma + b + X$ cross section agree well with experimental measurements at Tevatron [10, 11]. However, for the $\gamma + c + X$ process theoretical cross section underestimates data at large photon transverse momentum $p_{\perp}^{\gamma} \gtrsim 50$ GeV. Even in the latest measurements (more precise), the NLO QCD predictions fail to describe data for $p_{\perp}^{\gamma} \gtrsim 70$ GeV for the bottom cross section [9].

Besides, the inclusive jet production cross section at NLO QCD in p - $p(\bar{p})$ collisions also agree well with data measurements at Tevatron and LHC [12, 13, 14]. Hence, we hope that the jet+hadron production would provide an interesting investigation in putting further constraints on FFs of partons into hadrons. Since available FFs are mostly extracted from e^+e^- data, they have less constraints at large fraction momentum, $z \lesssim 0.7$. Moreover, in hadrons collisions, the dominant region of PDFs allow to probe the FFs at larger z (as discussed in section 1.3.2). Therefore, rich data at the Tevatron and, especially, at the LHC allows to set tighter constraints on FFs.

The goal of the Ph.D. thesis is to study the FF constraints from hadron-jet production and the phenomenology of prompt photon production in association with heavy-quark jet at the LHC. We improve, during the completion of the thesis, the current calculation of prompt photon/hadron+jet production in QCD at next-to-leading order (NLO) in the strong coupling constant. The studies are mostly based on the family of parton-level event NLO generators PHOX³ which allow for the calculation of single and double inclusive large- p_{\perp} cross sections for reactions involving photons, hadrons and jets. The PHOX generators [15] are the state-of-the-art of the present NLO generators of prompt photon cross sections. They have been applied successfully to various collision systems and to many observables, such as the inclusive prompt photon production at Tevatron and LHC (as presented in section 2.2.3).

The structure of the thesis is as follows.

- In chapter 1, we review the theoretical basis of QCD: running coupling constant, PDFs, and FFs. Besides, the status of the fits on PDFs and FFs are briefly discussed.
- In chapter 2, we review the theoretical point of view on two jet algorithms: the kt algorithm [16] and the flavor- k_t algorithm [17] and their applications in prac-

3. http://lapth.cnrs.fr/PHOX_FAMILY/main.html

tice. The technical details on physics analysis and numerical calculation in JETPHOX generators are presented. Then, the application of JETPHOX is discussed.

- In chapter 3, we show the results of the analysis of hadron–jet momentum in p – p collisions. We improve JETPHOX to be able to calculate same–side correlation and make detailed factorization scales studies: HJETX. The momentum correlation between a hadron and a same–side jet [18], and the momentum correlation between a hadron and an away–side jet are studied at LHC energies. We discuss in details the constraints put on FFs.
- In chapter 4, we discuss techniques for improving JETPHOX so that it is suitable to study the prompt photon production in association with heavy-quark jet using jet algorithms which are infrared safe. Then, using the new tool, bJETPHOX, we perform the analysis on $\gamma + b(c)$ –jet production at Tevatron and LHC based on the invariant mass (to re-obtain the previous calculations) and the flavor– k_t algorithm approaches. Besides, using DIPHOX, we perform the analysis with charm–meson FFs approach at Tevatron at $\sqrt{s} = 1.96$ TeV and discuss the discrepancies between previous theoretical prediction and data measurements. Then, we give a prediction on $\gamma + c + X$ production in p – p collisions at LHC at $\sqrt{s} = 8$ TeV.

This thesis includes two Appendices. In one appendix, we give some necessary analytical calculations which are used in the thesis. In the other, the demos of how to analyze JETPHOX/HJETX/bJETPHOX events are shown.

Chapter 1

Theoretical basic

Contents

1.1	The running coupling constant in QCD	6
1.2	Parton distribution functions	11
1.2.1	Deep inelastic electron-proton scattering	11
1.2.2	Naive parton model	13
1.2.3	QCD corrections	16
1.2.4	Altarelli-Parisi equation	22
1.2.5	PDF sets	24
1.3	Fragmentation Functions	29
1.3.1	Theoretical content	29
1.3.2	Fragmentation Functions sets	34

1.1 The running coupling constant in QCD

Let us consider the dimensionless physical observable R^1 which corresponds to a reaction containing a single energy scale Q . This observable can receive QCD corrections. At lowest order, R is independent of Q , because R is dimensionless while Q has the dimension of energy.

In a renormalizable quantum field theory, one calculates R as a series of power of α_S . A second mass scale μ is introduced when one performs the renormalization procedure to remove the ultraviolet (UV) divergences. For example, in the dimensional regularization, the UV divergences are regularized by performing the calculation in the $n < 4$ spacetime dimensions:

$$\frac{d^4k}{(2\pi)^4} \rightarrow (\mu)^{2\epsilon} \frac{d^{4-2\epsilon}k}{(2\pi)^{4-2\epsilon}} \quad (1.1)$$

where $\epsilon = 2 - n/2$ and μ is the renormalization scale.² From this point, one sees that the dimensionless observable like R generally can depend on the ratio Q^2/μ^2 and is not obviously constant. Thus the renormalized coupling α_S also depends on the choice of the subtraction point μ .

The choice of μ is necessary to define the theory at the quantum level. However, since μ is an arbitrary scale, a physical observable cannot depend on it. Thus, the μ dependence of R can appear only through the ratio of Q^2/μ^2 and through the renormalized α_S . Since R is a physical observable, mathematically, the independence of R on μ can be written as follows

$$\mu^2 \frac{d}{d\mu^2} R\left(\frac{Q^2}{\mu^2}, \alpha_S\right) = 0 \quad (1.2)$$

Conventionally, one can introduce the following notation:

$$t = \ln\left(\frac{Q^2}{\mu^2}\right), \quad \beta(\alpha_S) = \mu^2 \frac{\partial \alpha_S}{\partial \mu^2} \quad (1.3)$$

then uses them to rewrite Eq. (1.2) as

$$\left[-\frac{\partial}{\partial t} + \beta(\alpha_S) \frac{\partial}{\partial \alpha_S} \right] R = 0 \quad (1.4)$$

One can solve the equation (1.4) by introducing a new function $\alpha_S(Q^2)$, which is known as the running coupling constant, as follows:

$$t = \int_{\alpha_S(\mu^2)}^{\alpha_S(Q^2)} \frac{dx}{\beta(x)} \quad (1.5)$$

1. For example, the R ratio which will be discussed in section 1.3.

2. Technically, in dimensional regularization μ is introduced to keep the coupling constant dimensionless.

with $\alpha_S(\mu^2) \equiv \alpha_S$ is an arbitrary constant, at this point. One can differentiate Eq. (1.5) with respect to t and α_S , then gets

$$\frac{\partial \alpha_S(Q^2)}{\partial t} = \beta(\alpha_S(Q^2)), \quad \frac{\partial \alpha_S(Q^2)}{\partial \alpha_S} = \frac{\beta(\alpha_S(Q^2))}{\beta(\alpha_S)} \quad (1.6)$$

Thanks to Eq. (1.6), one can get that the dimensionless quantity such as the function $R(1, \alpha_S(Q^2))$ is a solution of Eq. (1.4). As one can see, the scale dependence in R comes from the coupling constant $\alpha_S(Q^2)$. Therefore, assuming the Eq. (1.5) can be solved, one is able to predict R at the scale Q from the calculation of $R(1, \alpha_S)$ in fixed-order perturbation theory.

We want to emphasize that the exact relationship between coupling defined at scales Q^2 and μ^2 is given by Eq. (1.5) and the coupling constant α_S obeys to

$$\frac{\partial \alpha_S}{\partial t} = \beta(\alpha_S). \quad (1.7)$$

In QCD, the β function can be expanded in perturbative series as follows

$$\beta(\alpha_S) = -b\alpha_S^2 \left(1 + b'\alpha_S + \mathcal{O}(\alpha_S^2) \right), \quad (1.8)$$

where

$$b = \frac{33 - 2n_f}{12\pi}, \quad b' = \frac{153 - 19n_f}{2\pi(33 - 2n_f)} \quad (1.9)$$

and n_f is the number of quark flavors. In fact, the coefficients of the β function are derived by calculating the higher order corrections for the "bare" vertices in the perturbation theory. Also note that, in QED, the β function is given by

$$\beta_{\text{QED}}(\alpha) = \frac{4}{12\pi}\alpha^2 + \dots \quad (1.10)$$

and therefore the b coefficients in QCD and QED have opposite signs since the number n_f is less than 17. This difference comes from the fact that the gluons carry color charges and so they can couple to themselves (self-coupling) but the photon is electrically neutral. The first loop-correction defined by graph (a) in Fig. 1.1 contributes to the term proportional to n_f in the coefficient b , Eq. (1.9), in QCD and gives a same sign contribution as in QED. The graphs (b) in Fig. 1.1 contribute to the first term in coefficient b in QCD and it leads to $\beta(\alpha_S)$ in Eq. 1.9 which has a negative sign. Thanks to Eqs. (1.7) and (1.8), one has

$$\frac{\partial \alpha_S(Q^2)}{\partial t} = -b\alpha_S^2(Q^2) \left(1 + b'\alpha_S(Q^2) + \mathcal{O}(\alpha_S^2(Q^2)) \right) \quad (1.11)$$

Assuming both $\alpha_S(\mu^2)$ and $\alpha_S(Q^2)$ are in the perturbative region, one is able to use the

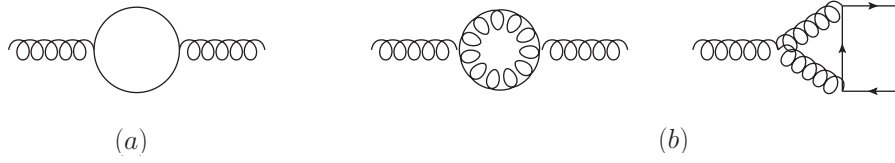


Figure 1.1: Examples of graphs for one loop correction.

lowest order (LO) of the expansion of $\beta(\alpha_S)$ in solving the Eq. (1.5). Then, one gets

$$\alpha_S(Q^2) = \frac{\alpha_S(\mu^2)}{1 + \alpha_S(\mu^2)bt} \quad (1.12)$$

When t is very large, the running coupling goes to zero. In other words, $\alpha_S(Q^2)$ becomes small for the short-distance interaction.³ Therefore, one says that the theory has the asymptotic freedom property.

By including the next-to-leading order (NLO) coefficient b' for $\beta(\alpha_S)$, the solution for Eq. (1.5) is

$$\frac{1}{\alpha_S(Q^2)} - \frac{1}{\alpha_S(\mu^2)} + b' \ln\left(\frac{\alpha_S(Q^2)}{1 + b'\alpha_S(Q^2)}\right) - b' \ln\left(\frac{\alpha_S(\mu^2)}{1 + b'\alpha_S(\mu^2)}\right) = bt \quad (1.13)$$

It is difficult to solve Eq. (1.13) in $\alpha(Q^2)$. In practice, given values of t and $\alpha_S(\mu^2)$, one can numerically calculate $\alpha_S(Q^2)$, thanks to Eq. (1.13) at a desired accuracy.

Now, let us carry out the type of terms which is resummed by performing the renormalization group on the physical quantity R . Supposing R is expanded, in perturbation theory, as follows

$$R = R_1\alpha_S + \dots \quad (1.14)$$

where \dots represent the terms of higher order in α_S . Thanks to Eq. (1.12), the solution of Eq. (1.4), $R(1, \alpha_S(Q^2))$, can be written in terms of $\alpha_S(\mu^2)$ as follows

$$\begin{aligned} R(1, \alpha_S(Q^2)) &= R_1\alpha_S(\mu^2) \sum_{i=0}^{\infty} \left[-\alpha_S(\mu^2)bt \right]^i \\ &= R_1\alpha_S(\mu^2) \left[1 - \alpha_S(\mu^2)bt + \alpha_S^2(\mu^2)(bt)^2 + \dots \right] \end{aligned} \quad (1.15)$$

(where t and b are given in Eqs. (1.3) and (1.9), respectively.) As one can see, at each order, the logarithmic terms like $\alpha_S^n(\mu^2) \ln^n(Q^2/\mu^2)$, with $n > 0$, are resummed by expressing R in terms of the running coupling constant $\alpha_S(Q^2)$. Note that including higher order terms in the R expansion, terms like $\alpha_S^n(\mu^2) \ln^{n-m}(Q^2/\mu^2)$, with $n > m$ are resummed.

It still remains a parameter μ which corresponds to the renormalization. As one can see the coupling $\alpha_S(Q^2)$ is large at low scale Q^2 . It is common to describe the asymptotic

3. Contrary to QED, where the "b" has the opposite sign, the running coupling $\alpha(Q^2)$ increases with increasing t .

solution for $\alpha_S(Q^2)$ with respect to parameter Λ^2 , which is defined by

$$\Lambda^2 = \mu^2 e^{-\frac{1}{\alpha_S(\mu^2)b}} \quad (1.16)$$

Thanks to Eq. (1.11), one gets

$$\alpha_S(Q^2) = \frac{1}{b \ln(Q^2/\Lambda^2)} \quad (1.17)$$

It is clear that for the scale Q^2 much larger than Λ^2 , the running coupling becomes weak, $\alpha_S(Q^2) \ll 1$, which justifies the use of perturbation theory.

On the one hand, from Eq. (1.17), if Q^2 is identical to Λ^2 , then $\alpha_S(Q^2)$ is divergent and therefore perturbation theory is untrustable. On the other hand, in practice, gluons and quarks significantly combine themselves into the bound states, which are known as hadrons. Therefore, one can think of Λ as a QCD parameter which separates perturbative and non-perturbative regions. Another argument to support this idea is that the partons are experimentally confined within the proton size. The energy scale corresponding to the proton size $\sim 10^{-15}\text{m}$, is around 200 MeV, i.e. roughly the value of Λ . But it is a very crude separation, a better scale to separate these regions would be the proton mass (m_p) where $\alpha_S(m_p^2)$ is of order 1. Moreover, the value Λ is not predicted by the theory, it has to be determined from the experiment.

Using the NLO formula for the $\beta(\alpha_S)$ expansion, the dependence of $\alpha_S(Q^2)$ on Λ^2 becomes

$$\frac{1}{\alpha_S(Q^2)} + b' \ln\left(\frac{\alpha_S(Q^2)}{1 + b'\alpha_S(Q^2)}\right) = b \ln\left(\frac{Q^2}{\Lambda^2}\right) \quad (1.18)$$

This allows one to calculate numerically $\alpha_S(Q^2)$ for a given Λ .⁴ In QCD, the value of Λ is found to be $\Lambda_{\overline{MS}}^{\text{QCD}} = 213 \pm 8 \text{ MeV}$ (for $n_f = 5$ active flavors) or equivalently at $Q = M_Z \equiv 91.2 \text{ GeV}$, the renormalized coupling $\alpha_S(Q^2)$ is predicted to be 0.1184 ± 0.0007 [19, 20]. The plots in Fig. 1.3 illustrate the summary of measurements for running coupling $\alpha_S(Q^2)$ as a function of the scale Q^2 . As one can see, at small scales, $\alpha_S \approx 1$ and therefore one can no longer use the perturbative expansion.

4. By approximating Eq. (1.18), one can solve it analytically (see [19].)

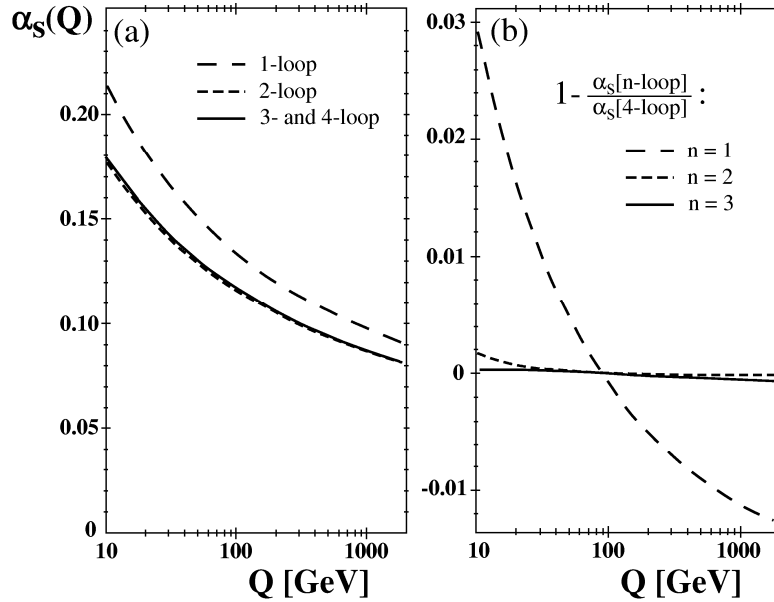


Figure 1.2: The prediction for running coupling constant $\alpha_s(Q^2)$ [21].

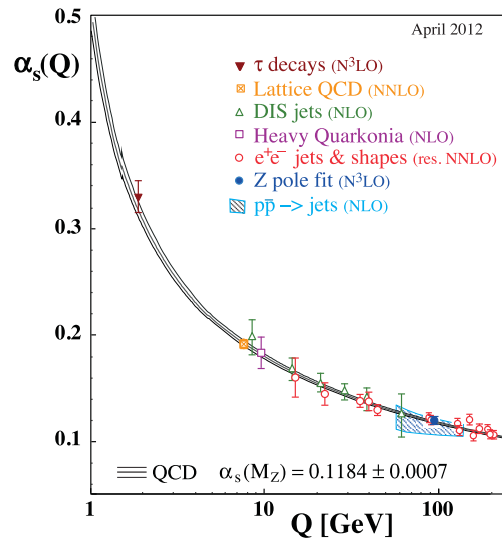


Figure 1.3: The summary of measurements of $\alpha_s(Q^2)$ [19, 20].

1.2 Parton distribution functions

1.2.1 Deep inelastic electron-proton scattering

Let us consider the inelastic electron–proton scattering given by the following diagram:

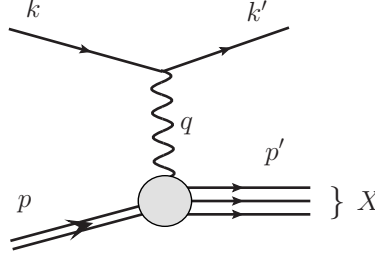


Figure 1.4: An illustration for $ep \rightarrow eX$ scattering.

The general form for the $ep \rightarrow eX$ cross section is given by

$$d\sigma \sim L_{\mu\nu}^e W^{\mu\nu} \quad (1.19)$$

The lepton tensor $L_{\mu\nu}^e$ is given by

$$L_{\mu\nu}^e = 2(k'_\mu k_\nu + k'_\nu k_\mu - (k' \cdot k - m_e^2)g_{\mu\nu}) \quad (1.20)$$

where k, k' are momenta of the initial and final electron, respectively, and m_e is the mass of the electron. In general, the hadronic tensor $W^{\mu\nu}$ can be parametrized with the help of $g^{\mu\nu}$, the combination of momenta of proton, p , and virtual photon, q (note that the momentum of the final hadronic system X is $p' = p + q$, $p'^2 > M^2$ where M is the mass of proton). Because $L_{\mu\nu}^e$ is a symmetric tensor, the anti-symmetric contribution of $W^{\mu\nu}$ is ignored. Also note that the electromagnetic current at hadronic vertex is conserved, so one has

$$q_\mu W^{\mu\nu} = q_\nu W^{\mu\nu} = 0 \quad (1.21)$$

Hence, the general form for $W^{\mu\nu}$ is found to be

$$W^{\mu\nu} = W_1 \left(-g^{\mu\nu} + \frac{q^\mu q^\nu}{q^2} \right) + W_2 \frac{1}{M^2} \left(p^\mu - \frac{p \cdot q}{q^2} q^\mu \right) \left(p^\nu - \frac{p \cdot q}{q^2} q^\nu \right) \quad (1.22)$$

Now, one can calculate the right hand side of Eq. (1.19) and gets

$$L_{\mu\nu}^e W^{\mu\nu} = 4W_1 k \cdot k' + \frac{2W_2}{M^2} [2(p \cdot k)(p \cdot k') - M^2 k \cdot k'] \quad (1.23)$$

where k and k' are the momenta of the initial and final electron, respectively, and the mass

of electron is ignored. In the laboratory frame, one has

$$\begin{aligned}
 p &= (M, \mathbf{0}) \\
 k &= (E, \mathbf{k}) \\
 k' &= (E', \mathbf{k}') \\
 \text{and } \theta &= \widehat{(\mathbf{k}, \mathbf{k}')}
 \end{aligned} \tag{1.24}$$

It is convenient to introduce the following variables

$$\begin{aligned}
 Q^2 &= -q^2 \\
 \nu &= \frac{p \cdot q}{M} = E - E' \\
 x &= \frac{Q^2}{2p \cdot q} = \frac{Q^2}{2M\nu}, \quad \text{the Bjorken variable} \\
 y &= \frac{p \cdot q}{p \cdot k} = \frac{E - E'}{E}
 \end{aligned} \tag{1.25}$$

Then, the Eq. (1.23) becomes

$$L_{\mu\nu}^e W^{\mu\nu} = 4EE' \left\{ W_2(\nu, Q^2) \cos^2 \frac{\theta}{2} + 2W_1(\nu, Q^2) \sin^2 \frac{\theta}{2} \right\} \tag{1.26}$$

In addition, the differential cross section for inelastic $ep \rightarrow eX$ scattering is specified by

$$d\sigma = \frac{1}{4(k \cdot p)} \overline{|\mathcal{M}|^2} \frac{d^3k'}{2E'(2\pi)^3} \tag{1.27}$$

where the total quadratic amplitude

$$\overline{|\mathcal{M}|^2} = \frac{e^4}{q^4} L_{\mu\nu}^e W^{\mu\nu} 4\pi M \tag{1.28}$$

The factor $4\pi M$ plays the role of normalizing $W^{\mu\nu}$. Thanks to Eqs. (1.26), (1.27), and (1.28), one has

$$\frac{d\sigma}{dE' d\Omega} = \frac{4\alpha^2 E'^2}{q^4} \left\{ W_2(\nu, Q^2) \cos^2 \frac{\theta}{2} + 2W_1(\nu, Q^2) \sin^2 \frac{\theta}{2} \right\} \tag{1.29}$$

Historically, in 1969 SLAC experiment, scaling law was observed: the structure functions $W_{1,2}$ depend only on the ratio $x = Q^2/2M\nu$ when Q^2 , ν become very large. This phenomenon can be explained very easily if the proton is made of non-interacting point-like constituents. Let us assume that these constituents are the quarks and consider the $eq \rightarrow eq$ scattering. Its differential cross section is

$$\frac{d\sigma}{dE' d\Omega} = \frac{4\alpha^2 E'^2}{q^4} e_q^2 \left(\cos^2 \frac{\theta}{2} - \frac{q^2}{2m^2} \sin^2 \frac{\theta}{2} \right) \delta \left(\nu + \frac{q^2}{2m} \right) \tag{1.30}$$

If there are point-like constituents inside the proton, the inelastic $ep \rightarrow eX$ should behave like elastic $eq \rightarrow eq$ at large Q^2 . Therefore, the structure function can be specified by

$$\begin{aligned} 2\hat{W}_1(\nu, Q^2) &= e_q^2 \frac{Q^2}{2m^2} \delta\left(\nu - \frac{Q^2}{2m}\right) \\ \hat{W}_2(\nu, Q^2) &= e_q^2 \delta\left(\nu - \frac{Q^2}{2m}\right) \end{aligned} \quad (1.31)$$

where the " $\hat{}$ " correspond to the structure functions for the constituents and m is the mass of the constituents. It is convenient to re-write Eq. (1.31) in terms of dimensionless ones

$$\begin{aligned} 2m\hat{W}_1(\nu, Q^2) &= e_q^2 \frac{Q^2}{2m\nu} \delta\left(1 - \frac{Q^2}{2m\nu}\right) \\ \nu\hat{W}_2(\nu, Q^2) &= e_q^2 \delta\left(1 - \frac{Q^2}{2m\nu}\right) \end{aligned} \quad (1.32)$$

At this stage, one can see the dimensionless structure functions depend only on the ratio $Q^2/2m\nu$ but not on Q^2 and ν independently. Generally, if the virtual photon, at large scale Q^2 , is able to probe the constituents of the proton, then the proton structure functions become

$$\begin{aligned} MW_1(\nu, Q^2) &\xrightarrow[Q^2, \nu \text{ large, } x \text{ fixed}]{} F_1(x) \\ \nu W_2(\nu, Q^2) &\xrightarrow[Q^2, \nu \text{ large, } x \text{ fixed}]{} F_2(x) \end{aligned} \quad (1.33)$$

where x is given in Eq. (1.25).

1.2.2 Naive parton model

Let us introduce the parton momentum distribution $f_i(\xi)$ as the probability of the quark i carrying the fraction momentum ξ of proton. The obvious requirement is that the sum of all fraction ξ must be equal to 1, i.e. one has

$$\sum_i \int_0^1 \xi f_i(\xi) d\xi = 1. \quad (1.34)$$

Assuming one works in the reference frame where the proton is moving with a very large momentum, we can neglect its mass and its 4-momentum is $p = (E, \mathbf{0}, E)$. Then, the parton 4-momentum is $\hat{p} = \xi p = (\xi E, \mathbf{0}, \xi E)$. Hence,

$$\frac{Q^2}{2\hat{p} \cdot q} = \frac{Q^2}{2\xi p \cdot q} = \frac{x}{\xi} \quad (1.35)$$

If the parton with momentum fraction ξ is probed by the electron, thanks to Eqs. (1.32)

and (1.33) the dimensionless structure functions relative to this parton become

$$\begin{aligned}\hat{F}_1(\xi) &= e_q^2 \frac{x}{2\xi^2} \delta\left(1 - \frac{x}{\xi}\right) = e_q^2 \frac{1}{2} \delta(\xi - x) \\ \hat{F}_2(\xi) &= e_q^2 \xi \delta(\xi - x)\end{aligned}\quad (1.36)$$

The results for the proton dimensionless structure functions are obtained by

$$\begin{aligned}F_2(\xi) &= \sum_i \int_0^1 f_i(\xi) \hat{F}_2(\xi) d\xi = \sum_i \int_0^1 f_i(\xi) e_i^2 \xi d\xi \delta(\xi - x) \\ F_1(\xi) &= \frac{1}{2\xi} F_2(\xi)\end{aligned}\quad (1.37)$$

By redefining $F_{1,2}$ as $F_{1,2}(x)$, Eq. (1.37) can be written in terms of x as follows

$$\begin{aligned}\nu W_2(\nu, Q^2) &\xrightarrow[Q^2 \text{ large, } x \text{ fixed}]{} F_2(x) = \sum_i e_i^2 x f_i(x) \\ MW_1(\nu, Q^2) &\xrightarrow[Q^2 \text{ large, } x \text{ fixed}]{} F_1(x) = \frac{1}{2x} F_2(x)\end{aligned}\quad (1.38)$$

As one can see, the momentum fraction ξ is exactly equal to the Bjorken variable x which is given in Eq. (1.25). It means that the variable x which is relative to the virtuality of the photon is equal to the momentum fraction of the parton i which absorbs this photon. The proton structure functions given by Eq. (1.38) depend only on x . They do not depend on Q^2 at given x . This property is known as the Bjorken scaling. We emphasize that this phenomena is true when Q^2 and the invariant mass of final hadronic state are both large.

The parton model leads to $2xF_1 = F_2$ which is known as the Callan-Gross relation. It inherits from the spin- $\frac{1}{2}$ property of the quarks. In order to illustrate this point, let us consider the virtual photon-proton cross section which is [22]

$$\sigma_{\gamma^* p \rightarrow X} = \frac{4\pi^2\alpha}{K} \epsilon_\lambda^{\mu*} \epsilon_\lambda^\nu W_{\mu\nu} \quad (1.39)$$

where $K = M(1-x)/\nu$, $W^{\mu\nu}$ is given by Eq. (1.22), λ is the helicity of the polarization vectors ϵ_λ^μ of the virtual photon and those polarization vectors are specified as follows

$$\begin{aligned}\epsilon_\pm &= \mp \sqrt{\frac{1}{2}} (0; 1, \pm i, 0), \\ \epsilon_0 &= \frac{1}{\sqrt{-q^2}} (\sqrt{\nu^2 - q^2}, 0, 0, \nu).\end{aligned}\quad (1.40)$$

One can get the transverse and longitudinal cross sections as follows

$$\begin{aligned}\sigma_T &\equiv \frac{1}{2}(\sigma_+^{\text{tot}} + \sigma_-^{\text{tot}}) = \frac{4\pi^2\alpha}{K} W_1(\nu, Q^2) \\ \sigma_L = \sigma_0^{\text{tot}} &= \frac{4\pi^2\alpha}{K} \left[\left(1 + \frac{\nu^2}{Q^2}\right) W_2(\nu, Q^2) - W_1(\nu, Q^2) \right]\end{aligned}\quad (1.41)$$

As is well known, the spin- $\frac{1}{2}$ quark cannot absorb a photon of helicity $\lambda = 0$. Therefore by assuming quark has spin $\frac{1}{2}$, only the transverse cross section remains, the longitudinal one vanishes, i.e. $\sigma_L \rightarrow 0$. Then, in the limit $\nu, Q^2 \rightarrow \infty$, one has

$$\frac{\nu^2}{Q^2} W_2(\nu, Q^2) = W_1(\nu, Q^2) \quad (1.42)$$

Using $MW_1(\nu, Q^2) = F_1(x)$ and $\nu W_2(\nu, Q^2) = F_2(x)$, the Eq. (1.42) becomes

$$F_2 = \nu W_2(\nu, Q^2) = \frac{Q^2}{\nu} W_1(\nu, Q^2) = 2xF_1 \quad (1.43)$$

which is the Callan-Gross relation.

Returning to the structure functions, from Eq. (1.38), one has the proton structure function for deep inelastic scattering:

$$\frac{1}{x} F_2(x) = \left(\frac{2}{3}\right)^2 [u(x) + \bar{u}(x)] + \left(\frac{1}{3}\right)^2 [d(x) + \bar{d}(x)] + \left(\frac{1}{3}\right)^2 [s(x) + \bar{s}(x)] \quad (1.44)$$

where $u(x)$ ($\bar{u}(x)$) is the probability distributions of (anti)up quark in proton, the same for $d(x)$, $s(x)$. In the Eq. (1.44), we assume that $Q^2 \sim 1 \text{ GeV}^2$ and so we do not consider quarks with mass greater than this scale. We emphasize that the proton consists of three-valence quarks $u_v u_v d_v$ and many sea quark–antiquark pairs, e.g. $u_s \bar{u}_s$, $s_s \bar{s}_s$. The valence quarks contribute to electric charge and baryon number of the proton. Let us assume the sea quarks are radiated from the valence quarks, the sea quarks approximately have the same momentum distribution:

$$u_s(x) = \bar{u}_s(x) = d_s(x) = \bar{d}_s(x) = s_s(x) = \bar{s}_s(x) = S(x) \quad (1.45)$$

where $S(x)$ is the common distribution for each sea quark. Then the d and u distributions in the proton are

$$\begin{aligned}u(x) &= u_v(x) + u_s(x) \\ d(x) &= d_v(x) + d_s(x)\end{aligned}\quad (1.46)$$

As is well known, the quantum numbers of the proton are: electric charge = 1, baryon number = 1, strangeness number = 0. Then the parton distributions must obey to the

following sum rules

$$\begin{aligned}\int_0^1 [u(x) - \bar{u}(x)] dx &= \int_0^1 u_v(x) dx \equiv 2 \\ \int_0^1 [d(x) - \bar{d}(x)] dx &= \int_0^1 d_v(x) dx \equiv 1 \\ \int_0^1 [s(x) - \bar{s}(x)] dx &= 0\end{aligned}\quad (1.47)$$

By summing over the momenta fraction of all possible partons within the proton, one must get 1 as in Eq. (1.34). Experimentally, the sum over the possible quarks gives

$$\sum_q \int_0^1 x [q(x) + \bar{q}(x)] dx = \int_0^1 x [u_v(x) + d_v(x) + 6S] dx \simeq 1 - 0.46 \quad (1.48)$$

Thus the proton contains neutral partons besides quarks: the gluons. Since the gluon does not carry an electric charge, the photon cannot probe the gluon inside proton. However, the momentum carried by partons within proton is about ~ 0.5 as shown in Eq. (1.48). Therefore, the remaining $\sim 50\%$ momentum of proton must be carried by the gluons within the proton.

1.2.3 QCD corrections

Gluon emission

In the naive parton model described in the previous section, the probed quarks are produced along the direction of the virtual photon. As soon as the emitted gluons are taken into account, the quark can recoil against the gluons and therefore the produced jets can have a certain transverse momenta relative to the virtual photon. At this stage, beyond the naive parton model, the structure function $F_{1,2}$ no longer scale but can depend on ν and Q^2 , so they are

$$\begin{aligned}F_1 &= MW_1(\nu, Q^2) \\ F_2 &= \nu W_1(\nu, Q^2)\end{aligned}\quad (1.49)$$

where ν and Q^2 are given in Eq. (1.25). Then, by using the formulas for transverse and longitudinal $\gamma^* p$ total cross section, Eq. (1.41), one has

$$\begin{aligned}2F_1 &= \frac{\sigma_T}{\sigma_0} \\ \frac{F_2}{x} &= \frac{\sigma_T + \sigma_L}{\sigma_0}\end{aligned}\quad (1.50)$$

where σ_0 is defined by

$$\sigma_0 \equiv \frac{4\pi^2\alpha}{2MK} \simeq \frac{4\pi^2\alpha}{s} \quad (1.51)$$

where $K = M(1 - x)/\nu$. In order to relate the ratios in Eq. (1.50) to the ratio for the γ^* -parton scattering, one can consider the gluon emission

$$\gamma^*(q) + q(p_i) \rightarrow q(p_f) + g \quad (1.52)$$

where $p_i = yp$ (with p is the momentum of proton.) Analogous to the variable $x = \frac{Q^2}{2p \cdot q}$ for the γ^* -proton scattering, let us introduce

$$z \equiv \frac{Q^2}{2p_i \cdot q} = \frac{x}{y} \quad (1.53)$$

$$\frac{\sigma_T(x, Q^2)}{\sigma_0} = \sum_i \int_0^1 dz \int_0^1 dy f_i(y) \delta(x - zy) \frac{\hat{\sigma}_T(z, Q^2)}{\hat{\sigma}_0} \quad (1.54)$$

where $f_i(y)$ is the momentum distribution which is introduced in previous section, the symbol " $\hat{\sigma}$ " indicates the partonic process, the integration over z corresponds to adding up all possible gluon emission states, and the delta function takes care of the constraint $x = zy$. After performing the integration over z , one gets

$$\frac{\sigma_T(x, Q^2)}{\sigma_0} = \sum_i \int_x^1 \frac{dy}{y} f_i(y) \frac{\hat{\sigma}_T(x/y, Q^2)}{\hat{\sigma}_0} \quad (1.55)$$

and the same as for $(\sigma_T + \sigma_L)/\sigma_0$.

We want to emphasize that by ignoring all the gluon effects, one must obtain the naive parton model results from Eq. (1.55). The cross section ratio for $\gamma^*q \rightarrow q$, see Fig. 1.5,

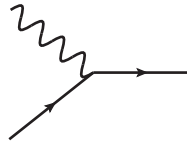


Figure 1.5: Diagrams for $\gamma^*q \rightarrow q$ scattering.

are

$$\frac{\sigma_T + \sigma_L}{\hat{\sigma}_0} = e_i^2 \delta(1 - z) \quad (1.56)$$

Then

$$\begin{aligned} \frac{F_2(x)}{x} &= \sum_i \int_0^1 \frac{dy}{y} f_i(y) e_i^2 \delta(1 - z) = \sum_i e_i^2 f_i(x) \\ 2F_1(x) &= \frac{F_2(x)}{x} \end{aligned} \quad (1.57)$$

Therefore, one does indeed re-obtain the naive parton model results as given in Eqs. (1.38).

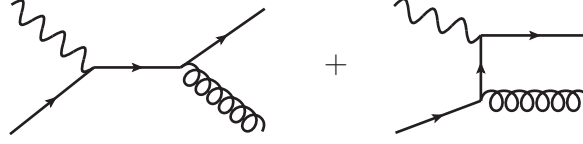


Figure 1.6: Diagrams for $\gamma^* q \rightarrow qg$ scattering.

Let us now include a gluon emission as in Fig. 1.6 and denote the invariant variables

$$\begin{aligned}\hat{s} &= (q + p_i)^2 \\ \hat{t} &= (q - p_f)^2 \\ \hat{u} &= (p_i - p_f)^2\end{aligned}\tag{1.58}$$

where q , p_i , and p_f are momenta of virtual photon, initial quark, and final quark, respectively. In the limit of $-\hat{t} \ll \hat{s}$, one gets the differential cross section

$$\frac{d\hat{\sigma}}{dp_\perp^2} = e_q^2 \hat{\sigma}_0 \frac{1}{p_\perp^2} \frac{\alpha_S}{2\pi} \tilde{P}_{qq}(z)\tag{1.59}$$

where p_\perp is the transverse momentum of the final quark with respect to the virtual photon direction, $\hat{\sigma}_0 = 4\pi^2\alpha/\hat{s}$, and $\tilde{P}_{qq}(z)$ represents the probability of finding a quark carrying a momentum fraction z from the parent quark (which emits a gluon carrying the fraction $1 - z$):

$$\tilde{P}_{qq}(z) = \frac{4}{3} \left(\frac{1+z^2}{1-z} \right)\tag{1.60}$$

The Eq. (1.59) represents a p_\perp^2 distribution of final parton jets. Therefore, the observation of high transverse momentum jets proves the presence of gluon emission.

Scaling violations

In order to study the contribution of gluon emission to structure functions, let us perform the p_\perp^2 integration in Eq. (1.59)

$$\begin{aligned}\hat{\sigma}(\gamma^* q \rightarrow qg) &= \int_{\kappa^2}^{\hat{s}/4} dp_\perp^2 \frac{d\hat{\sigma}}{dp_\perp^2} \\ &\simeq e_q^2 \hat{\sigma}_0 \left(\frac{\alpha_S}{2\pi} \tilde{P}_{qq}(z) \frac{\ln Q^2}{\kappa^2} \right)\end{aligned}\tag{1.61}$$

where the cutoff for transverse momentum κ^2 is used to regularize the divergence when $p_\perp^2 \rightarrow 0$ and we apply $\ln \hat{s}/4 \simeq \ln Q^2$ given the Q^2 is large. From Eqs. (1.55) and (1.61),

one can find the modifications for the structure function given by

$$\frac{\hat{F}_2(z, Q^2)}{z} = e_q^2 \left[\delta(1-z) + \frac{\alpha_S}{2\pi} \left(\tilde{P}_{qq}(z) \ln \frac{Q^2}{\kappa^2} \right) \right] \quad (1.62)$$

The calculation shows that the structure functions are Q^2 dependent and that the variation with Q^2 is logarithmic. In other words, the Bjorken scaling is weakly violated and this violation gives the hint for the presence of emitted gluons.

At order α_S in the cross section, one also have the distribution where the initial gluon splits into $q\bar{q}$ pair then one of them couples to virtual photon as in the $\gamma^* g \rightarrow q\bar{q}$ scattering (see Fig. 1.7).

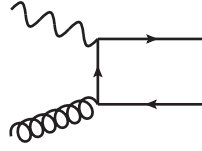


Figure 1.7: An example for $\gamma^* g \rightarrow q\bar{q}$ probing.

This process also contributes to the scaling violation of the structure function as

$$\frac{\hat{F}_2(z, Q^2)}{z} = e_q^2 \frac{\alpha_S}{2\pi} \left(\tilde{P}_{qg}(z) \ln \frac{Q^2}{\kappa^2} \right) \quad (1.63)$$

where the gluon splitting function $\tilde{P}_{qg}(z)$ is given by

$$\tilde{P}_{qg}(z) = \frac{1}{2} (z^2 + (1-z)^2) \quad (1.64)$$

Again, beyond naive parton model, the scaling violation via Eq. (1.63) is a signature of probing the gluon distribution inside proton.

Scale dependence of parton densities

By using the dimensional regularization method, where space-time is treated to be of dimension $n = 4 - 2\epsilon$ with $\epsilon > 0$, one can calculate the full α_S correction to the structure functions $F_{1,2}(z, Q^2)$ as the following [23, 24].

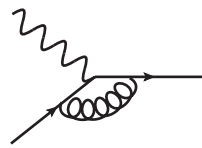


Figure 1.8: An example for $\gamma^* g \rightarrow q\bar{q}$ scattering.

The processes such as in Figs. 1.5, 1.6, and 1.8 contribute to quark structure functions

as

$$\frac{\hat{F}_2^q(z, Q^2)}{z} = e_q^2 \left[\delta(1-z) + \frac{\alpha_S}{2\pi} \left\{ -\frac{1}{\epsilon} P_{qq}(z) \left(\frac{4\pi\mu^2}{Q^2} \right)^\epsilon \frac{\Gamma(1-\epsilon)}{\Gamma(1-2\epsilon)} + \tilde{c}_{qq}(z) \right\} \right] \quad (1.65)$$

where $P_{qq}(z)$, $\tilde{c}_{qq}(z)$, and $\Gamma(z)$ are given in appendix A.2 and μ is an arbitrary scale coming from

$$e_n = e \mu^{2-\frac{n}{2}}, \quad [\mu] = 1. \quad (1.66)$$

and e (e_n) is the electric charge in 4 (n) spacetime dimensions. The $1/\epsilon$ term in Eq. (1.65) arises when the gluon emitted parallel to the quark $p_\perp = 0$ due to the dimensional regularization. This divergence is known as the quark-gluon collinear divergence (singularity).⁵ We notice that the gluon emission as in Figs. 1.6 gives rise to a divergence when $z \rightarrow 1$ (soft gluon singularity), see Eqs. (1.59) and (1.60). This divergence cancels with the divergence coming from virtual process as diagram in Fig. 1.8.

One can expand Eq. (1.65) in series of power of ϵ and gets

$$\begin{aligned} \frac{\hat{F}_2^q(z, M^2)}{z} = e_q^2 \left[\delta(1-z) + \frac{\alpha_S}{2\pi} \left\{ P_{qq}(z) \left(-\frac{1}{\epsilon} - \ln(4\pi) + \gamma_E \right. \right. \right. \\ \left. \left. \left. + \ln\left(\frac{M^2}{\mu^2}\right) \right) + c_{qq}(z) \right\} \right] \end{aligned} \quad (1.67)$$

where we introduce a scale M^2 which is of order of Q^2 then redefine a M^2 dependent structure function $\hat{F}_2^q(z, M^2)$ and put $c_{qq}(z) = \tilde{c}_{qq}(z) + P_{qq}(z) \ln\left(\frac{Q^2}{M^2}\right)$, and γ_E is the Euler constant.

The processes such as diagram in Fig. 1.7 contribute to the structure function as follows

$$\begin{aligned} \frac{\hat{F}_2^g(z, M^2)}{z} = \sum_q e_q^2 \left[\frac{\alpha_S}{2\pi} \left\{ P_{qg}(z) \left(-\frac{1}{\epsilon} - \ln(4\pi) + \gamma_E \right. \right. \right. \\ \left. \left. \left. + \ln\left(\frac{M^2}{\mu^2}\right) \right) + c_{qg}(z) \right\} \right] \end{aligned} \quad (1.68)$$

where $c_{qg}(z) = \tilde{c}_{qg}(z) + P_{qg}(z) \ln\left(\frac{Q^2}{M^2}\right)$, and the calculable quantities $P_{qg}(z)$ and $\tilde{c}_{qg}(z)$ are given in Eqs. (A.18) and (A.23), respectively. The term $1/\epsilon$ in \hat{F}_2^g , Eq. (1.68), is related to the quark-antiquark collinear singularity.

By convoluting $\hat{F}_2^{q,g}$ with the quark distributions, introduced in section 1.2.2, and summing over the quark flavors one can calculate the proton structure, see Eq. (1.55), as

5. Those quantities $P_{qq}(z)$ and $\tilde{c}_{qq}(z)$ are calculable and finite, see Eqs (A.17) and (A.22).

follows

$$\begin{aligned} \frac{F_2(x, M^2)}{x} &= \int_x^1 \frac{dy}{y} \left[\sum_q q(y) \frac{\hat{F}_2^q(x/y, M^2)}{x/y} + g(y) \frac{\hat{F}_2^g(x/y, M^2)}{x/y} \right] \\ &= \sum_q e_q^2 q(x, M^2) + \dots \end{aligned} \quad (1.69)$$

where the \dots means terms of order α_S . We have introduced the scale dependence distribution $q(x, M^2)$ which is defined by [25]

$$\begin{aligned} q(x, M^2) &= q(x) + \frac{\alpha_S}{2\pi} \int_x^1 \frac{dy}{y} q(y) \left\{ P_{qq}\left(\frac{x}{z}\right) \left[-\frac{1}{\epsilon} - \ln(4\pi) + \gamma_E + \ln\left(\frac{M^2}{\mu^2}\right) \right] \right. \\ &\quad \left. + f_{qq}\left(\frac{x}{z}\right) \right\} + \frac{\alpha_S}{2\pi} \int_x^1 \frac{dy}{y} g(y) \left\{ P_{qg}\left(\frac{x}{z}\right) \left[-\frac{1}{\epsilon} - \ln(4\pi) + \gamma_E \right. \right. \\ &\quad \left. \left. + \ln\left(\frac{M^2}{\mu^2}\right) \right] + f_{qg}\left(\frac{x}{z}\right) \right\} \end{aligned} \quad (1.70)$$

where $f_{qq}(z)$ $f_{qg}(z)$ are arbitrary functions which define the factorization scheme. In fact, we regard $q(x)$, $g(x)$ as the bare distribution which are unmeasurable. Then the collinear singularities are absorbed into this bare distribution at a factorization scale M and therefore the redefined distribution depends on scale M , which plays the same role as renormalized scale. The $q(x, M^2)$ can be determined by comparison with structure function data in given $\{x, M^2\}$ thanks to Eq. (1.69).

Note that the renormalized quark distribution function is not unique. It depends on the finite part which also can be absorbed into the redefined distribution (besides the singular part $1/\epsilon$). In the \overline{MS} scheme, $f_{qq}(z) = f_{qg}(z) = 0$. In another scheme called DIS (Deep Inelastic Scattering), the relations valid in the naive parton model are required to remain at every order. In our case, from Eq. (1.69), this implies that $f_{qq}(z) = c_{qq}(z)$ and $f_{qg}(z) = c_{qg}(z)$.

Let us briefly interpret the scale dependence of the quark distribution. Assuming up to scale M_0 the photon starts to see the valence quarks inside the proton. If the quarks do not interact, the proton structure would not change when M increases then it gives rise the naive parton model. However, when one increases the resolution, each valence quark is seen to be surround by the cloud of partons due to QCD radiations. In other words, there are also sea quarks at higher scale M and therefore the number of probed partons carrying a low fraction momentum x of the proton increases with M . Indeed, there is more chance to find a parton at small x than at large x because the gluon bremsstrahlung degrade the high momentum quarks.

1.2.4 Altarelli-Parisi equation

The parton distributions cannot be predicted from perturbative QCD. Only the M evolution of these distributions can be computed by theory. Assuming the parton distributions are given at the scale M_0 . For an arbitrary scale, let us denote $t = \ln(M^2/M_0^2)$ and take the t partial derivative of Eq. (1.70), then we get

$$\frac{dq(x, t)}{dt} = \frac{\alpha_S(t)}{2\pi} \int_x^1 \frac{dy}{y} \left[q(y, t) P_{qq}\left(\frac{x}{y}\right) + g(y, t) P_{qg}\left(\frac{x}{y}\right) \right] \quad (1.71)$$

This is a DGLAP evolution equation [26]. It plays the role of the renormalization group equation, Eq. (1.6), which describes the variation of α_S with t . Eq. (1.71) illustrates the fact that a quark with momentum fraction x comes from a parent quark (gluon) with larger momentum fraction, y , which emits gluon (splits into $q\bar{q}$ pair).

In general, the DGLAP equation is a matrix equation in the quarks, antiquarks, and gluons space as follows

$$\frac{\partial}{\partial t} \begin{pmatrix} q(x, t) \\ g(x, t) \end{pmatrix} = \frac{\alpha_S(t)}{2\pi} \int_z^1 \frac{dy}{y} \begin{pmatrix} P_{qq}\left(\frac{x}{y}, \alpha_S(t)\right) & P_{gq}\left(\frac{x}{y}, \alpha_S(t)\right) \\ P_{qg}\left(\frac{x}{y}, \alpha_S(t)\right) & P_{gg}\left(\frac{x}{y}, \alpha_S(t)\right) \end{pmatrix} \begin{pmatrix} q(y, t) \\ g(y, t) \end{pmatrix} \quad (1.72)$$

where the kernels P_{ij} [27, 28], the splitting functions, are expanded as a power series in α_S as follows

$$P_{ij}(z, \alpha_S) = P_{ij}^{(0)}(z) + \frac{\alpha_S}{2\pi} P_{ij}^{(1)}(z) + \dots \quad (1.73)$$

This kernel of DGLAP equation represents the probability for finding a parton (type i) carrying a fraction of momentum z from its parent parton (type j). At the LO, the DGLAP kernel $P_{ij}(z)$ physically represents this probability. The LO kernels $P_{ij}(z)$ are given appendix A.2.

For the simplest case where there is only one flavor of quarks, consider the non-singlet quark distribution which is defined by

$$q^{NS}(x, t) = q(x, t) - \bar{q}(x, t) \quad (1.74)$$

The q^{NS} represents the net number of quarks seen within the proton. The gluon density does not couple to this quantity because the quark and antiquark couple in the same way to the gluon. The corresponding DGLAP equation is

$$\frac{d}{dt} q^{NS}(x, t) = \frac{\alpha_S}{2\pi} \int_x^1 \frac{dy}{y} q^{NS}(y, t) P_{qq}\left(\frac{x}{y}, \alpha_S\right) \quad (1.75)$$

To solve this equation one can use the Mellin transform method, which is given by:

$$f(n) = \int_0^1 dx x^{n-1} f(x) \quad (1.76)$$

In Mellin space, the Eq. (1.75) becomes

$$\frac{d}{dt} q_n^{NS}(t) = \frac{\alpha_S(t)}{2\pi} q_n^{NS}(t) \gamma_{qq}(n, \alpha_S(t)) \quad (1.77)$$

and the solution is given by

$$q_n^{NS}(t) = q_n^{NS}(0) \exp \left[\int_0^t dx \frac{\alpha_S(x)}{2\pi} \gamma_{qq}(n, \alpha_S(x)) \right] \quad (1.78)$$

where γ_{qq} is the Mellin transform of kernel P_{qq} . As discussed in section 1.1, the running coupling α_S , can be specified by the following formula

$$\alpha_S(t) = \frac{\alpha_S(0)}{1 + \alpha_S(0) bt} \quad (1.79)$$

where $b = \frac{11N-2n_f}{12\pi}$ with N and n_f are the number of colors and flavors, respectively. Thanks to the Eq. (1.79), at leading logarithmic (LL) approximation, a solution given in Eq. (1.78) can be computed as

$$q_n^{NS}(t) = q_n^{NS}(0) \exp \left[\frac{\gamma_{qq}(n)}{2\pi b} \ln \left(\frac{\alpha_S(0)}{\alpha_S(t)} \right) \right] \quad (1.80)$$

In the perturbative region where $\alpha_S(t) \ll 1$, one has the expansion

$$\begin{aligned} \ln \left(\frac{\alpha_S(0)}{\alpha_S(t)} \right) &= \ln(1 + \alpha_S(0) bt) \\ &\approx \alpha_S(0) bt - \frac{1}{2} \alpha_S^2(0) (bt)^2 + \dots \end{aligned} \quad (1.81)$$

Therefore, one can expand $q_n^{NS}(t)$, Eq. (1.80) in a series of power of $\alpha_S(0)$ as follows

$$q_n^{NS}(t) = q_n^{NS}(0) \left[1 + \frac{\gamma_{qq}(n)}{2\pi b} \alpha_S(0) bt + \frac{\gamma_{qq}(n)}{2\pi b} \left(\frac{\gamma_{qq}(n)}{2\pi b} - 1 \right) \alpha_S^2(0) (bt)^2 + \dots \right] \quad (1.82)$$

As one can see in Eq. (1.82), the logarithmic terms of M^2/M_0^2 are automatically resummed in the perturbation theory by using the redefined distribution functions.

Let us consider the Mellin transform of the non-singlet proton cross section, it can be written as follows

$$\sigma_n(Q^2) = \int_0^1 dx x^{n-1} \frac{d\sigma}{dx dQ^2} = \hat{\sigma}_n(Q^2) q_n^{NS}(t). \quad (1.83)$$

The partonic cross section $\hat{\sigma}$ stands for cross section related to the reactions involving

electron and partons. If this partonic cross section is calculated at LO, the partonic densities are evolved in the leading logarithmic (LL) approximation. If $\hat{\sigma}$ is computed in the NLO approximation, the partonic densities must be evolved in the next to leading-logarithmic (NLL) approximation. In short, the DGLAP kernels have to be at the same order of α_S as the calculated cross section.

1.2.5 PDF sets

In this section, we briefly discuss the data used to constrain PDFs and the status of some available PDF sets. The possible processes which can be used to determine the PDFs are listed in Table 1.1.

Table 1.1: The main processes associated with global PDF analyses are ordered in three groups: fixed-target experiments, HERA and $p\bar{p}$ (pp) Tevatron (LHC). Their dominant subprocesses, the primary partons which are probed, and the approximated range of x allowed by data are shown. Taken from Refs. [29, 19].

Process	Subprocess	Partons	x range
$\ell^\pm \{p, n\} \rightarrow \ell^\pm X$	$\gamma^* q \rightarrow q$	q, \bar{q}, g	$x \gtrsim 0.01$
$\ell^\pm n/p \rightarrow \ell^\pm X$	$\gamma^* d/u \rightarrow d/u$	d/u	$x \gtrsim 0.01$
$pp \rightarrow \mu^+ \mu^- X$	$u\bar{u}, d\bar{d} \rightarrow \gamma^*$	\bar{q}	$0.015 \lesssim x \lesssim 0.35$
$pn/pp \rightarrow \mu^+ \mu^- X$	$(u\bar{d})/(u\bar{u}) \rightarrow \gamma^*$	\bar{d}/\bar{u}	$0.015 \lesssim x \lesssim 0.35$
$\nu(\bar{\nu}) N \rightarrow \mu^-(\mu^+) X$	$W^* q \rightarrow q'$	q, \bar{q}	$0.01 \lesssim x \lesssim 0.5$
$\nu N \rightarrow \mu^- \mu^+ X$	$W^* s \rightarrow c$	s	$0.01 \lesssim x \lesssim 0.2$
$\bar{\nu} N \rightarrow \mu^+ \mu^- X$	$W^* \bar{s} \rightarrow \bar{c}$	\bar{s}	$0.01 \lesssim x \lesssim 0.2$
$e^\pm p \rightarrow e^\pm X$	$\gamma^* q \rightarrow q$	g, q, \bar{q}	$0.0001 \lesssim x \lesssim 0.1$
$e^+ p \rightarrow \bar{\nu} X$	$W^+ \{d, s\} \rightarrow \{u, c\}$	d, s	$x \gtrsim 0.01$
$e^\pm p \rightarrow e^\pm c\bar{c} X, b\bar{b} X$	$\gamma^* c \rightarrow c, \gamma^* g \rightarrow c\bar{c}$	c, b, g	$0.0001 \lesssim x \lesssim 0.01$
$e^\pm p \rightarrow \text{jet} + X$	$\gamma^* g \rightarrow q\bar{q}$	g	$0.01 \lesssim x \lesssim 0.1$
$p\bar{p}, pp \rightarrow \text{jet} + X$	$gg, qg, q\bar{q} \rightarrow 2j$	g, q	$0.01 \lesssim x \lesssim 0.5$
$p\bar{p} \rightarrow (W^\pm \rightarrow \ell^\pm \nu) X$	$ud \rightarrow W^+, \bar{u}\bar{d} \rightarrow W^-$	u, d, \bar{u}, \bar{d}	$x \gtrsim 0.05$
$pp \rightarrow (W^\pm \rightarrow \ell^\pm \nu) X$	$u\bar{d} \rightarrow W^+, d\bar{u} \rightarrow W^-$	u, d, \bar{u}, \bar{d}	$x \gtrsim 0.001$
$p\bar{p}(pp) \rightarrow (Z \rightarrow \ell^+ \ell^-) X$	$uu, dd, \dots (u\bar{u} \dots) \rightarrow Z$	$u, d \dots$	$x \gtrsim 0.001$
$pp \rightarrow (\gamma^* \rightarrow \ell^+ \ell^-) X$	$u\bar{u}, d\bar{d}, \dots \rightarrow \gamma^*$	\bar{q}	$x \gtrsim 10^{-5}$
$pp \rightarrow b\bar{b} X$	$gg \rightarrow b\bar{b}$	g	$x \gtrsim 10^{-5}$
$pp \rightarrow \gamma X$	$gq \rightarrow \gamma q, g\bar{q} \rightarrow \gamma \bar{q}$	g	$x \gtrsim 10^{-5}$

A couple of decades ago, there were few attempts to extract PDF based on global fits. These first attempts had been performed at LO, e.g the fits in Ref. [30] included data on deep-inelastic scattering [31, 32, 33], dimuon mass distributions [34], and x_F distributions of J/ψ produced in pN collisions [35]. Later on, based on NLO analyses, the

PDFs, such as MRS [36] (using deep-inelastic μN and νN scattering), ABFOW [2] (using deep-inelastic μN scattering and large p_{\perp} prompt photon in hadronic collisions) were extracted. Thanks to the hadronic data the gluon distribution is better constrained. At the end of 90s and in the beginning of 2000s, the deep-inelastic measurements of proton structure function F_2 from HERA data provided further constraints on the parton distributions, especially on the gluon distribution at low x , low Q^2 regime. Those measurements were taken into account in PDF sets such as CTEQ5 [37] (used H1 [38], ZEUS [39]), MRST2001 [40] (used H1 [41], ZEUS [42]). At the same time, the data in $p\text{-}\bar{p}$ collisions from D0, CDF collaborations at Tevatron ($\sqrt{s} = 1.8$ TeV) were available and offered further constraints on PDFs. The measurements of lepton charged asymmetry in W -production constrain the ratio of d and u quark PDFs. In addition, inclusive large p_{\perp} jet production at the Tevatron especially provided a much more reliable experimental constraint on the gluon distribution. Those data were also included in CTEQ5 (such as D0 [43], CDF [44]) and MRST2001 (such as D0 [45], CDF [46]).

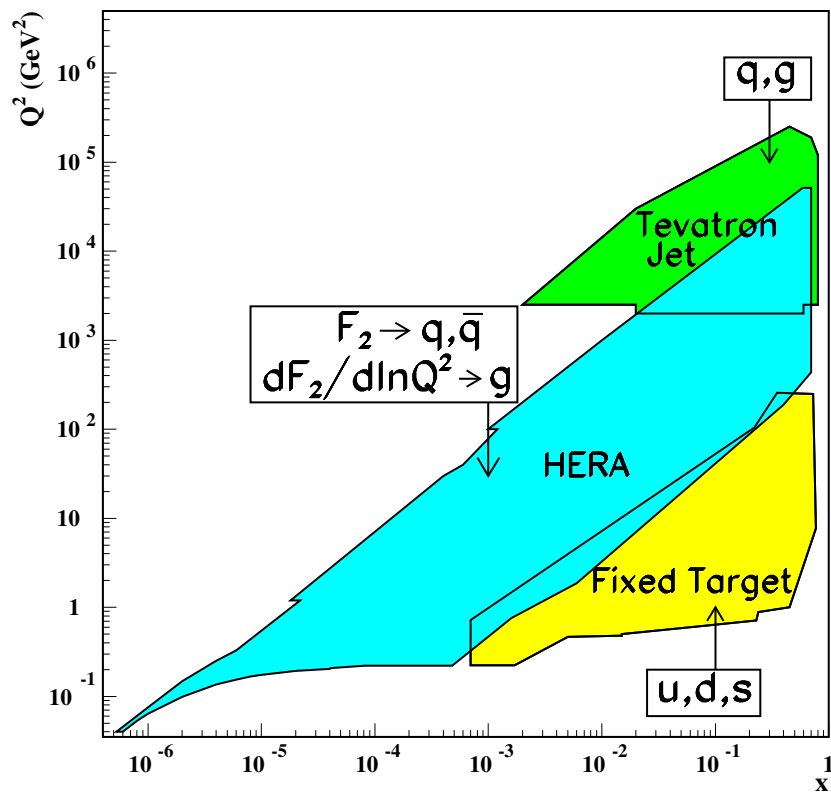


Figure 1.9: Kinematic domains in (x, Q^2) plane given by fixed-target and collider experiments. Taken from Ref. [19].

The current PDFs are extracted from experimental measurements of various physical processes, which provide the determination of different PDFs and their fits in various

kinematical regions. One can find the available PDF sets on the LHAPDF interface [47]. Various groups extract PDF from global fits of data, for instance MSTW [29], CTEQ/CT (CTEQ6.6 [48], CT10 [49]), and NNPDF [50]. They fit a full range of types of data that are available including HERA and fixed-target DIS data, fixed-target Drell-Yan production, and Tevatron data on W , Z , and jet production ($\sqrt{s} = 1.96$ TeV). The kinematic range given by those experiments enables the determination of PDFs over six orders of magnitude in both x and Q^2 as shown in Fig. 1.9. The fixed-target data with charged lepton and neutrino DIS experiments and proton beams on nuclear targets provide the PDF probe in the region of low Q^2 and large x . The data at HERA allows to extract PDF in a wide kinematical range, complementary to fixed-target and Tevatron experiments because they include the low x low Q^2 region. The high energy region $Q^2 \sim 3 \cdot 10^5$ GeV² is provided by $p\bar{p}$ collider data at Tevatron via inclusive jet measurements. As an illustration for recent PDFs set, a typical (MSTW08) PDFs at two scales $Q^2 = 10$ and 10^4 (GeV²) is shown in Fig. 1.10. As one can see, the uncertainties are rather small, except at very small x ($\sim 10^{-4}$).

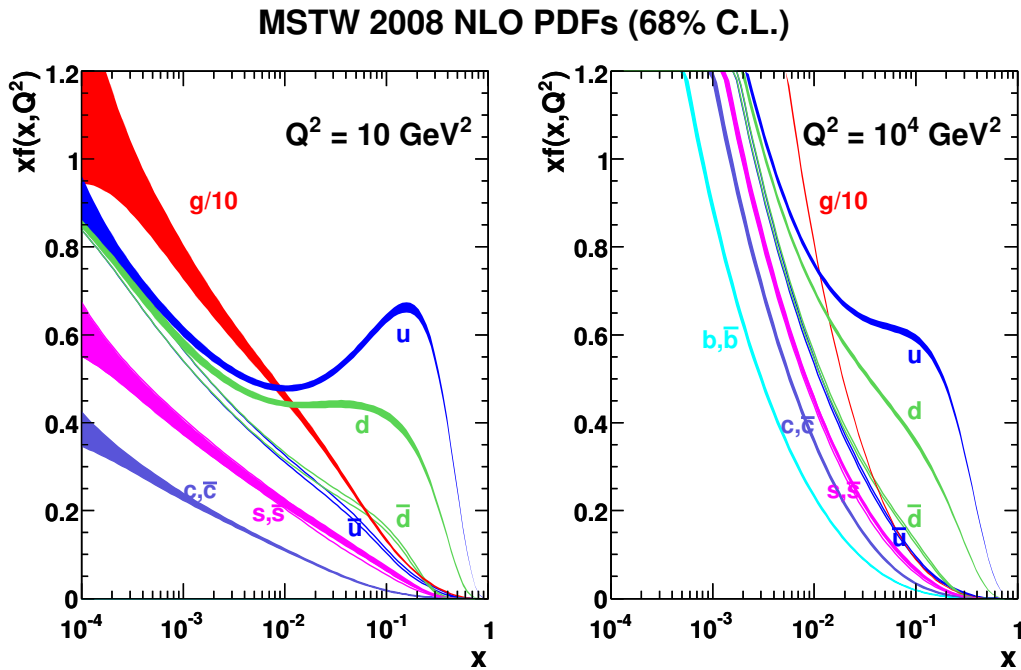


Figure 1.10: MSTW 2008 NLO PDFs at $Q^2 = 10$ GeV² and $Q^2 = 10^4$ GeV². Taken from Ref. [29].

Since PDFs become a tool to study physical processes which involve hadron in initial state, especially for prediction in pp collisions at LHC experiment, it is necessary to determine an estimate of their uncertainties. The PDFs with uncertainties which are performed by the MSTW and CTEQ sets are based on the tolerance method, while the one from NNPDF follows a Monte Carlo approach [51, 52]. The comparison between the uncertainties of those sets are illustrated in Fig. 1.11. The strange-quark densities $s^+ = s + \bar{s}$

and $s^- = s - \bar{s}$ predicted by these three sets are very different. In fact, CTEQ and MSTW

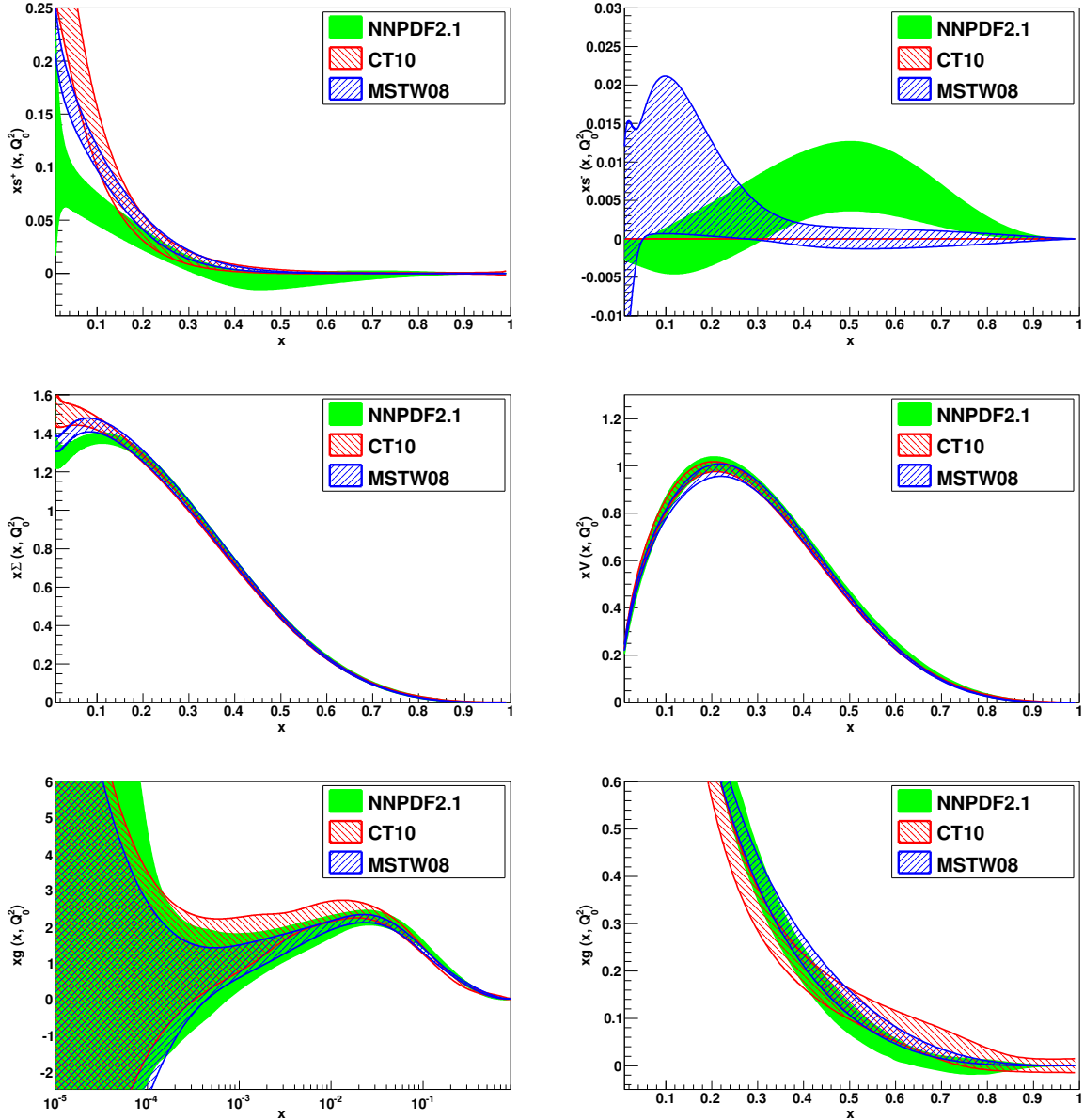


Figure 1.11: Comparison between MSTW, CTEQ, and NNPDF PDF sets at $Q^2 = 2 \text{ GeV}^2$. Taken from Ref. [53].

sets use a certain assumption on the shape of s^+ , while NNPDF makes no assumptions on strangeness density. Therefore, it contributes to the disagreement of strange quark densities prediction from those sets. The agreement for the singlet density $\Sigma = \sum(q + \bar{q})$ as well as total valence distribution $V = u_v + d_v$ at large x are very good. Besides, the various determination of gluon densities agree well at low and medium x , but at high x they are sizably different. In fact, the gluon does not couple with electroweak final states and it is mostly determined by scaling violations, or by its strongly-coupling final state-jet,

especially at small x . This leads to the fact that the large x gluon density is poorly known.

We want to emphasize that the heavy quark densities are smaller than light quark densities (see Fig. 1.10) and therefore, they are difficult to extract in processes involving also light quarks or gluons in the initial states. On the other hand, looking at photon production in association with heavy-flavor jet may help to put more constraints on heavy-quark PDF. This point will be discussed in chapter 4.

1.3 Fragmentation Functions

1.3.1 Theoretical content

The hadronic production process in the electron-positron annihilation gives an important illustration for QCD understanding [54]. In e^+e^- annihilation, the lowest order diagram to produce hadrons is $e^+e^- \rightarrow q\bar{q}$, Fig. 1.12(a). According to QCD, right after

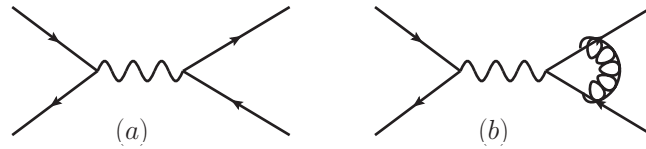


Figure 1.12: The $e^+e^- \rightarrow q\bar{q}$ process. (a) the Born contribution and (b) one of the virtual correction.

being created, the quark and the antiquark begin to separate themselves. Each of them carries momentum $\frac{q^2}{2}$, in the center of mass frame. The color force between them increases when the distance increases until the increasing potential energy is significant enough to create another pair of quark and antiquark. At later times more $q\bar{q}$ pairs are produced and they interact themselves [22]. Subsequently, the quarks and antiquarks combine into hadrons in the final state. Given the e^+e^- process has a pure QED initial state, its hadronic production is considered as a clean process to study the hadronization of quarks and gluons.

The total cross section at Born level [55] is

$$\sigma_B = N \frac{4\pi\alpha^2}{3q^2} e_i^2 \quad (1.84)$$

where N is the number of color charges for the quarks, e_i is the charge of the quark i in unit of e , α is the electromagnetic coupling, and q^2 is center of mass energy. The higher order corrections include virtual terms such as in Fig. 1.12(b) and real emission terms (see Fig. 1.13). Assuming the dimensional regularization is used to regularize the UV and IR

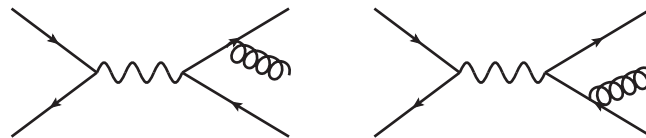


Figure 1.13: The real emission correction to the $e^+e^- \rightarrow q\bar{q}$ process.

divergences and after dealing with the UV renormalization, the total virtual cross section

is given by:

$$\begin{aligned} \sigma_v &= \sigma_B \frac{\alpha_S}{2\pi} C_F \left(\frac{4\pi\mu^2}{q^2} \right)^{-\epsilon_{ir}} \frac{\Gamma(1 - \epsilon_{ir}) \Gamma^2(1 + \epsilon_{ir})}{\Gamma(1 + 2\epsilon_{ir})} \\ &\times \left\{ -\frac{2}{\epsilon_{ir}^2} + \frac{3}{\epsilon_{ir}} - 8 + \pi^2 + \mathcal{O}(\epsilon_{ir}) \right\} \end{aligned} \quad (1.85)$$

where $C_F = \frac{4}{3}$ is the color factor, μ is the renormalization scale, $\epsilon_{ir} = \frac{1}{2}(n - 4)$, and $\Gamma(z)$ is the gamma function given appendix A.2. Let us introduce the reduce energy $z_i = 2\frac{E_i}{\sqrt{q^2}}$, with $i = 3, 4, 5$ corresponding to the q , the \bar{q} and the g in the final state. The constraint on energy conservation leads to the condition: $z_3 + z_4 + z_5 = 2$. Assuming the quarks are massless, then one has

$$\begin{aligned} 2 p_4 \cdot p_5 &= q^2 (1 - z_3) \\ 2 p_3 \cdot p_5 &= q^2 (1 - z_4) = q^2 (z_3 + z_5 - 1) = q^2 z_3 (1 - t) \\ 2 p_3 \cdot p_4 &= q^2 (1 - z_5) = q^2 z_3 t \end{aligned} \quad (1.86)$$

where t is given by $z_5 = 1 - z_3 t$. The cross section for the real emission contribution is given by

$$\begin{aligned} \sigma_R &= g^2 \mu^{4-n} C_F \frac{1}{(2\pi)^{n-1}} \frac{\pi^{(n-2)/2}}{2 \Gamma((n-2)/2)} (q^2)^{(n-4)/2} \sigma_B \\ &\times \int_0^1 dz_3 z_3^{n-3} (1 - z_3)^{(n-4)/2} \int_0^1 dt t^{(n-4)/2} (1 - t)^{(n-4)/2} \\ &\times \left\{ (n-2) \frac{1 - z_3}{z_3 (1 - t)} + (n-2) \frac{z_3 (1 - t)}{1 - z_3} + \frac{4t}{(1 - z_3)(1 - t)} + 2(n-4) \right\} \end{aligned} \quad (1.87)$$

It is clear that, the Eq. (1.87) seems singular when $t = 1$ and $z_3 = 1$ but these singularities are regularized for $n > 4$ ($\epsilon_{ir} > 0$). From a more detailed calculation, one knows that those singular points correspond to $E_5 = 0$ or/and $\vec{p}_3 // \vec{p}_5$ ($\vec{p}_4 // \vec{p}_5$). After performing the integration, the total real emission cross section becomes

$$\begin{aligned} \sigma_R &= \sigma_B \frac{\alpha_S}{2\pi} C_F \left(\frac{4\pi\mu^2}{q^2} \right)^{-\epsilon_{ir}} \frac{\Gamma(1 - \epsilon_{ir}) \Gamma^2(1 + \epsilon_{ir})}{\Gamma(1 + 2\epsilon_{ir})} \\ &\times \left\{ \frac{2}{\epsilon_{ir}^2} - \frac{3}{\epsilon_{ir}} + \frac{19}{2} - \pi^2 + \mathcal{O}(\epsilon_{ir}) \right\} \end{aligned} \quad (1.88)$$

As one can see in Eq. (1.88), the real correction contains terms which are proportional to ϵ_{ir}^{-2} and ϵ_{ir}^{-1} , which become divergent when $\epsilon_{ir} \rightarrow 0$. These divergences are related to $t = 1$ or/and $z_3 = 1$ in Eq. (1.87). In other words, the total real emission cross section is divergent when the gluon is soft or/and is collinear to the other partons.

The total cross section of the process $e^+e^- \rightarrow$ hadrons including the QCD corrections

of order α_S is given by

$$\begin{aligned}\sigma &= \sigma_B + \sigma_R + \sigma_v \\ &= \sigma_B \left(1 + \frac{\alpha_S(q^2)}{\pi} + \mathcal{O}(\alpha_S^2) \right)\end{aligned}\quad (1.89)$$

thanks to Eqs. (1.84), (1.85), and (1.88). In the massless quark limit we used above, the cancellation of the soft and collinear divergences among the real and virtual contributions is not accidental. In fact, it is a consequence of the Kinoshita-Lee-Nauenberg (KLN) theorem, which states that the inclusive degenerate observables (where one takes into account all possible configuration in the final state) are free of singularities. The single inclusive parton cross section is not of that kind. Therefore, a suitable procedure, as the following, is required in order to get rid of the divergences.

To describe the hadronization of quarks and gluons, one can use an analogous formalism as the one used for PDF. As shown in Fig. 1.14, one introduces the quantity $\mathcal{D}_{0,q/g}^h(z_h)$

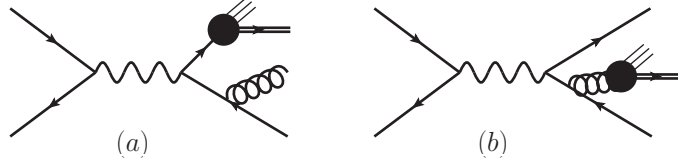


Figure 1.14: The single hadron production from e^+e^- annihilation. (a) $e^+e^- \rightarrow gq\mathcal{D}_q^h$ and (b) $e^+e^- \rightarrow q\bar{q}\mathcal{D}_{\bar{q}}^h$.

to describe the probability of having a parton of energy E which fragments into a hadron carrying a fraction of energy,

$$z_h = \frac{E_h}{E}. \quad (1.90)$$

Note that, if we neglect all the masses at parton and hadron level then z_h is also the fraction of 4-momentum. Thus, the differential cross section for the process $e^+e^- \rightarrow hX$ can be written as

$$\begin{aligned}\frac{d\sigma}{dz_h} &= \sum_{flavour} \left[\int_{z_h}^1 \frac{dz}{z} \mathcal{D}_{0,q}^h(z) \frac{d\sigma(e^+e^- \rightarrow qX)}{dz_p} + \int_{z_h}^1 \frac{dz}{z} \mathcal{D}_{0,\bar{q}}^h(z) \frac{d\sigma(e^+e^- \rightarrow \bar{q}X)}{dz_p} \right] \\ &\quad + 2 \int_{z_h}^1 \frac{dz}{z} \mathcal{D}_{0,g}^h(z) \frac{d\sigma(e^+e^- \rightarrow gX)}{dz_p}\end{aligned}\quad (1.91)$$

where

$$z_p = \frac{z_h}{z}. \quad (1.92)$$

The quark and anti quark differential cross sections are identical and equal to

$$\frac{d\sigma(e^+e^- \rightarrow q_i X)}{dz_p} = \sigma_B \left[\delta(1 - z_p) + \frac{\alpha_S}{2\pi} \left\{ K(\epsilon_{ir}) P_{qq}(z_p) \frac{1}{\epsilon_{ir}} + b_{qq}(z_p) \right\} \right] \quad (1.93)$$

where σ_B is given by Eq. (1.84) and $P_{qq}(z)$, $K(\epsilon_{ir})$, and $b_{qq}(z_p)$ are given in Eqs. (A.17), (A.25), and (A.27), respectively. The gluon differential cross section is

$$\frac{d\sigma(e^+e^- \rightarrow gX)}{dz_p} = \left(\sum_{flavour} \sigma_B \right) \frac{\alpha_S}{2\pi} \left\{ K(\epsilon_{ir}) P_{gq}(z_p) \frac{1}{\epsilon_{ir}} + b_{gq}(z_p) \right\} \quad (1.94)$$

where $P_{gq}(z)$ and $b_{gq}(z_p)$ is given in Eqs. (A.19) and (A.28).

By substituting Eqs. (1.93) and (1.94) to Eq. (1.91), one gets that the hadron differential cross section has a singularity when $\epsilon_{ir} \rightarrow 0$: the term which contains $\frac{1}{\epsilon_{ir}}$. In fact, this singularity comes from the configurations where the gluon is collinear to the quark or the anti quark. (The soft singularity no longer takes place due to its cancellation between the real and virtual contributions for (anti)quark differential cross sections.) Let us call $\mathcal{D}_{0,q(\bar{q})}^h(z)$ the bare FFs of (anti)quark. One can redefine the bare FFs so that the collinear divergences are absorbed into the FFs at a certain scale, say M_F , as follows

$$\begin{aligned} \mathcal{D}_q^h(z, M_F^2) = & \int_z^1 \frac{dy}{y} \left[\mathcal{D}_{0,q}^h(y) \delta\left(1 - \frac{z}{y}\right) \right. \\ & \left. + \frac{\alpha_S}{2\pi} K(\epsilon_{ir}) \frac{1}{\epsilon_{ir}} \left(P_{qq}\left(\frac{z}{y}\right) \mathcal{D}_{0,q}^h(y) + P_{gq}\left(\frac{z}{y}\right) \mathcal{D}_{0,g}^h(y) \right) \right] \end{aligned} \quad (1.95)$$

In terms of the FFs of quarks, the single hadron differential cross section, in Eq. (1.91), is re-written as

$$\begin{aligned} \frac{d\sigma}{dz_h} = & \sigma_0 \sum_{flavour} \int_{z_h}^1 \frac{dz}{z} e_q^2 \left(\mathcal{D}_q^h(z, M_F^2) + \mathcal{D}_{\bar{q}}^h(z, M_F^2) \right) \hat{\sigma}_q(z_p) \\ & + 2 \sum_{flavour} e_q^2 \int_{z_h}^1 \frac{dz}{z} \mathcal{D}_g^h(z, M_F^2) \hat{\sigma}_g(z_p) \end{aligned} \quad (1.96)$$

where

$$\sigma_0 = N \frac{4\pi\alpha^2}{3q^2} \quad (1.97)$$

$$\hat{\sigma}_q = \delta(1 - z_p) + \frac{\alpha_S}{2\pi} b_{qq}(z_p) \quad (1.98)$$

$$\hat{\sigma}_g = \frac{\alpha_S}{2\pi} b_{gq}(z_p)$$

(thus, thanks to Eq. (1.84) one gets $\sigma_B = \sigma_0 e_i^2$.) Instead of the scale-independent bare FFs, the scale-dependent FFs are used with an arbitrary (must be of order of Q^2 !) non-physical scale M_F then the finite differential cross section formula is found.

In addition to the divergent terms, one is free to include any finite parts, such as $b_{qq}(z_p)$, $b_{gq}(z_p)$, into the definition of FFs $\mathcal{D}_{q(\bar{q})}^h(z, M_F)$, this choice determines the factor-

ization scheme. For example, the \overline{MS} choice for the factorization/renormalization scheme includes the finite term: $\{-\ln(4\pi) + \gamma\}$. The FFs at the scale M_F satisfy the evolution equations as follows

$$\frac{\partial}{\partial \ln\left(\frac{M_F^2}{M_0^2}\right)} \begin{pmatrix} \mathcal{D}_q^h(z, M_F^2) \\ \mathcal{D}_g^h(z, M_F^2) \end{pmatrix} = \frac{\alpha_S(M_F^2)}{2\pi} \int_z^1 \frac{dy}{y} \begin{pmatrix} P_{qq}(y, \alpha_S(M_F^2)) & P_{gq}(y, \alpha_S(M_F^2)) \\ P_{qg}(y, \alpha_S(M_F^2)) & P_{gg}(y, \alpha_S(M_F^2)) \end{pmatrix} \begin{pmatrix} \mathcal{D}_q^h\left(\frac{z}{y}, M_F^2\right) \\ \mathcal{D}_g^h\left(\frac{z}{y}, M_F^2\right) \end{pmatrix} \quad (1.99)$$

where the DGLAP kernels P_{ij} [27, 28] have been introduced in the previous section, see also appendix A.2. Thanks to the FF evolution equations Eq. (1.99), one can predict the FFs at the arbitrary scale M_F , given that the FFs at the scale M_0 is measured.⁶

Now, let us show how the evolution functions Eq. (1.99) plays the role in resumming the logarithmic approximations in renormalized FFs. As an example, we consider the non-singlet FFs \mathcal{D}_{NS}^h which is defined as the difference between the quark FF and anti-quark FF. The advantage of this quantity is that it decouples from the gluon FF so the corresponding calculation becomes simpler than that of the quark FFs. The evolution equation for the non-singlet FFs is

$$\frac{\partial}{\partial \ln\left(\frac{M_F^2}{M_0^2}\right)} \mathcal{D}_{NS}^h(z, M_F^2) = \frac{\alpha_S(M_F^2)}{2\pi} \int_z^1 \frac{dy}{y} P_{qq}(y) \mathcal{D}_{NS}^h\left(\frac{z}{y}, M_F^2\right) \quad (1.100)$$

Applying the Mellin transform, given in Eq. (1.76), to the Eq. (1.100), one gets

$$\frac{\partial}{\partial \ln\left(\frac{M_F^2}{M_0^2}\right)} \mathcal{D}_{NS}^h(n, M_F^2) = \frac{\alpha_S(M_F^2)}{2\pi} \mathcal{D}_{NS}^h(n, M_F^2) \gamma_{qq}(n) \quad (1.101)$$

One can get the solution of Eq. (1.101): it has the form

$$\mathcal{D}_{NS}^h(n, M_F^2) = \mathcal{D}_{NS}^h(n, M_0^2) \exp \left[\int_0^{\ln\left(\frac{M_F^2}{M_0^2}\right)} dx \frac{\bar{\alpha}_S(x)}{2\pi} \gamma_{qq}(n) \right] \quad (1.102)$$

where $\bar{\alpha}_S\left(\ln\frac{M_F^2}{M_0^2}\right) \equiv \alpha_S(M_F^2)$ and $\bar{\alpha}_S(0) = \alpha_S(M_0^2)$. To first order in α_S , one can re-write Eq. (1.102) as follows, see Eq. (1.80),

$$\mathcal{D}_{NS}^h(n, M_F^2) = \mathcal{D}_{NS}^h(n, M_0^2) \exp \left[\frac{\gamma_{qq}(n)}{\pi b} \ln \left(\frac{\alpha_S(M_0^2)}{\alpha_S(M_F^2)} \right) \right] \quad (1.103)$$

6. Note that, to perform the LO calculation, one has to use the LO formula of $P_{ij}(z)$ for the evolution kernels, Eq. (1.99), and solve it to get the LL evolution for FFs, and also one has to use the LO partonic cross section $\hat{\sigma}_{i(j)}(z, p)$. The same idea is performed for the NLO calculation.

Given that one is working in the perturbative region, i.e. $\alpha_S(M_0^2) \ll 1$, therefore the solution formula for the non-singlet FFs can be written as follows, see Eq. (1.82),

$$\mathcal{D}_{NS}^h(n, M_F^2) = \mathcal{D}_{NS}^h(n, M_0^2) \left[1 + \frac{\gamma_{qq}(n)}{2\pi b} \alpha_S(M_0^2) bt + \frac{\gamma_{qq}(n)}{2\pi b} \left(\frac{\gamma_{qq}(n)}{2\pi b} - 1 \right) \alpha_S^2(M_0^2) (bt)^2 + \dots \right] \quad (1.104)$$

As proven in Eq. (1.104), the term $t = \ln(M_F^2/M_0^2)$, which appears for any small-angle gluon emission have been resummed, by using the evolution functions, see Fig. 1.15.

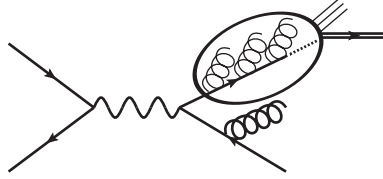


Figure 1.15: The collinear logarithms are resummed into the scale-dependent FFs.

1.3.2 Fragmentation Functions sets

In this section, we will focus mainly on the data used to constrain FFs of partons into hadrons. This FFs approach is an approximation of hadronization which does not take into account the correlations between the partons of the final state, these correlations, however, must exist to build colorless hadron states. This approximation is relevant in the case where the hadron carries large fraction of parent parton 4-momentum. As the PDFs, the FFs are independent of the process from which they are extracted and therefore their measurements in one reaction can be used to perform predictions for another reaction. The processes which are suitable to study FFs can be: e^+e^- annihilation into hadron ($e^+e^- \rightarrow hX$), lepto-production of a hadron ($lp \rightarrow lhX$), hadro- and photo-production of a hadron ($h_1h_2/(\gamma h_3) \rightarrow hX$).

Based on the cleanest hadron energy spectrum in e^+e^- annihilation at ALEPH [56], DELPHI [57], OPAL [58], SLD [59] experiments, there are several attempts to parametrize the FF of parton into hadrons such as in Refs. [57, 60, 61], in the following labeled as BFGW, Kretzer, and KKP, respectively. The FF of partons into a photon (BFG sets I and II) are extracted from HRS [62] and ALEPH [63] data as presented in Ref. [64]. In particular, the FFs of the (anti-)quark and the gluon into identified hadrons ($\pi^0, \pi^\pm, K^\pm, p/\bar{p}$) and all-charged hadrons are extracted. However, the produced hadrons in e^+e^- collisions, generally, come from the fragmentation of both quark and antiquark because emission from gluon does not occur at LO and therefore the gluon FF is not well constrained. Therefore, those data are only suitable to extract flavor-inclusive FF, e.g. $D_q^h + D_{\bar{q}}^h$. Beside including those data, the more recent FF sets, such as AKK05 [65], also take into account the separated measurements of light charged hadron production data at OPAL [66] and

extract the flavor dependent FFs of light quarks. However, the low energy e^+e^- data do not have a very good statistics. In addition, the large momentum fraction z bins have rather large statistical error bars, as shown in Fig 1.16. Therefore, less constraints on the determination of partons into charged particles are set in those regions.

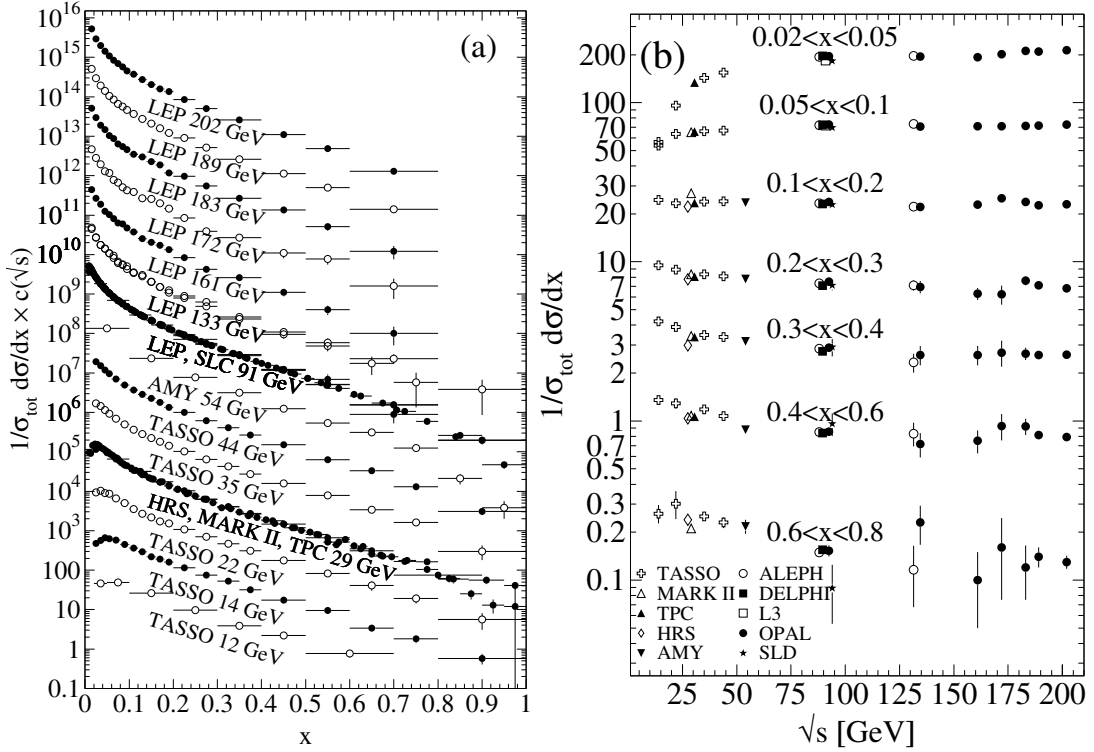


Figure 1.16: The e^+e^- fragmentation function for all charged particles is shown (a) for different CM energies \sqrt{s} with respect to momentum fraction x (equivalent to z in text); (b) for various range of x with respect to \sqrt{s} [19].

Using fragmentation functions for charged pions, charged kaons, and (anti)protons extracted from experimental data in e^+e^- annihilation, the inclusive charged-hadron production in $p\bar{p}$, γp , and $\gamma\gamma$ collisions are calculated at NLO by using KKP set; then, those distributions are compared with $p\bar{p}$ data from CERN $S\bar{p}\bar{p}S$ and the Fermilab Tevatron, γp data from DESY HERA, and $\gamma\gamma$ data from CERN LEP2 and a good agreement is obtained as presented in Ref [67]. That supports the universality of the fragmentation processes which is expected from factorization theorems. Also, the theoretical predictions using AKK05, Kretzer, KKP FF sets are found to be in good agreement with single hadron inclusive production measurements in deep inelastic scattering (ep) of older H1 [68] and ZEUS [69, 70] results (a completed discussion is given in Ref [71]). However, despite the fact that these FFs describe the same data, there are the discrepancies when comparing each FFs individually. As is well known, the gluon FF is poorly constrained by e^+e^- and those (anti)quark FFs are not well determined at large z and therefore they also contribute to these discrepancies. The predictions using the AKK05, Kretzer and KKP FF sets are not able to describe the Q -dependence of the more recent H1 data [72].

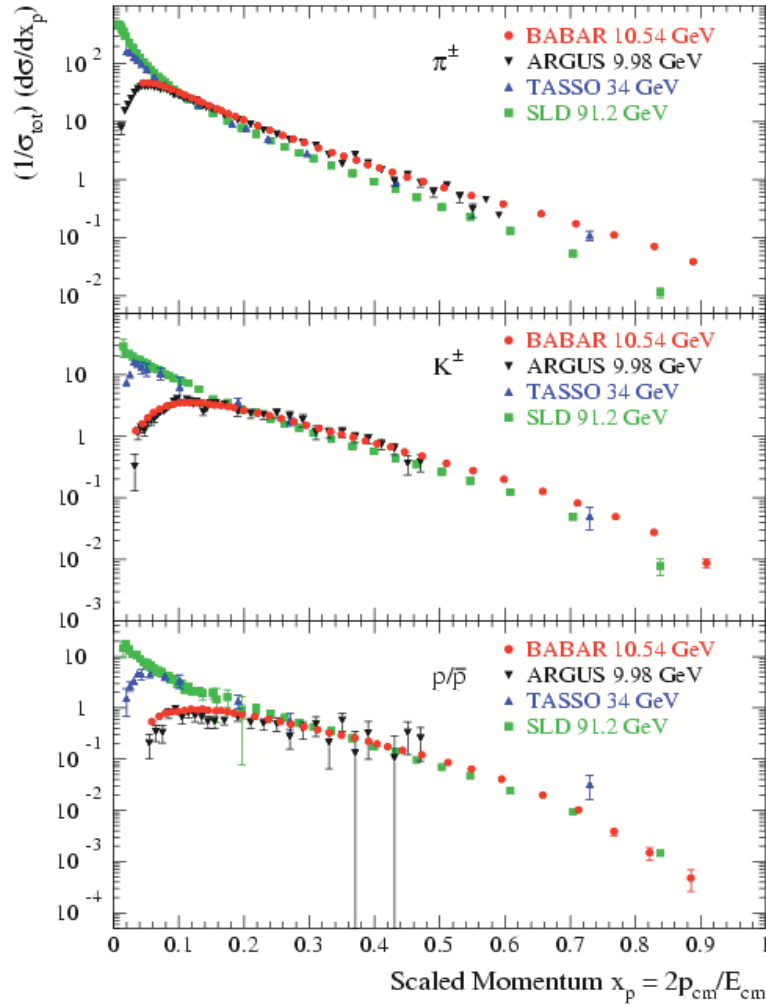


Figure 1.17: BABAR *preliminary* measurements for identified hadrons production in e^+e^- annihilation [73].

The e^+e^- data from B-factories (BaBar, BELLE, CLEO) around $\Upsilon(4S)$ -mass, $\sqrt{s} = 10.58$ GeV provide high accuracy measurements on identified hadron production. The further constraints on FFs at low energy scale should be set by using those data. As an illustration, preliminary measurements of π^\pm , K^\pm , and $p\bar{p}$ spectra in e^+e^- scattering by the BABAR Collaboration are compared to older data from ARGUS, TASSO, and SLD in Fig. 1.17. The difference in shape between SLD and BaBar data, for instance, can be understood by perturbative QCD evolution. The high accuracy measurements of charm-meson spectra at BaBar [74], CLEO [75], BELLE [76] offer a more accurate determination of charm-meson FFs. Recently, the charm-meson FFs were extracted from the CLEO, BELLE, and ALEPH [77] data in Refs [78, 79], labeled in the following by CNO, KKKS08 (also include OPAL [80] data) FF sets.

The data from single-inclusive hadron collision, e.g. PHENIX [81], STAR [82], BRAHMS [83] collaborations in $p-p$ at RHIC and CDF [84] in $p-\bar{p}$ at Tevatron, allows to put more con-

straints on FF parametrization. These data allow to determine the FFs of quark and anti-quark into hadron independently. The data of the $p\text{-}p(\bar{p})$ scattering also helps to constrain the gluon FF when the momentum fraction x of the PDF is small, where the gluon PDF is dominant. Because the PDFs decrease steeply when x is large, the hadronic collision data typically enable to extract hadron FF at large momentum fraction, e.g. $z \simeq 0.7\text{--}0.8$ at RHIC, because the value of x is typically of order of $2p_{\perp}^h / \sqrt{s} z$. Therefore, they complement the e^+e^- annihilation data. Recently, the FF sets DSS [85, 86] and AKK08 [87] have used the single-inclusive hadron data for setting further constraints on FFs (as mentioned Chapter 3).

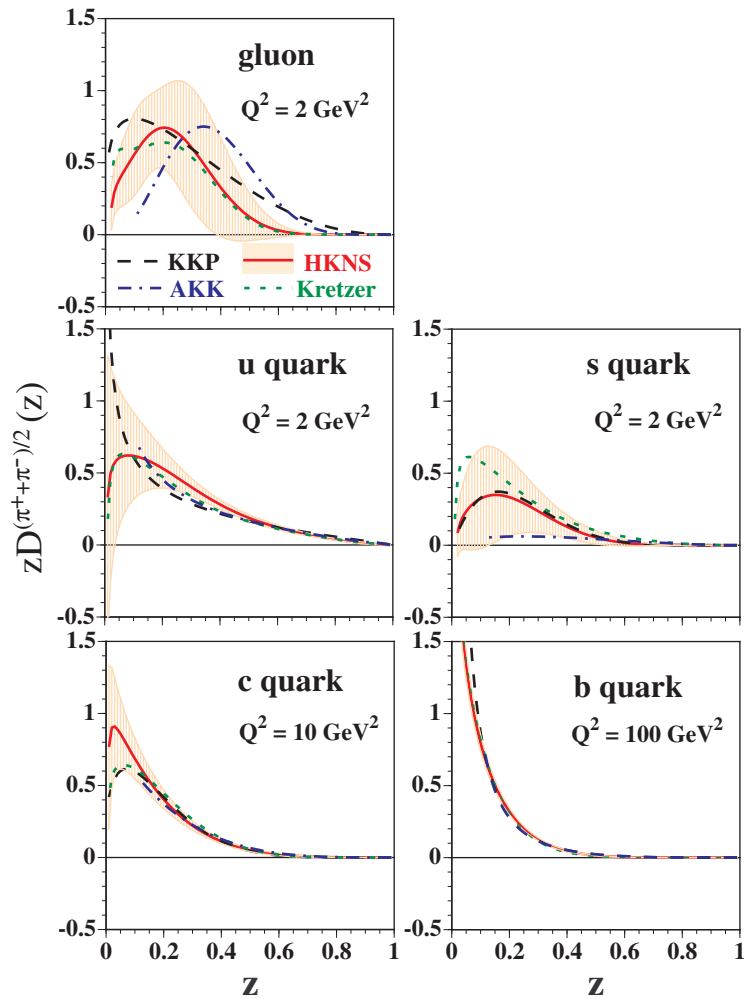


Figure 1.18: HKNS parametrization for charged pions compared to KKP, AKK, and Kretzer [73].

Let us briefly review the comparison of pion FFs from most recent sets HKNS [73], AKK08 and DSS. As one can see in fig. 1.18, the fragmentation of quarks into π^\pm is similar for those FF sets, at least for $z > 0.1$. Given the HKNS extracts the FFs from e^+e^- data only, its gluon FF is less constrained than those of AKK08 and DSS which additionally include the data from the hadron collisions. This fact represents the discrepancy for gluon

FF from those sets as in upper left panel of fig. 1.18. Even though the $p\text{-}p(\bar{p})$ data help to set further constraints on gluon FF, they have larger error bars than the e^+e^- one. This explains the uncertainty on the gluon FFs between AKK08 and DSS. Note that the FF into kaons and protons are even less known than FF into pions. The gluon and light quark FF into kaons and protons are much different between the preceding sets, especially at low z . The low energy data such as at BELLE and BABAR should be able to improve the kaon FF at this stage. The complete discussion can be found in Refs [73, 85, 86, 87]. Also, in order to compare the parton FFs into hadrons for various sets, one can use the FFs generator available at LAPTh webpage [88].

The data in $p\text{-}p$ collision at LHC is now available at $\sqrt{s} = 8$ TeV, the highest energy ever reached before. This motivates us to perform the study in jet-hadron correlation by using various FF sets in order to get better constraints on them. The detail of this study is presented in chapter 3.

Chapter 2

Aspects of jet production

Contents

2.1	Jet definition	40
2.1.1	Theoretical content	40
2.1.2	The k_t algorithm	41
2.1.3	The flavor- k_t algorithm	44
2.1.4	Jet phenomenology	48
2.2	JETPHOX overview	51
2.2.1	Theoretical content	51
2.2.2	Generation of events in JETPHOX with BASES-SPRING	56
2.2.3	Comparison between JETPHOX and the inclusive prompt photon data	61

2.1 Jet definition

In perturbative QCD, the hard partonic scattering includes quarks and gluons in the final state. However, in the experiment, there is no colored particle to be seen in its "free" state [22] but the beam of collimated (colorless) energetic hadrons – a jet. This phenomenon is understood as the parton fragmentation and hadronization. In this thesis, we discuss two aspects of jet production *a*) $pp \rightarrow \text{hadron} + \text{jet}$ (chapter 3) and *b*) $pp(p\bar{p}) \rightarrow \text{photon} + \text{heavy-quark jet}$ (chapter 4). In the present NLO calculations, the maximum number of final partons which accompany with the photon (hadron) is two. In case there is one final parton, this parton is regarded as a jet. In case there are two final partons, either a jet can be formed by those partons if they are produced quite close to each other or there are two jets correspond to two partons if they are produced with a distance greater than R which is the experimental jet size. far apart. In order to perform this systematically and to enable to compare the experimental data with theoretical calculation, suitable jet algorithm is required and needs to be applied.

2.1.1 Theoretical content

In the partonic processes such as $q\bar{q} \rightarrow \gamma q\bar{q}$, $q\bar{q} \rightarrow \gamma gg$, there are divergences when two final partons are collinear. They have the following form $\frac{1}{\epsilon} P_{qg}(z)$, $\frac{1}{\epsilon} P_{gg}$, where $P_{ij}(z)$ are the splitting functions [26]. Those divergences vanish when all flavor-quarks and gluon are taken into account and when the integration over z is performed, thanks to

$$\int_0^1 dz z [2 n_f P_{qg}(z) + P_{gg}(z)] = 0, \quad (2.1)$$

where n_f is the number of flavors. Moreover, there are also the collinear divergences proportional to $P_{qq}(z)$, $P_{gq}(z)$, which correspond to γqg production. Thanks to

$$\int_0^1 dz z [P_{qq}(z) + P_{gq}(z)] = 0, \quad (2.2)$$

those divergences cancel. Hence, it is not the inclusive parton but the degenerate states of all final partons which can be associated with an observable. This statement represents the fact that no quark or gluon can be detected in the experiment but the jets. It makes sense when one identifies the degenerate states of final partons in theoretical calculations with the jets in experiment measurement for a given jet resolution d_{cut} . By using a suitable jet algorithm, the corresponding cross sections are expected to be infrared and collinear safe.¹ Then one may compare the experimental data with the theoretical calculation at the parton level.

1. The jet configuration is not changed if a soft or a collinear parton is added when computing higher order.

Assuming one is interested in the jets in the final state, it is required to have an algorithm to convert the final particles of each event into jets. As an example, one may introduce the quantities which play the role of the distances between the pairs of jets. The rule for merging two jets into one single jet somehow depends on those quantities. To be able to compare the theoretical predictions with experimental measurements, the same approach has to be used.

In fact, the jet algorithms (or the clustering algorithms) approximately invert the probabilistic picture of QCD branching which is a quantum mechanical process. The notion of distance measure allows one to determine the order in which the emitted particles are recombined into their parent particle. The number of "particles" left when the analysis has been done is considered the number the jets of final state. We want to emphasize that the way of inverting the branching is not unique. For example, it may depend on how the distance measures are defined, i.e. for particle–particle, particle–beam, on how the momentum for the jet from two particles are constructed,² etc.

In the next sections, we give an overview of two jet algorithms: the k_t algorithm and the flavor- k_t algorithm which are used for calculations in this thesis.

2.1.2 The k_t algorithm

The k_t algorithm in the e^+e^- collision

Let us start the jet algorithm discussion by considering the standard k_t algorithm in e^+e^- collisions [16]. The algorithm can be formulated as follows:

1. Define the distance between two partons i and j by

$$y_{ij} = \frac{2 \min(E_i^2, E_j^2) (1 - \cos \theta_{ij})}{Q^2} \quad (2.3)$$

where Q , E_i , and θ_{ij} are the total energy of the reaction (also the center of mass energy), the energy of particle i , and the angle between two particles, respectively.

2. Find the minimum among all y_{ij} , then recombine the pair of particles i and j which minimizes the distance y_{ij}
3. Continue the procedure until all $y_{ij} > y_{\text{cut}}$. At the end, one gets the number of jets as expected.

It is interesting to demonstrate that by using the k_t algorithm one gets an infrared and collinear safe cross section. For this purpose, let us consider an example of a gluon k which branches into two gluons 1 and 2. In the limit where the gluon 1 is soft and collinear to gluon 2, one reaches the divergent region and the matrix element for this splitting is proportional to

$$|\mathcal{M}_{k \rightarrow 12}|^2 \sim \alpha_s \frac{dE_1}{E_1} \frac{d\theta_{12}^2}{\theta_{12}^2} \quad (2.4)$$

2. In the present calculation, the momentum of the jet is the sum of the 4-momenta of the two partons.

On the other hand, the distance measure, given in Eq. (2.3), is approximated by

$$y_{12} \approx \frac{E_1^2 \theta_{12}^2}{Q^2}, \quad (E_1, \theta_{12} \ll 1.) \quad (2.5)$$

Thus, as one can see, the two gluons are described as being close when either the gluon 1 is soft or/and collinear to gluon 2. In other words, this distance measure is the key to group together collinear partons which have the same parent if the splitting gives rise to a divergence. is IR and collinear safe.

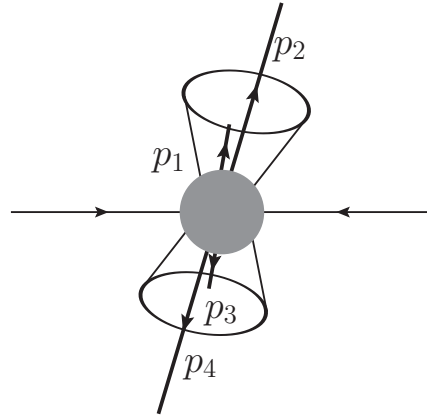


Figure 2.1: An example graph for distance measure in k_t algorithm.

A second example is to consider also another soft parton, the gluon 3, which is produced back-to-back to the gluon 1 (and gluon 2) as illustrated in Fig. 2.1. Using the distance measure which is defined as in Eq. (2.5), one gets that

$$\begin{aligned} y_{13} &= \frac{2 \min(E_1^2, E_3^2)(1 - \cos \theta_{13})}{Q^2} \\ &\approx \frac{2E_1^2(2 + \theta_{13}/2)}{Q^2}, \quad (E_1 < E_3 \ll 1.) \end{aligned} \quad (2.6)$$

One can see that, y_{13} is small and therefore it seems that the gluon 1 and gluon 3 should be merged into a single jet but they do not. In practice, it seems natural to merge partons flying in the same direction. For this reason, since the gluon 1 and gluon 3 are produced back-to-back, they will not be recombined into a single jet. Moreover, as y_{12} is given in Eq. (2.5), one gets that $y_{13} > y_{12}$. Hence, this algorithm ensures that the two particles which are recombined at this level are the collinear pair and not the soft back-to-back one. At the end of the procedure, gluon 1 and 2 are recombined into a single jet and the gluon 3 is clustered into another jet.

In short, with the distance measure which is defined as in Eq. (2.3), the k_t algorithm provides the IR safe observable for studying jet production.

The k_t algorithm in hadron–hadron collisions

In hadron–hadron collisions, one cannot know the total energy of the hard scattering which is essentially the partonic process. Thus instead of the dimensionless distance measure as in Eq. (2.3), one should choose the dimensionful one given by

$$d_{ij} = 2 \min(E_i^2, E_j^2) (1 - \cos \theta_{ij}) \quad (2.7)$$

We want to emphasize that, in the limit where the particles i and j are collinear together, $\theta_{ij} \ll 1$, and the distance d_{ij} is proportional to the squared energy of i , given i is the softer one:

$$\begin{aligned} d_{ij} &\approx E_i^2 \theta_{ij}^2, & (\theta_{ij} \ll 1, E_i \ll E_j) \\ &\approx (E_i \sin \theta_{ij})^2. \end{aligned} \quad (2.8)$$

In addition, there is also the divergence in the cross section calculation when the final parton is collinear to the initial hadrons, that is to say which belongs to the incoming beam. Therefore, it is necessary to introduce an additional parameter which stands for the distance measure between the beam and final particle, such as

$$d_i = 2E_i^2 (1 - \cos \theta_i) \quad (2.9)$$

where θ_i is the angle between the beam and particle i . Again, in the limit where the particle i is collinear to the beam, $\theta_i \ll 1$, the distance d_i is proportional to the squared energy of i . Then if d_i is the smallest one among the distances, the particle i is included in the beam-jet and therefore the corresponding calculation is free from the collinear divergence between the initial hadron and a final particle.

In fact, a direct adaptation of the k_t jet algorithm is made from the e^+e^- collisions, so the energies and angles are defined in the center of mass frame of initial partons. Then, to be able to compare with the experimental data which are defined in the CMS of initial hadrons, i.e. proton–proton CMS, a longitudinal boost must be applied to the corresponding calculation. Therefore, it is necessary to choose the distance measure which is invariant under the boost along beam direction. In addition, the distance measure must be an increasing function with respect to angle.

In the small-angle limit, $\theta_{ij}, \theta_i \ll 1$, the distances d_{ij} and d_i are approximated by

$$d_{ij} \approx \min(p_{\perp i}^2, p_{\perp j}^2) \frac{(y_i - y_j)^2 + (\phi_i - \phi_j)^2}{R^2} \quad (2.10a)$$

$$d_i \approx p_{\perp i}^2 \quad (2.10b)$$

(see Eq. (A.13)) where $p_{\perp i}$ and ϕ_i are the transverse momentum and the azimuthal angle of particle i , respectively, its rapidity³ $y_i \approx -\ln(\tan(\theta_i/2))$, and R is the size of the jet.

3. to be more precise, y_i is the pseudo-rapidity which is equal to the rapidity for massless particle (see appendix A.1)

It is clear that the left-hand sides of Eqs. (2.10a, 2.10b) are invariant under longitudinal boost and are an increasing function of angles. Therefore, those left-hand formulas are a possible choice for defining the distance measures.

In the calculations at NLO, there are no more than two partons which are associated with the photon or the hadron, in the final state. In the case where there is one parton, this parton is regarded as the jet. In the case where there are two final partons, one can perform the k_t algorithm in hadron-hadron collisions [89, 90] as the following:

1. The distance between two final partons and the distance of parton i ($i = 1, 2$) to the beam are defined, respectively, as:

$$d_{12} = \min(p_{\perp 1}^2, p_{\perp 2}^2) \frac{\Delta R_{12}^2}{R^2}, \quad \Delta R_{12}^2 \equiv (y_1 - y_2)^2 + (\phi_1 - \phi_2)^2 \quad (2.11)$$

$$d_i = p_{\perp i}^2$$

where p_{\perp} , y , and ϕ are the transverse momentum, rapidity, and azimuthal angle, respectively, and R is the size of the defined jet.⁴

2. Consider the smallest value among d_{12} , d_1 , and d_2 . If d_{12} is the smallest one, then the two final partons are merged into a single jet.
3. Otherwise, regard those two partons as two different jets.

In order to illustrate the k_t algorithm, let us consider the case where $p_{\perp 1} < p_{\perp 2}$, then from Eq. (2.11) one gets

$$d_{12} = p_{\perp 1}^2 \frac{\Delta R_{12}^2}{R^2}, \quad (2.12)$$

$$d_1 < d_2$$

Thus the fact that d_1 is the smallest one, where partons 1, 2 form the different jets, is equivalent to $R^2 < \Delta R_{12}^2$. Therefore, in the case of two final partons, it ensures that whenever the distance between two particles is greater than the size of the desired jet, those particles are regarded as belonging to two separated jets. However, in this case, the parton 1 which forms the jet can be an arbitrarily soft parton and this jet cannot be identified to the constructed jet in experiment. In practice, the interesting jet is required to have the transverse momentum greater than a $p_{\perp \text{min}}$, which depends on the experiment. Again, the procedure of the k_t algorithm in hadron-hadron collision is IR and collinear safe.

2.1.3 The flavor- k_t algorithm

In this section, we discuss the flavor- k_t algorithm which is introduced in the reference [17]. This algorithm is one of the procedures used for the study of the photon + heavy-flavor jet production in hadronic collisions presented in the chapter 4.

4. We choose $R = 0.4$ or $R = 0.5$ for the present calculations.

The flavor k_t algorithm in the e^+e^- collision

Assuming one is interested in the jet which has a specific flavor, we will look for the suitable algorithm for this kind of study. Again, the good algorithm is the one providing the IR-safe jet flavor observable. Depending on how one defines the jet flavor, different procedures are introduced to deal with the corresponding one. One of these approaches is that the jet flavor is specified by considering its net flavor.⁵ Without loss of generality, let us assume that we want to study b-jets. One assigns a value 1(-1) for b-quark(anti-b-quark) and a value 0 to the other quarks(anti-quarks) and to the gluon. The net flavor of the jet is determined by the sum of the jet component values:

1. The jet net flavor is 1(-1), it is regarded as (anti)b-flavor jet.
2. The jet with zero net flavor is considered as b-flavorless jet.
3. The jet which has the net flavor greater than one unit cannot be identified with a single QCD parton.⁶

Consider the $b\bar{b}$ pair which is produced from a soft gluon splitting, each of those partons can go into already formed jets and then may change the flavor of them. As an example, let us assume there are two jets in the final state which are gluon jets (see Fig. 2.2(a)). At higher order, a soft gluon can be produced which, then, splits into a $b\bar{b}$ pair at large angle, as illustrated in Fig. 2.2(b). Using the k_t algorithm, the (anti)b-quark can be clustered into the jet 1 (jet 2), so the total net flavor of it becomes 1(-1) and therefore the jet 1 (jet 2) is considered as the (anti)quark jet at this order. Note that, the effect of a very soft gluon splitting (the soft quarks) must not change the flavor of the hard jets. Because of that, the k_t algorithm does not provide the IR flavor safe observable.

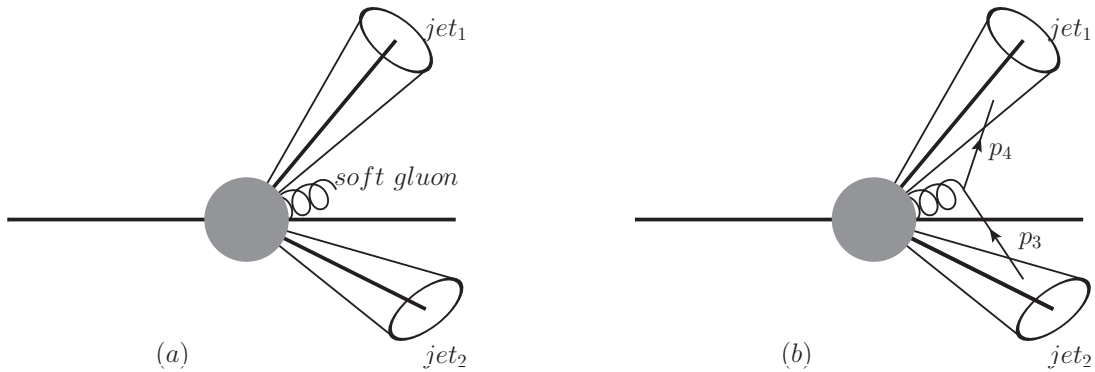


Figure 2.2: An example graph for an arbitrary soft gluon splits into q (p_3) and \bar{q} (p_4) which are added to the jet 1 and 2, respectively.

The closeness of distance measure, which is introduced in the k_t algorithm, aims to invert the branching which can give the divergence, i.e. collinear and/or soft split partons.

5. There are two other approaches. We postpone to introduce them in chapter 4, where we also apply the flavor- k_t algorithm and discuss the results among those approaches.

6. This is not the case for the present NLO calculations.

While the splitting matrix elements such as $g \rightarrow q\bar{q}$, $q \rightarrow gq$ have no divergence related to the soft quark but to the collinearity of the two partons.

$$|\mathcal{M}_{q_k \rightarrow q_i g_j}|^2 \sim \alpha_s \frac{dE_i}{E_j} \frac{d\theta_{ij}^2}{\theta_{ij}^2}, \quad (\theta_{ij} \ll 1, E_i \ll E_j) \quad (2.13)$$

Thus it is not necessary to recombine the partons if the softer one is a quark, given that they are not collinear together. Now, supposing the soft parton is a quark, it is safe to modify the distance measure, in Eq. (2.3) for the e^+e^- annihilation, by

$$y_{ij} = \frac{2 \max(E_i^2, E_j^2) (1 - \cos \theta_{ij})}{Q^2} \quad (2.14)$$

instead of $\min(E_i^2, E_j^2)$ in its original formula. This partially modified distance measure ensures that the soft-quark emission has the distance no smaller than non-soft-quark one and therefore one is able to get rid of the IR flavor unsafe problem above. This modification introduces the procedure known as the flavor- k_t algorithm [17] which provides the IR flavor safe observable in studying jet flavor.

For the e^+e^- annihilation, the flavor- k_t algorithm is formulated in the same way as the standard k_t algorithm except that the corresponding distance measure between two partons i, j is defined by

$$y_{ij} = \frac{2 (1 - \cos \theta_{ij})}{Q^2} \times \begin{cases} \max(E_i^2, E_j^2) & \text{if softer among } i, j \text{ is flavored} \\ \min(E_i^2, E_j^2) & \text{if softer among } i, j \text{ is flavorless} \end{cases} \quad (2.15)$$

The flavor k_t algorithm in hadron-hadron collisions

Analogous to the y_{ij} modification, the d_{ij} of the flavor k_t algorithm in hadron-hadron collisions is defined by

$$d_{ij} = (\Delta y_{ij}^2 + \Delta \phi_{ij}^2) \times \begin{cases} \max(p_{\perp i}^2, p_{\perp j}^2) & \text{if softer among } i, j \text{ is flavored} \\ \min(p_{\perp i}^2, p_{\perp j}^2) & \text{if softer among } i, j \text{ flavorless} \end{cases} \quad (2.16)$$

where $\Delta y_{ij} = y_i - y_j$, $\Delta \phi_{ij} = \phi_i - \phi_j$ and $p_{\perp i}$, y_i , with ϕ_i are transverse momentum, rapidity, and azimuthal angle of parton i , respectively and the "softer" parton means the parton which has the smallest transverse momentum. In addition, the corresponding beam

distance is given by

$$d_{iB} = \begin{cases} \max(p_{\perp i}^2, p_{\perp B}^2(y_i)) & \text{if } i \text{ is flavored,} \\ \min(p_{\perp i}^2, p_{\perp B}^2(y_i)) & \text{if } i \text{ is flavorless} \end{cases} \quad (2.17)$$

and the same definition for the anti-beam distance with replacing B in Eq. (2.20) by \bar{B} , where

$$\begin{aligned} p_{\perp B}(y) &= \sum_i p_{\perp i} (\Theta(y_i - y) + \Theta(y - y_i) e^{y_i - y}), \\ p_{\perp \bar{B}}(y) &= \sum_i p_{\perp i} (\Theta(y - y_i) + \Theta(y_i - y) e^{y - y_i}) \end{aligned} \quad (2.18)$$

with $\Theta(y)$ is the Heaviside step function and $\Theta(0) = 1/2$ is imposed. In fact, this closeness beam distance aims to avoid the analogous IR flavor unsafe problem which can happen for the beam jet flavor. Therefore, the flavor- k_t provides IR flavor safe for both the outgoing jets and the beam jets.⁷

Assuming there are two partons in the final state, the flavor- k_t algorithm can be performed as follows

1. Define the distance measure d_{12} between parton 1 and 2:

$$\begin{aligned} d_{12} &= (\Delta y_{12}^2 + \Delta \phi_{12}^2) \\ &\times \begin{cases} \max(p_{\perp 1}^2, p_{\perp 2}^2) & \text{if softer among them is flavored,} \\ \min(p_{\perp 1}^2, p_{\perp 2}^2) & \text{if softer among them is flavorless.} \end{cases} \end{aligned} \quad (2.19)$$

In addition, a distance $d_{iB(\bar{B})}$, $i = 1, 2$ between parton i and the beam at positive rapidity (negative rapidity) is defined by

$$d_{iB(\bar{B})} = \begin{cases} \max(p_{\perp i}^2, p_{\perp B(\bar{B})}^2(y_i)) & \text{if softer among partons 1, 2 is flavored,} \\ \min(p_{\perp i}^2, p_{\perp B(\bar{B})}^2(y_i)) & \text{if softer among partons 1, 2 is flavorless} \end{cases} \quad (2.20)$$

where the transverse beam scale $p_{\perp B(\bar{B})}(y)$ is given by Eq. (2.18).

2. Consider the smallest one among d_{12} , $d_{iB(\bar{B})}$. If d_{12} is the smallest one, then merged parton 1 and parton 2 into one jet. Else, the event is considered as having two jets in final state.

In studying heavy-quark jets, one can consider gluon and light-quark as flavorless and heavy-(anti)quark as flavored [91]. Then, the flavor of heavy-(anti)quark can be identified as value of 1(-1), the flavor of gluon and light-quark as 0. The net heavy-flavor of the jet can be determined as follows

1. If the net value of the jet differs from 0, this jet is considered as the heavy-quark jet.
2. Otherwise, it is specified as the non-heavy-quark jet.

7. We are not interested in the beam jet flavor in present calculations.

Then the flavor k_t algorithm can be used for the heavy-quark jets probing with the modification: replace "flavor" by "heavy-flavor" in the corresponding procedure, i.e. in Eqs (2.19), (2.20).

As one can see, by using this algorithm, it is required to know which parton is the heavy-(anti)quark. Therefore it is not necessary to specify the flavor of light-quark nor gluon in applying the procedure. As in the standard k_t algorithm, the transverse momenta of two partons are required to be known as well.

We want to emphasize that the flavor k_t algorithm is not quite obvious to use from the experimental point of view. The experimentalist have to know the flavor of the clusters in order to apply this algorithm.

2.1.4 Jet phenomenology

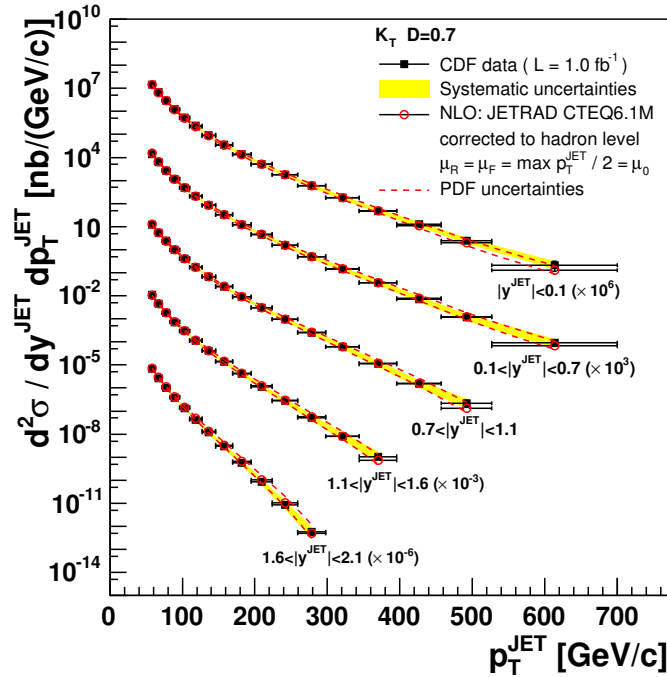


Figure 2.3: The summary of inclusive jet cross section measurements at Tevatron in comparison with the NLO QCD prediction [12].

Recently, the inclusive jet (dijet) cross section measurements at Tevatron and LHC has shown a good agreement between data measurement and NLO pQCD prediction [12, 92, 13, 14].

The jet reconstruction in $p\bar{p}$ collisions at $\sqrt{s} = 1.96$ TeV is performed using the k_t algorithm. The differential cross section measurements with respect to transverse momentum of the jet p_{\perp}^{jet} are shown in Fig. 2.3. As one can see, the various measurements in different region of rapidity agree well on almost ten orders of magnitude with theoretical calculations.

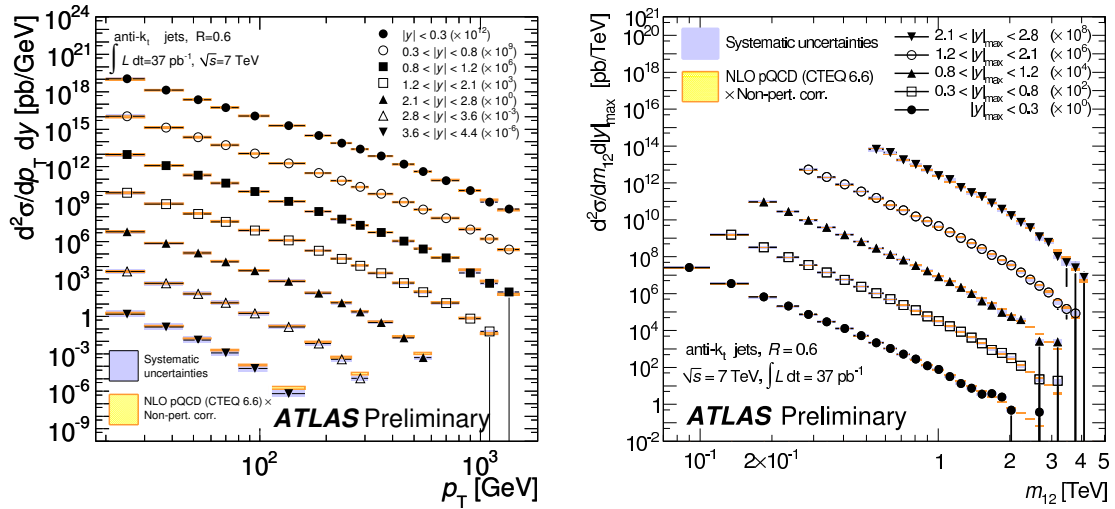


Figure 2.4: The summary of inclusive jet (left) and dijet (right) cross section measurements by ATLAS detector at LHC in comparison with the NLO QCD prediction [14].

In pp collisions at $\sqrt{s} = 7$ TeV, the inclusive jet cross sections are measured by using the ATLAS [14] and CMS [13] detectors at LHC. For these measurements, the anti- kt algorithm⁸ is used to reconstruct the jets. Again, the p_{\perp}^{jet} distributions in various rapidity y^{jet} are studied. Figs. 2.4 and 2.5 show the good agreement between data measurements and theoretical predictions within the experimental and theoretical uncertainties for inclusive jet productions in pp collisions.

These results confirm the confidence in the QCD improved parton model to describe jet physics. Therefore, by using other QCD fits such as, the (heavy-flavor)jet+photon production, we hope to have a better understanding of the hadron structure, e.g PDF inside proton, as well as to put more constraints on the hadron FFs via the jet+hadron production.

8. The anti- kt algorithm [93] is performed analogous to the kt algorithm with p_{\perp}^2 is replaced by p_{\perp}^{-2} in the distance measures.

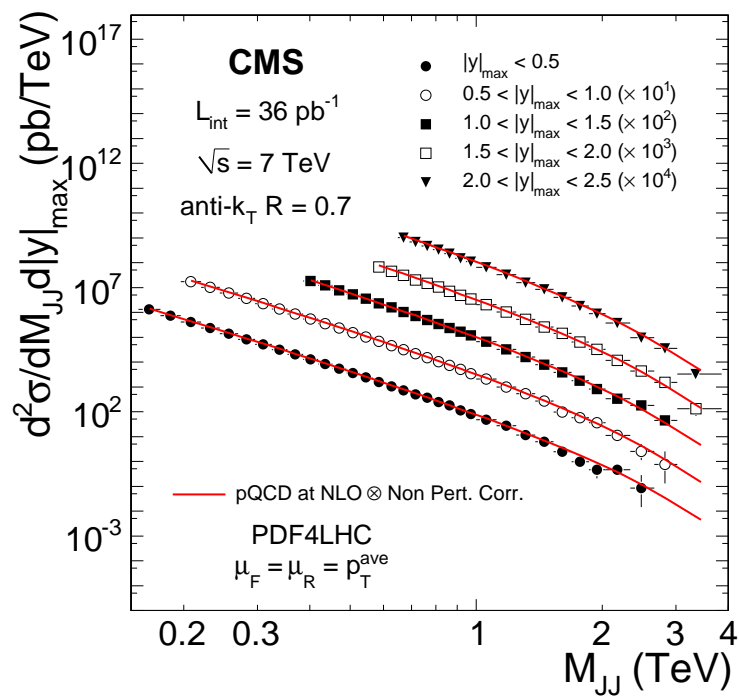


Figure 2.5: The summary of dijet cross section measurements by CMS detector at LHC in comparison with the NLO QCD prediction [13].

2.2 JETPHOX overview

JETPHOX is a parton-level event NLO generator program which is designed to compute reactions including photon in the final state such as $hh \rightarrow \gamma$ (hadron) + $jet + X$. One easily switches from the production of a photon to the production of a hadron by choosing the corresponding FFs in the input. It also allows one to implement any experimental cuts, e.g. on kinematics, isolation. The single inclusive photon/hadron cross section at NLO can be obtained by integrating over the particles other than the photon/hadron in the final state. One can use this program to perform the calculation for both inclusive and isolated prompt-photon production cross section, or the differential one, in the hadron collision. The overview of theoretical points is presented in section 2.2.1. The technical part which is related to the event generation is discussed in section 2.2.2.

2.2.1 Theoretical content

Prompt-photon production mechanisms

Let us consider the NLO cross section to the process $h+h \rightarrow \gamma + jet + X$ in which the jet is a degenerate state of quarks and gluons. The LO contribution is given by the partonic processes (subprocesses) such as $gq \rightarrow \gamma q$, $q\bar{q} \rightarrow \gamma g$ (top-diagrams in Fig. 2.6.) This contribution corresponds to the order $\alpha\alpha_s$, where α and α_s are the electromagnetic and the strong couplings, respectively. The NLO corrections, which is of the order $\alpha\alpha_s^2$, contain subprocesses such as $gg \rightarrow \gamma q\bar{q}$, $q\bar{q} \rightarrow \gamma gg$, and the corresponding virtual correction (bottom-diagrams in Fig. 2.6.)

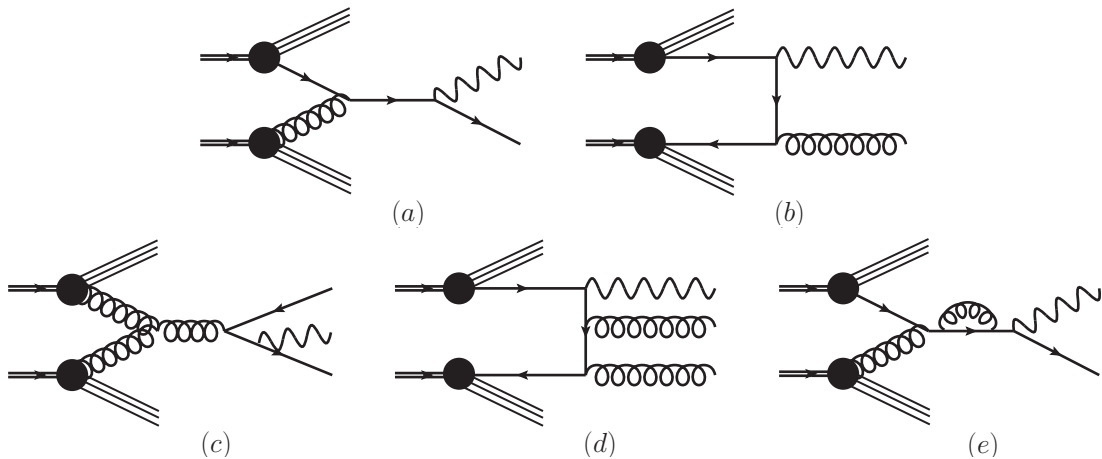


Figure 2.6: An example of the (D) photon subprocesses.

Considering the subprocess $gg \rightarrow \gamma q\bar{q}$, there is the quark-photon collinear divergence when integrating over the q or \bar{q} phase space. At higher-orders, this kind of singularity appears for any contribution which includes the collinear splitting into a photon of the high transverse momentum parton. The corresponding singularity is absorbed into the

FF of quark or gluon into a photon (the photon FF) which obeys an evolution equation. We note that this photon FF, denoted by $\mathcal{D}_{q(g)}^\gamma(z, M_F^2)$, is defined in a specific fragmenta-

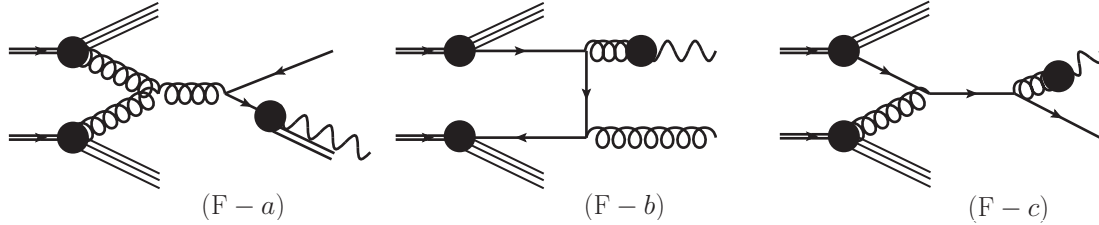


Figure 2.7: An example of the (F) photon subprocesses at LO.

tion scheme and at an arbitrarily fragmentation scale M_F and it represents the number of photon carrying a momentum fraction z of the parent quark (gluon). At the large fragmentation scale, e.g. $M_F \gg M_0$ (M_0 is the scale of order of the proton mass), the photon FF behaves roughly as $\alpha/\alpha_S(M_F^2)$. Then the contributions such as those described by diagrams in Fig. 2.7 are asymptotically of the order of $\alpha\alpha_S$ as LO terms. In order to have a consistent NLO calculation for the corresponding photon production, the $O(\alpha\alpha_S^2)$ corrections for those contributions are also taken into account. As a result, the subprocesses such those illustrated by the diagrams in Fig. 2.9 are included in the NLO contribution.

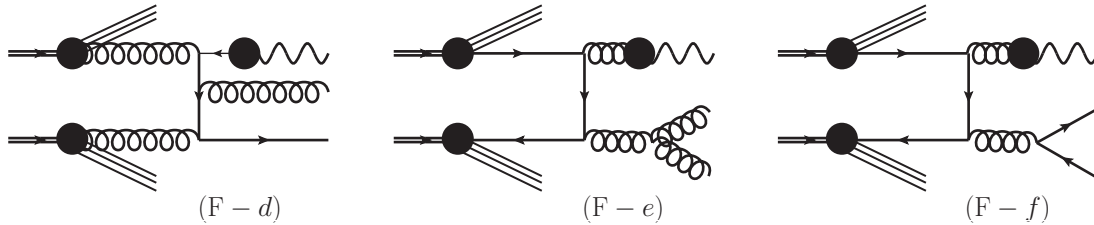


Figure 2.8: An example of the (F) photon subprocesses at NLO.

In practice, JETPHOX is designed to perform the prompt-photon production calculation via two mechanisms, conventionally, they are called "direct" (D) and "fragmentation" (F). The (D) stands for the case where the photon, with high p_\perp , is a part of the hard subprocess and is well separated from the hadronic region. The (D) part contains the Born term and the fraction of higher order correction from which final state collinear divergences have been subtracted according to the \overline{MS} factorization scheme. The (F) stands for the case where the photon comes from the fragmentation of a high p_\perp parton; therefore, the photon is almost accompanied with hadrons – except in the case where the photon carries large fraction energy, $z \sim 1$, of the fragmenting parton. The (F) contribution is given by the photon FF from any parton in the \overline{MS} factorization scheme.

Let us denote the differential cross section in photon rapidity y^γ and transverse momentum p_\perp^γ by $\sigma^\gamma \equiv d\sigma/(dp_\perp^\gamma dy^\gamma)$ and the arbitrarily scales for the renormalization, initial-state factorization, and fragmentation, respectively by μ_R , M , and M_F . As men-

tioned above, the σ^γ is given by the sum of the (D) and (F) contributions as follows

$$\sigma^\gamma = \sigma^{(D)}(\mu_R, M, M_F) + \sum_{i=q,\bar{q},g} \sigma_i^{(F)}(\mu_R, M, M_F) \otimes D_i^\gamma(M_F) \quad (2.21)$$

where $\sigma_i^{(F)}$ stands for the parton i production in hard scattering subprocess and the symbol \otimes means the convolution over the fragmentation variable z is taking place.⁹ We emphasize that the splitting of the photon production cross section into the (D) and (F) ones comes from the treatment for the final-state photon-parton collinear singularities, which are absorbed into FFs at scale M_F in a specific scheme i.e. the \overline{MS} ; hence, the (D) and (F) contributions depend on fragmentation scale M_F . Only the sum of them is free of M_F dependence, up to the designed accuracy, and can be the physical observable.

Phase space parametrization

In order to deal with the IR soft and collinear divergences in calculating the inclusive cross sections, a method which is the combination of the phase space slicing [94, 95] and the subtraction [96, 97, 98] techniques is used.

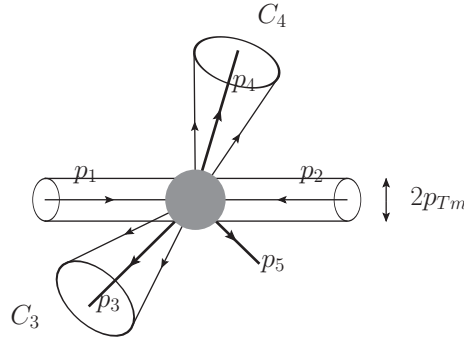


Figure 2.9: A generic partonic process $1 + 2 \rightarrow 3 + 4 + 5$. The cones C_3 and C_4 have radius R_{Th} .

Given the generic partonic process: $1 + 2 \rightarrow 3 + 4 + 5$, assuming that the two final partons 3 and 4 have high transverse momenta and are well separated; while the parton 5 can be soft or/and collinear to either one of the four others. In practice, parton 5 always stands for the final parton which has the transverse momentum lower than the parton which is marked by parton 3: $p_{\perp 5} < p_{\perp 3}$. The parton 4 stands for the photon in the (D) case or the parton which fragments into photon in the (F) case. Two arbitrarily (unphysical) parameters R_{Th} and p_{Tm} are introduced with $p_{Tm} \ll |\vec{p}_{\perp 3,4}|$ and $R_{Th} \ll 1$. Then the phase space is sliced into four parts as the following:

1. Part I is the cylinder which satisfies $|\vec{p}_{\perp 5}| < p_{Tm}$. It includes IR soft and initial-state collinear divergences and the final-state soft+collinear divergences.

⁹ The $\sigma^{(D)}$ and $\sigma_i^{(F)}$ include the convolution with PDF of initial hadrons, thus they are not the hard partonic cross sections.

2. Part II a is determined by $|p_{\perp 5}| > p_{\perp m}$ and $p_{\perp 5} \in C_3$, where C_3 is the cone which is defined by $(y_5 - y_3)^2 + (\phi_5 - \phi_3)^2 \leq R_{Th}^2$. It includes the final collinear divergence which comes from the collinearity of partons 5 and 3.
3. Part II a is determined by $|p_{\perp 5}| > p_{\perp m}$ and $p_{\perp 5} \in C_4$, where C_4 is the cone which is defined by $(y_5 - y_4)^2 + (\phi_5 - \phi_4)^2 \leq R_{Th}^2$. It includes the final collinear divergence which comes from the collinearity of partons 5 and 4. (Note that this part is similar to part II a except the parton 3 replacing by parton 4.)
4. Part II c is the remaining phase space region, where $|\vec{p}_{\perp 5}| \geq p_{Tm}$ and $\vec{p}_{\perp 5} \notin C_3, C_4$. It is a finite part.

The dimensional regularization is used to regularize the IR soft and collinear divergences on parts I, II a, and II b: the dimension is $n = 4 - 2\epsilon$ with $\epsilon < 0$. Consequently, one can perform the integration over the parton 5 for these parts and gets the results including the divergent terms as $1/\epsilon$ and non-divergent terms when $\epsilon \rightarrow 0$. By combining with the corresponding virtual correction, those IR soft divergences vanish and the remaining divergences, i.e. the collinear ones, are factorized out and absorbed in the PDFs or FFs, respectively for part I or part II a and II b. Note that, the corresponding cross sections depend on the arbitrarily choice of factorization scheme and so they are not necessary positive. They are called "quasi" $2 \rightarrow 2$ cross section. (In fact, after the parton 5 is integrated out, these cross sections have the kinematics comparable to the $2 \rightarrow 2$ ones.) The part II c contains no divergence; therefore, it is safe to take $\epsilon = 0$ in dealing with it.

The isolation on photon tagging

The photon which is produced from the decay of mesons such as π^0 , η , ω etc, gives a huge background in studying the prompt-photon production at hadron colliders. In order to suppress the background of those secondary photons, the events are selected by applying an isolation criterion (see for example [99] and references inside) on the photon candidates.¹⁰

A widely used photon isolation criterion is defined as the following. A cone around the photon direction in the rapidity y and azimuthal angle ϕ plane is introduced. The isolation criterion requires that inside this cone, of radius R fixed by experiment, the accompanying hadronic transverse energy $E_{T \text{ had}}$ deposited must be less than a finite amount $E_{T \text{ max}}$ fixed by experiment. This can be formulated as follows

$$\left. \begin{aligned} (y - y^\gamma)^2 + (\phi - \phi^\gamma)^2 &\leq R^2, \\ E_{T \text{ had}} &\leq E_{T \text{ max}} \end{aligned} \right\} \quad (2.22)$$

10. In the study of diphoton production, for example, this requirement plays an important role for Higgs decay channel since the background of the mesons decay channel is about eight orders of magnitude larger than the signal. In addition, the NLO QCD calculation for diphoton with isolation cuts in p - p collision is also a part of the background for Higgs decay at LHC. This interest for this channel goes beyond the present study in this thesis. Its investigation can be found in reference [15].

Instead of a fixed value $E_{T \max}$, one can use a fixed fraction ϵ_h of the photon transverse momentum, the requirement of the criterion is:

$$\left. \begin{aligned} (y - y^\gamma)^2 + (\phi - \phi^\gamma)^2 &\leq R^2, \\ E_{T \text{ had}} &\leq \epsilon E_T^\gamma \end{aligned} \right\} \quad (2.22')$$

From a theoretical point of view, the isolation, given in Eq. (2.22'), implies that the region where the FF fraction z is lower than $(1 + \epsilon_h)^{-1}$ does not contribute. Thus for the contribution (F), only the $\mathcal{D}_{q(\bar{q},g)}^\gamma(z, M_F^2)$ which corresponds to $z \geq (1 + \epsilon_h)^{-1}$ still remains. Moreover, the mean $\langle z_h \rangle$ is roughly 0.7 at Tevatron and 0.6 at LHC for the inclusive case, while $(1 + \epsilon_h)^{-1}$ is greater than 0.9 with $\epsilon \sim 0.07$. Therefore, the contribution (F) is much more suppressed than the (D) contribution when applying isolation cuts.

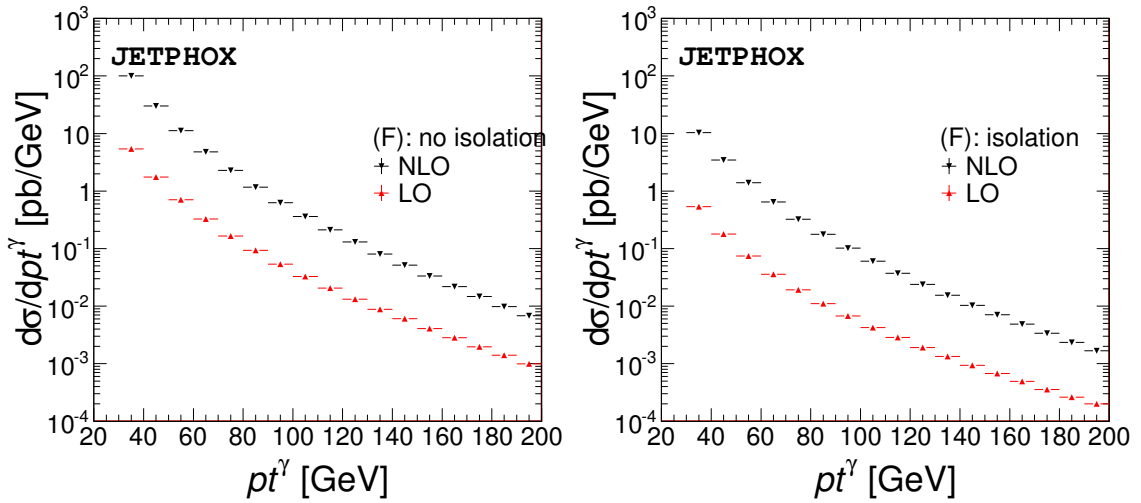


Figure 2.10: The photon transverse momentum distribution of (F): (left) without any photon isolation cut, (right) with photon isolation cuts: $R_{\text{iso}} = 0.4$ and $\epsilon_h = 0.07$. (The constraint $M_{q\bar{q}}^2 > m_b^2$ is used for technical test.)

For the isolation purposes, the amount of $E_{T \max}$ and R must not be large. However, if the value $E_{T \max}$ (or fraction ϵ_h) is chosen to be zero, the cross section is IR divergent, e.g. (D), contains term like $\alpha_S R^2 \log(p_\perp/E_{T \max})$ which is divergent when $E_{T \max} \rightarrow 0$.¹¹ Also for the cone radius, R , it must not be too small, $R \geq 0.2$, otherwise crazy results are got: the isolation cross section is greater than the inclusive one! Therefore the large log R need to be resummed order by order [99, 100].

¹¹ Again, only the sum of (D) and (F) contributions has a physical meaning, while each of them does not.

2.2.2 Generation of events in JETPHOX with BASES-SPRING

Generate events for non negative integrand

To evaluate a non-negative function $f(x)$ over a certain domain X BASES-SPRING [101] generates N_{call} configurations¹² x_i , $i = 1..N_{call}$, using an adaptive MC algorithm [102], such that the event x_i has the estimated probability distribution

$$\rho(x_i) = \frac{f(x_i)}{\sigma} \quad (2.23)$$

where $\sigma = \int_X f(x)dx$, which plays the role of cross section.

Thanks to Eq. (2.23), the probability for an event to belong to a bin (range) $(a, b) \subset X$ is

$$\frac{\Delta N}{N_{call}} = \sum_{k=1}^{\Delta N} \frac{f(x_k)}{\sigma} \Delta x_k, \quad N_{call} \rightarrow \text{large enough} \quad (2.24)$$

where $\Delta x_k = x_{k+1} - x_k$, ΔN is number of events in bin (a, b) . It follows that the integral of $f(x)$ over bin (a, b) can, then, be estimated at

$$\begin{aligned} S(a, b) &\equiv \sum_{k=1}^{\Delta N} f(x_k) \Delta x_k \\ &= \frac{\sigma}{N_{call}} \Delta N \end{aligned} \quad (2.25)$$

and the differential cross section (with respect to x) contributing to bin (a, b) is averaged by

$$\frac{S(a, b)}{b - a} = \frac{\sigma}{N_{call}} \frac{\Delta N}{b - a} \quad (2.26)$$

Generate events for arbitrarily sign integrand

In practice, the integrands, $f(x)$, which are implemented in JETPHOX¹³ have an arbitrary sign for any configurations. In addition, BASES-SPRING only supports non-negative functions due to the event generation purpose. One cannot directly apply BASES-SPRING for $f(x)$. One has to apply it for $|f(x)|$ instead and includes sign information of $f(x)$ in the generated events. It is clear that the event probability distribution is given as

$$\rho(x_i) = \frac{|f(x_i)|}{\sigma_p}, \quad (2.27)$$

12. N_{call} also plays a role of number of integrand evaluations.

13. http://lapth.cnrs.fr/PHOX_FAMILY/main.html

where $\sigma_p = \int_X |f(x)| dx$ does not play the role the cross section. From the derivation of Eq. (2.24), one gets

$$\frac{\Delta N}{N_{call}} = \sum_{k=1}^{\Delta N} \frac{|f(x_k)|}{\sigma_p} \Delta x_k \quad (2.28)$$

The left hand side of Eq. (2.28) results in filling the histogram with weight equals +1, as default, for every event in bin (a, b) and of normalizing the histogram by $1/N_{call}$. Assign the sign of $f(x_k)$ to the new weight, saying w_k , of event k then fill the histogram, one will get

$$\sum_{k=1}^{\Delta N} \text{sign}[f(x_k)] = \Delta N^+ - \Delta N^- \equiv \text{Total event contribution at bin (a,b)} \quad (2.29)$$

where $\Delta N^+ + \Delta N^- = \Delta N$ with ΔN^+ and ΔN^- are number of events whose weights are positive and negative, respectively. Then

$$\sum_{k=1}^{\Delta N} \frac{\text{sign}[f(x_k)]}{N_{call}} = \frac{\Delta N^+}{N_{call}} - \frac{\Delta N^-}{N_{call}} \equiv \text{Total event distribution at bin (a,b)} \quad (2.30)$$

On the right hand side of Eq. (2.30), the term $\frac{\Delta N^+}{N_{call}}$ (or $\frac{\Delta N^-}{N_{call}}$) plays the role of the probability of event with positive (or negative) weight which belongs to bin (a, b) . Using the probability distribution formula in Eq. (2.27), those terms are approximated as follows

$$\begin{aligned} \frac{\Delta N^+}{N_{call}} &\approx \sum_{k=1}^{\Delta N^+} \frac{|f(x_k^+)|}{\sigma_p} \Delta x_k = \frac{1}{\sigma_p} \sum_{k=1}^{\Delta N^+} f(x_k^+) \Delta x_k \\ \frac{\Delta N^-}{N_{call}} &\approx \sum_{k=1}^{\Delta N^-} \frac{|f(x_k^-)|}{\sigma_p} \Delta x_k = -\frac{1}{\sigma_p} \sum_{k=1}^{\Delta N^-} f(x_k^-) \Delta x_k \end{aligned} \quad (2.31)$$

where x_k^+ and x_k^- are solutions for equation $f(x_k) = |f(x_k)|$ and $f(x_k) = -|f(x_k)|$, respectively. Substitute Eq. (2.31) to (2.30), one gets

$$\begin{aligned} \sum_{k=1}^{\Delta N} \frac{\text{sign}[f(x_k)]}{N_{call}} &= \frac{\Delta N^+}{N_{call}} - \frac{\Delta N^-}{N_{call}} \\ &\approx \frac{1}{\sigma_p} \sum_{k=1}^{\Delta N^+} f(x_k^+) \Delta x_k + \frac{1}{\sigma_p} \sum_{k=1}^{\Delta N^-} f(x_k^-) \Delta x_k \\ &= \frac{1}{\sigma_p} \sum_{k=1}^{\Delta N} f(x_k) \Delta x_k \end{aligned} \quad (2.32)$$

Therefore, the integral $\int_a^b f(x)dx$ is, given N_{call} large enough, estimated at

$$\begin{aligned} S(a, b) &\equiv \sum_{k=1}^{\Delta N} f(x_k) \Delta x_k = \frac{\sigma_p}{N_{call}} (\Delta N^+ - \Delta N^-) \\ &= \frac{\sigma_p}{N_{call}} \sum_{k=1}^{\Delta N} \text{sign}[f(x_k)] \end{aligned} \quad (2.33)$$

and formula in Eq. (2.26) is re-written as

$$\begin{aligned} \frac{S(a, b)}{b-a} &= \frac{\sigma_p}{N_{call}} \frac{\Delta N^+ - \Delta N^-}{b-a} \\ &= \frac{\sigma_p}{N_{call}} \frac{\sum_{k=1}^{\Delta N} \text{sign}[f(x_k)]}{b-a} \end{aligned} \quad (2.34)$$

In short, one has to save the sign of $f(x_j)$ to weight of event x_j , which is generated by dealing with $|f(x)|$, then one estimates the cross section and differential cross sections contribution as in Eqs. (2.33) and (2.34), respectively.

Test of generation with well known function

For illustration purpose, let us consider following functions:

$$f_1(x) = x - x^2, \quad f_2(x) = x^3 - x^2, \quad \text{and} \quad f(x) = x^3 - 2x^2 + x. \quad (2.35)$$

As is well known, $f(x)$ is a non negative function, while $f_1(x)$ and $f_2(x)$ are the functions of arbitrary sign with $x \in [0, 1.5]$. On the other hand, one can use the method above for generating events related to those functions and filling the histograms with those events. As illustrated in Fig. 2.11, the numerical histograms agree very well with the exact graphs. The agreement shows that the approximation is acceptable with $N_{call} = 10^5$.

Let us take another example with 2-variable functions

$$\begin{aligned} g_1(x, y) &= \frac{x+y}{25} [x^2 - (x+y)] \\ g_2(x, y) &= \frac{x}{5} \frac{\sin(x+y)}{x+y} \\ g(x, y) &= \frac{x+y}{25} [x^2 - (x+y)] + \frac{x}{5} \frac{\sin(x+y)}{x+y} \end{aligned} \quad (2.36)$$

and their integrals are performed over region $\Omega = \{0 < x < 5, 0.1 - x < y < 8 - x\}$

$$\sigma_i(g) = \int_{\Omega} g_i(x, y) dx dy, \quad i = 1, 2, \text{ or } \emptyset \quad (2.37)$$

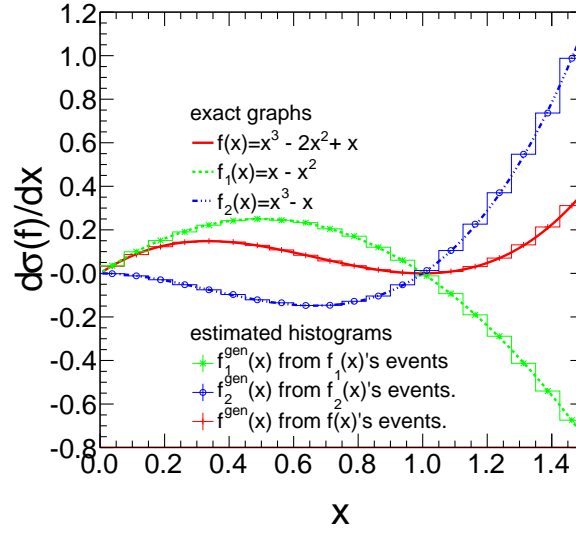


Figure 2.11: Comparison between histograms constructed from their generated events and exact graphs, with respect to x

Assume that one is interested in $d\sigma_i(g)/dz$, where $z = x + y$. Given the intrinsic form of an integral, such as

$$\sigma_1(g) = \int_0^5 dx \int_{0.1-x}^{8-x} dy \frac{x+y}{25} [x^2 - (x+y)], \quad (2.38)$$

it is obvious that one can replace the integral over variable y by z where $z = x + y$. The necessary information to carry out the calculation is:

$$\begin{aligned} dy &= dz \\ z_{min} &= x + (0.1 - x) = 0.1 \\ z_{max} &= x + (8 - x) = 8 \end{aligned} \quad (2.39)$$

then

$$\sigma_1(g) = \int_0^5 dx \int_{0.1}^8 dz \frac{z}{25} [x^2 - z] = \int_{0.1}^8 dz \left[\frac{5z}{3} - \frac{z^2}{5} \right] \quad (2.40)$$

It is straightforward to derive from Eq. (2.40) the z distribution of $\sigma_1(g)$, as function of z , as

$$g_1(z) \equiv \frac{d\sigma_1(g)}{dz} = \frac{5z}{3} - \frac{z^2}{5}, \quad z \in (0.1, 8). \quad (2.41)$$

With the same algebra, one also gets the z distribution of $\sigma_2(g)$ and $\sigma(g)$, respectively, as

$$g_2(z) \equiv \frac{d\sigma_2(g)}{dz} = \frac{5}{2} \frac{\sin(z)}{z}$$

$$g(z) \equiv \frac{d\sigma(g)}{dz} = \frac{5z}{3} - \frac{z^2}{5} + \frac{5}{2} \frac{\sin(z)}{z}, \quad z \in (0.1, 8). \quad (2.42)$$

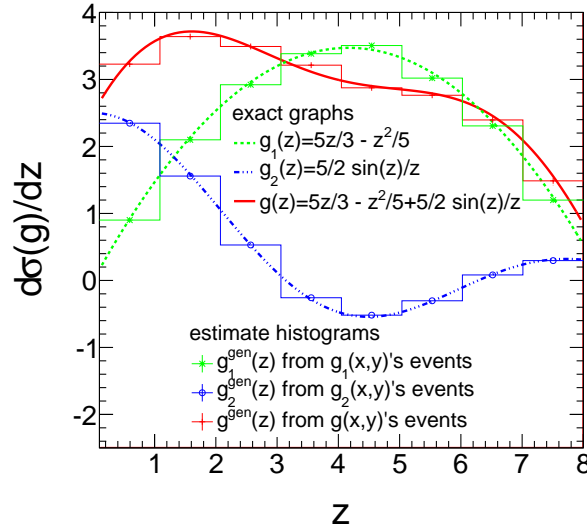


Figure 2.12: The comparison between histograms constructed from their generated events and exact graphs, with respect to $z = x + y$

Now suppose one uses the technique of the previous discussion to generate events for the integrands, which depend on x and y , in Eq. (2.36). From those events, one will calculate $z = x + y$ for each event, then estimate $d\sigma_i(g)/dz$ as a z histogram, which is filled with variable z and event weight. The estimated results agree very well with these exact graphs as shown in Fig. 2.12, given $N_{call} = 10^5$.

Partonic events of JETPHOX

The differential cross sections of the parts I, II a, II b, and II c (see section 2.2.1) of phase space are integrated by using Monte Carlo method and the corresponding probability distributions are produced. (At this step, the kinematic cut, such as 4-momentum and rapidity, may be already implemented.) Those are used to sample the partonic events and the events which include 4-momenta of final partons are generated. From the 4-momenta, one can construct the variable which is of interest, then projects those partonic events with respect to this variable onto a histogram to get the desired distribution. In addition, further constraints can be applied at the events selection step. Therefore, for given event sample, one can study various observables and their dependences with respect to physical parameters of interest, such as kinematics, isolation criteria, and jet algorithm. We emphasize

that for the jet algorithm or/and isolation criteria dependence study, the corresponding constraint(s) must not be implemented when generating probability distributions. This is easily controlled from the input of the program.

In practice, the generated events are treated separately for different mechanisms, i.e. (D) or (F), and from different contributions, i.e. $2 \rightarrow 3$, $2 \rightarrow 2$, and quasi $2 \rightarrow 2$ one, at given mechanism. For practical purposes, the label which identifies the contribution is stored for the corresponding event. Since the quasi $2 \rightarrow 2$ differential cross sections almost always give negative contributions while the $2 \rightarrow 3$ ones almost always give the positive one, the above arbitrary sign approach is systematically used for generating events. The weight of the event is, therefore, ± 1 depending on the sign of the integrand for the corresponding configuration in phase space.

We recall that only the sum of those contributions, but not each of them, has a physical meaning; therefore, each event which is generated by this program does not represent the realistic phase space configuration. Given a specific region with large enough number of events, all contributions are present and the mean contribution for this region is comparable with the realistic one, e.g. it is the mean of the bin content of the projected histogram which is of interest.

After running the program, one gets the ntuple which is the file storing the generated events. The file `read_tree.C` (or `read_tree_1.C`), which is included in JETPHOX package, illustrates how the event contents can be loaded to be ready for analyses (see appendix B.2).

2.2.3 Comparison between JETPHOX and the inclusive prompt photon data

Since the prompt photon production in hadronic colliders at Tevatron ($\sqrt{s} = 1.96$ TeV) and LHC ($\sqrt{s} = 7$ TeV) has been measured, the study on prompt photon production provides a precision tests on understanding pQCD as well as a chance to put further constraints on gluon density [2, 99, 100, 103]. On the theoretical side, JETPHOX which is a general-purpose NLO generator for photon/hadron+jet production in hadron collisions provides a suitable tool for this study. A part from that, in this section, we discuss the use of JETPHOX in studying inclusive isolated prompt photon production in hadro-production at fixed-target experiments and in hadron-hadron collisions at the Tevatron and LHC.

A decade ago, JETPHOX was first presented in Ref. [99] as an introduction of the tool for studying isolated prompt photon in hadron-hadron collisions at full NLO in QCD. Later, the first attempts to compare its prediction with experimental measurements for the isolated photon production were performed as in Ref. [104] (D0 Run II preliminary) and by JETPHOX group [100] (Tevatron Run II at $\sqrt{s} = 1.96$ TeV as well as fixed-target experiments). The isolation criteria for photon is accounted by requiring that the photon should not be surrounded by hadronic energy carrying more than 10% of the photon energy within the cone of radius $R \equiv \sqrt{\Delta y^2 + \Delta \phi^2} = 0.4$. The cross section is measured

in the range of transverse momentum $23 < p_{\perp}^{\gamma} < 300$ (GeV) and in the central rapidity region $|y^{\gamma}| < 0.9$. Ignoring the E706 results, perfect agreement between data and NLO QCD from $\sqrt{s} = 23$ GeV to 1.96 TeV is obtained as in Fig 2.13, even though the cross

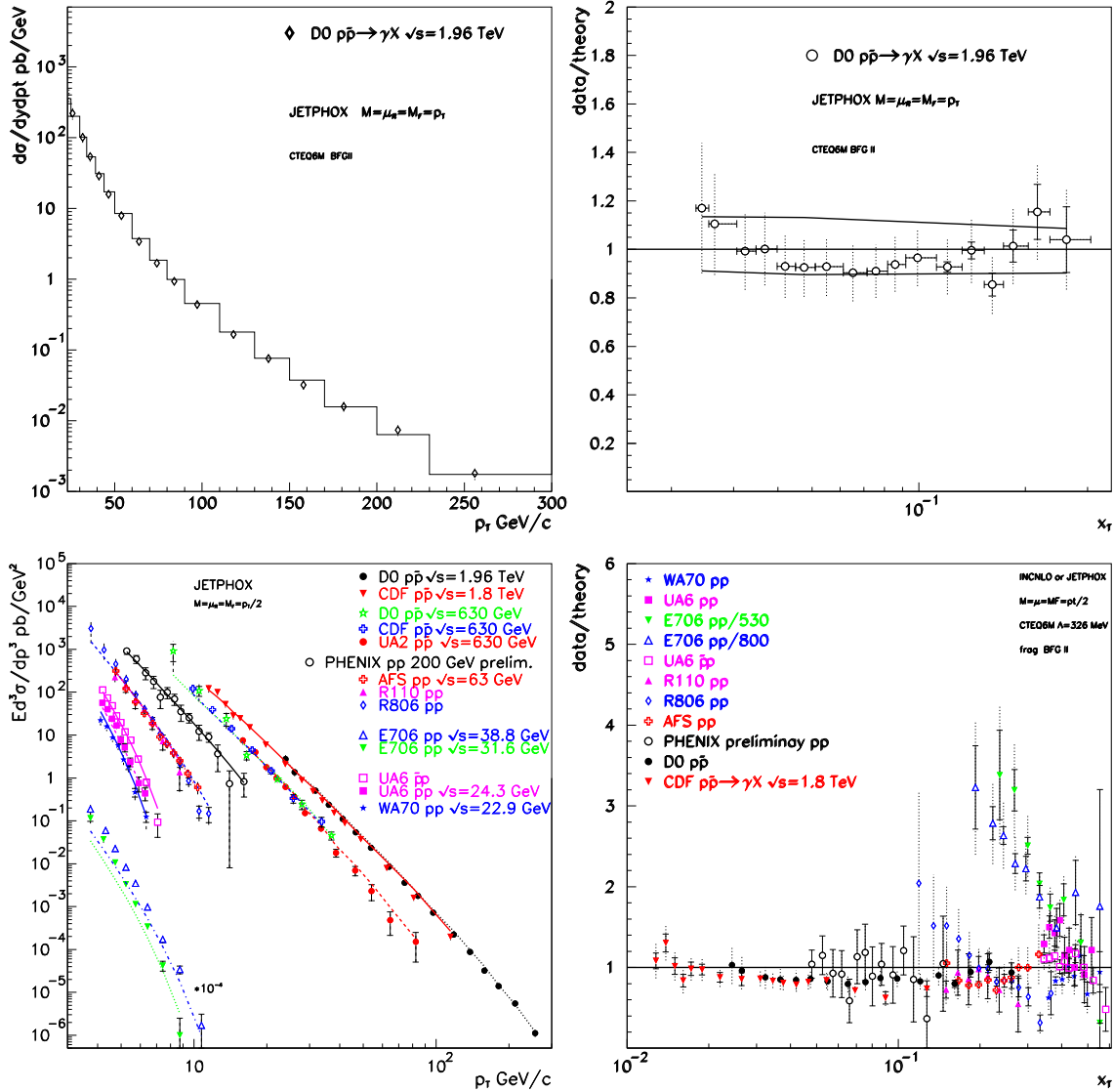


Figure 2.13: The comparison of inclusive prompt photon production between data measurements (at fixed targets and the Tevatron) and the JETPHOX NLO predictions using BFG II (CTEQ6M) for fragmentation (structure) functions. Taken from Ref. [100].

section goes down 9 orders of magnitude in the considered p_{\perp} range (the left plots). For probing how the scale choices affect the theoretical calculation, the ratio of differential cross section with respect to scaled momentum $x_T = 2p_T/\sqrt{s}$ for $\mu = p_{\perp}/2$ and $\mu = 2p_{\perp}$ to $\mu = p_{\perp}$ are plotted on the right top plot, where the three scales are equal. The ratio of data to the prediction for $\mu = p_{\perp}$ is presented and agrees well with theoretical scales

dependence band. The disagreement between prediction and E706 experiment, bottom plots in Fig 2.13, shed some doubt about the validity of these experimental results, a complete discussion is given in the considered reference [100].

Recently, CDF has measured the inclusive isolated prompt photon cross section in $p\text{-}\bar{p}$ collisions at $\sqrt{s} = 1.96$ TeV with photon transverse energy up to $E_T \sim 400$ GeV. The photons are required to have $|\eta^\gamma| < 0.1$, $E_T^\gamma > 30$ GeV, and to be isolated with the hadronic deposited energy $E_T^{\text{iso}} < 2$ GeV in a cone of radius $R = 0.4$ around it. The NLO pQCD predictions which are shown use JETPHOX with CTEQ6.1M PDF. The normalizations, factorization, and fragmentation scales are set to order of E_T^γ and criteria for isolated photon is the same as for data. The measured cross section agrees with the predictions within the uncertainties in range of $E_T^\gamma \gtrsim 40$ GeV (see Fig. 2.14). However, at

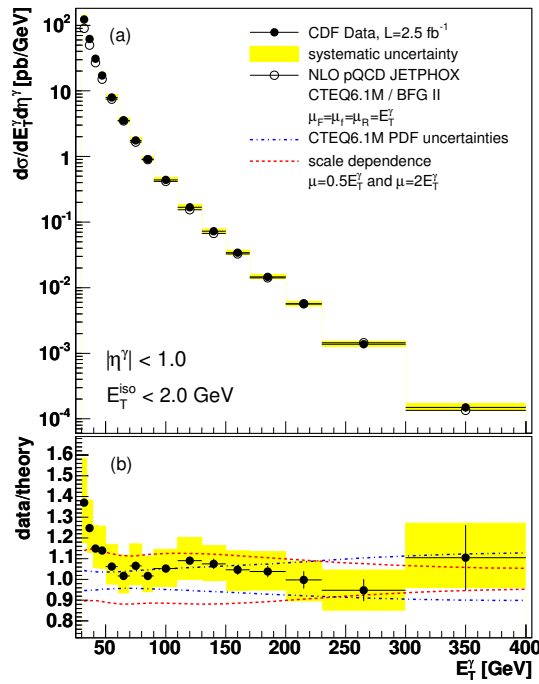


Figure 2.14: The comparison of inclusive prompt photon production between CDF data measurement at $\sqrt{s} = 1.96$ TeV in $p\text{-}\bar{p}$ collisions and the JETPHOX NLO predictions using BFG II (CTEQ6M) for fragmentation (structure) functions. Taken from Ref. [105].

lower range of $E_T^\gamma < 40$ GeV, the data steeply increases when E_T^γ decreases and is higher than the theory. This fact is somewhat similar to the comparison of D0 measurements with predictions using JETPHOX at low $x_T \lesssim 0.03$ as in the top right plot in Fig. 2.13.

CMS [3] (ATLAS [4]) collaborations had performed measurements of the isolated prompt photon production in $p\text{-}p$ collisions at $\sqrt{s} = 7$ TeV in 2010 with 36pb^{-1} (35pb^{-1}) used 25 GeV (45 GeV) cuts on E_T^γ . An example of the comparison between CMS (ATLAS) measurements and NLO prediction using JETPHOX is shown on top (left bottom) plots of Fig. 2.15. Photon is said isolated if E_T^{iso} in cone of radius $R = 0.4$ is lower than

5 GeV for CMS or 4 GeV for ATLAS. The most recent results of inclusive prompt photon production from ATLAS [5] cover the kinematic range $100 \leq E_T \leq 1000$ (GeV) and uses the 2011 data set with 4.6 fb^{-1} . The right bottom plot of Fig. 2.15 measurement and

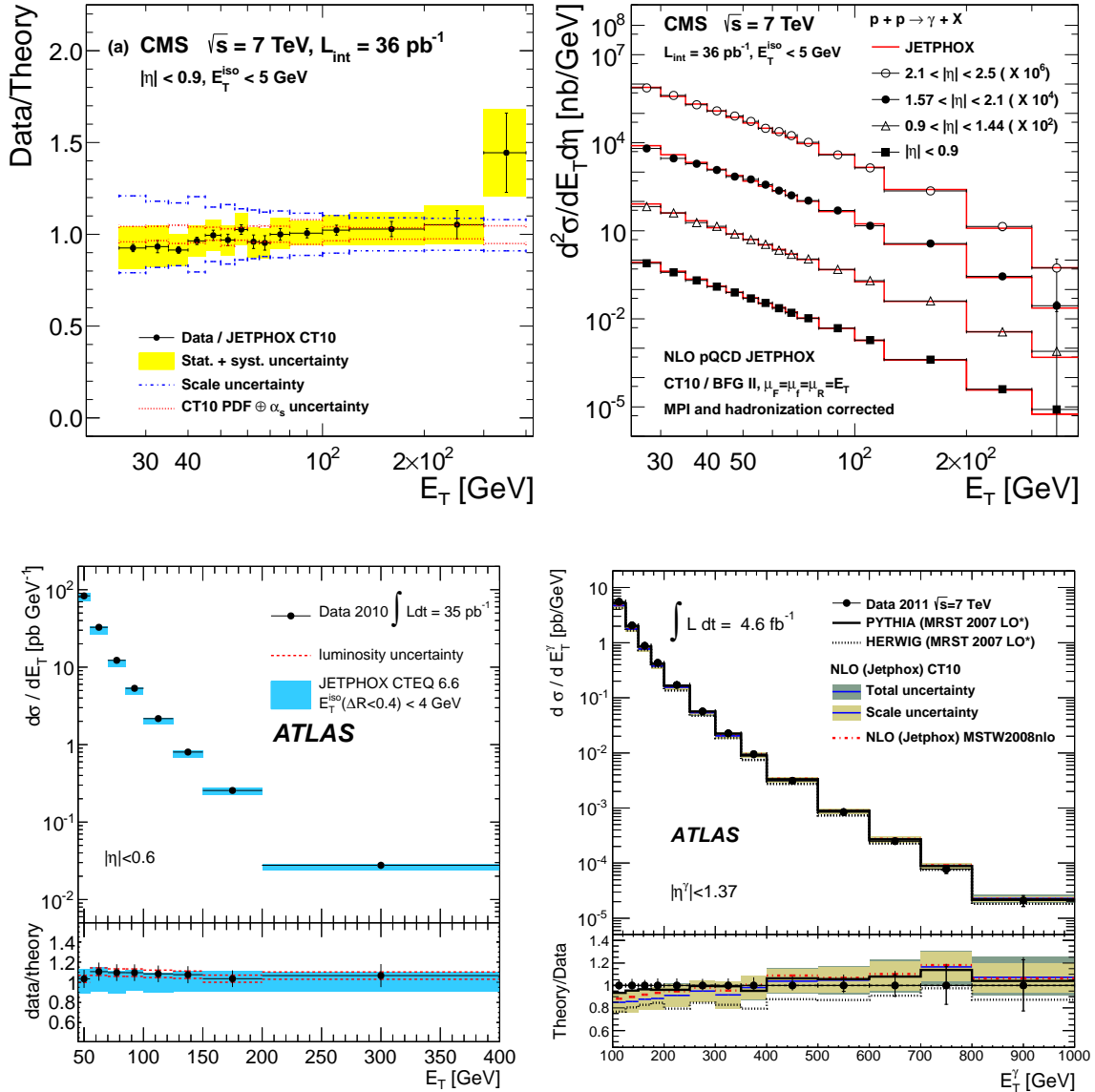


Figure 2.15: The comparison of inclusive prompt photon production between data measurement at LHC at $\sqrt{s} = 7 \text{ TeV}$ and the NLO QCD generator *JETPHOX*. Taken in Refs. [3] (CMS) and [4, 5] (ATLAS).

JETPHOX simulation prediction with requirement of isolation parameter is $E_T^{\text{iso}} < 7 \text{ GeV}$. Those comparisons illustrated in Fig. 2.15 show that the NLO calculations agree with the data up to the highest E_T^γ . The data somewhat higher than the central NLO prediction for $50 \lesssim E_T^\gamma \lesssim 400 \text{ GeV}$ and lower for low (large) $E_T^\gamma \lesssim 50 \text{ GeV}$ ($E_T^\gamma > 400 \text{ GeV}$), but agree within the theoretical uncertainty bands of NLO calculation using *JETPHOX*.

The low transverse energy region E_T^γ is interesting. On the one hand, *JETPHOX* seems to

overestimate the very preliminary ALICE data in p - p collisions at LHC at $\sqrt{s} = 7$ TeV in the region 10–25 GeV [106]. On the other hand, it underestimates CDF data in p - \bar{p} collisions at Tevatron at $\sqrt{s} = 1.96$ TeV in the region 30–39 GeV. This is an illustration of the fact that it is difficult to extract the isolated photon from the background in this region. From the theoretical point of view, the NLO pQCD predictions may also not be reliable for very small x_T values.

The agreements of NLO QCD predictions and data measurements from fixed-target to hadronic colliders at Tevatron and LHC confirm that the \sqrt{s} dependence of the reaction can be described within the NLO QCD formalism. As shown in the different pictures, JETPHOX can be regarded as a suitable tool for prompt photon production at LHC. For that reason, JETPHOX is used as the basic framework for those studies which are presented in chapters 3 and 4.

Chapter 3

Hadron jet correlations and constraints on FFs at LHC

Contents

3.1	Introduction	68
3.2	Framework	70
3.2.1	Fragmentation function sets	70
3.2.2	A quick look at LO calculation	70
3.2.3	The FF scale M_F issue	72
3.3	Same-side hadron-jet momentum correlations	75
3.3.1	Framework	75
3.3.2	Correlations with inclusive charged hadrons	77
3.3.3	Correlations with identified hadrons	80
3.4	Away-side hadron-jet momentum correlations	82
3.4.1	Framework	82
3.4.2	Correlations with inclusive charged hadrons	83
3.4.3	Correlations with identified hadrons	86
3.5	Conclusion	88

3.1 Introduction

The perturbative QCD calculation of large transverse-momentum (p_{\perp}) hadron production at hadronic colliders requires the knowledge of the non-perturbative fragmentation functions (FF), D_i^h , which describe the transition from partons to hadrons. On top of constraining non-perturbative aspects of QCD, fragmentation functions are also often used and needed in the context of “jet quenching” studies in heavy-ion collisions, in order to describe parton energy loss processes in the quark-gluon plasma (see e.g. [107]).

Fragmentation functions have first been determined from global fits of e^+e^- data (e.g. BFGW [57], KKP [61], Kretzer [60]), at LEP and other facilities at lower energies. However, measurements in e^+e^- collisions essentially constrain the *quark* FF¹ and at not too large momentum fraction z . In order to get additional constraints, various groups recently included data on single hadron production at hadronic colliders, e.g. RHIC (AKK08 [87], DSS [85, 86]), Tevatron (AKK08), as well as data in low- Q^2 semi-inclusive deep inelastic scattering (DSS). Also, attempts to estimate theoretical uncertainties have been performed by DSS and HKNS [73] which confirmed the lack of constraints on gluon FF at large z .

Unlike in e^+e^- collisions, for which the (anti-)quark momentum is known at leading order, single hadron production in hadronic collisions does not allow the energy of the fragmenting parton to be estimated, because the partonic center of mass energy is not fixed. As a consequence, the measurement of hadron p_{\perp} -spectra in p–p collisions is sensitive to some moments of FF only.² On the contrary, performing momentum correlations in double inclusive hadron–jet production would in principle be able to probe more precisely the z dependence of fragmentation functions. Similarly, analyses of photon–jet [109] and photon–hadron [110] momentum correlations aiming at setting additional constraints on FF into photons and into hadrons have also been carried out recently. In the latter study, the photon is produced in the away side of the measured hadron; its momentum can therefore serve as a proxy for that of the recoiling parton as long as only one jet is produced in the event, i.e. if real higher order corrections (with $2 \rightarrow 3$ kinematics for the parton scattering dynamics) remain small.

In order to circumvent this issue and to increase counting rates, we firstly investigate in this study the energy distribution of energetic hadrons inside identified jets in p–p collisions at the LHC as a mean to further constrain FF. Then the same investigation if the hadron is away-side of the identified jets is also presented. The analysis is carried out at NLO accuracy with JETPHOX and using various FF sets available (AKK08, BFGW, DSS, HKNS, Kretzer).

For convenience, we denote the jet which includes the hadron by *jeth* for the same-side hadron-jet study, see Fig 3.1 (a), (b). The leading jet which is away side of the produced

1. In e^+e^- collisions, gluon FF, D_g^h , can only be probed via scaling violations of D_q^h , or through 3-jet events.

2. A recent analysis [108] of collider data compared with theoretical predictions based on these FF parametrizations lead to the conclusion that most of the theoretical predictions tend to overpredict the measured LHC and Tevatron cross sections.

hadron is denoted by jet3 for the away-side hadron-jet study, see Fig 3.1 (c), (d).

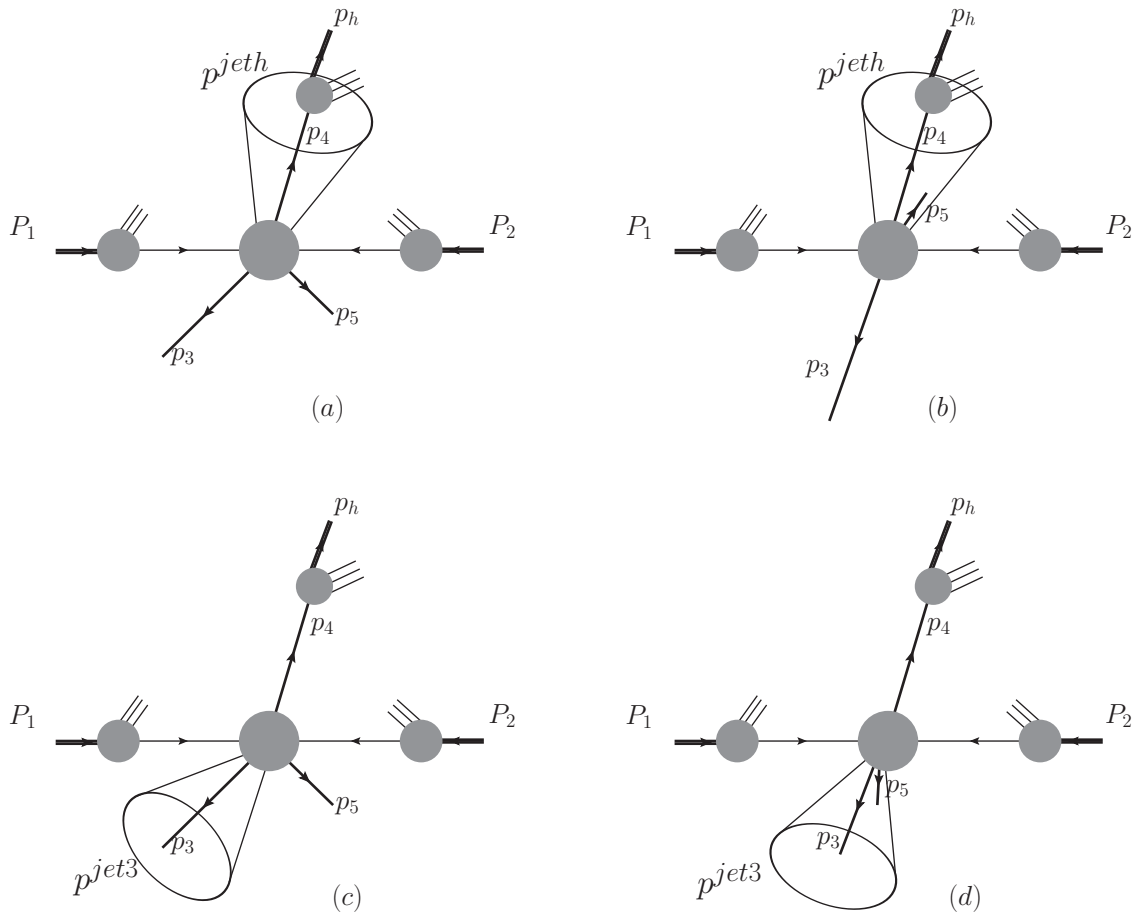


Figure 3.1: An illustration for the jeth and the jet3.

On the experimental side, such a former measurement has been measured e.g. by CMS in Ref. [111] although this study focused on the medium-modifications of hadron distributions at small energy fraction, $z \ll 1$.

3.2 Framework

3.2.1 Fragmentation function sets

The goal of the study in this chapter is to explore the sensitivity of fragmentation functions on the jet–hadron momentum correlations. We shall therefore compare results using various FF sets presently available, namely AKK08 [87], BFGW [57], DSS [85], HKNS [73], Kretzer [60]. (In addition it is also possible in principle, yet CPU-time expensive, to perform the NLO calculations using the theoretical uncertainty bands provided by the DSS and HKNS sets. This goes beyond the scope of this prospective study and is left for future work when precise data become available.) This choice reflects well the variety of the FF sets and the spread in the different predictions, both in shape and in magnitude. In order to illustrate this, the gluon fragmentation into charged hadrons is plotted³ in Fig. 3.2 (left) as a function of z ($Q^2 = 100 \text{ GeV}^2$), showing significant differences between the different parametrizations, especially at large values of z . As shown later, the hadron–jet momentum correlations exhibit similar features thus allowing one to disentangle among the various sets available. The spread among the different FF become even larger when considering fragmentation into identified hadrons, as shown from the AKK08, DSS and HKNS parametrizations of FF into protons+anti-protons (Fig. 3.2, right).

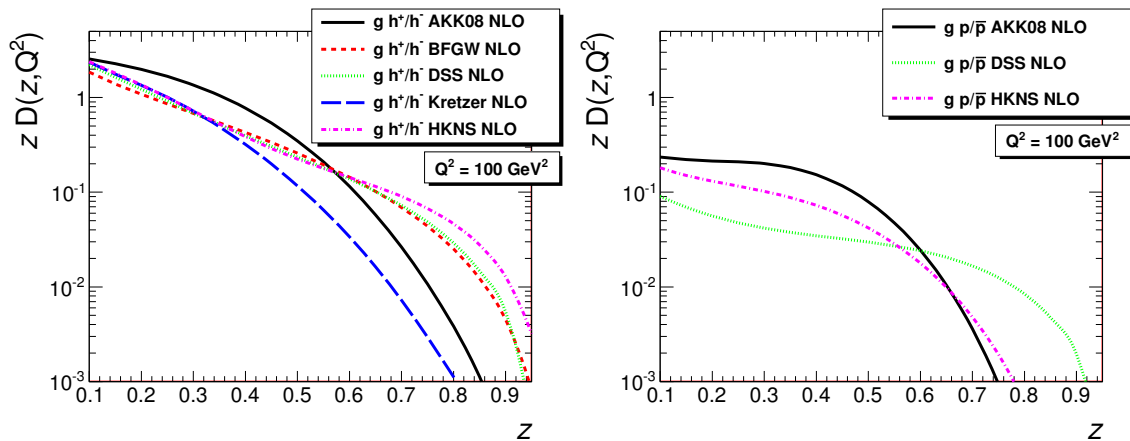


Figure 3.2: Comparison of gluon fragmentation functions into charged hadrons (left) and protons+anti-protons (right), as a function of z and at $Q^2 = 100 \text{ GeV}^2$.

3.2.2 A quick look at LO calculation

At LO calculation for the process $pp \rightarrow h + \text{jet}$, one knows that there are only two final partons produced at partonic level. There is one parton who fragments into the hadron and the other who forms the jet. Because their transverse momenta are equal, one

3. We used the FFGenerator <http://laph.cnr.fr/ffgenerator>.

can identify the FF z as the constructed z_3 , which is defined by $\frac{|p_\perp^h|}{|p_\perp^{\text{jet}3}|}$ at LO, and one also gets the following relation: $p_\perp^{\text{jet}3} > p_\perp^h$. By using JETPHOX, one can calculate the z_3 (which is also the FF z) distribution which are plotted in Fig. 3.3. The results is carried out with

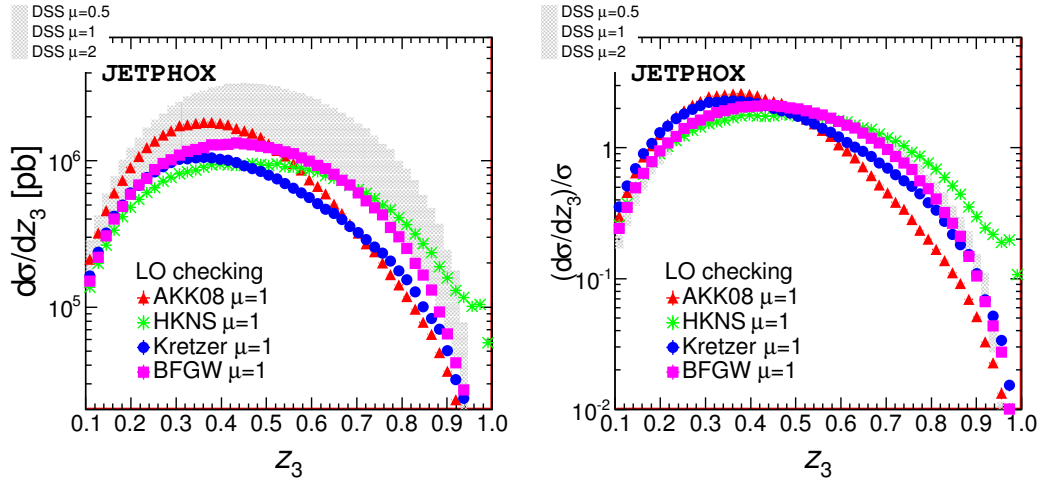


Figure 3.3: Comparison of the constructed z_3 distributions from various FF sets in the LO approximation, for $pp \rightarrow h + \text{jet}$ at $\sqrt{s} = 8$ TeV.

kinematics: $30 < p_\perp^h < 200$ (GeV), $|y^h| < 1$, $p_\perp^{\text{jet}3} > 30$ GeV, and $|y^{\text{jet}3}| < 6$. The discussion on the cuts of calculation is presented later in section 3.3. Here, we just want to notice that the renormalized FF scale, M_F , is taken to be proportional to p_\perp^h in these LO plots. The FF scale choice is itself an interesting aspect and the M_F choice for this study is presented in the next section.

As in the left plot in Fig. 3.3, at large z_3 up to 0.9, there are discrepancies among the group of AKK08, Kretzer and a group of BFGW, DSS, HKNS. Since these behaviors come from their different magnitude, it is may interesting to take a look on their normalized behaviors which are given by normalizing them by their own integrals. They are illustrated in the right plot of Fig. 3.3. The first thing one can see is that the scale dependence for DSS, which is shown as in band plot, is significantly reduced. This is related to the fact that the scale variation mainly changes the normalization of the cross section instead of the shape. In the large z_3 region, $z_3 > 0.7$, the normalized behaviors enable to disentangle HKNS from DSS and also Kretzer from AKK08 comparing to the true distribution case. On contrary, the Kretzer plot becomes entangled with the group of BFGW, DSS. Those effects result from the fact that their shapes are not analogous.

The behavior of the FFs distribution together with the raw approximated results at LO gives us a strong motivation for this study. To get more precise on putting constraints for currently available FF sets, the NLO calculations for the process $pp \rightarrow h + \text{jet}$ are investigated and presented, as discussed in sections 3.3 and 3.4.

3.2.3 The FF scale M_F issue

As discussed in chapter 1, it is necessary to find out the suitable choice for the arbitrary renormalized FF scale M_F .⁴ Given the purpose of hadron fragmentation study, let us start by choosing the scale M_F of the order of p_\perp^h . In the NLO calculation for the process $pp \rightarrow h + \text{jet}$, one cannot reconstruct exactly the FF z due to the fact that the p_\perp of the partons corresponding to the produced hadron and the leading jet are no longer equal. We prefer to use the hadron-jet correlation (momentum correlation [109]) variable,

$$z_3 = - \frac{\vec{p}_\perp^h \cdot \vec{p}_\perp^{\text{jet}3}}{\|\vec{p}_\perp^{\text{jet}3}\|^2} \quad (3.1)$$

which reduces to the exact FF z at LO.

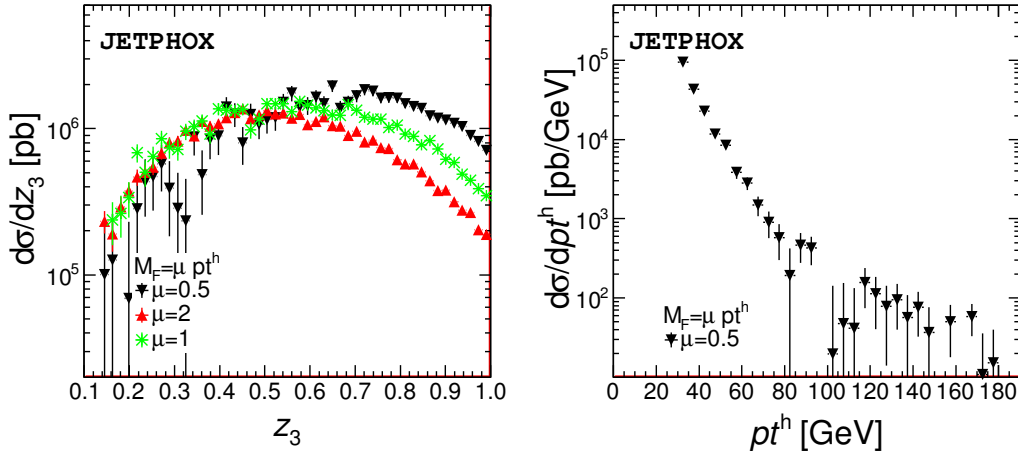


Figure 3.4: (left) Comparison z_3 distribution from various scale $M_F \sim p_\perp^h$, (right) the p_\perp^h distribution. (The BFGW set is used.)

The corresponding distributions involving this variable at the scale $M_F \sim p_\perp^h$ are plotted in Fig. 3.4. The kinematics for the hadron and jet are the same as in the LO discussion (described in section 3.2.2.) As one can see, the behavior of the z_3 distribution becomes more irregular when z_3 gets closer to 0.1, especially for $\mu = 0.5$ case. It seems that the irregular distribution in z_3 corresponds to the bad behavior of the p_\perp^h distribution, but this is not the case. As one can see, the region where the p_\perp^h is not too large is regular. Let us select the events with the additional constraint on hadron, i.e. $p_\perp^h < 80$ GeV, and plot the z_3 and $p_\perp^{\text{jet}3}$ distributions as the top plots in Fig. 3.5. The top-left plot shows that, being given in the region where the p_\perp^h distribution is regular, the corresponding z_3 distributions behave as for the previous one. Together with the top-right plot, one gets that the bad

4. For the full order calculation, in principle, the result does not depend on M_F . As soon as the fixed order calculation, e.g. at NLO, is used in the study, the M_F has been chosen so that one is able to apply the perturbative approach at considering order.

behavior of the $p_{\perp}^{\text{jet}3}$ distribution in the large region is related to the irregular part of the z_3 distribution in the low region.

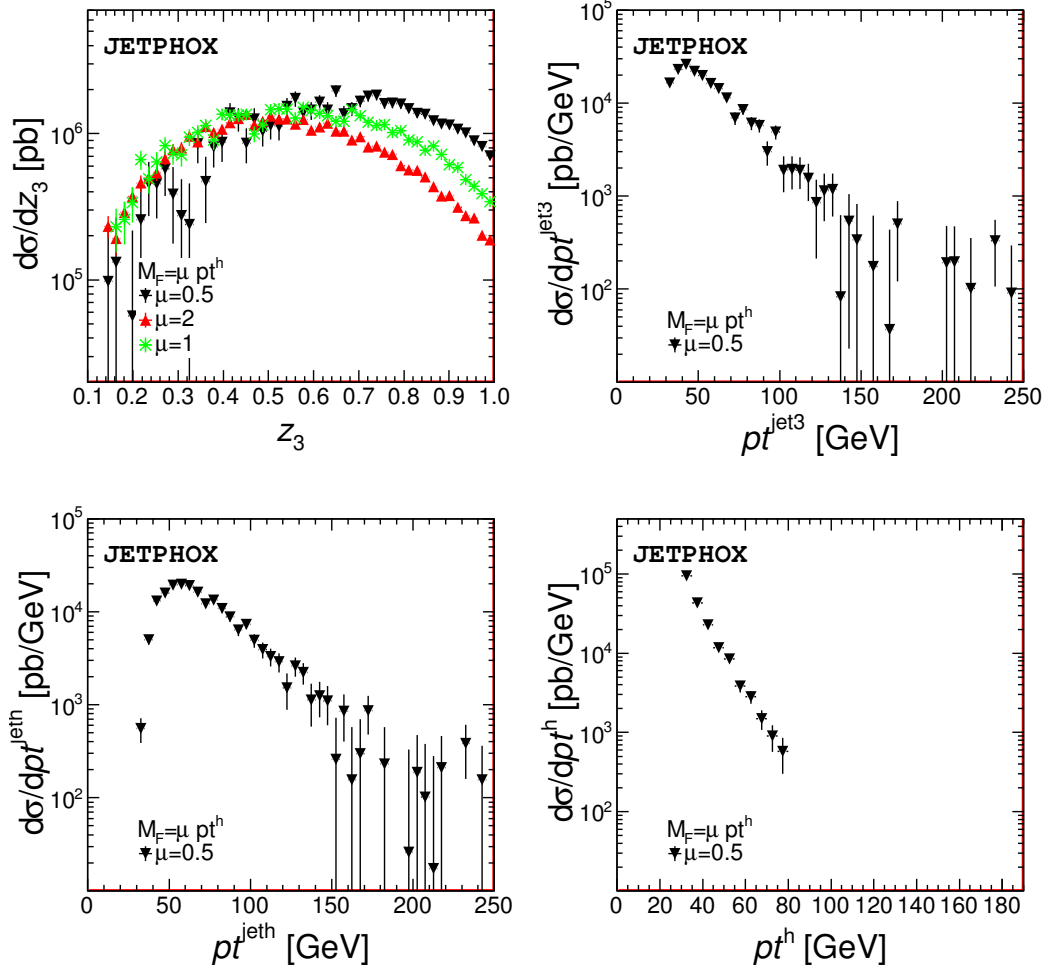


Figure 3.5: An example of various corresponding distributions when the extra condition $p_{\perp}^h < 80$ GeV is used. (The BFGW set is used.)

However, as mentioned, the momentum correlation z_3 plays the role for probing the z dependence for FF, the bad behavior in the low region of z_3 distribution is related to the low z region. Note that, the ratio $p_{\perp}^h/p_{\perp}^{\text{jet}h}$ can be approximately regarded as the FF z . Thus it is also interesting to study the $p_{\perp}^{\text{jet}h}$ distribution for the given accepted events as it is shown at the bottom-left plot in Fig 3.5. As one can see the bad behavior of the jeth transverse momentum distribution start at $p_{\perp}^{\text{jet}h} \gtrsim 160$ GeV. It must be related to the value of the FF $z < 0.5$, therefore also to the constructed $z_3 < 0.5$. Given the cross section is divergent at low p_{\perp}^h and suppressed at large $p_{\perp}^{\text{jet}h}$, the small z region has a strong potential to give rise to the irregular distribution problem in this case.

Moreover, comparing to the LO case, Fig. 3.3, the bad behavior clearly results from the (adding) NLO correction where the LL and NLL resummation into FF are imple-

mented. This statement is illustrated as the bad behavior of the small z_3 distribution, Fig 3.5.

Indeed, as the discussion in section 1.3.1, the corresponding calculation is sensitive to the term which is proportional to $\alpha_S(M_F^2)^3 \ln\left(\frac{(p_\perp^{\text{jeth}})^2}{M_F^2}\right)$. Thus, by choosing $M_F = \mu p_\perp^h$, one can get

$$\alpha_S(M_F^2)^3 \ln\left(\frac{(p_\perp^{\text{jeth}})^2}{M_F^2}\right) = \alpha_S(M_F^2)^3 \ln\left(\frac{1}{\mu^2 z^2}\right) \quad (3.2)$$

It is clear that when z is small, this term is of order of 1 (given μ is 0.5, 1, or 2) and therefore one is not allowed to use the perturbation expansion in corresponding calculation. This fact is illustrated by the z_3 distribution in Fig 3.5. The z_3 distribution for $\mu = 2$ is regular at $z_3 > 0.2$ (where μz_3 is not small), but is irregular when z_3 is close to 0.1 (where $\mu z_3 \ll 1$.) In short, the choice for the FF scale being of order p_\perp^h is not suitable for this calculation.

As the jeth and jet3 momenta are the measurable quantities, let us choose the FF scale being in one of their order. The z_3 distribution for choosing $M_F \sim p_\perp^{\text{jet3}}$ are shown in Fig. 3.6. From this result, one can get that the choice of M_F being in order of p_\perp^{jet3}

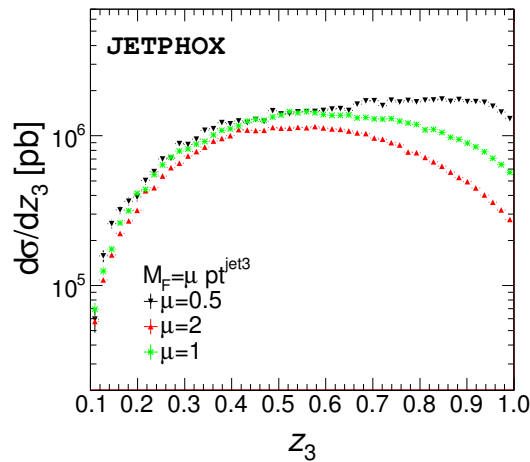


Figure 3.6: Comparison of z_3 distributions from various scale $M_F = \mu p_\perp^{\text{jet3}}$, with $\mu = 0.5, 1, \text{ or } 2$. (The BFGW set is used.)

(therefore also p_\perp^{jeth}) is suitable for the hadron production in association with the heavy-quark jet in pp collision.

This choice motivates us to modify the current version of JETPHOX so that the corresponding numerical calculations can be performed. This point is addressed in appendix B.3 where the upgraded version of JETPHOX, for this purpose, is introduced.

3.3 Same-side hadron-jet momentum correlations

The outline of this study is as follows. In section 3.3.1 we present and motivate the theoretical framework of this aspect. Results on charged and identified hadron–jet momentum correlations are shown and discussed respectively in section 3.3.2 and section 3.3.3.

3.3.1 Framework

Perturbative calculation

The double-inclusive hadron–jet production cross section is computed in p–p collisions at $\sqrt{s} = 8$ TeV at next-to-leading order (NLO) accuracy using the JETPHOX Monte Carlo program [99], with CTEQ6.6 [48] parton distribution functions. Jets are reconstructed using the k_{\perp} algorithm⁵ [89, 90] with a jet radius $R = 0.4$.

The initial-state factorization scale, M , and the renormalization scale, μ , are taken to be equal and proportional to the jet transverse momentum, $M = \mu = p_{\perp}^{\text{jet}}$. For the fragmentation scale we use $M_F = R p_{\perp}^{\text{jet}}$ in order to resum in the fragmentation function $D_q^h(z, M_F)$ all the $\log(R p_{\perp}^{\text{jet}}/M_F)$ -terms present in the higher-order corrections.⁶

In order to estimate the uncertainty of the NLO predictions, all scales are varied simultaneously by a factor of two, up and down, in the calculations. The scale dependence of our results will be discussed in more detail in section 3.3.2 and section 3.3.3.

Hadron momentum distribution inside jets

We consider the distribution in the momentum fraction

$$z_h = \frac{\vec{p}_{\perp}^h \cdot \vec{p}_{\perp}^{\text{jet}}}{|\vec{p}_{\perp}^{\text{jet}}|^2} \quad (3.3)$$

carried by hadrons inside identified jets. At leading order, the fraction z_h reduces to the fragmentation variable z . Also note that the typical angle between the hadron and the jet direction is very small, therefore almost identical results would be obtained using transverse momentum, $p_{\perp}^h/p_{\perp}^{\text{jet}}$, or energy, E^h/E^{jet} , fractions. For consistency with the photon–jet analysis [109], we shall keep the usual momentum imbalance variable (3.3).

The distribution $d\sigma/dz_h$ of hadrons inside jets of *fixed* momentum p_{\perp}^{jet} should therefore directly reflect the z dependence of the fragmentation functions at a hard scale $Q \sim R p_{\perp}^{\text{jet}}$. In this aspect, we rather propose to study the z_h distribution of hadrons inside jets of *all* transverse momenta above p_{\perp}^h , i.e. $p_{\perp}^h < p_{\perp}^{\text{jet}} < \sqrt{s}/2$. With such a requirement, the distribution reflects, at leading order, the (un-normalized) conditional probability distribution

5. Note that at NLO accuracy, there are at most two partons in a given hemisphere, making in this context the widely used anti- k_{\perp} algorithm [93] exactly equivalent to the k_{\perp} algorithm.

6. A detailed discussion of the resummation of the $\log(R p_{\perp}^{\text{jet}}/M_F)$ -terms is given in chapter 1 and in Ref. [112].

that the hadron of momentum p_{\perp}^h carries the momentum fraction z_h of its parent parton. As a consequence, these distributions are naturally peaked at large values of $z_h \gtrsim 0.5$, i.e. the relevant range for hadron production in hadronic collisions, unlike the distribution of hadrons produced in e^+e^- collisions.

Cuts

Because of the QCD evolution, differences between the various FF sets are expected to weaken at very large scales, $Q \gg \Lambda_{\text{QCD}}$, since this evolution is only logarithmic. Also note that at very large p_{\perp}^{jet} , hadrons predominantly come from the fragmentation of quarks instead of gluons, for which FF are better constrained from e^+e^- measurements (see below section 3.3.1). Therefore, in order to possibly disentangle (gluon) fragmentation functions from hadron–jet momentum correlations we require the jet momentum to be not too large, nevertheless keeping in mind that the experimental jet reconstruction cannot be achieved below a given transverse momentum. We apply in this analysis a minimal hadron/jet p_{\perp} -cut of $(p_{\perp}^{\text{jet}})^{\text{min}} = (p_{\perp}^h)^{\text{min}} = 30$ GeV above which the experimental determination of the jet energy scale remains under control. We also restrict the hadron transverse momenta to remain below ⁷ $p_{\perp}^h < (p_{\perp}^h)^{\text{max}} = 200$ GeV and apply no restriction on the jet upper transverse momentum. Finally, a lower cut on the momentum imbalance is applied, $z_h > 0.1$, below which the fixed-order calculation may no longer be appropriate because of the appearance of large logarithms $\ln(1/z_h)$ which would need to be resummed to all orders (as discussed in section 3.2.3).

Flavor composition

As mentioned above, hadron production in e^+e^- collisions naturally comes predominantly from the fragmentation of quarks and anti-quarks. In high-energy p–p collisions, however, gluon production dominates over quark production at small $p_{\perp}^{\text{jet}}/\sqrt{s}$. As a consequence, hadron production essentially arises from gluon fragmentation, at least on a very large range of momentum fractions carried by the detected hadron. It is one of the reasons why the theoretical uncertainty associated to the calculation of large- p_{\perp} hadron production at LHC is important because of the rather unknown gluon FF [108, 113].

In order to illustrate this, z_h distributions have been computed using the different sets assuming gluon fragmentation only (by setting artificially the quark fragmentation to zero), normalized to the “full” z_h distribution, i.e. including both quark and gluon fragmentation. The result is shown in Fig. 3.7 for the different FF sets and for both charged hadron (left) and protons+antiprotons (right) production. As can be seen, Fig. 3.7 confirms the dominance of gluon fragmentation, which contributes to 60-80% to charged hadron production at all z_h for the BFGW, DSS and HKNS sets. Interestingly, charged

7. This cut will have basically no effect on the computed distributions; however this avoids using FF at very large scales for which they are not always available.

hadron production proceeds essentially through quark fragmentation above $z_h \gtrsim 0.75$ (respectively $z_h \gtrsim 0.6$) when using the AKK08 (respectively, Kretzer) FF set; the reason comes from the very soft gluon fragmentation function of these two sets, see Fig. 3.2. Regarding protons+antiprotons production, the situation is analogous for the DSS and AKK08 sets. The HKNS fragmentation function, however, leads to a strong depletion of gluon to (anti)protons at large z_h , and similar to AKK08, unlike what was observed for charged hadron production. This could also have been anticipated from a glance at Fig. 3.2.

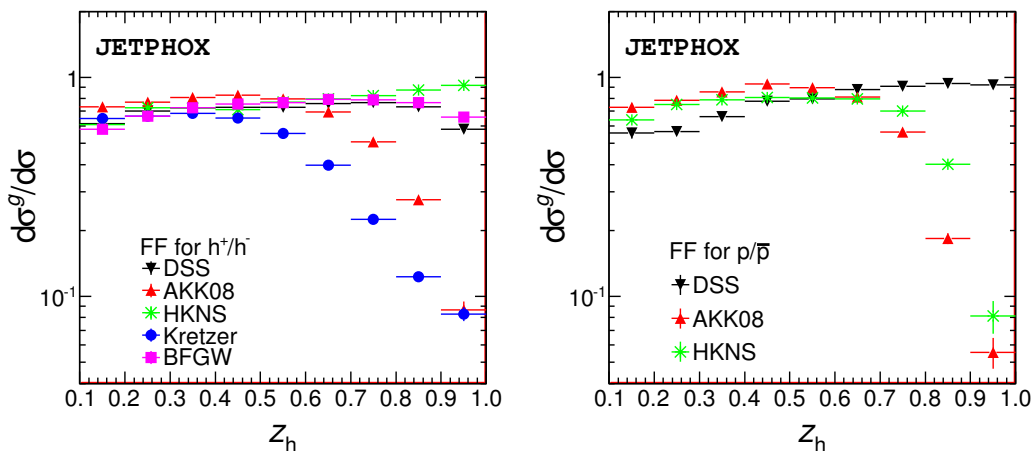


Figure 3.7: Relative contribution of gluon fragmentation to the production of charged hadrons (left) and protons+antiprotons (right) inside jets, using the various FF sets. See text for details.

3.3.2 Correlations with inclusive charged hadrons

The z_h distribution of inclusive charged hadrons in p–p collisions at the LHC (we choose $\sqrt{s} = 8$ TeV) is shown in Fig. 3.8 (left) using the AKK08, BFGW, DSS, HKNS and Kretzer FF sets and the scales given by the central values discussed in section 3.3.1.

As can be seen, differences between the various predictions can be rather large. The distributions using the BFGW and DSS (and to a lesser extent HKNS) fragmentation functions prove rather similar, both in shape and in magnitude. Distributions using AKK08 and Kretzer have a similar shape – yet a different magnitude – and somehow steeper than the results obtained using BFGW, DSS and HKNS. Such features are reminiscent to those of the gluon fragmentation functions (Fig. 3.2) which appeared significantly softer for AKK08 and Kretzer; it is a hint that this observable should provide tight constraints on the various FF sets.

Another interesting observation is the scale dependence of the predictions, which quantifies the strength of higher-order corrections, shown as a band in the DSS prediction in Fig. 3.8 (left). Although the scale dependence is not negligible at large z_h , it is remarkable that the spread of the predictions using the various FF sets exceed somehow

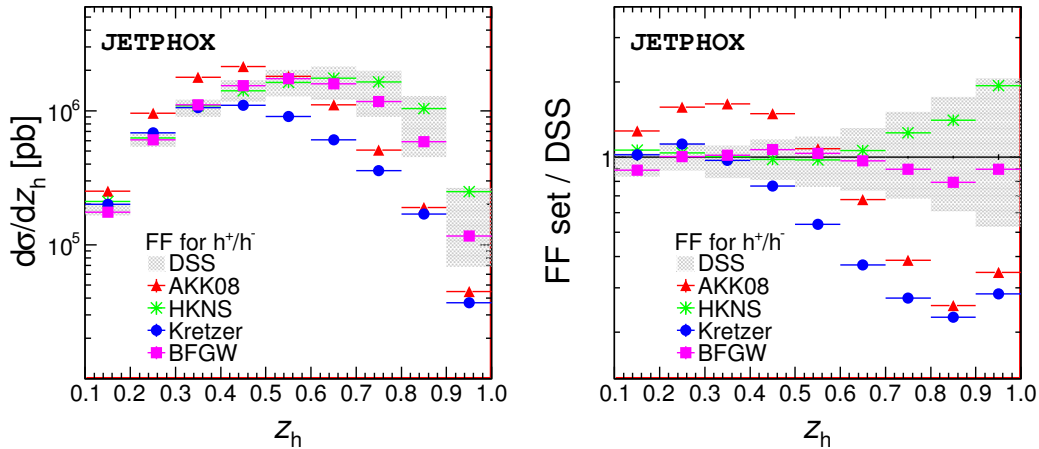


Figure 3.8: Left: z_h distributions of charged hadrons inside jets, using the AKK08, BFGW, DSS, HKNS and Kretzer FF sets. The band indicates the scale dependence of the DSS calculation (see text). Right: Same distributions normalized to the DSS prediction.

the scale dependence of the calculations. In other words, the discrepancy between the different sets proves beyond the intrinsic uncertainty of the NLO predictions.

In order to be more quantitative, the various NLO calculations are normalized to those using a set of reference (here taken to be DSS), $d\sigma^{\text{FF set}}/d\sigma^{\text{DSS}}$, see Fig. 3.8 (right). This figure illustrates further the different shapes expected when using BFGW and DSS on the one hand and AKK08 and Kretzer on the other hand. The shape of HKNS is rather similar to that of BFGW/DSS except at large $z_h \gtrsim 0.7$. The ratio r between the FF sets can be significant at large z_h , from $r = 0.3$ (Kretzer/DSS) to $r = 1.4$ (HKNS/DSS) at $z_h = 0.8$.

As already noted, the scale dependence becomes increasingly large as z_h gets closer to 1, from 10% at $z_h \simeq 0.1$ up to 50–80% at $z_h \gtrsim 0.8$. The origin is twofold. At large z_h , the extra radiated parton in $2 \rightarrow 3$ processes is forced to be soft, leading to large logarithms $\ln^2(1 - z_h)$ which would need to be resummed to all orders (a work which is beyond the scope of the present paper). As a consequence, the scale variation at NLO becomes of the same order as the one at leading order when z_h is close to 1, see Fig. 3.9. The other reason comes from the behavior of the anomalous dimension of the fragmentation functions, $\mu^2 \partial \ln D(z, \mu^2) / \partial \mu^2$, which becomes increasingly large as $z \rightarrow 1$. Note however that the scale dependence of the present NLO calculation remains below the spread of the various calculations, at least when comparing AKK08 & Kretzer to BFGW & DSS.

The differences between the FF sets prove largest at very large z_h (say, $z_h \gtrsim 0.8$), where the differential cross section becomes very much suppressed. However, note that with the cuts used in this analysis, the counting rates remain significant even in the highest z_h bin, thanks to the huge integrated luminosity delivered at the LHC. Taking $\mathcal{L} = 20 \text{ fb}^{-1}$ at $\sqrt{s} = 8 \text{ TeV}$ [114, 115], the expected rates in the bin $z_h = [0.9, 1.0]$ are $\mathcal{N} = 7 \times 10^4$ using the lowest prediction $d\sigma/dz_h = 3.5 \text{ pb}$ given by the Kretzer set.

Despite very different shapes, it might be difficult to disentangle, say, AKK08 from

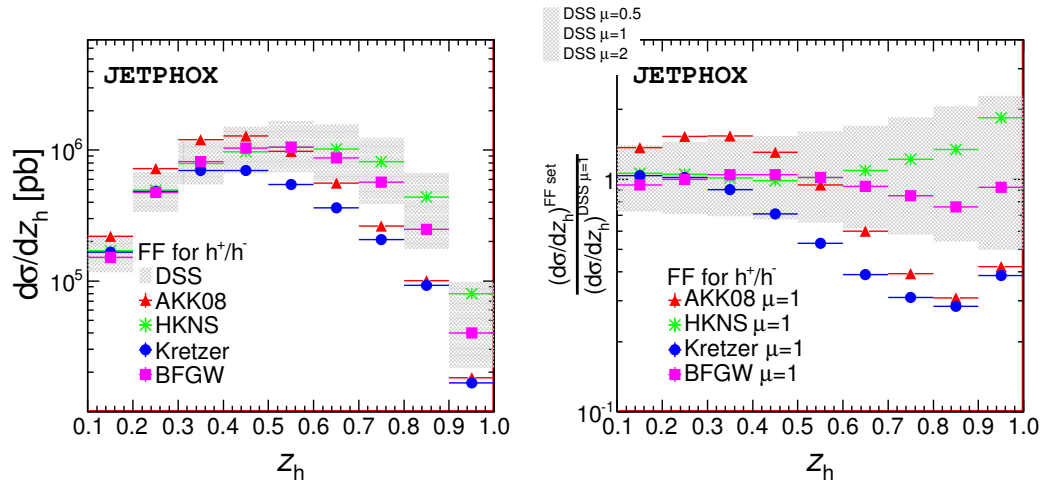


Figure 3.9: Left: z_h LO distributions of charged hadrons inside jets, using the AKK08, BFGW, DSS, HKNS and Kretzer FF sets. The band indicates the scale dependence of the DSS calculation (see text). Right: Same LO distributions normalized to the DSS prediction.

BFGW/DSS predictions, from the *absolute* distribution $d\sigma/dz_h$. In order to truly probe the *shape* of the z_h distribution, we determine the distribution normalized to its value in the bin $z_h = [0.2, 0.3]$, $(d\sigma/dz_h)/(d\sigma/dz_h)_{z_h=[0.2,0.3]}$ in Fig. 3.10 (left). Results using AKK08 and Kretzer FF prove rather similar since both predictions on the absolute $d\sigma/dz_h$ essentially differ in the overall magnitude (see Fig. 3.8), which cancels in the normalized distributions. Apart from emphasizing the shape of the FF, a clear advantage of the normalized distribution is to reduce the scale dependence of the NLO calculations, which mostly affects the magnitude (than the shape) of the distributions.

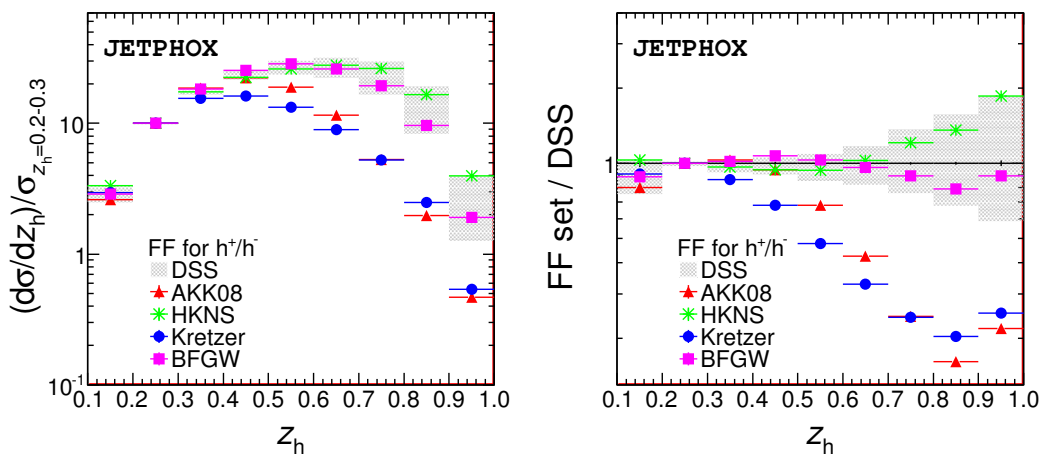


Figure 3.10: Left: Normalized z_h distributions of charged hadrons inside jets, using the AKK08, BFGW, DSS, HKNS and Kretzer FF sets. The band indicates the scale dependence of the DSS calculation (see text). Right: Same distributions normalized to the DSS prediction.

For completeness, the normalized distributions are also compared to the DSS (nor-

malized) prediction in Fig. 3.10 (right). As can be seen, the scale dependence is somehow reduced especially at large values of z_h , of the order of 30–40%. Clearly the (normalized) distributions prove really different depending on the FF set used in the calculation. This illustrates how the normalized distributions of hadrons inside jets in p–p collisions at the LHC could also bring significant constraints on the current knowledge of fragmentation functions.

Another way to compare the different predictions is to compute the mean value of z_h , $\langle z_h \rangle$. This quantity has the obvious advantage to also characterize the shape while being insensitive to the magnitude of the distribution $d\sigma/dz_h$. The numbers corresponding to the various FF sets are given in Table 3.1, the errors quoted in the case of the DSS FF set corresponds to the scale variation. When looking at $\langle z_h \rangle$ of charged hadrons, the features already discussed are clearly apparent. Namely, the BFGW and DSS (and HKNS within the scale uncertainty) are compatible, $\langle z_h \rangle = 0.52 \pm 0.02$ and $\langle z_h \rangle = 0.51$, while significantly smaller values, $\langle z_h \rangle = 0.44$, are reported in the case of AKK08 and Kretzer, which FF are much softer. Similar observations can be made for kaon and (anti)proton production, which are discussed in the next section.

Table 3.1: Mean value of $\langle z_h \rangle$ for $30 < p_\perp^h < 200$ GeV and $p_\perp^{\text{jet}} > 30$ GeV. The error indicated in the DSS results reflects the scale uncertainty of z_h .

FF set	$h^+ + h^-$	$K + \bar{K}$	$p + \bar{p}$
DSS	0.52 ± 0.02	0.57 ± 0.02	0.58 ± 0.03
AKK08	0.44	0.49	0.44
BFGW	0.51	–	–
HKNS	0.54	0.60	0.46
Kretzer	0.44	0.48	–

3.3.3 Correlations with identified hadrons

As mentioned in the introduction, the most important constraints are put on (quark) fragmentation functions into charged hadrons, due to the abundance of e^+e^- precise measurements. After demonstrating the constraints brought by charged hadron momentum spectra inside jets, we investigate more specifically the production of identified hadrons, kaons and protons, in this section. Calculations are carried out using AKK08, DSS and Kretzer FF sets only (kaon and proton FF are not available in the BFGW parametrization).

Kaons

Using the same cuts as for inclusive charged hadrons, the z_h distributions of kaons inside jets using the different FF sets are shown in Fig. 3.11 (left). As can be seen, the

differences are very large and significantly beyond the scale uncertainty of the DSS set prediction. This is confirmed in Fig. 3.11 (right) where each prediction is normalized to that of DSS. This ratio takes extreme values at high z_h : at $z_h = 0.8$ it is $r = 0.3$ for AKK08 and Kretzer and almost $r = 5$ for HKNS. Note also the discrepancy between the various sets and DSS at small values of $z_h \lesssim 0.4$.

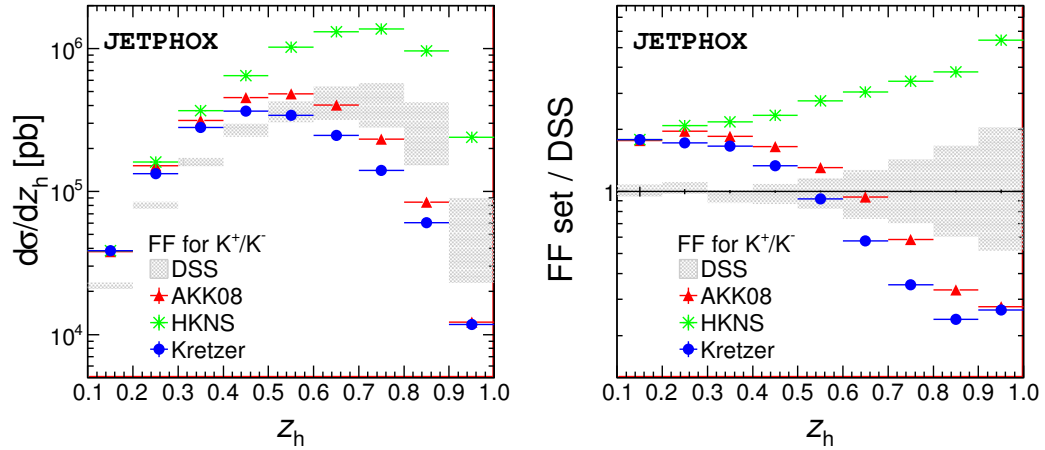


Figure 3.11: Left: z_h distributions of charged kaons inside jets, using the AKK08, DSS and Kretzer FF sets. The band indicates the scale dependence of the DSS calculation (see text). Right: Same distributions normalized to the DSS prediction.

As mentioned in section 3.3.2, the mean value of the z_h distributions of charged hadrons can be used to discriminate among the various FF sets. It is also the case for kaon production (see Table 3.1) where a rather large value $\langle z_h \rangle \simeq 0.6$ is reported for DSS and HKNS while $\langle z_h \rangle \simeq 0.5$ for AKK08 and Kretzer fragmentation functions.

Protons

Finally we discuss in this section the distributions of (anti)protons inside jets. Due to a lack of constraints from data, the fragmentation functions into protons+antiprotons is by far the most uncertain (see e.g. Fig. 3.2).

As shown in Fig. 3.12, the z_h distribution of protons+antiprotons inside jets exhibit a very different behavior depending on which fragmentation function set is used, DSS, AKK08 and HKNS (Kretzer set is not available for protons). In this channel, predictions using HKNS prove remarkably similar to those using AKK08 and much softer than the expectations from DSS (this is also true at the level of the FF themselves, Fig. 3.2). The ratio between AKK08/HKNS and DSS is $r = 3$ at small $z_h \simeq 0.4$ and as low as $r \simeq 0.1$ in the largest z_h bins. The mean values of z_h reflect also these differences, with $\langle z_h \rangle \simeq 0.45$ for AKK08 and HKNS, and $\langle z_h \rangle \simeq 0.6$ for DSS (see Table 3.1).

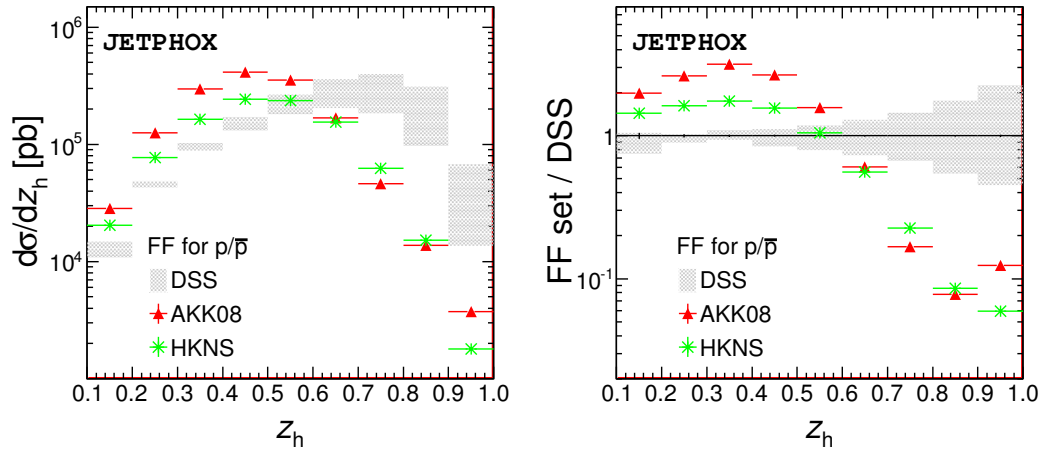


Figure 3.12: Left: z_h distributions of protons+anti-protons inside jets, using the AKK08, BFGW, DSS and Kretzer FF sets. The band indicates the scale dependence of the DSS calculation (see text). Right: Same distributions normalized to the DSS prediction.

3.4 Away-side hadron-jet momentum correlations

In this section, the constraints on available FF sets is carried out by studying the momentum correlation with the away-side hadron-jet. We want to investigate how much the away-side hadron-jet correlation can disentangle the different FF sets. Also, we want to probe what is the advantage for this aspect. The issues discussed in this study are quite the same as in the previous section.

3.4.1 Framework

To compare with the same-side hadron-jet study, the kinematic for the hadron and jet is chosen to be as in section 3.3.1 and note that the kinematic for the "jet3" in this study corresponds to the kinematic for the "jeth" in the previous study. The momentum correlation variable, z_3 , is given in Eq. 3.1. Like z_h , z_3 reduces to the fragmentation variable z at LO. However, at NLO, especially for the $2 \rightarrow 3$ process (Fig. 3.13), the z_3 is not a good approximation for z like z_h . As a consequence, the z_3 investigation may give different result compared to the z_h study.

As an example, let us discuss the plots for gluon fragmentation into hadron as in Fig. 3.14. The same results is found as in the previous study, the z_3 distribution also confirms the dominance of gluon fragmentation. The z_3 distribution for charged hadron production for BFGW, DSS, and HKNS sets are analogous to the z_h distribution, but not for AKK08 FF set where the fragmentation from quark is not dominant at large z_3 . For the Kretzer set, the quark fragmentation is less important in Fig. 3.14 (aways-side) than in Fig. 3.7 (same-side). For the proton+antiprotons production, all considered FF sets give the same result in which gluon fragmentation contributes dominantly, but it is not the case

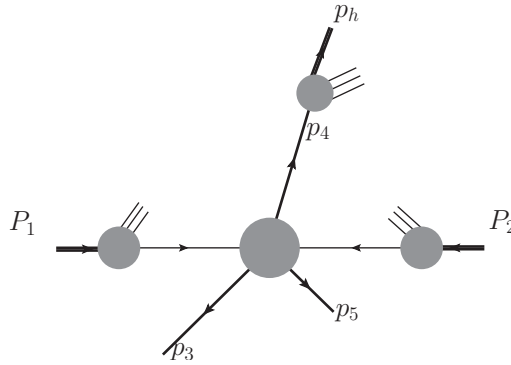
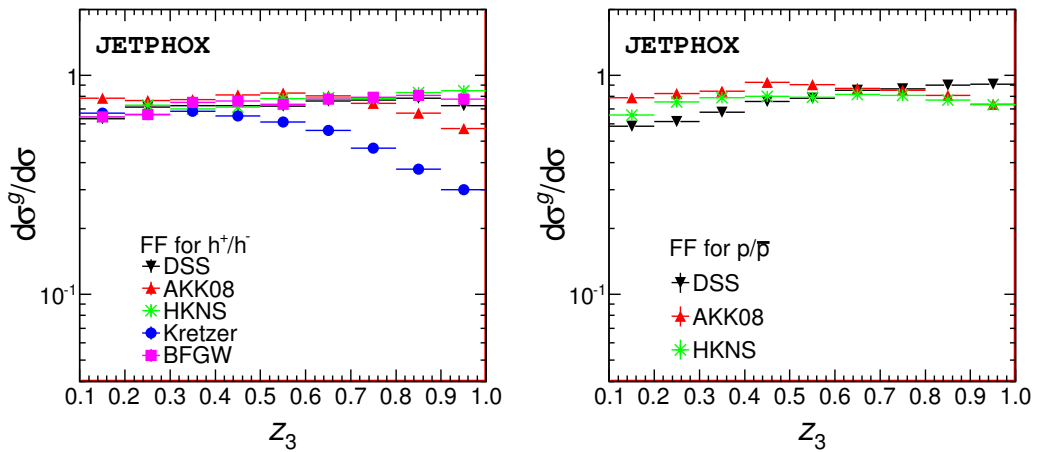
Figure 3.13: An illustration for $2 \rightarrow 3$ process.

Figure 3.14: Relative contribution of gluon fragmentation to the production of charged hadrons (left) and protons+antiprotons (right) recoiling jets, using the various FF sets. See text for details.

in the z_h plots for AKK08 and HKNS sets. In short, the investigation for BFGW, DSS (and Kretzer, slightly) gives analogous results to the same-side study. The effect of very soft gluon becomes invisible for AKK08 and HKNS sets in this observable.

3.4.2 Correlations with inclusive charged hadrons

In this section, we discuss the z_3 distribution of inclusive charged hadrons in p-p collisions at $\sqrt{s} = 8$ TeV for the away-side hadron-jet production.

As shown in Fig. 3.15, the z_3 distribution gives the possibility to disentangle between the group of DSS, BFGW, and HKNS sets and the group of AKK08 and Kretzer sets at the LO approximation. One can find that the z_h LO distribution in Fig. 3.9 is exactly the same as the z_3 LO distribution in Fig. 3.15. This fact is not by accident, it follows from the fact that both momentum correlations z_h and z_3 exactly reduce to FF momentum fraction z and $p_{\perp}^{\text{jet}h} = p_{\perp}^{\text{jet}3}$ at LO.

The NLO distribution of z_3 is shown in Fig. 3.16. Again, the distribution for the

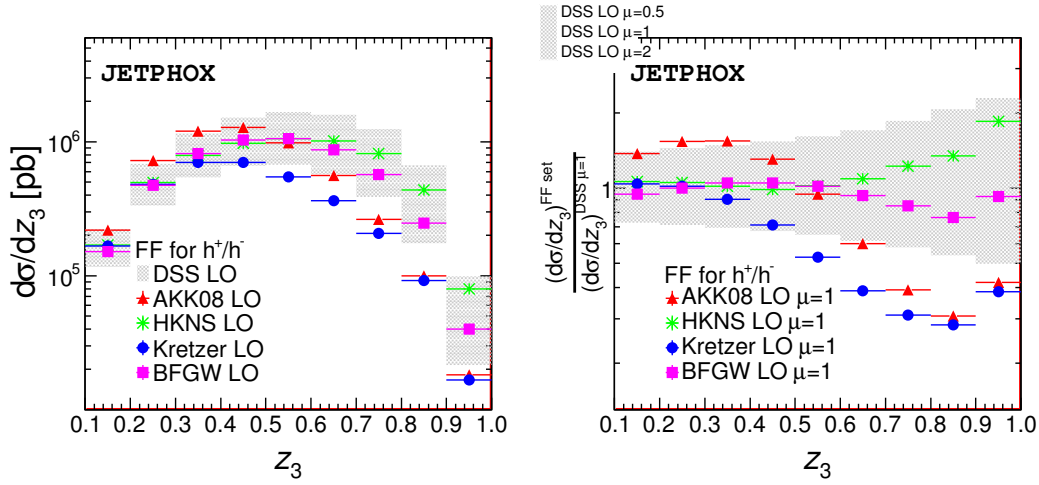


Figure 3.15: Left: z_3 LO distributions of charged hadrons recoiling jets, using the AKK08, BFGW, DSS, HKNS and Kretzer FF sets. The band indicates the scale dependence of the DSS calculation. Right: Same LO distributions normalized to the DSS prediction.

BFGW, DSS, and HKNS sets gives the same predictions for all z_3 . The difference between those sets and Kretzer contributions is large enough above $z_3 \gtrsim 0.55$. The distribution using AKK08 seems quite close to DSS scale dependence band, even for ratio plots, i.e. $d\sigma^{\text{FFset}}/d\sigma^{\text{DSS}}$. This fact is different from the same-side hadron-jet study because the effect of very soft gluon fragmentation for AKK08 is rather weak in this study (as mentioned in section 3.4.1.) However, this fact becomes an advantage of this study because it gives a chance to disentangle between Kretzer and AKK08, which is not possible for the same-side hadron-jets correlation study.

Table 3.2: The magnitude reduction for the differential cross section $d\sigma/dw$, w is z_3 , or z_h . The magnitude reduction is defined as $\frac{c(0.55)-c(0.95)}{c(0.55)}$, with $c(x) = d\sigma/dx$.

FF set	z (LO study)	z_h (same-side study)	z_3 (away-side study)
DSS	94–97%	87–95%	–28–61%
AKK08	98%	98%	76%
BFGW	96%	93%	49%
HKNS	92%	85%	20%
Kretzer	97%	96%	71%

Comparing to the z_h distribution which is given in Fig. 3.8, the z_3 distribution decreases quite slowly for z_3 between 0.55–0.95 (as described in Table 3.2.) Because the z_3 distribution for LO strongly goes down at large z_3 , the high magnitude of NLO must come from the $2 \rightarrow 3$ contributions. Moreover, from the LO distribution of momentum correlation (Figs. 3.15 and 3.9), where the FF z is the same as z_3 or z_h , one can get that

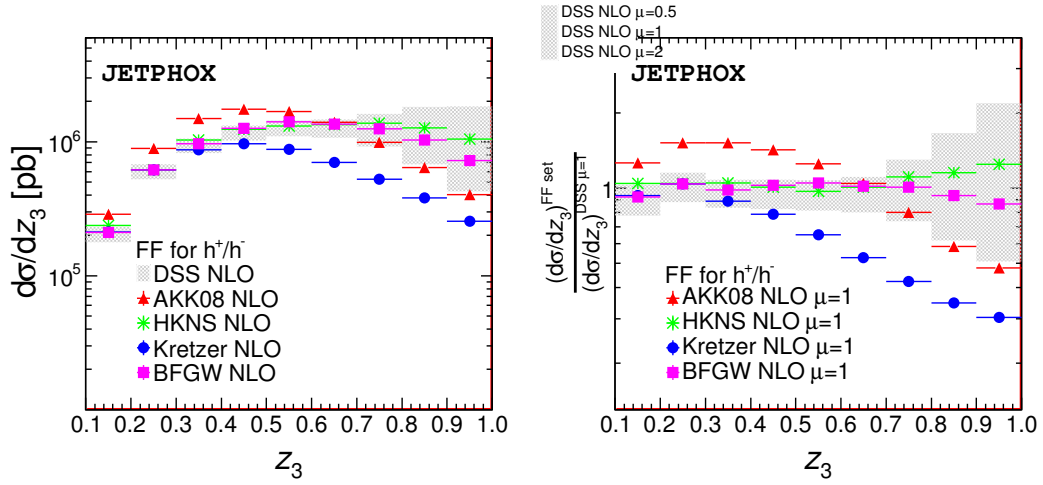


Figure 3.16: Left: z_3 distributions of charged hadrons recoiling jets, using the AKK08, BFGW, DSS, HKNS and Kretzer FF sets. The band indicates the scale dependence of the DSS calculation (see text). Right: Same distributions normalized to the DSS prediction.

the z distribution must be significantly reduced when $z \rightarrow 1$. Thus the small reduction (even small excess as for DSS with $\mu = 0.5$) reflects the raw approximation of FF z by momentum correlation z_3 for the $2 \rightarrow 3$ contribution.

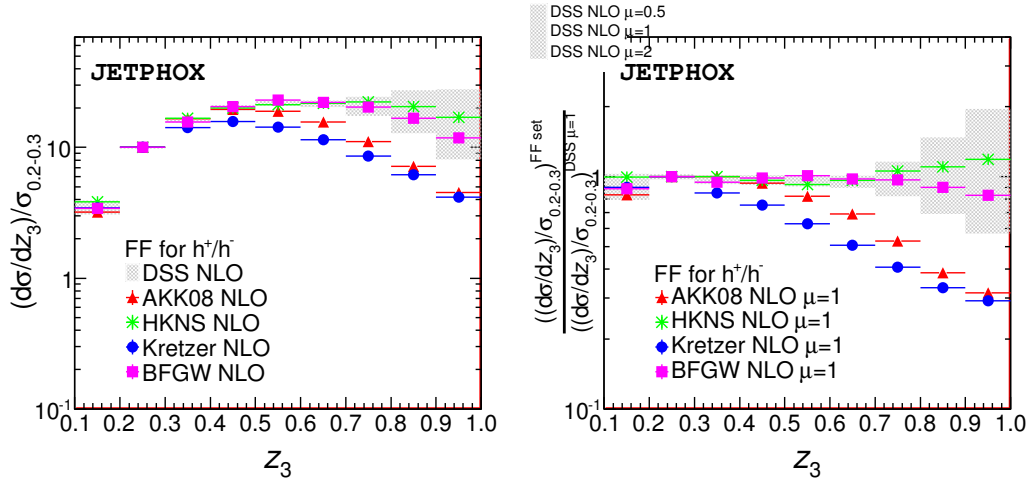


Figure 3.17: Left: Normalized z_3 distributions of charged hadrons recoiling jets, using the AKK08, BFGW, DSS, HKNS and Kretzer FF sets. The band indicates the scale dependence of the DSS calculation. Right: Same distributions normalized to the DSS prediction (see text).

So far, what we obtain is that it is difficult to disentangle the AKK08 prediction from a group of BFGW, DSS, and Kretzer thanks to z_3 distribution. However, analogous to the discussion in section 3.3.2, this fact is also really affected by the scale dependence of NLO calculation. To illustrate that let us consider the normalized distribution where the prediction of each set is normalized by its value at bin $z_3 = [0.2, 0.3]$,

$(d\sigma/dz_3) / (d\sigma/dz_3)_{z_3=[0.2,0.3]}$ in Fig. 3.17 (left). As expected, the scale dependence reduces significantly, as shown by the DSS band plot behavior. Furthermore, the AKK08 prediction becomes analogous to Kretzer, therefore it is possible to disentangle the AKK08 contribution from BFGW/DSS for this observable.

3.4.3 Correlations with identified hadrons

As for the same-side aspect, we also want to put more constraints on FF sets by considering the kaon and proton fragmentations from quarks and gluons. One advantage for the ratio $d\sigma^{\text{FFsets}}/d\sigma^{\text{DSS}}$ plots is to show more precisely the differences among the FF sets, this is the reason that we prefer to use them in this section.

Kaons

As shown by the left plots in Fig. 3.18 for the ratio by DSS of the other FF sets, the HKNS contribution is strongly different from the others for all z_3 . At large $z_3 \gtrsim 0.75$, the AKK08 gives contribution matching with distribution for DSS band, while the Kretzer is slightly separate from DSS band (and/so of course from AKK08).

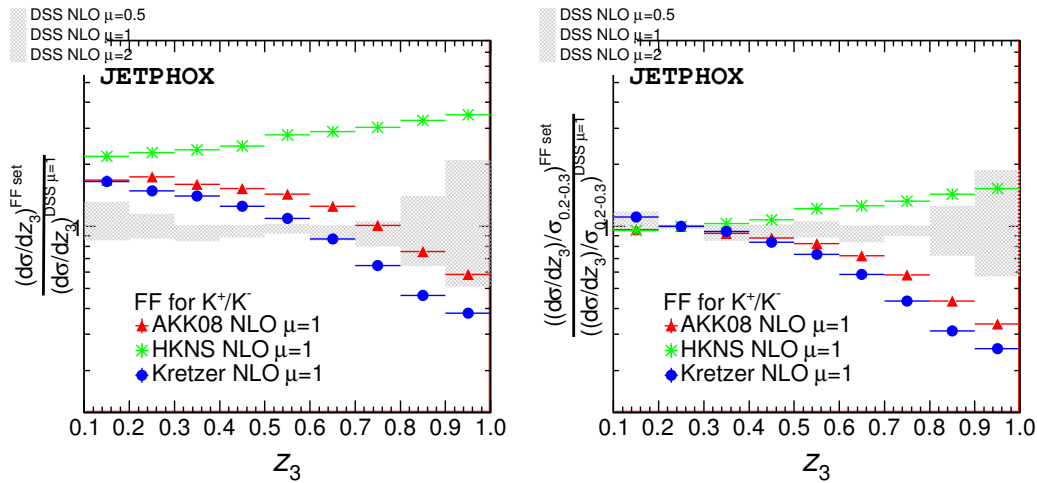


Figure 3.18: Left: z_3 distribution ratios, $d\sigma^{\text{FFsets}}/d\sigma^{\text{DSS}}$, of charged kaons recoiling jets, using the AKK08, DSS, HKNS and Kretzer FF sets. The band indicates the scale dependence of the DSS calculation. Right: The same ratios for normalized distributions (see text).

Again, one can use the mean value of z_3 distribution to study the differences among FF sets. As listed in Table 3.3, the fact that the large value $\langle z_3 \rangle \simeq 0.6$ for DSS&HKNS and $\langle z_3 \rangle \simeq 0.49$ for AKK08&Kretzer corresponds to their differences from the ratio of normalized distributions. Those are illustrated by the right plots in Fig. 3.18, where the advantage for probing the shape of z_3 distributions is obvious.

Table 3.3: Mean value of $\langle z_3 \rangle$ for $30 < p_{\perp}^h < 200$ GeV and $p_{\perp}^{\text{jet}} > 30$ GeV. The error indicated in the DSS results reflects the scale uncertainty of z_3 .

FF set	$h^+ + h^-$	$K + \bar{K}$	$p + \bar{p}$
DSS	0.53 ± 0.02	0.57 ± 0.03	0.58 ± 0.03
AKK08	0.45	0.50	0.44
BFGW	0.52	–	–
HKNS	0.54	0.60	0.47
Kretzer	0.45	0.48	–

Protons

As can be seen, the left plots in Fig. 3.19 show that the AKK08&HKNS distributions for proton fragmentation are different from the DSS band. However, this observable does not give tighter constraint than the z_h distribution in Fig. 3.12. The AKK08 and HKNS have the same contribution at large z_3 . The mean value of z_3 which is listed on Table 3.3 give a hint to disentangle among DSS, AKK08, and HKNS by the normalized distributions as the left plots in Fig. 3.19. It is clear that with this observable, one re-obtained the constraint derived from the absolute z_h distribution.

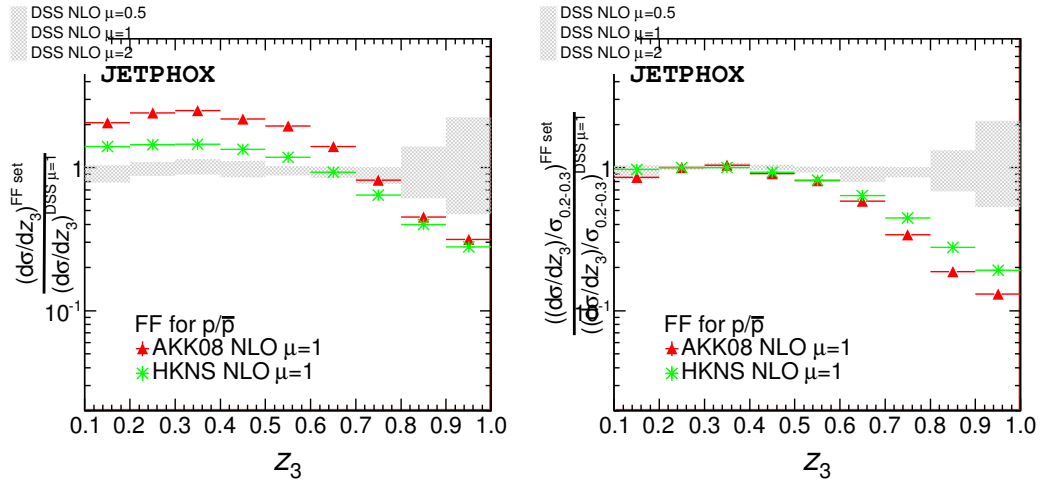


Figure 3.19: Left: z_3 distribution ratios, $d\sigma^{\text{FFsets}}/d\sigma^{\text{DSS}}$, of proton+anti-proton recoiling jets, using the AKK08, DSS and HKNS FF sets. The band indicates the scale dependence of the DSS calculation. Right: The same ratios for normalized distributions (see text).

3.5 Conclusion

The study on charged-hadron/kaon/proton fragmentations from partons, shows that the z_3 (absolute) distribution does not give as tight constraint as the z_h distribution, considering the analogous distributions. However, one of the advantages of the away-side hadron-jets study is to be able to disentangle between AKK08 and Krezer for charged hadron/kaon fragmentation. On the contrary, for the proton+anti-proton fragmentation, the same-side hadron-jet study give better results than the away-side hadron-jet one in putting constraint on AKK08, DSS, and HKNS sets.

For either the same-side hadron-jets study or the away-side hadron-jets study, the normalized distribution for the momentum correlation in p-p collisions at the LHC enables to distinguish the group of BFGW/DSS/HKNS from the group of AKK08/Kretzer. The absolute distributions for z_h somehow prove the same results with tighter constraint.

A NLO perturbative analysis of hadron-jet momentum correlations in p-p collisions at the LHC has been carried out. Results indicate that predictions using various FF sets available exhibit large differences, beyond the scale dependence of the NLO calculation. This is a clear sign that those observables – which can be measured with a high statistical accuracy at the LHC – could be used in order to bring extra constraints, especially in the gluon sector and at large values of z for which the spread of theoretical predictions is the largest. This is particularly true regarding kaon and proton spectra inside jets, especially if hadron identification can be performed up to rather large momenta.

Chapter 4

Photon Production in Association with Heavy-Flavor Jet

Contents

4.1	bjETPHOX: An upgrading from JETPHOX	92
4.1.1	Picking up sub-processes using random number generator	92
4.1.2	Select among flavor-contributions on bjETPHOX	99
4.1.3	Events with flavor selection	102
4.1.4	Analytical macros	104
4.2	The aspects of photon + heavy-quark jet production at LHC	105
4.2.1	The $Q\bar{Q}$ -pair invariant mass approach	105
4.2.2	The flavor- k_t algorithm approach	112
4.2.3	Charm meson FF approach	119
4.2.4	A look on bottom quark's distribution inside the proton	125

Prompt photon production at high energy colliders allows for studying constraints on parton distribution functions (PDFs) and fragmentation functions (FFs). The inclusive (or isolated) photon in association with the jet cross section also provides other constraints for this study. The jets in this study are specified as degenerate state of final partons, thereby the information on partons in underlying process is not well identified. The fact that the flavor of the jets is tagged would give more information on the underlying process. In addition to the fact that the heavy-quark jets can be tagged in hadronic collisions [116], the study of photon + heavy-quark jets production would give an interesting observable for probing the substructure of hadrons, especially heavy quark distributions in protons. The heavy quarks in the discussion of this chapter are either charm or bottom. There have been previous a study on the associated production of photon and heavy-quark jets [117] and a good agreement between the theoretical calculation and experimental measurement has been found for process $p\bar{p} \rightarrow \gamma + b + X$ in D0 experiment [10]. However, there exist large discrepancies in the case of the process $p\bar{p} \rightarrow \gamma + c + X$ (see Fig. 4.1).

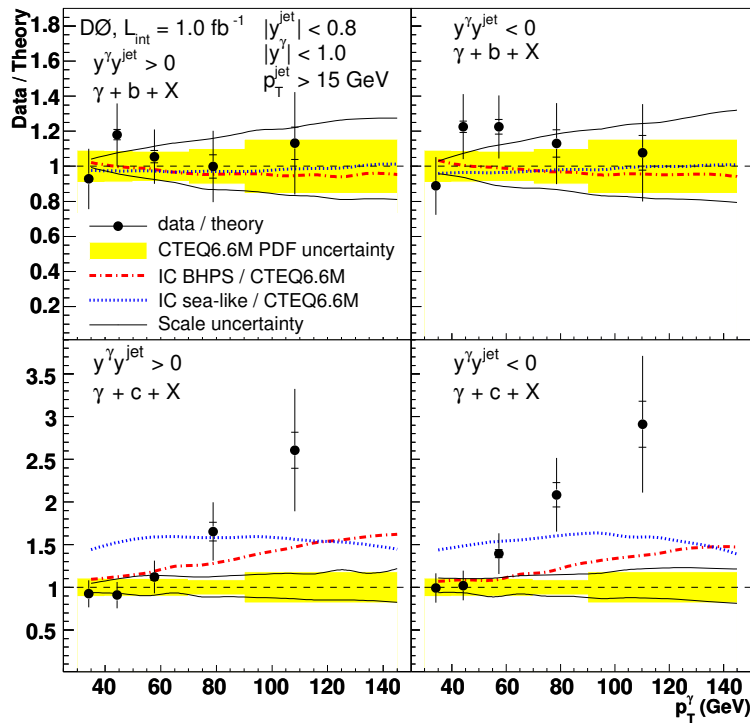


Figure 4.1: The $\gamma + b(c) + X$ production: comparison between theoretical calculation and experimental measurement [10].

The aim of this chapter is to perform the $p\bar{p}$ (pp) $\rightarrow \gamma + c/b\text{-jet} + X$ calculation for various infra-red (IR) safe observable. The tool which is developed for this purpose is described in section 4.1. As it is introduced in section 2.2, the JETPHOX generator is a state of art computational program for studying $\gamma(h)$ +jet production at NLO QCD in hadronic colliders. However, the study on the production of heavy-quark jets, as it would be, requires the knowledge on the flavor information of the final states at the partonic

calculation level. It was beyond the original purpose of JETPHOX because the flavors are summed over when constructing standard jets. Our motivation is to improve JETPHOX so that the photon+heavy-quark jet events are able to be selected with the requirement of IR flavor safety. To get that, first of all, the flavor information of final partons in a certain kinematical configuration is taken into account, then is generated together with the corresponding event. The technique, usage, and detail performance in upgrading JETPHOX into bJETPHOX are presented.

The numerical results and discussion are carried out in the section 4.2. The first objective is to re-obtain the results of the previous theoretical calculation. Then we want to use the flavor- k_t algorithm, which provides IR-flavor safe results, and the heavy-quark fragmentation in performing our calculation. Finally, the comparison among those approaches and a preliminary study on bottom PDF are presented. From the obtained results, we hope to understand the discrepancies between theory and experiment on $\gamma + c + X$ production and therefore we want to give some predictions for the LHC in pp and nuclear collisions.

4.1 bJETPHOX: An upgrading from JETPHOX

In practice, one wants to improve JETPHOX so that it is possible to apply different constraints to various sub-processes and/or separately investigate certain selections among them, such as selecting events associated with a b jet or a c jet. A naive way is that one can decompose the contribution of a given generic partonic process into its flavor components, build the generating program for each of them and run those programs. In the events analysis step, one can put constraint type i^{th} while filling the histogram of sub-process i^{th} as usual. The desired histogram is, therefore, the sum of histogram i^{th} over those sub-processes. However, the run-time performance is multiplied by the number of sub-processes comparing to the run of one like-JETPHOX program¹. The randomly picking up sub-processes technique which is presented in this section addresses this problem.

4.1.1 Picking up sub-processes using random number generator

Our aim is to estimate a certain variable distribution which receives contribution from several sub-processes, namely $l = 1, 2, \dots$. One can use BASES-SPRING to generate events which corresponds to phase space configurations. Then, a distribution with respect to a variable can be estimated by analyzing those events. Assume, for a certain purpose, that some constraints are required. Those constraints, in general, may be different depending on various sub-processes. One can either modify the original program so that those constraints are included or separately generates events for each flavor sub-process, then build their contributions and add them all to get the total contribution. The sum is the desired distribution. However, there are disadvantages for both approaches. The former leads to lose the original information. The latter increases run-time performance in proportion to the number of sub-processes. The method which is suggested in this thesis is that one can randomly pick up among sub-processes of certain configuration, then mark the corresponding event with the gotten sub-process, e.g. by value l . The estimation of the distribution can be carried out by analyzing the event associated to its label. At given large enough N_{Call} , the estimated result is found to agree well with the desired distribution. The disadvantage of this approach is that the statistics for histograms of sub processes are not as good as for the main process. The advantage of this approach is that *a*) the consuming time for creating an event ntuple is almost the same as in the original program; *b*) one can select any group of sub-processes in the same given event ntuple; and *c*) one can apply different constraints on corresponding sub-process in analyzing events. Moreover, if no

1. Let us quickly estimate the run-time performance to calculate the $pp \rightarrow Qjet + \gamma + X$ cross section distribution as the following. Use JETPHOX to calculate to NLO cross section distribution of $pp \rightarrow jet + \gamma + X$ with respect to an observable, such as p_{\perp}^{γ} . The constraints to be applied is flavor- k_t algorithm, which is required the flavor information of final partons. Then the subprocesses which should be considered are $ud \rightarrow ud\gamma$, $ub \rightarrow ub\gamma$...+ crossing terms + h.c terms. Therefore, one need to separately run a hundred of sub-processes. Thus, the run-time performance is counted in month given each run is around 8 hours. Not to mention the time for analyzing those events yet.

constraint is required, this approach plays the role of original calculation. The same goals will be addressed in improving JETPHOX into BJETPHOX.

Select among non negative integrands

In the programming languages, such as FORTRAN, C++, a random number generator is already provided in their standard libraries. The `RANDOM_NUMBER(GETNUMBER)`² method, which is included in FORTRAN 95 and later, assigns GETNUMBER value of a single pseudo-random number from an uniform distribution between 0 and 1. The probability that the GETNUMBER value belongs to range (r_1, r_2) , where $0 \leq r_1 < r_2 \leq 1$ is $r_2 - r_1$. Let us consider function $f(x)$ which stands for a process in a phase space configuration x . Moreover, the process is defined by n other subprocesses, $f_l(x)$, in such a way that

$$f(x) = \sum_{l=1}^n f_l(x) \quad (4.1)$$

where $f(x)$ and $f_l(x)$ are positive in all the investigated phase space domain X . One can perform the following method at the generating step, to keep track of sub-processes on each event.

1. For a certain configuration x , which is fed by a Monte Carlo generator, assign values of $f_l(x)$, $l = 1..n$, to an array as

$$ao[l] = f_l(x), \quad l = 1..n \quad (4.2)$$

and define another array as

$$as[l] = \frac{\sum_{k=1}^l ao[k]}{\sum_{j=1}^n ao[j]}, \quad l = 1..n, \quad (4.3)$$

$$as[0] = 0$$

2. Generate a random number rb , by calling `RANDOM_NUMBER(rb)`.
3. Make a loop over $l = 1..n$ for checking conditions $as[l - 1] < rb \leq as[l]$:
 - (a) If at iteration l^{th} the condition l is satisfied, return the value l and exit the current loop.
 - (b) If the loop finishes without passing any condition, set l to 0 and return l .
4. Repeat the procedure until the main program ends.

2. http://gcc.gnu.org/onlinedocs/gfortran/RANDOM_005fNUMBER.html#RANDOM_005fNUMBER

As a result, the probability of subprocess l is

$$\frac{as[l] - as[l-1]}{\sum_{j=1}^n ao[j]} = \frac{ao[l]}{\sum_{j=1}^n ao[j]}, \text{ with } l = 1..n; \quad (4.4)$$

In other words, the probability for picking up a sub-process l for a given configuration x_i , $i = 1..N_{call}$, is

$$\begin{aligned} p_l(x_i) &= \frac{ao[l]}{\sum_{j=1}^n ao[j]} \\ &= \frac{f_l(x_i)}{f(x_i)}, \quad l = 1..n. \end{aligned} \quad (4.5)$$

Combined with Eq. (2.23), the probability density for generating event i in association with sub-process l is approximated by

$$\begin{aligned} \rho_l(x_i) &= p_l(x_i) \rho(x_i) \\ &= \frac{f_l(x_i) f(x_i)}{f(x_i) \sigma} \\ &= \frac{f_l(x_i)}{\sigma} \end{aligned} \quad (4.6)$$

where $\sigma = \int_X f(x) dx$. Thus the probability of event k considered as a contribution of the sub-process l and which belongs to the bin (a, b) is

$$\frac{\Delta N_l}{N_{call}} = \sum_{k=1}^{\Delta N_l} \frac{f_l(x_k)}{\sigma} \Delta x_k \quad (4.7)$$

where $\Delta x_k = x_{k+1} - x_k$ and ΔN_l is number of events marked by $f_l(x)$ in bin (a, b) . The number of events in bin (a, b) is counted by $\Delta N = \sum_{l=1}^n \Delta N_l$. It is obvious that the estimated integration on $f_l(x)$ over $x \in (a, b)$ is carried out as

$$\begin{aligned} S_l(a, b) &\equiv \sum_{k=1}^{\Delta N_l} f_l(x_k) \Delta x_k \\ &= \frac{\sigma}{N_{call}} \Delta N_l \end{aligned} \quad (4.8)$$

Then the contribution to the differential cross section of the sub-process l which belongs to the bin (a, b) is approximated by

$$\frac{S_l(a, b)}{b-a} = \frac{\sigma}{N_{call}} \frac{\Delta N_l}{b-a} \quad (4.9)$$

It is straightforward to derive that the sum of contributions in Eqs. (4.8) and (4.9) over sub-process l is identical to the desired contributions of cross section and differential cross section of the main process as in Eqs. (2.25) and (2.26), respectively.

$$\begin{aligned} \sum_{l=1}^n S_l(a, b) &= \sum_{l=1}^n \frac{\sigma}{N_{call}} \Delta N_l \\ &= \frac{\sigma}{N_{call}} \Delta N \equiv S(a, b) \end{aligned} \quad (4.10)$$

$$\sum_{l=1}^n \frac{S_l(a, b)}{b-a} = \frac{\sigma}{N_{call}} \frac{\Delta N}{b-a} \equiv \frac{S(a, b)}{b-a} \quad (4.11)$$

Those Eqs. (4.8) and (4.9) give a chance of studying distributions from any group of sub-processes and on applying different constraints on various sub-processes. However, the procedure which is presented above is only available for non-negative functions. The completed approach which can be applied for functions and sub-functions of arbitrary sign is discussed in the following section.

Select among arbitrarily sign integrands

The goal of this section is to estimate the sub-process distributions from events which are generated for the main process, given the functions of main process and sub-processes have arbitrarily sign in domain X . An obvious approach to build the method would be to start with the procedure in the previous section. Due to the fact that $f_l(x)$ have arbitrary signs, the formulas Eqs. (4.4) and (4.5) cannot be used to represent probability of picking up among those sub-processes. The way to include this property is to define $ao[l]$ in step 1. by $|f_l(x)|$, $l = 1..n$, instead of $f_l(x)$. Thus Eq. (4.5), which represents the probability for picking up a sub-process l in a given configuration x_i , $i = 1..N_{call}$, is re-written as

$$p_l(x_i) = \frac{ao[l]}{\sum_{j=1}^n ao[j]} = \frac{|f_l(x_i)|}{\sum_{j=1}^n |f_j(x_i)|}, \quad l = 1..n. \quad (4.12)$$

There is no ambiguity for using generation method which is applied for arbitrarily sign function, $f(x)$. Therefore, the probability density for generating event i associated with the sub-process l is

$$\begin{aligned} \rho_l(x_i) &= p_l(x_i)\rho(x_i) \\ &= \frac{|f_l(x_i)|}{\sum_{j=1}^n |f_j(x_i)|} \frac{|f(x_i)|}{\sigma_p} \quad (\text{see Eqs. (2.27) and (4.12)}) \end{aligned} \quad (4.13)$$

where $\sigma_p = \int_X |f(x)| dx$. One of the information one needs in constructing the distribution of sub-process l is its sign. However, one cannot estimate the integration of $f_l(x)$ over bin

(a, b) thanks to its sign and Eq. (4.13), given large enough N_{call} ,

$$\begin{aligned}
\sum_{k=1}^{\Delta N_l} \text{sign}[f_l(x_k)] \rho_l(x_k) \Delta x_k &= \sum_{k=1}^{\Delta N_l} \text{sign}[f_l(x_k)] \frac{|f_l(x_k)|}{\sum_{j=1}^n |f_j(x_k)|} \frac{|f(x_k)|}{\sigma_p} \Delta x_k \\
&= \frac{1}{\sigma_p} \sum_{k=1}^{\Delta N_l} \frac{|f(x_k)|}{\sum_{j=1}^n |f_j(x_k)|} f_l(x_k) \Delta x_k \\
&\neq \frac{1}{\sigma_p} S_l(a, b)
\end{aligned} \tag{4.14}$$

where $\Delta x_k = x_{k+1} - x_k$ and x_k is a configuration in which the sub-process l be chosen. Fortunately there is a hint derived from Eq. (4.14). Instead of saving $\text{sign}[f_l(x_i)]$, $i = 1..N_{call}$, one has to save a quantity

$$w_p(x_i) = \frac{\sum_{j=1}^n |f_j(x_i)|}{|f(x_i)|} \text{sign}[f_l(x_i)], \tag{4.15}$$

given sub-process l be chosen in a configuration x_i . Thanks to Eqs. (4.13) and (4.15) one is able to construct $\int_a^b f_l(x) dx$ as follows

$$\begin{aligned}
\sigma_p \sum_{k=1}^{\Delta N_l} w_p(x_k) \rho_l(x_k) \Delta x_k &= \sum_{k=1}^{\Delta N_l} w_p(x_k) \frac{|f_l(x_k)|}{\sum_{j=1}^n |f_j(x_k)|} |f(x_k)| \Delta x_k \\
&= \sum_{k=1}^{\Delta N_l} f_l(x_k) \Delta x_k \\
&\equiv S_l(a, b)
\end{aligned} \tag{4.16}$$

On the one hand, an event x_i which is in an increment Δx_i , is marked by one and only one sub-process, namely l , and its probability is $1/N_{call}$ due to the MC generator. On the other hand, the probability for an event being in increment Δx_i and being marked by l is $\rho_l(x_i) \Delta x_i$ where $\rho_l(x_i)$ is probability density for generating event i in associated with sub-process l , $\Delta x_i = x_{i+1} - x_i$, $i = 1..N_{call}$. Therefore, considering the events type l in bin (a, b), one has

$$\sum_{k=1}^{\Delta N_l} \frac{w_p(x_k)}{N_{call}} = \sum_{k=1}^{\Delta N_l} w_p(x_k) \rho_l(x_k) \Delta x_k \tag{4.17}$$

where $\Delta x_k = x_{k+1} - x_k$, ΔN_l is the number of events of type l in the bin (a, b), $l = 1..n$. Thanks to Eqs. (4.16) and (4.17), the cross section of sub-process l over the bin (a, b) is

estimated by

$$S_l(a, b) = \frac{\sigma_p}{N_{call}} \sum_{k=1}^{\Delta N_l} w_p(x_k) \quad (4.18)$$

where $w_p(x_k)$ is a number for a given event. Thus a differential cross section with respect to variable x at the bin (a, b) is approximated by

$$\frac{S_l(a, b)}{b - a} = \frac{\sigma_p}{(b - a) N_{call}} \sum_{k=1}^{\Delta N_l} w_p(x_k) \quad (4.19)$$

One can see, so far, that it is the absolute value of sub-contributions that are randomly chosen but not their algebraic value. To get the true contribution, these absolute contributions have to be weighted by the quantity which is defined as in Eq. (4.15). That makes the method obvious and understandable.

Let us now summarize the procedure for randomly picking up a sub-process given main process is treated by MC generator.

1. At certain configuration x , which is fed by a Monte Carlo generator, assign values of $|f_l(x)|$, $l = 1..n$, to an array as

$$ao[l] = |f_l(x)|, \quad l = 1..n \quad (4.20)$$

and define another array as

$$as[l] = \frac{\sum_{k=1}^l ao[k]}{\sum_{j=1}^n ao[j]}, \quad l = 1..n, \quad (4.21)$$

$$as[0] = 0$$

2. Generate a random number rb between 0 and 1.
3. Make a loop over $l = 1..n$ for checking conditions $as[l - 1] < rb \leq as[l]$:
 - (a) If at iteration l^{th} this condition is satisfied, save the value l , calculate the quantity

$$w_p = \frac{\sum_{j=1}^n |f_j(x)|}{|f(x)|} \text{sign}[f_l(x)], \quad (4.22)$$

save w_p , and exit the current loop.

- (b) If the loop finishes without passing any condition, set l and w_p to 0.

4. Repeat the procedure until the main program ends.

Eqs. (4.18), (4.23) guarantee that one can construct the sub-process contributions by using the procedure we discuss above. Moreover, consider the bin (a, b) , the term

$\sum_{k=1}^{\Delta N_l} w_p(x_k)$ is identical to the bin content if the histogram is filled with type l events whose weight is $w_p(x_k)$. Therefore, the estimations in Eqs. (4.18) and (4.23) can be re-written as

$$\begin{aligned} S_l(a, b) &= \frac{\sigma_p}{N_{call}} \times l\text{-type-Content of bin } (a, b) \\ \frac{S_l(a, b)}{b-a} &= \frac{\sigma_p}{(b-a) N_{call}} \times l\text{-type-Content of bin } (a, b) \end{aligned} \quad (4.23)$$

where l -type-Content of bin means the bin content of the sub-process type l .

In short, by using the procedure which we present in this section, one has a opportunity to study the flavor sub-contributions from events which are generated by a MC generator. The procedure plays a crucial role in modifying JETPHOX into BJETPHOX.

Test selection on well known functions

As before, let us consider the functions given in Eq. (2.35). It is clear that the function $f(x)$ is the sum of those $f_1(x)$ and $f_2(x)$. We use the procedure above for dealing with sub-contributions $f_1(x)$ and $f_2(x)$, given the main process $f(x)$ is treated by a MC generator. As illustrated in Fig. 4.2, the distributions which are constructed by the procedure agree

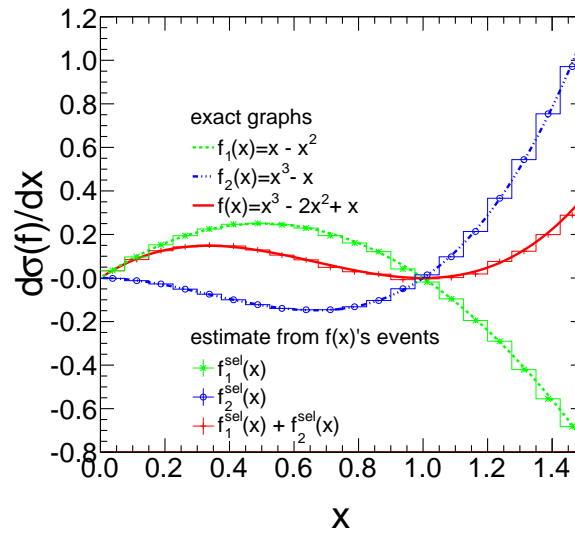


Figure 4.2: Estimate $f_1(x)$, $f_2(x)$ contributions from MC generated events.

well with the exact graphs. As a result, the sum of those constructed distributions matches with the $f(x)$ contribution which is carried out by the method as in JETPHOX and the exact graph.

Back to the example in which one generates events with respect to variables $\{x, y\}$ but considers distribution on another variable, e.g. $z = x + y$. Those integrands are given in Eq. (2.36) and their z distribution have exact formulas as in Eqs. (2.41) and (2.42). For

the purpose of testing the picking-up procedure, the function $g(x, y)$ was chosen to be the sum of $g_1(x, y)$ and $g_2(x, y)$. Thus, it is obvious to state that $\sigma_1(g)$ and $\sigma_2(g)$ play a role of sub-processes which contribute to process $\sigma(g)$.

Assume that one wants to construct distributions $d\sigma_1(g)/dz$, $d\sigma_2(g)/dz$ from those events which are generated for integrand $g(x, y)$ over $\Omega = \{0 < x < 5, 0.1 - x < y < 8 - x\}$. The picking-up procedure, with $N_{call} = 10^5$, is used to perform the requirement. The good agreement between these estimations and the exact graphs are obtained as in Fig. 4.3.

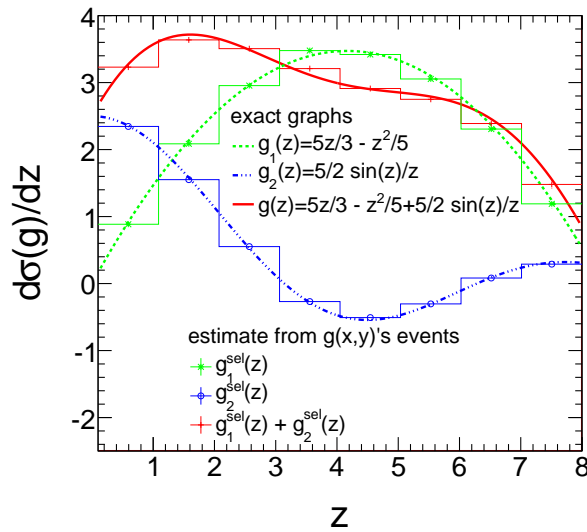


Figure 4.3: Estimate of $g_1(z)$, $g_2(z)$ contributions from MC generated events.

The demonstration above confirms that the picking-up procedure is a heuristic method for sub-processes construction from the main process generation. This procedure is our choice for the study of heavy-flavor jets from events which are generated for standard jets in JETPHOX.

4.1.2 Select among flavor-contributions on BJETPHOX

In this section, we briefly show how to implement the picking up procedure in JETPHOX generator code so the flavor information of final partons is added to each event. As default in JETPHOX, the calculation is split into various channels, labeled by $j\mathbf{0}$. The channels are defined by independent classes of partonic reactions as shown in appendix B.1. It is obvious that the information of final flavors depends on the different channels. Thus, one would require a selection among channels. Moreover, for a given channel $j\mathbf{0}$, there are various possible initial flavor partons. The flavor of initial partons may restrict the final parton flavors determination. This information is implemented in term of combinations of PDF and FF. Therefore, a second selection is performed among these combinations for a chosen channel $j\mathbf{0}$. In the case where the photon is produced together with two partons, such as part IIc, see section 2.2.1, a further selection is performed to specify the flavor of

the hardest partons. The detail to apply those modifications will be different among the following parts of JETPHOX (see section 2.2.1):

1. $2 \rightarrow 3$ contribution

This contribution corresponds to part IIc of JETPHOX, where two visible partons are produced with the photon. The approach will follow three steps presented below

- (a) Introduce an array $\mathbf{vj0}$ and assign to its elements the contributions of channel $\mathbf{j0}$. Apply the pick up procedure among elements of array $\mathbf{vj0}$, where the element plays the role of $f_i(x)$. Assign values l and w_p , which are saved at the step 3. of the pick up procedure given in section 4.1.1, to the variables $\mathbf{indexj0}$ and $\mathbf{adpwj0}$, respectively.
- (b) For a chosen $\mathbf{j0}$, introduce an array \mathbf{vini} and assign to its elements the contributions of sub-structure of PDF or PDF \times FF. Apply the pick up procedure among elements of array \mathbf{vini} . Assign values l and w_p to the variables $\mathbf{indexini}$ and \mathbf{wini} , respectively.
- (c) For a chosen $\mathbf{j0}$, introduce an array \mathbf{vfin} and assign to its elements the contributions of sub-partonic processes, where sub-partonic processes depending on which final parton has the hardest momentum. Apply the pick up procedure among elements of array \mathbf{vfin} . Assign values l and w_p to the variables $\mathbf{indexfin}$ and $\mathbf{adpwfin}$, respectively.
- (d) Then, create the new branches in the generated event. The saved values: $\mathbf{indexj0}$, $\mathbf{indexini}$, $\mathbf{indexfin}$, $\mathbf{adpwj0}$, $\mathbf{adpwini}$, $\mathbf{adpwfin}$ are used to feed those branches.

2. Quasi $2 \rightarrow 2$ contribution

This contribution comes from the part I, IIa, and IIb. In this case, several finite parts are carried out together in one calculation while they may have different structure terms. By saying finite part, we mean the term which is left after IR or collinear divergences contribution are removed.

- (a) As in 1. (a)
- (b) For a chosen $\mathbf{j0}$. For each finite part, let us introduce two arrays \mathbf{ainip} and \mathbf{afinp} . Assign calculations of sub-structure and sub-partonic terms to \mathbf{ainip} and \mathbf{afinp} elements, respectively. Then, define three arrays with their elements specified as follows

$$\begin{aligned}
 \mathbf{vsub}[k] &\equiv \sum_{\text{finite parts}} \mathbf{ainip}[i] \mathbf{afinp}[j] \\
 \mathbf{kini}[k] &\equiv i \\
 \mathbf{kfin}[k] &\equiv j
 \end{aligned} \tag{4.24}$$

Apply the pick up procedure among elements of array \mathbf{vsub} . where the element plays the role of $f_i(x)$. Assign values $\mathbf{kini}[l]$, $\mathbf{kfin}[l]$, 1, and w_p to $\mathbf{indexini}$, $\mathbf{indexfin}$, $\mathbf{adpwini}$ and $\mathbf{adpwfin}$, respectively.

(c) As in 1. (d).

3. $2 \rightarrow 2$ contribution

This contribution stands for the part I, where $p_{\perp 5} = 0$, including virtual (ipro=10), born terms (ipro=11) contributions. In practice, the Born term corresponds to the case in which there is one and only one parton produced together with the photon. Thus, the array which is filled by sub-partonic processes has one and only one non-zero element or no non-zero element, for a chosen j_0 . Thus, one can pick up sub-processes as (a) Apply the pick up procedure among channels j_0 ; (b) For a chosen j_0 , apply the pick up procedure among terms of PDF or PDF \times FF. Or one can use the procedure which is applied for $2 \rightarrow 3$ contributions. Both approaches give the same result. One can apply the same tricks for the true virtual contribution. However, the virtual calculation in JETPHOX also includes partial contribution of quasi $2 \rightarrow 2$, i.e. the finite parts which have the same phase space than the Born term. Thus, the sub-partonic array has arbitrary number of non-zero elements. Hence there is no ambiguity to perform, in this case, the selections as in the $2 \rightarrow 3$ case. In short, the approach of the $2 \rightarrow 3$ contribution is performed to select the flavor in the $2 \rightarrow 2$ case.

The new branches of events illustrate how bJETPHOX events differ from JETPHOX. For a given label set $\{\text{index}j_0, \text{index}ini, \text{index}fin\}$, flavor of parton p_1 and p_2 are determined. For a purpose of automatic events analysis, a spurious flavor for p_2 is introduced in case where there is one and only one visible parton, p_1 , associated with the photon in final state. To construct flavor of final partons, the flavor converter tables are introduced for (D) and (F) cases, which are introduced in section 2.2.1. One can access them thanks to the following subroutines

- `flavor_convert(indexj0, indexini, indexfin, ..., fl1, fl2)` for (D) case,
- `flavor_converto(indexj0, indexini, indexfin, ..., fl1, fl2)` for (F) case,

where `fl1` and `fl2` are flavor outputs for p_1 and p_2 , respectively. The possible values of `fl1` are B, C, S, D, U, g, u, d, s, c, b, in which B, C, S, D, and U stand for flavors \bar{b} , \bar{c} , \bar{s} , \bar{d} , and \bar{u} , respectively.

As in the previous version, one can select bJETPHOX events to construct a contribution cross section of jet+photon production by filling accepted events into histogram with their original weight, i.e. `pdf_weight[0]`. However, as soon as the flavor of jet is taken into account, one has to fill accepted events with other weight which is defined by

$$wp = |\text{adpw}j_0| \times \text{wadp}ini \times \text{adpw}fin \quad (4.25)$$

Due to the fact that one wants to construct the flavor contribution, the sign of this contribution has to be respected. Thus, the absolute value of `adpwj0` is used, instead of its algebraic value, to avoid of polluting weight's sign. The aspect of heavy-quark analysis,

for a given events ntuple, will be discussed in the next section.

4.1.3 Events with flavor selection

To upgrade JETPHOX without losing its original usage, first of all, bJETPHOX can be used as JETPHOX. In addition, the events which are generated for both inclusive and isolated single prompt photon+X production in hadronic collisions, now, include the flavor information of final partons. Therefore, at the events analysis level, not only the jets but also the flavor-jets can be constructed by using a suitable algorithm. It leads to a new critical study of jet photon production in which flavor of the jet is invoked, especially the study of photon in association with heavy-quark jet. After the jets/flux-jets are defined, one can calculate interesting observables, such as invariant mass, transverse momentum, rapidity. One then apply the experimental cuts, e.g. kinematics, to select events. The accepted events are used to fill the histograms, which correspond to the differential cross section with respect to an observable. In this section, let us show how to construct the $p_{\perp}^{Q\text{-jet}}$ distribution for the associated production of heavy-quark jet+photon in the pp collisions from the event ntuple³ generated by bJETPHOX.

The aim of this part is to show in detail how to select the heavy-flavor jet(s) event from bJETPHOX event ntuple by using flavor- k_t algorithm. From the discussion in section 2.1.3 of chapter 2, we parametrize the heavy-flavor jet(s) selection among various partonic processes as following.

Events corresponding to $Q\bar{Q}\gamma(\mathcal{D}_i^\gamma)$ production

These events were generated for partonic processes such as, $q\bar{q} \rightarrow Q\bar{Q}\gamma$, $gg \rightarrow Q\bar{Q}\gamma$ (direct case) or $q\bar{q} \rightarrow Q\bar{Q}\mathcal{D}_g^\gamma$, $qg \rightarrow Q\bar{Q}\mathcal{D}_q^\gamma$, $gg \rightarrow Q\bar{Q}\mathcal{D}_g^\gamma$ (fragmentation case).

1. $2 \rightarrow 3$ contribution (flag `ipro=34` or `ipro=44`)

Apply flavor- k_t algorithm for specifying merged condition.

- (a) If partons Q and \bar{Q} are in merged condition, it counts as a gluon-jet. Thus, ignore this event.
- (b) Otherwise, partons Q and \bar{Q} do not merge together,
 - i. If either parton Q or \bar{Q} passes the jet cuts, collect this event as $\gamma(\mathcal{D}_i^\gamma)+Q$ jet production.
 - ii. If both partons pass the jet cuts, the event is counted once with respect to higher energetic parton.
 - iii. If neither of Q nor \bar{Q} passes the jet cuts, ignore this event.

3. The guide for declaration inputs in parameter file as well as run program can be found in the readme of PHOX package or at the following link http://lapth.cnrs.fr/PHOX_FAMILY/readme_jetphox.html in PHOX family's website.

2. quasi $2 \rightarrow 2$ contribution (flag `ipro=23` or `ipro=21`)
Conventionally, final parton which is collinear with γ (`ipro=23`) or beam (`ipro=21`) is denoted by particle p_5 , the other by p_3 , see section 2.2.1.
 - (a) If p_3 passes the jet cuts then keep this event as $\gamma(\mathcal{D}_i^\gamma) + Q$ jet production.
 - (b) Otherwise, ignore this event.
3. $2 \rightarrow 2$ contribution (flag `ipro=10` or `ipro=11`)
 - (a) If `ipro` is 11: Born term. It is clear that there is no born contribution in considered process.
 - (b) If `ipro` is 10, the possible contributions are:
 - Virtual correction.
 - Partial finite term from collinear divergence of Q and \bar{Q} .
 - Partial finite term from collinear divergence of Q (\bar{Q}) and γ .
 - Partial finite term from collinear divergence of Q (\bar{Q}) and beam.
 In fact, in our case, there is no contribution from this part because the coefficient in front of the collinear divergences is proportional to non diagonal Altarelli-Parisi Kernels (P_{qg} or P_{gq}).

In short, this type event is ignored.

Events corresponding to Q +parton+ $\gamma(\mathcal{D}_i^\gamma)$ production, where Q is heavy quark or anti heavy quark and the parton differs from Q .

1. $2 \rightarrow 3$ contribution
Apply flavor- k_t algorithm for specifying merged condition.
 - (a) If Q and the parton are in the merged condition then the merged jet is considered as Q jet.
 - (b) Otherwise, Q and the parton is considered as heavy-quark jet and non-heavy-quark jet, respectively.
 - (c) If Q jet passes jet cuts then keep event. Otherwise, ignore the event.
2. $2 \rightarrow 2$ (quasi) contribution
 - (a) In case Q has a greater transverse momentum than the parton, Q is considered as the heavy-quark jet. If the jet passes the cuts then keep event. Otherwise, ignore event.
 - (b) In case where the parton has a greater transverse momentum than the Q , ignore this event.

Events corresponding to $Q\gamma(\mathcal{D}_i^\gamma)$

Those events come from the Born and virtual contributions. Parton Q is considered as heavy-quark jet. If the Q jet passes the cuts then keep this event. Otherwise, ignore this event.

The other events, where there is no Q in final state

It is obvious that there exist no Q_{jet} in this case. Therefore, we have to ignore those event.

4.1.4 Analytical macros

One can learn from the script `demo_analyse.cxx` given in appendix B.4 for analyzing events of `bjetphox` in practice. In this demo, the C++ class `ajetphox` and its dependencies, which are included in the package, are required. They are illustrated via the following Root scripts. This macros plays the role as an tutorial on how to get events and use event contents to calculate an observable. From that, users can build their own macros to study differential cross sections with respect to an interesting observable.

4.2 The aspects of photon + heavy-quark jet production at LHC

There are several ways to study an observable in association with heavy-quark jets depending on how the heavy-quark jets are defined. We have to be careful in the way we define the heavy-quark jets to avoid IR-unsafety in the theoretical calculation. The requirement that the heavy quark has a transverse momentum greater than a certain value will prevent the exact cancellation given by Eqs. (2.1) and (2.2). Then the corresponding calculation, in general, does include the collinear divergence terms like $\frac{1}{\epsilon} P_{gQ}$, $\frac{1}{\epsilon} P_{Qg}$. Therefore, it is necessary to use the jet algorithms which is flavor sensitive in order to avoid those collinear divergence (IR-unsafety) problems. In this study, we discuss three different approaches for dealing with heavy-quark jets so that the corresponding calculations are IR-safe. *a)* The approach which is presented in section 4.2.1 is treated with an invariant mass cut on the $Q\bar{Q}$ pair in final partonic state. Our results, which are performed by using `BJETPHOX`, agree well with previous calculation [117]; *b)* The approach of using the flavor- kt algorithm is discussed in section 2.1.3. The comparable results with the first approach are found as shown in section 4.2.2; and *c)* In the section 4.2.3, we show the approach where one uses the renormalized FF of partons into the heavy-quark [118] to absorb the collinear singularities. There have been previous calculation of charm FF [119]. In this reference study, the photon fragmentation contribution are treated only in LO. In our results, we extend this component up to NLO. One can perform those first two calculations by using `BJETPHOX` (which is introduced in previous section) and the last calculation by using `DIPHOX`.

As an application of prompt photon and heavy-quark jet production in hadronic collisions, the effect of heavy-quark densities in proton on this process is discussed in section 4.2.4.

4.2.1 The $Q\bar{Q}$ -pair invariant mass approach

One may define the heavy-quark jet as the jet which contains the heavy quark or anti heavy quark [117]. Since, the heavy quarks and photon are detected, their transverse momentum p_{\perp} are required to be greater than a certain value depending on the experimental apparatus. The lower bounds for the transverse momenta of prompt photon and heavy-quark measurements at D0 and CDF are greater than 10 GeV. At LHC, the minimal value for the p_{\perp} of jets in which the experimental determination remains under control is around 30 GeV. Also note that the observed photon and heavy quark have to be well separated in the case there is only one heavy quark in the final state otherwise they cannot be both detected. In the case there are two heavy quark jets which are well separated, one can accept the event even if the photon is collinear to one of the jets. However, if one wants to observe the photon accompanied with two heavy-quark jets, the photon must not be

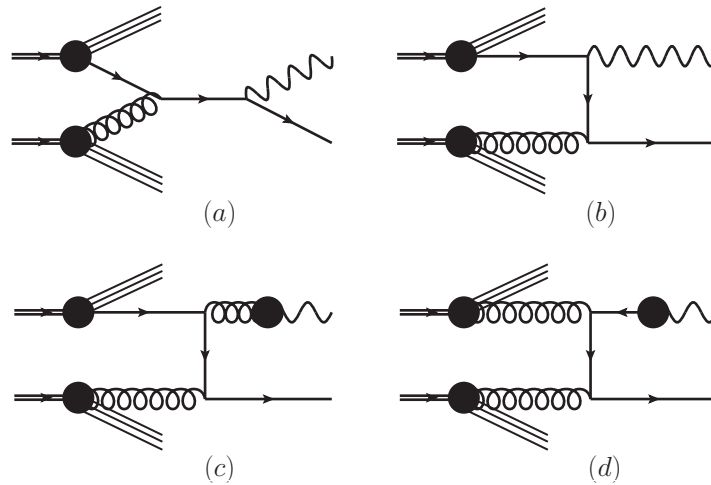


Figure 4.4: An example of the LO processes: (a), (b) the direct photon contributions; and (c), (d) the photon fragmentation contributions. The quark line stands for a heavy flavor quark.

produced collinear to both of them.

The Born term for the $\gamma + Q$ -jet production includes the subprocesses $gQ \rightarrow Q\gamma$ as shown in Fig. 4.4. As it is described in section 2.2.1 of chapter 2, the photon fragmentation $\mathcal{D}_{q/\bar{q},g}^\gamma(z, M_F^2)$ behaves roughly as $\frac{\alpha}{\alpha_S(M_F^2)}$. Hence the convolution of the partonic processes of order $\alpha_S^2(M_F^2)$ such as $gg \rightarrow Q\bar{Q}$, $gQ \rightarrow Qg$, where one final parton fragments into photon contribute for the LO calculation at the same order: $\alpha\alpha_S(M_F^2)$. The diagrams (c) and (d) in Fig. 4.4 represent an example of those corrections, e.i. $gQ \rightarrow Q\mathcal{D}_g^\gamma$ and $gg \rightarrow Q\mathcal{D}_{\bar{Q}}^\gamma$, respectively.

The computation for NLO corrections comes from the subprocesses such as, (a), (b) in Fig. 4.5. The same power counting argument as in LO case, the diagrams (c), (d) in

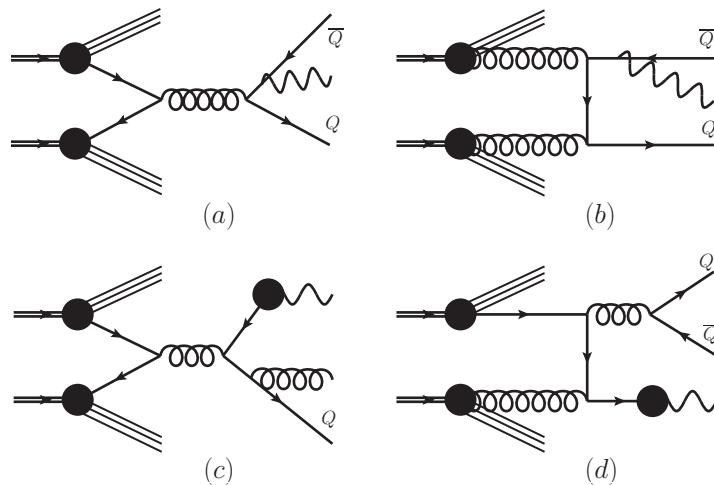


Figure 4.5: An example of the NLO processes: (a), (b) the direct photon contributions; and (c), (d) the photon fragmentation contributions.

Fig. 4.5 give rise to the contribution for NLO. Conventionally, we call "direct" (D) the contribution where the photon with high p_{\perp} is emitted by the quark and "fragmentation" (F) the contribution involving the photon fragmentation from parton, see section 2.2.1.

It is obvious that there are many more direct partonic subprocesses at NLO than LO, the same argument is true for fragmentation. One may be interested in the possible subprocesses and can find them in Tables 4.1 and 4.2 where are listed all the possible direct and fragmentation subprocesses, respectively. By considering side by side in the same line, one can get what/how the LO and NLO subprocesses are involved in NLO calculation given they have the same initial partons state. The discussion about the theoretical content for this NLO calculation can be found in chapter 1 and 2.

As mentioned above, the fact that the heavy quark is detected gives rise to a divergence for the process including the collinear $Q\bar{Q}$ pair in final state. One can find that this comes from the case where the produced γg^* is followed by the splitting of the virtual gluon into $Q\bar{Q}$ pair. In general, in the massless limit calculation for the general jet observation, the arbitrary soft gluon is not only able to split in to gg pair but also $q\bar{q}$ pair. (The addition of those corresponding contributions is finite even though each of them includes collinear divergence.) Physically, to produce the heavy quark $Q\bar{Q}$ pair on shell, the gluon virtuality has to exceed a certain value, e.g. $\sim m_Q^2$ with m_Q is the mass of heavy quark Q . For this reason, the cut-off of $Q\bar{Q}$ invariant mass below $4m_Q^2$ can be used and one gets

$$E_Q^2(1 - \cos(\theta)) > m_Q^2 \quad (4.26)$$

where E_Q is heavy quark energy in CMS frame of the Q and \bar{Q} , θ is the angle between the Q and \bar{Q} . Therefore, one can get rid of the $Q\bar{Q}$ collinear region by imposing the condition: invariant mass exceeds $4m_Q^2$.

The final mentioned problem is related to the divergence which appears when the emitted gluon is collinear to the heavy quark in the final state. Given the discussion on the kt algorithm in chapter 2, the jet which is specified thanks to this algorithm gives rise to the observable which is free of this divergence. When the quark and gluon are produced almost collinear together, they are always merged into a single jet. Moreover, the corre-

Table 4.1: A list of possible direct subprocesses for the $\gamma + Q$ -jet production in hadronic collisions.

LO	NLO
	$Qq \rightarrow Q\gamma q \quad (Q \leftrightarrow \bar{Q})$
	$Q\bar{q} \rightarrow Q\gamma\bar{q} \quad (Q \leftrightarrow \bar{Q})$
	$Q\bar{Q} \rightarrow Q\gamma\bar{Q}$
	$QQ \rightarrow Q\gamma Q \quad (Q \leftrightarrow \bar{Q})$
	$q\bar{q} \rightarrow Q\gamma\bar{Q}$
$Qg \rightarrow Q\gamma \quad (Q \leftrightarrow \bar{Q})$	$Qg \rightarrow Q\gamma g \quad (Q \leftrightarrow \bar{Q})$
	$gg \rightarrow Q\gamma\bar{Q}$

Table 4.2: A list of possible fragmentation subprocesses for the $\gamma + Q$ -jet production in hadronic collisions.

LO		NLO	
$Qq \rightarrow Q\mathcal{D}_q^\gamma$	$(Q \leftrightarrow \bar{Q})$	$Qq \rightarrow Q\mathcal{D}_q^\gamma g / Q\mathcal{D}_g^\gamma q$	$(Q \leftrightarrow \bar{Q})$
$Q\bar{q} \rightarrow Q\mathcal{D}_{\bar{q}}^\gamma$	$(Q \leftrightarrow \bar{Q})$	$Q\bar{q} \rightarrow Q\mathcal{D}_{\bar{q}}^\gamma g / Q\mathcal{D}_g^\gamma \bar{q}$	$(Q \leftrightarrow \bar{Q})$
$QQ \rightarrow Q\mathcal{D}_Q^\gamma$	$(Q \leftrightarrow \bar{Q})$	$QQ \rightarrow Q\mathcal{D}_Q^\gamma g / Q\mathcal{D}_g^\gamma Q$	$(Q \leftrightarrow \bar{Q})$
$Q\bar{Q} \rightarrow Q\mathcal{D}_{\bar{Q}}^\gamma / Q\mathcal{D}_Q^\gamma$		$Q\bar{Q} \rightarrow Q\mathcal{D}_{\bar{Q}}^\gamma g / Q\mathcal{D}_g^\gamma \bar{Q} / Q\mathcal{D}_Q^\gamma g$	
$q\bar{q} \rightarrow Q\mathcal{D}_Q^\gamma / Q\mathcal{D}_{\bar{Q}}^\gamma$		$q\bar{q} \rightarrow Q\mathcal{D}_Q^\gamma g / Q\mathcal{D}_g^\gamma \bar{Q} / Q\mathcal{D}_{\bar{Q}}^\gamma g$	
$Qg \rightarrow Q\mathcal{D}_g^\gamma$	$(Q \leftrightarrow \bar{Q})$	$Qg \rightarrow Q\mathcal{D}_q^\gamma q / Q\mathcal{D}_q^\gamma \bar{q} / Q\mathcal{D}_g^\gamma g$	$(Q \leftrightarrow \bar{Q})$
		$Qg \rightarrow Q\mathcal{D}_{\bar{Q}}^\gamma Q / Q\mathcal{D}_Q^\gamma \bar{Q}$	$(Q \leftrightarrow \bar{Q})$
		$qg \rightarrow Q\mathcal{D}_Q^\gamma q / \bar{Q}\mathcal{D}_Q^\gamma q / Q\mathcal{D}_q^\gamma \bar{Q}$	
		$\bar{q}g \rightarrow Q\mathcal{D}_{\bar{Q}}^\gamma \bar{q} / \bar{Q}\mathcal{D}_Q^\gamma \bar{q} / Q\mathcal{D}_q^\gamma \bar{Q}$	
$gg \rightarrow Q\mathcal{D}_Q^\gamma / \bar{Q}\mathcal{D}_Q^\gamma$		$gg \rightarrow Q\mathcal{D}_{\bar{Q}}^\gamma g / \bar{Q}\mathcal{D}_Q^\gamma g / Q\mathcal{D}_g^\gamma \bar{Q}$	

sponding cross section diverges as the emitted gluon is soft, thus the final phase space is dominated by the configurations where $p_\perp^{Q\text{jet}} \approx p_\perp^Q$ (with $p_\perp^{Q\text{jet}}$ and p_\perp^Q are the transverse momenta of heavy-quark jet and heavy quark, respectively.) For that reason, the cut on p_\perp^Q of the heavy quark can be transformed into a cut on $p_\perp^{Q\text{jet}}$ of heavy-quark jet [117] and, as in this approach, the kt algorithm is used to avoid this collinear divergence.

Tevatron 1.96 TeV

The generated events for the inclusive prompt photon production $p\bar{p} \rightarrow \gamma X$, at the center of mass energy $\sqrt{s} = 1.96$ TeV corresponding to the Tevatron experiment, are described by the 4-momenta of the photon and final partons. We perform the numerical calculation with the parton distribution functions CTEQ6.6 [48] and the photon fragmentation functions at NLL determined by Bourhis, Fontannaz, and Guillet (BFG) [64]. We reconstruct heavy-quark jets via the kt algorithm [89, 90] (as described in section 2.1.2) with radius $R = 0.4$. If there are two heavy-quark jets in the final state, the corresponding event is counted once with respect to higher energetic jet. The lower bounds for transverse momenta of the photon and jets are taken from D0 experiment and they are $p_\perp^\gamma > 30$, $p_\perp^{Q\text{jet}} > 15$ (GeV). We investigate the region where the p_\perp^γ does not exceed 200 GeV, while the $p_\perp^{Q\text{jet}}$ is up to the kinematical limit of $\frac{\sqrt{s}}{2}$. Due to the fact that particles can only be detected in the central region of the detector, the rapidities are followed by the condition: $|y^\gamma| < 1$ and $|y^{Q\text{jet}}| < 0.8$. In order to avoid the photon production from the decays of mesons an isolation criterion has been put: the cone centered around the detected photon is required to have a transverse hadronic energy E_t^h deposited not greater than $E_t^h \approx \epsilon E_t^\gamma$, where E_t^γ is the transverse energy of the photon. In the following result the isolated cone radius is equal to $R_{iso} = 0.4$ and $\epsilon = 0.07$ is presented.

The p_\perp^γ differential cross section of process $p\bar{p} \rightarrow \gamma Q$ -jet is illustrated in Fig. 4.6. Note that the b (c)-flavor means the bottom or anti bottom (the charm or anti charm)

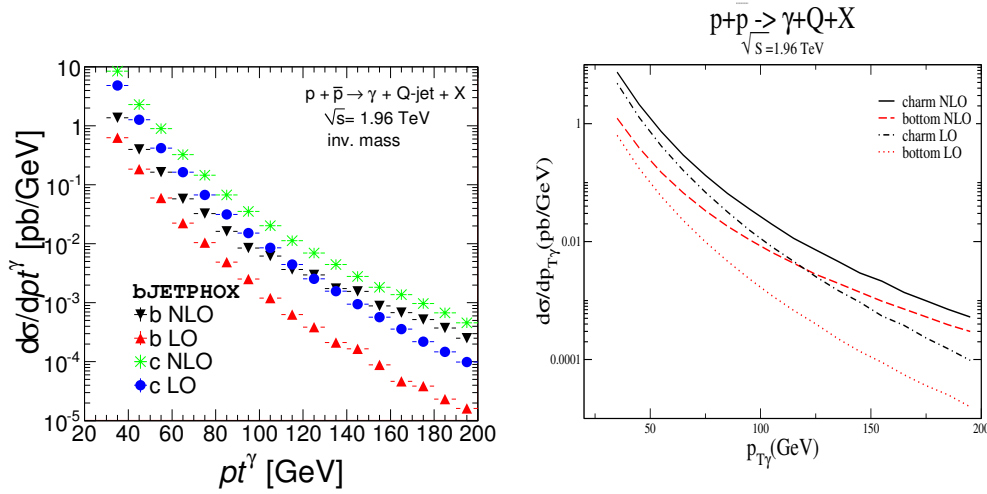


Figure 4.6: Left: bJETPHOX simulation. Right: Previous results [117] (in proton anti-proton collision at $\sqrt{s} = 1.96$ TeV).

quark. As one can see, the result which is calculated by using bJETPHOX, agrees well with the previous one. In fact, here the isolated cuts for photon slightly different.⁴ In fact, the results is not much different when we choose the radius of cone $R_{iso} = 0.4$ and vary hadronic energy fraction ϵ from 0.07 to 0.04 as shown in Fig. 4.7. As we can see, the cross sections for different values of ϵ are compatible within the error bars. This is an expected result because we know that the dependence on ϵ is logarithmic.

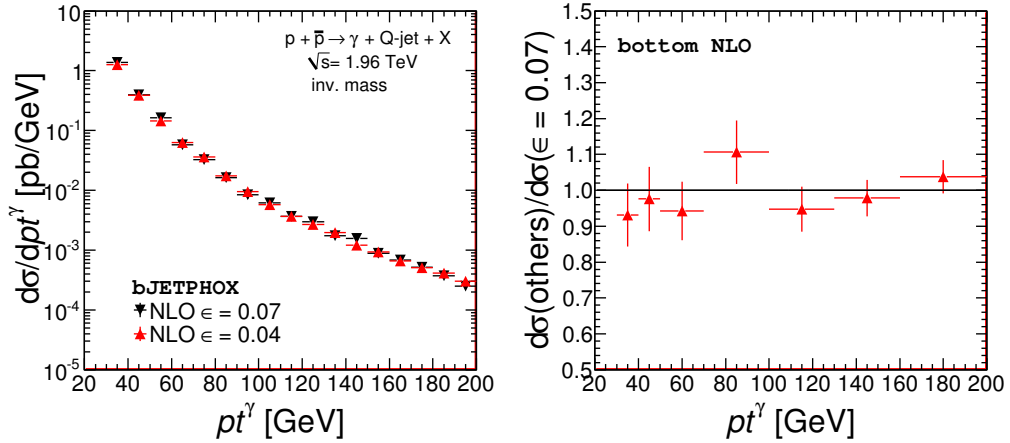


Figure 4.7: Isolation cut dependences: 0.07 vs. 0.04 for an invariant mass cut of $4 m_b^2$ in proton anti-proton collisions at $\sqrt{s} = 1.96$ TeV.

We also compare the production of non-isolated γ to that of isolated one and find that they are in agreement with results of [117], (see Fig. 4.8).

The invariant mass constraint which are applied on the event generated for $q\bar{q} \rightarrow Q\gamma\bar{Q}$ is somehow a theoretical parameter. Thus we expect that the results should not much

4. In previous isolated condition: $R_1 < 0.2$, $\epsilon_1 < 0.04$ and $R_1 < 0.4$, $\epsilon_1 < 0.07$, instead.

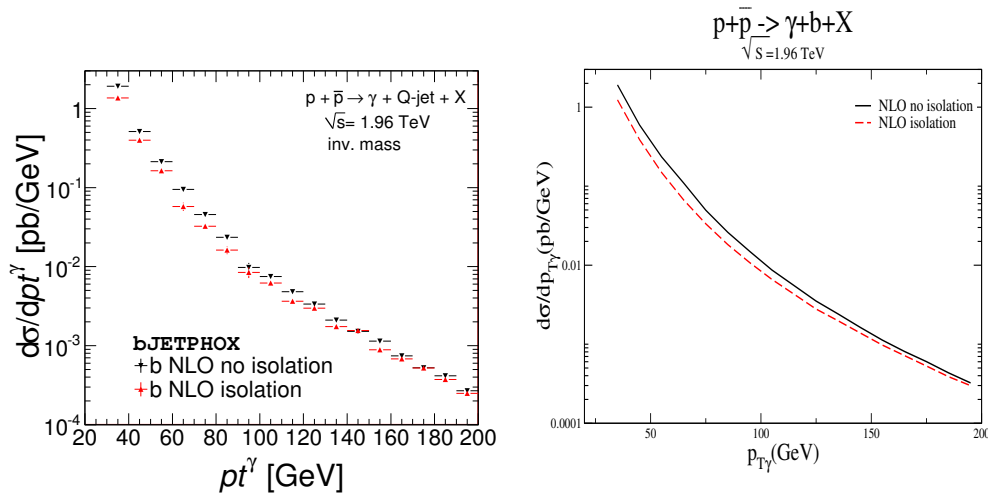


Figure 4.8: Cross section comparison between isolated case and non-isolated one, **bJETPHOX** dir + onef contributions. Left: **bJETPHOX** results and Right: results of reference [117] (in proton anti-proton collisions at $\sqrt{s} = 1.96$ TeV).

depend on this cut when one varies the lower bounds for invariant mass (keeping it of order of m_Q^2), otherwise one cannot trust the prediction of the corresponding observable. The results in Figs 4.9 illustrate this statement, where the invariant mass is varied among m_Q^2 , $4m_Q^2$, and $8m_Q^2$.

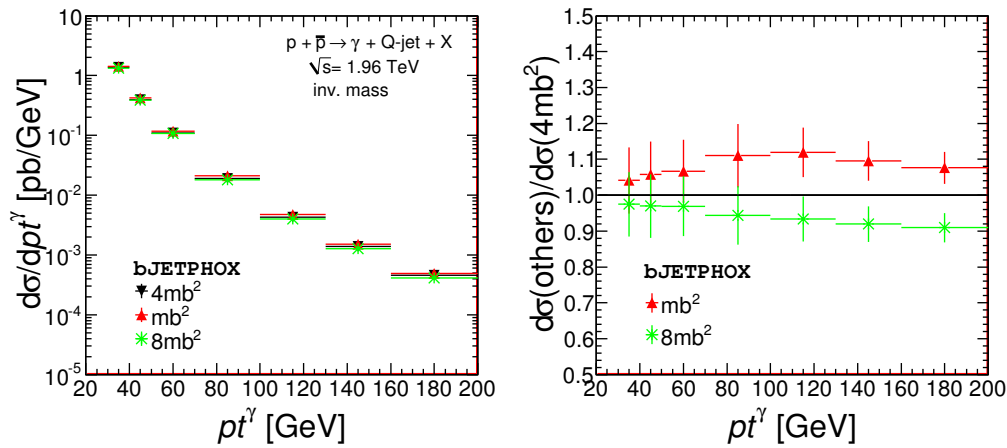


Figure 4.9: Cross section comparison for different invariant mass cuts $4m_b^2$ vs. m_b^2 and $8m_b^2$ (bottom) for an isolation cut: $\epsilon = 0.07$ in proton anti-proton collision at $\sqrt{s} = 1.96$ TeV.

In the ratio plots, one cannot distinguish among those contributions due to the error bar overlap. Therefore, from the theoretical point of view, one can say that this approach does not depend on the invariant mass cuts.

LHC 14 TeV

We carry out the same study for the LHC at $\sqrt{s} = 14$ TeV. We choose the kinematics for photon and heavy-quark jets the same as for Tevatron. Again, our results agree well with the previous calculation of reference [117].

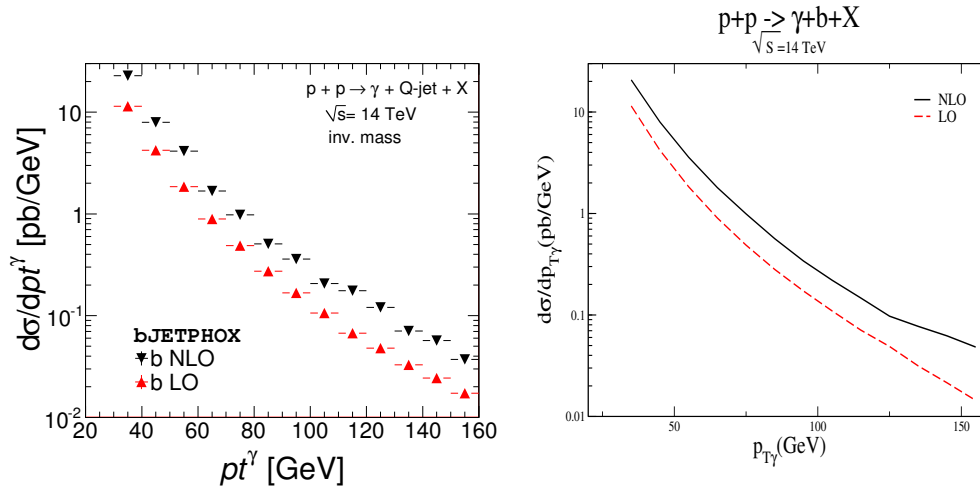


Figure 4.10: Left: bJETPHOX simulation. Right: Previous results [117] (in proton proton collisions at $\sqrt{s} = 14$ TeV).

4.2.2 The flavor- k_t algorithm approach

In this section, we present the result using the flavor- k_t algorithm [17] (described in section 2.1.3). The kinematics for the photon and the heavy-quark jets are imposed as in section 4.2.1

Tevatron at 1.96 TeV: $p\bar{p} \rightarrow Qjet + X$

The results for proton anti-proton collision are given in Fig. 4.11. Although, the in-

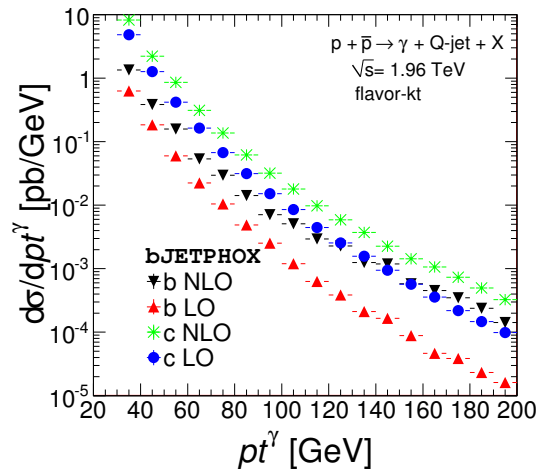


Figure 4.11: Tevatron $\sqrt{s} = 1.96$ TeV. The differential cross section with respect to p_{\perp}^{γ} .

variant mass approach and flavor- k_t approach are different observables it is interesting to compare them in order to cross check our results. Comparing to the invariant mass approach, the result for flavor- k_t approach is smaller when p_{\perp}^{γ} is larger Fig. 4.12. This be-

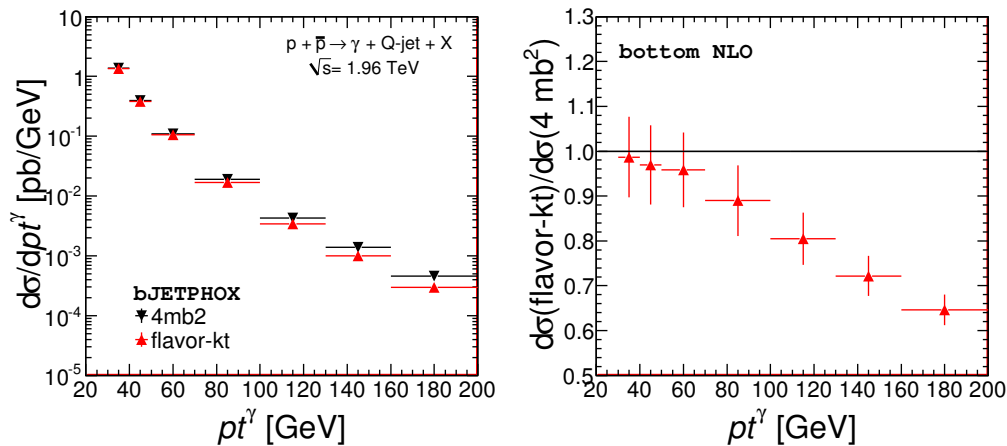


Figure 4.12: Comparison of photon spectrum using flavor- k_t with spectrum using invariant mass constraint in proton anti-proton collisions at $\sqrt{s} = 1.96$ TeV.

havior can be understood. In proton anti-proton collisions, at lower p_{\perp}^{γ} the cross section is dominated by Qg initial state and at larger p_{\perp}^{γ} the process which involves $q\bar{q}$ in the initial state becomes dominant, described in Fig. 4.13, due to the parton densities in the proton. Moreover, while the flavor k_t approach drops any event which includes jet formed by $Q\bar{Q}$, the invariant mass approach keeps the events if $(p_Q + p_{\bar{Q}})^2$ greater than $4m_Q^2$. Thus this effect is almost invisible at lower p_{\perp}^{γ} but it is not the case for higher p_{\perp}^{γ} .

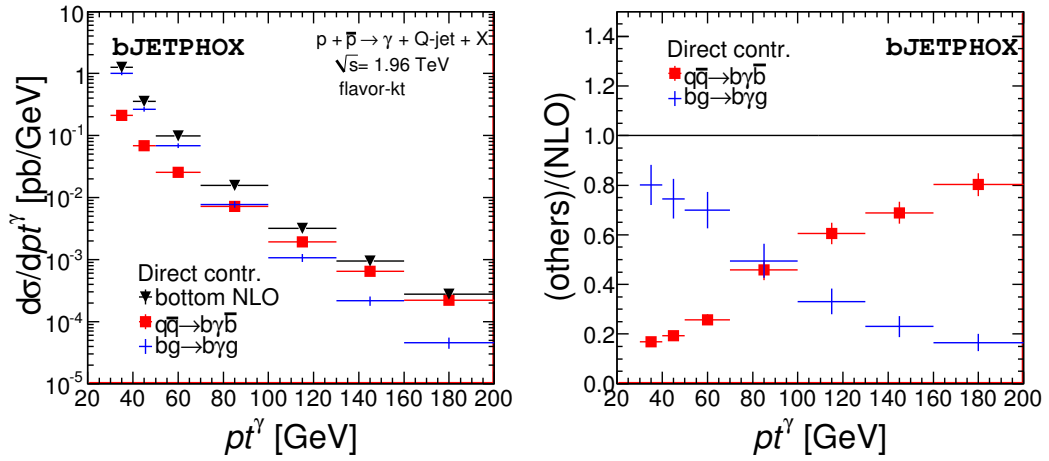


Figure 4.13: An example for direct subprocess contributions in proton anti-proton collisions at $\sqrt{s} = 1.96$ TeV.

The left plot in Fig. 4.14 represents the ratio of charm by bottom for the differential cross section with respect to p_{\perp}^{γ} . As one can see, the LO ratio is almost unchanged for all p_{\perp}^{γ} . At LO, the cross section receives contributions from the subprocesses shown in Fig. 4.4 (as listed in Table 4.1 and 4.2) where the amplitude $gQ \rightarrow \gamma Q$ is dominant. Therefore, the LO ratio almost depends on *a*) the ratio of charm and bottom charges and *b*) the ratio of charm and bottom distributions in the (anti-)proton. Because the charge ratio is $e_c^2/e_b^2 \sim 4$, and the charm ratio is larger than the bottom rate. Moreover, the LO ratio slightly decreases $\sim 7-6$ when $p_{\perp}^{\gamma} \sim 30-200$ GeV Fig. 4.14 left. This fact shows that difference between the charm PDF and bottom slightly decreases when scale of PDF increases.⁵ Those are analogous with the ratio behavior of charm PDF by bottom as in the right plot in Fig. 4.2.

The NLO ratio behaves analogous with the LO for $p_{\perp}^{\gamma} \sim 30-70$ GeV. As in the above discussion, at low p_{\perp}^{γ} the dominant process is $gQ \rightarrow \gamma Qg$ and again the same behavior as for LO ratio must find for NLO at $p_{\perp}^{\gamma} \sim 30-70$ GeV. At larger values, i.e. $p_{\perp}^{\gamma} \sim 70-200$ GeV where the annihilation $q\bar{q}$ is dominant, the NLO ratio strongly decreases $\sim 5-2$. As the initial states are the same and the probability for producing c-jets association with the photon is the same as for b-jets in the massless quark limit, the NLO ratio of charm by bottom for $q\bar{q}$ initial state is about ~ 1 . Therefore, the larger the contribution of the

5. The same results are obtained for the invariant mass constraint approach is given in reference [117].

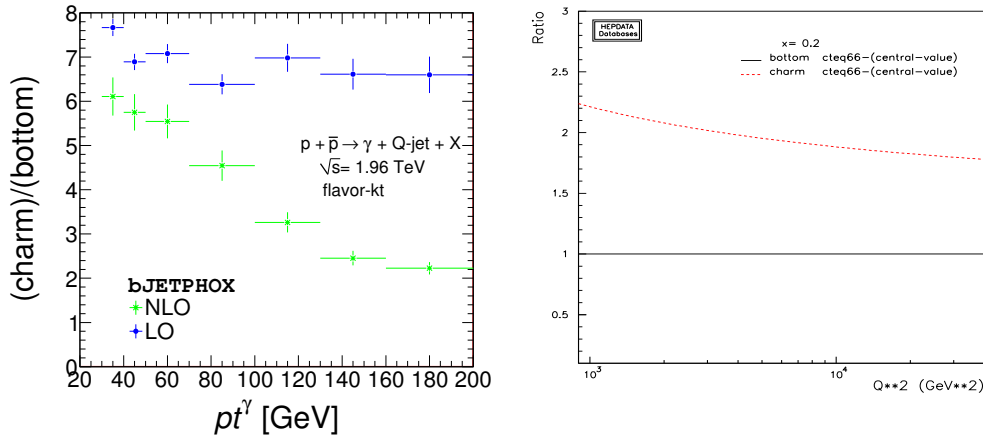


Figure 4.14: Left: The ratio of charm differential cross section by bottom in proton anti-proton collisions at $\sqrt{s} = 1.96$ TeV. Right: The ratio of the charm PDF by the bottom PDF in proton.

dominant process $q\bar{q} \rightarrow Q\gamma\bar{Q}$ is, the closer to 1 the NLO ratio is found.

LHC at 8 TeV: $pp \rightarrow Q\text{jet} + X$

The data for proton proton collision at center of mass energy $\sqrt{s} = 8$ TeV is available at LHC. Given that, it is interesting to have the numerical calculation at this energy and the result for produced photon accompanying with heavy quark jets is presented as in Fig. 4.15.

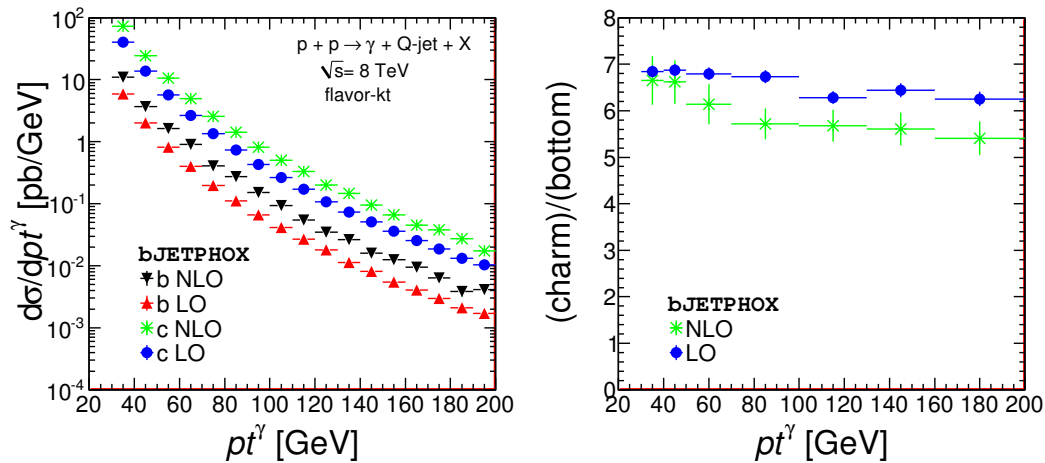


Figure 4.15: LHC $\sqrt{s} = 8$ TeV. (Left) The differential cross section with respect to p_\perp^γ ; (Right) The ratio of the charm differential cross section by the bottom.

As known, in the pp collisions, the contributions should not be dominated by the process including the $q\bar{q}$ in the initial state at low energy due to the fact that valence

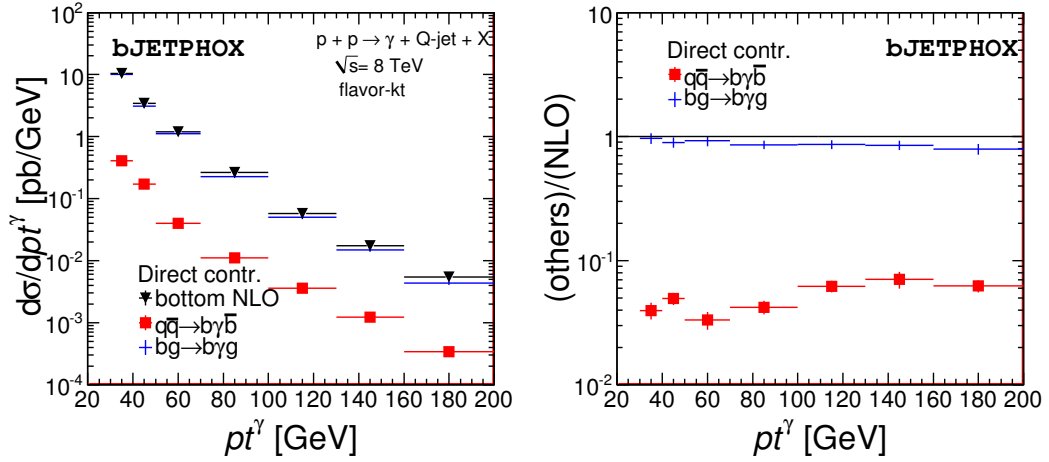


Figure 4.16: An example for direct subprocess contributions in proton proton collisions at $\sqrt{s} = 8$ TeV.

quarks in the proton are u and d . As a result, the subprocess $Qg \rightarrow \gamma Qg$ gives the higher contribution compared to the subprocess $q\bar{q} \rightarrow Q\gamma\bar{Q}$. This behavior is illustrated by the plots in Fig. 4.16. The annihilation subprocess is almost suppressed by the $Qg \rightarrow \gamma Qg$. Thus, the behaviors of the LO and NLO ratio of charm differential cross section by the bottom in p - p collision (see the right plots in Fig. 4.15) are analogous with the LO ratio in p - \bar{p} collision (Fig. 4.14 left). Therefore, the results indicate that the heavy-quark jet production in association with the photon for $p_{\perp}^{\gamma} = 30$ – 200 GeV in p - p collisions significantly depends on the corresponding heavy quark PDFs. The PDFs sensitivity in

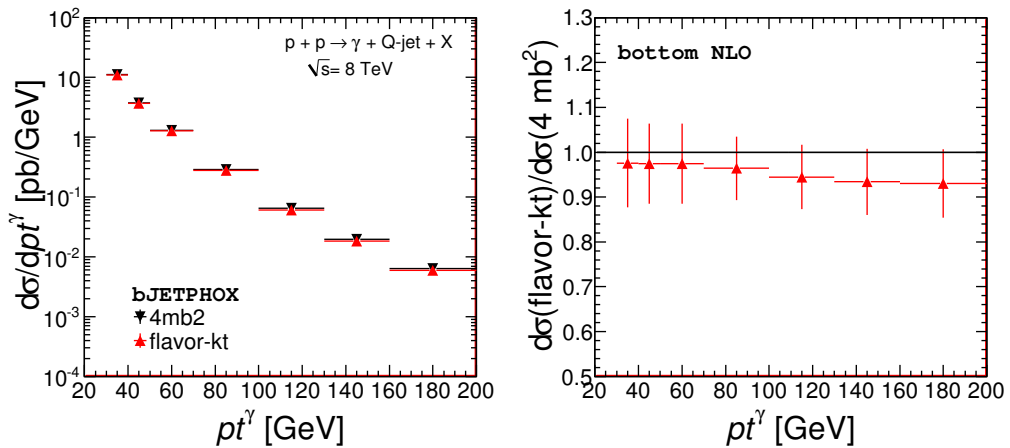


Figure 4.17: Comparison of photon spectrum using flavor- k_t with spectrum using invariant mass constraint in proton proton collisions at $\sqrt{s} = 8$ TeV.

the study of γ +Qjets production is discussed more detail in section 4.2.4. Also note that this behavior is not the same as in proton anti-proton collision (Fig. 4.13). It is obvious

because the valence quarks in anti-proton are \bar{u} and \bar{d} , thus, in $p\bar{p}$ collisions, there is more chance to have initial partons including $q\bar{q}$ scattering than the qq one.

We find that the two approaches, the flavor k_t and invariant mass constraint, give the same prediction for $pp \rightarrow \gamma + Q\text{jet} + X$ at $\sqrt{s} = 8$ TeV, as shown in Fig. 4.17.

LHC at 14 TeV: $pp \rightarrow Q\text{jet} + X$

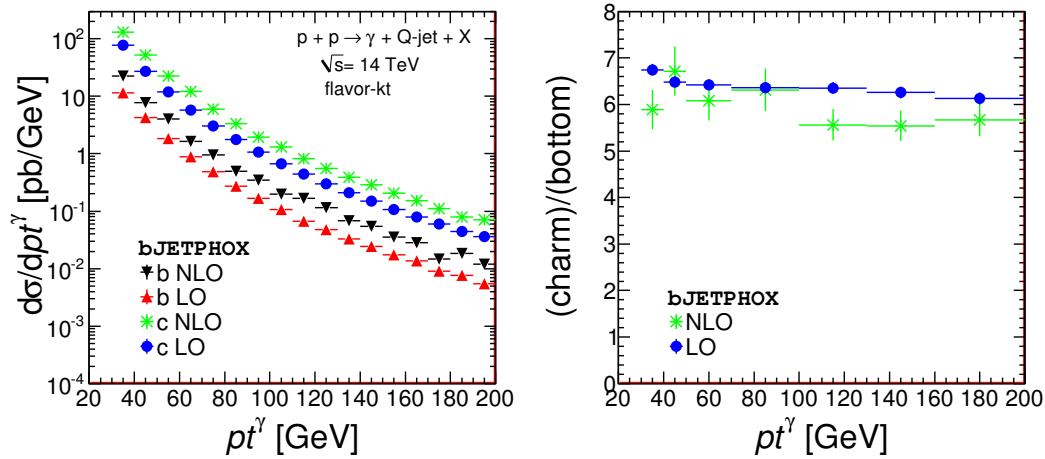


Figure 4.18: LHC $\sqrt{s} = 14$ TeV: (Left) The differential cross section with respect to p_{\perp}^{γ} ; (Right) The ratio of the charm differential cross section by the bottom.

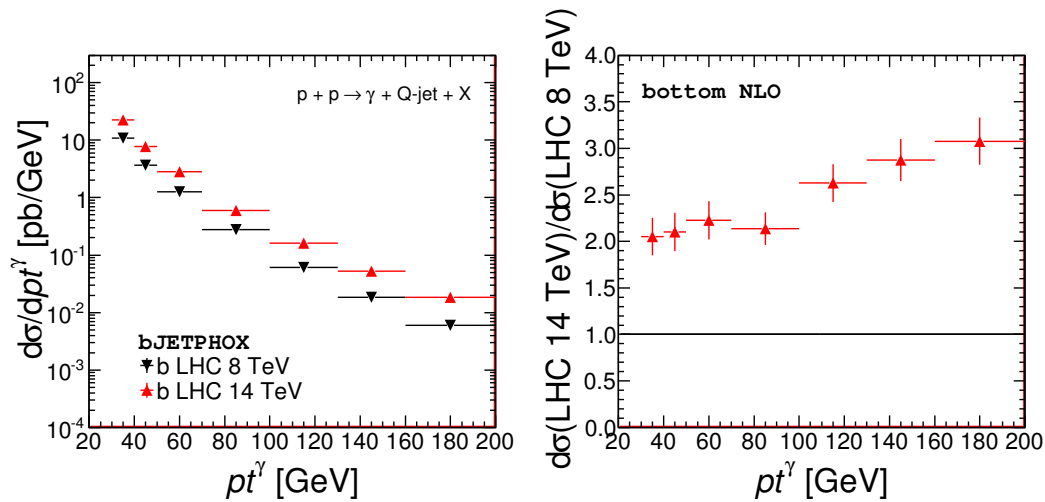


Figure 4.19: Comparing the differential cross section for p - p collision at $\sqrt{s} = 14$ TeV and $\sqrt{s} = 8$ TeV.

We also present the result for p - p collision at $\sqrt{s} = 14$ TeV. This is the highest center of mass energy which experimentalists can get at LHC. Similar behaviors are found for differential cross section for the photon + b(c)-jets production at center of mass $\sqrt{s} =$

14 TeV as at $\sqrt{s} = 8$ TeV, except that the corresponding contributions are a factor 2 higher.

As the center of mass energy increases the corresponding differential cross section with respect to p_{\perp}^{γ} almost doubles. This behavior is illustrated in Fig 4.19. Again, the dominant subprocess is $Qg \rightarrow \gamma Qg$. The ratio between subprocesses and the direct contribution in the p-p collision at $\sqrt{s} = 14$ TeV (Fig 4.20) are the same as at $\sqrt{s} = 8$ TeV (Fig 4.16). Also, the good agreement between the invariant mass constraint approach and the flavor- k_i is obtained as shown in Fig. 4.21.

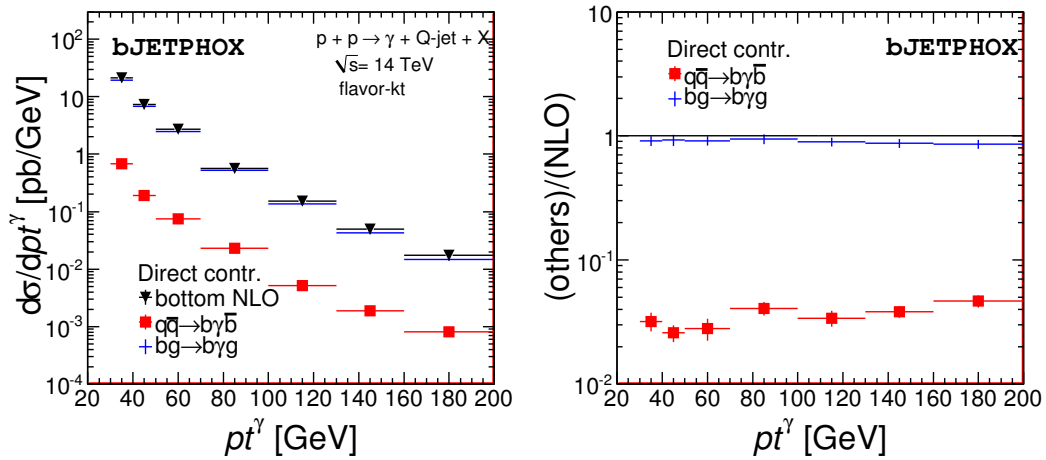


Figure 4.20: An example for direct subprocess contributions in proton proton collisions at $\sqrt{s} = 14$ TeV.

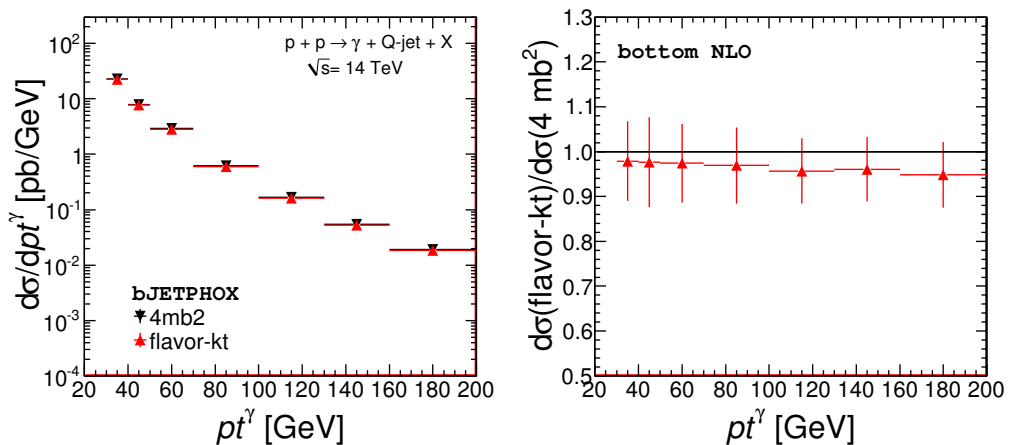


Figure 4.21: Comparison of photon spectrum using flavor- k_i with spectrum using invariant mass constraint in proton proton collisions at $\sqrt{s} = 14$ TeV.

In short, both the invariant mass constraint approach and the flavor- k_i prove that the differential cross section for photon+heavy-quark jets production in p-p collisions is sen-

sitive to the PDF of heavy-quark. In $p\text{-}\bar{p}$ collision, i.e. at Tevatron, the heavy-quark PDFs strongly effects the low p_{\perp}^{γ} region $\sim 30\text{--}70$ GeV but it is not the case at large $p_{\perp}^{\gamma} \sim 70\text{--}200$ GeV.

4.2.3 Charm meson FF approach

One can also use another approach based on FF of partons into heavy quark hadrons. The justification of this approach is the following. In some experiment (e.g. CDF), to sign a heavy quark(hadron), experimentalists search for a secondary vertex (whose origin is the decay of the heavy quark). Then, they look if a muon track is pointed toward this secondary vertex. If it is the case, and if the muon direction also points to a hadronic jet direction, this jet is then called a heavy quark jet. To proceed like that, the heavy quark must have a large transverse momentum otherwise the secondary vertex will be too close to the primary one and cannot be detected. To take into account this cut, it is difficult to use a jet approach for a jet is a degenerate state, that means that the relative momentum between the partons forming the jet must have been integrated out. On the contrary, a FF approach can accommodate this cut easily, a heavy quark hadron is produced with a certain transverse momentum. The jet size is taken into account by choosing the fragmentation scale of order of $R P_T$ where R is the jet cone size and P_T a typical hard scale. The disadvantage of this method is that we have to know the FF of partons into heavy quark hadrons.

In this approach, at the partonic level, it remains some collinear divergences associated with the final state. One can absorb those remaining divergences in the fragmentation function of final parton into heavy-quark(hadron), i.e. $g \rightarrow c(\text{charm meson})$, see Fig. 4.22. In this section, we will use the program DIPHOX, which was built to compute

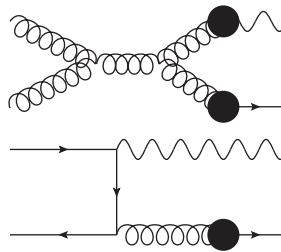


Figure 4.22: An example of fragmentation of parton into heavy-quark.

the di-photon cross section at NLO approximation including the case where one(two) photon(s) come(s) from the fragmentation of a hard parton. This program can be used also to compute in the NLO approximation the associated production of a photon and a hadron or di-hadron production in hadronic collisions.

For the charm production, two approaches can be followed. Either, we can consider the FF of partons into charm quark with suitable initial conditions or we can use the FF of partons into charm hadrons. Here we will follow the second approach⁶ and we will assume that the charm hadron production is dominated by the production of D^* , D_0 and D^\pm mesons. The FF of partons in such mesons are available in the literature [79].

6. In the reference [119], the authors used fixed order FF just to deal with the collinear final state divergences. We do not expect any enhancement in the differential cross section at large $p_{\perp\gamma}$ by using this approach.

The prediction for Tevatron at $\sqrt{s} = 1.96$ TeV

We computed the associated production $\gamma +$ charm hadron in the NLO approximation at Tevatron energy ($\sqrt{s} = 1.96$ TeV), using the CTEQ6 PDFs. The kinematic cuts applied are: $p_{\perp}^{\gamma} > 30$ GeV, $-1 \leq y_{\gamma} \leq 1$, $p_{\perp}^D > 15$ GeV and $-0.8 \leq y^D \leq 0.8$, D stands for a charm meson. For the scale choice, we took for the initial factorization scale and for the renormalization scale: $\max(p_{\perp}^{\gamma}, p_{\perp}^D)/2$ and for the final state factorization scale $R^{\text{jet}} \max(p_{\perp}^{\gamma}, p_{\perp}^D)$, where R^{jet} is a typical cone jet size 0.4. An isolation cut is also applied for the photon (the same as the one used for the associated production of $\gamma +$ charm jet), that is to say: $R = 0.4$ and the maximum of transverse energy allowed in the cone must be less than $\varepsilon E_{\perp}^{\gamma}$ with $\varepsilon = 0.07$. With such isolation criterion, the fragmentation component is completely negligible: three orders of magnitude less than the direct contribution.

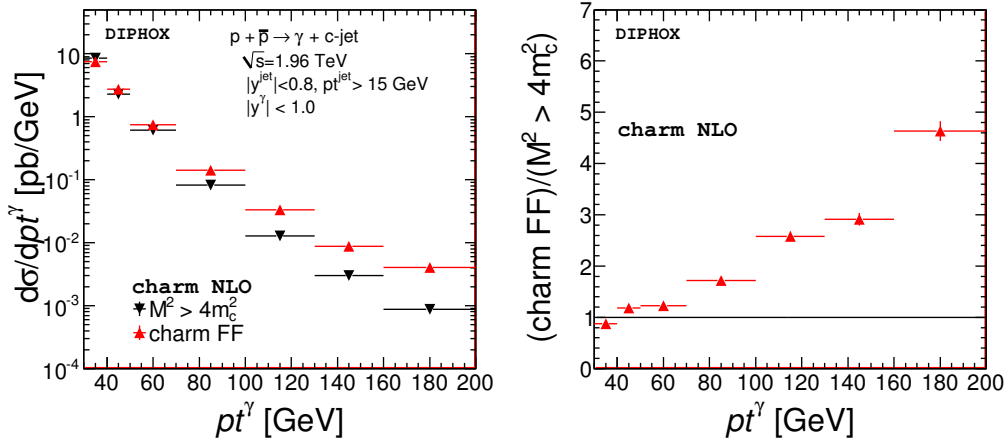


Figure 4.23: Comparison of photon spectrum using charm FF with spectrum using invariant mass constraint in $p\text{-}\bar{p}$ collisions at $\sqrt{s} = 1.96$ TeV.

Again, to cross check our results, we compare the cross sections using the invariant mass approach and fragmentation approach. It is always interesting to see if we can understand the differences between the cross sections. The Fig. 4.23 shows the p_{\perp}^{γ} dependence of the cross section using the FF approach and the approach of section 4.2.1. The FF approach give a much higher cross section at large p_{\perp}^{γ} than the jet approach. This can be easily understandable. Indeed, to simplify the discussion, let consider only the LO approximation. At this level, there are only two partonic subprocesses which contribute to the production of $\gamma +$ charm: $qg \rightarrow q\gamma$ and $q\bar{q} \rightarrow \gamma g$. In the jet approach, we require to have a charm quark(anti-quark) in the final state, that means that the only contribution is : $c(\bar{c})g \rightarrow c(\bar{c})\gamma$, but in the FF approach both initial state can contribute. At small p_{\perp}^{γ} , the dominant parton flux is qg , while the $q\bar{q}$ one is negligible. In addition, at low evolution scale the dominant FF is the fragmentation of a charm quark into a charm meson. So we expect that the FF approach and the jet approach give almost the same result. But at high p_{\perp}^{γ} , the dominant partonic flux is $q\bar{q}$ and there is no partonic reaction having such

an initial state in the jet approach, so we expect that the FF approach give a much higher cross section. At NLO, there are more partonic channels opened in both approaches, the initial states of these new channels are the same. So we do not expect that the LO behavior change at NLO.

As mentioned at beginning of this chapter, there are discrepancies between the theoretical prediction [117] and D0 measurements [10] for the $p\bar{p} \rightarrow \gamma + c + X$ differential cross section with respect to p_{\perp}^{γ} , see Fig. 4.1. The ratio of data over theory using invariant mass approach is about 1.8 ± 0.3 (2.7 ± 0.6) when $p_{\perp}^{\gamma} \sim 80$ GeV (~ 110 GeV). On the other hand, the ratio of charm FF approach over invariant mass approach is about ~ 1.7 (~ 2.6) at $p_{\perp}^{\gamma} \sim 70$ – 100 GeV (~ 100 – 130 GeV). Then it is straightforward to state that the charm meson FF prediction is comparable with the experimental measurement.

As one can see, now, the discrepancy is understandable. They result from the absence of subprocesses involving charm(meson) FF (e.g. Fig. 4.22) in using the invariant mass approach and also the flavor kt approach. In conclusion, in studying the $p\bar{p} \rightarrow \gamma + c + X$ process, the charm(meson) FF plays an important role and one has to include its contribution into the NLO cross section.

The prediction for LHC at $\sqrt{s} = 8$ TeV

By using the charm meson FF approach, we give the prediction for the $pp \rightarrow \gamma + c + X$ cross section at LHC for $\sqrt{s} = 8$ TeV as shown in Fig 4.24. Note that the kinematics for the photon and the c -jet in this calculation are the same as in previous subsection.

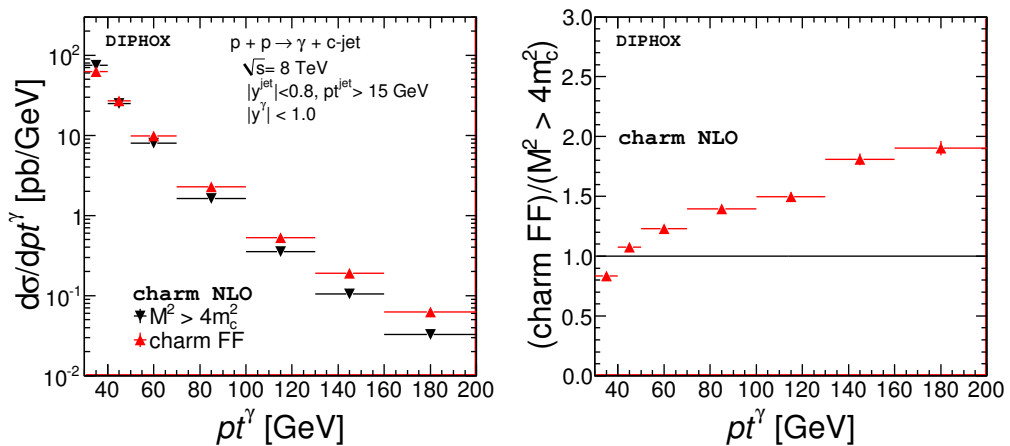


Figure 4.24: Comparison of photon spectrum using charm FF with spectrum using invariant mass constraint in p - p collisions at $\sqrt{s} = 8$ TeV.

The ratio of the prediction using this approach to the invariant mass approach is shown in the right plot of Fig 4.24. As one can see, this ratio at low p_{\perp}^{γ} is somehow the same as the one in the right plot of Fig 4.23 (for Tevatron at $\sqrt{s} = 1.96$ TeV). As discussed in previous subsection, these behaviors resulted from the fact that both the initial qg flux

and the fragmentation of charm into charm meson are dominant at low scale p_{\perp}^{γ} for both LHC and Tevatron. At large p_{\perp}^{γ} , for the same center-of-mass energy, the $q\bar{q}$ partonic flux in p - p collisions (valence–sea) is lower than the one in p - \bar{p} collisions (valence–valence). In addition, when \sqrt{s} increases, the x_T decreases and then the g flux increases much faster than the q . Therefore, the ratio at large p_{\perp}^{γ} in p - p collisions is expected to be lower than the ratio in p - \bar{p} collisions (see the right plots of Fig 4.23 and Fig 4.24).

Comparison between the Charm FF approach and the data: at Tevatron

In this subsection, we show the comparison between the FF approach predictions at NLO pQCD with CTEQ6 PDFs (using DIPHOX) and the current data measurements of γ + c -jet production at Tevatron at $\sqrt{s} = 1.96$ TeV. The scale uncertainties are made by varying three scales simultaneously up or down two times, i.e. $\mu = 0.5, 1, \text{ or } 2$.

We use the kinematical cuts which are applied for D0 measurements [8] as follows: $|y^{\gamma}| < 1$, $|y^{D}| < 1.5$, $30 < p_{\perp}^{\gamma} < 300$ GeV, and $p_{\perp}^D > 15$ GeV. We assume that the value of the minimum transverse momentum for the D -meson is the experimental value for the minimum transverse momentum of the c -jet. The photon is isolated if the hadronic deposited energy is $E^{\text{iso}} < 2.5$ GeV within the cone of radius $R = 0.4$ around it. Our prediction agrees well with the D0 measurement up to the highest possible scale p_{\perp}^{γ} within the uncertainties, as illustrated in Fig 4.25. Also note that the invariant mass approach fails to describe the data at $p_{\perp}^{\gamma} \gtrsim 70$ GeV as presented in Ref. [8]. Therefore, this result confirms the dominance of the subprocesses involving charm FF of partons in the current measurement of the $\gamma + c + X$ production in p - \bar{p} collisions at Tevatron at large scale p_{\perp}^{γ} .

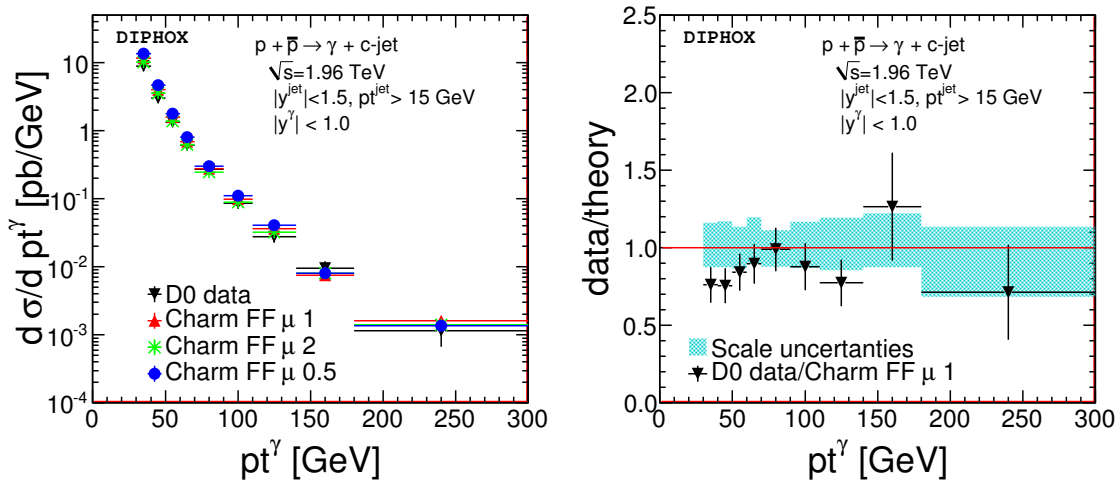


Figure 4.25: Comparison of photon spectrum using charm FF (DIPHOX) with D0 data measurements in p - \bar{p} collisions at Tevatron at $\sqrt{s} = 1.96$ TeV. The data is taken from D0 Collaboration [8], see Table 4.3.

Using the same event ntuple which has been compared with the D0 measurement, we

perform another analysis for the CDF measurement [9] and show the results in Fig 4.26. Note that, in this case, $p_{\perp}^{\text{jet}} > 20$ GeV instead. Again, as in the inclusive prompt photon case, Fig 2.14, the CDF data measurement at $p_{\perp}^{\gamma} \sim 30\text{--}40$ GeV overestimates the prediction using PHOX generators for the prompt photon plus c -jet production. Except at low p_{\perp}^{γ} , we find a good agreement between the theoretical prediction and the CDF measurement.

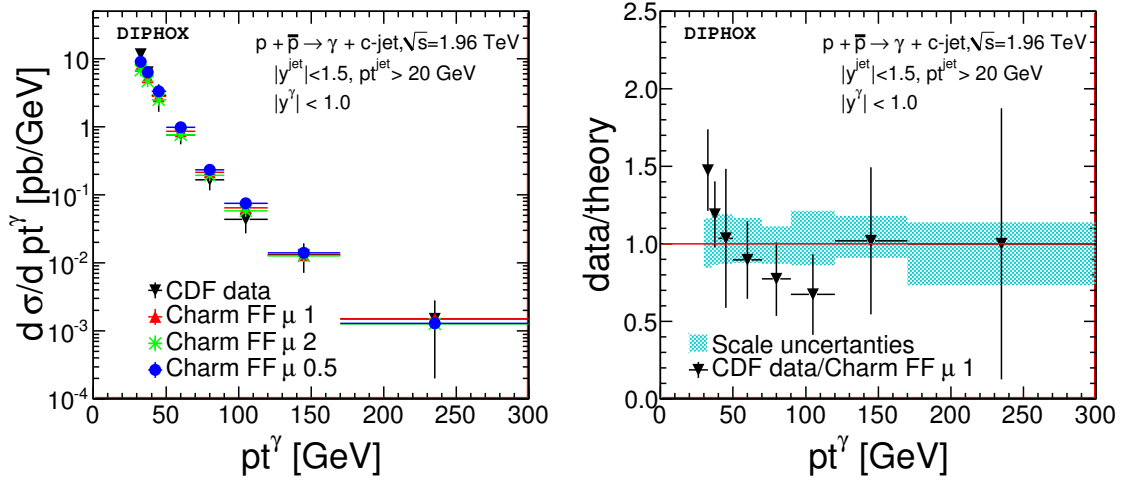


Figure 4.26: Comparison of photon spectrum using charm FF (DIPHOX) with CDF data measurement in $p\text{-}\bar{p}$ collisions at Tevatron at $\sqrt{s} = 1.96$ TeV. The data is taken from CDF Collaboration [9], see Table 4.4.

In short, by including the charm-meson fragmentation processes, we get the cross section which is comparable with data measurements at Tevatron, keeping in mind our assumptions. This results confirm our statement on the discrepancies between previous theoretical prediction NLO pQCD [117] and data: because of the missing of the charm(–meson) FF process, which plays an important role in the current measurements of $\gamma + c + X$ in $p\text{-}\bar{p}$ collisions at Tevatron at $\sqrt{s} = 1.96$ TeV.

Table 4.3: The $\gamma + c + X$ cross section in intervals of p_{\perp}^{γ} . Comparison between NLO pQCD using DIPHOX and data measurements from D0 Collaboration [8].

p_{\perp}^{γ} bins (GeV)	$d\sigma/dp_{\perp}^{\gamma}$ (pb/GeV)		$\delta(\%)$					
	Data: D0	NLO pQCD: charm-meson FF approach using DIPHOX						
		$\mu = 0.5$	$\mu = 1$	$\mu = 2$				
30–40	8.83	15	13.39	0.4	11.6	0.4	10.18	0.3
40–50	3.02	15	4.64	0.7	4.00	0.6	3.53	0.5
50–60	1.33	14	1.76	1.2	1.58	1	1.38	0.8
60–70	6.15×10^{-1}	14	8.04×10^{-1}	1.7	6.87×10^{-1}	1.5	6.25×10^{-1}	1.3
70–90	2.73×10^{-1}	14	2.99×10^{-1}	2	2.76×10^{-1}	1.6	2.47×10^{-1}	1.4
90–110	8.61×10^{-2}	17	1.1×10^{-1}	3.1	9.79×10^{-2}	2.7	8.85×10^{-2}	2.3
110–140	2.79×10^{-2}	19	4.07×10^{-2}	4.2	3.6×10^{-2}	3.7	3.24×10^{-2}	3.1
140–180	9.54×10^{-3}	26	8.11×10^{-3}	10.6	7.54×10^{-3}	8.7	8.07×10^{-3}	6.4
180–300	1.16×10^{-3}	43	1.35×10^{-3}	14.9	1.63×10^{-3}	9.5	1.42×10^{-3}	8.5

Table 4.4: The $\gamma + c + X$ cross section in intervals of p_{\perp}^{γ} . Comparison between NLO pQCD using DIPHOX and data measurements from CDF Collaboration [9].

p_{\perp}^{γ} bins (GeV)	$d\sigma/dp_{\perp}^{\gamma}$ (pb/GeV)		$\delta(\%)$					
	Data: CDF	NLO pQCD: charm-meson FF approach using DIPHOX						
		$\mu = 0.5$	$\mu = 1$	$\mu = 2$				
30–35	11.6	18	9.06	0.8	7.86	0.7	6.72	0.6
35–40	6.33	18	6.31	0.9	5.32	0.8	4.66	0.7
40–50	2.92	43	3.31	0.9	2.82	0.8	2.48	0.7
50–70	7.62×10^{-1}	28	9.78×10^{-1}	1.2	8.5×10^{-1}	1	7.56×10^{-1}	0.8
70–90	1.67×10^{-1}	30	2.33×10^{-1}	2.4	2.16×10^{-1}	1.9	1.93×10^{-1}	1.6
90–120	4.37×10^{-2}	38	7.55×10^{-2}	3.1	6.48×10^{-2}	2.8	5.79×10^{-2}	2.4
120–170	1.32×10^{-2}	46	1.41×10^{-2}	6.3	1.29×10^{-2}	5.3	1.26×10^{-2}	4.2
170–300	1.51×10^{-3}	86	1.3×10^{-3}	15	1.51×10^{-3}	9.8	1.27×10^{-3}	9.

4.2.4 A look on bottom quark's distribution inside the proton

The study of the process $\gamma + Q$ -jets production at hadron colliders give the chance for testing this aspect. We are interested, in this section, on how the present results is sensitive to bottom-PDFs. More precisely, we want to constrain the non-perturbative input for the b quark PDF. In order to do that, we have to have an evolution program for PDFs. In addition, this PDF is also correlated with the other PDFs and so the full study needs global fit analysis of proton data which is beyond the scope of this thesis. We will use two approaches the first one is to test different PDF sets and the second one is to put roughly the bottom PDF to zero.

For the first approach, we chose two different sets CTEQ6.6 and CT10. The bottom distribution⁷ in proton for those sets is plotted in Fig. 4.27. It shows us how the bottom

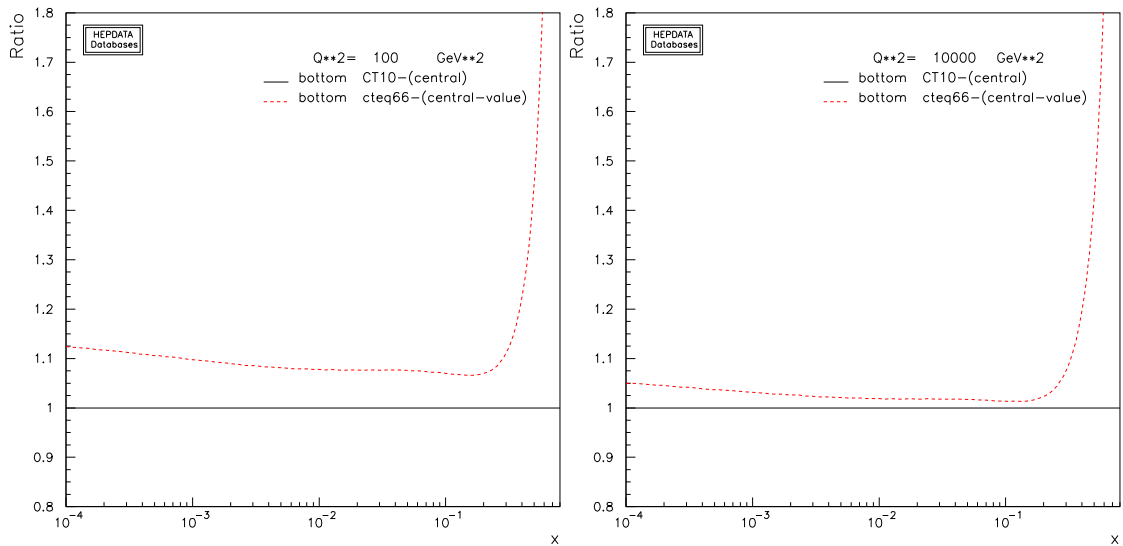


Figure 4.27: The bottom density comparison between CTEQ6.6 and CT10 at (left) $Q^2 = 100 \text{ GeV}^2$ and (right) $Q^2 = 10^4 \text{ GeV}^2$.

PDFs behave for different value of Q^2 . At the small energy scale, say $Q^2 = 100 \text{ GeV}^2$, the difference is found to be around 8–12% as $x \sim 10^{-1} - 10^{-4}$ and it is less than 5% at the large energy scale, say $Q^2 = 10^4 \text{ GeV}^2$.

Tevatron at 1.96 TeV: $p\bar{p} \rightarrow \gamma Qjet + X$

The following results, shown in Fig. 4.28, for the $\gamma + Q$ -jets production are calculated by using either CTEQ6.6 or CT10 set. The results are not sensitive to the considered PDF sets, see the top plots. Another investigation is made as well, it is putting to zero the bottom PDF in the calculation where CTEQ6.6 set is used. The results for this case is illustrated as the bottom plots in Fig. 4.28

7. <http://hepdata.cedar.ac.uk/pdf/pdf3.html>

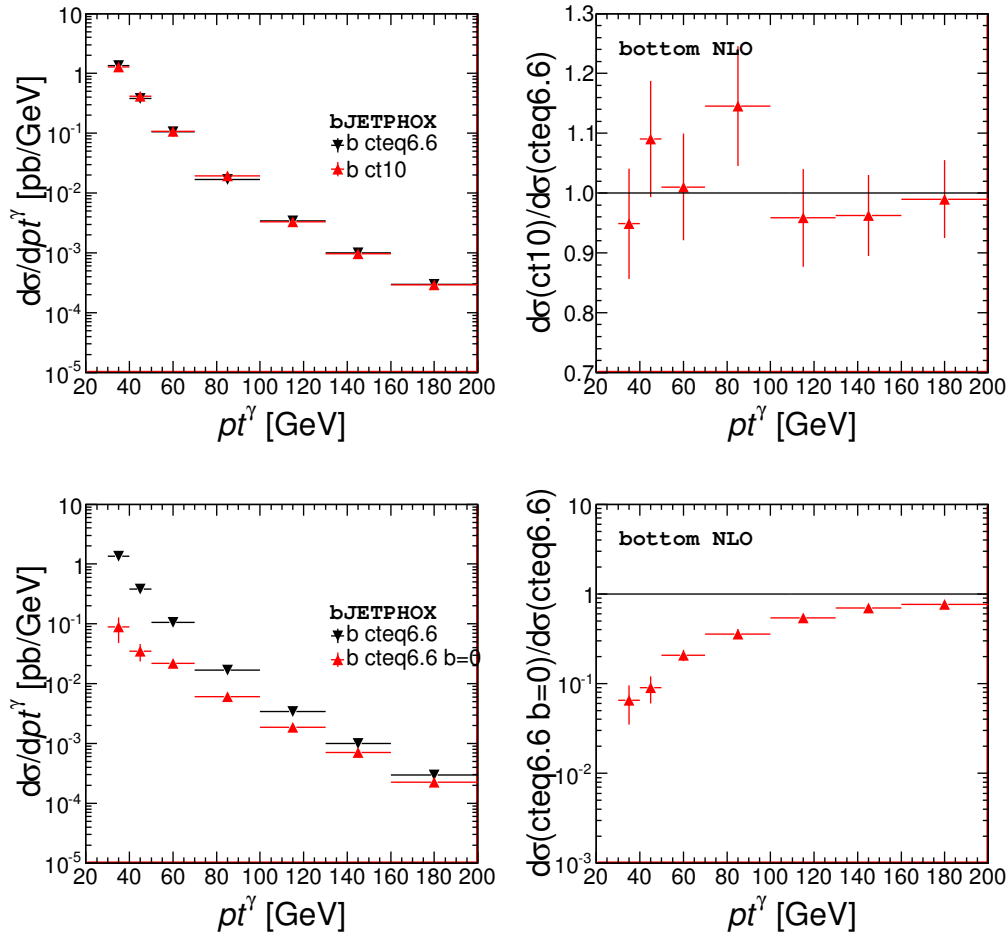


Figure 4.28: Top: Comparison between CTEQ6.6 and CT10. Bottom: Comparison between CTEQ6.6 with b 's PDF = 0 and "full" CTEQ6.6 (in $p\bar{p}$ collisions at $\sqrt{s} = 1.96$ TeV.)

One finds that, the cross section using a zero- b -PDF is much lower than the one with non-zero b -PDF by about one order of magnitude at $p_{\perp}^{\gamma} \sim 30 - 70$ GeV, by about 60% less at $p_{\perp}^{\gamma} \approx 80$ GeV and about 20% less at $p_{\perp}^{\gamma} \approx 180$ GeV. As the result of putting bottom density equal to zero, the subprocess $Qg \rightarrow Q\gamma g$ which is dominant at low p_{\perp}^{γ} vanishes. Thus, the strong effect of the suppression is taking place at low p_{\perp}^{γ} . However, at large p_{\perp}^{γ} , e.g. $\gtrsim 130$ GeV, the $q\bar{q}$ initial state is the dominant one (see Fig. 4.13) and therefore the dependence on heavy-quark PDF is no longer significant.

LHC at 14 TeV: $pp \rightarrow \gamma Q jet + X$

As in the case of $p\bar{p}$ collisions, the results depend very weakly on the use of either CTEQ6.6 set or CT10 in the $p\bar{p}$ collisions at $\sqrt{s} = 14$ TeV, i.e. Fig 4.29.⁸

For the second approach, as discussed in section 4.2.2, the dominant subprocess in

8. The analogous results are also obtained for $\sqrt{s} = 8$ TeV.

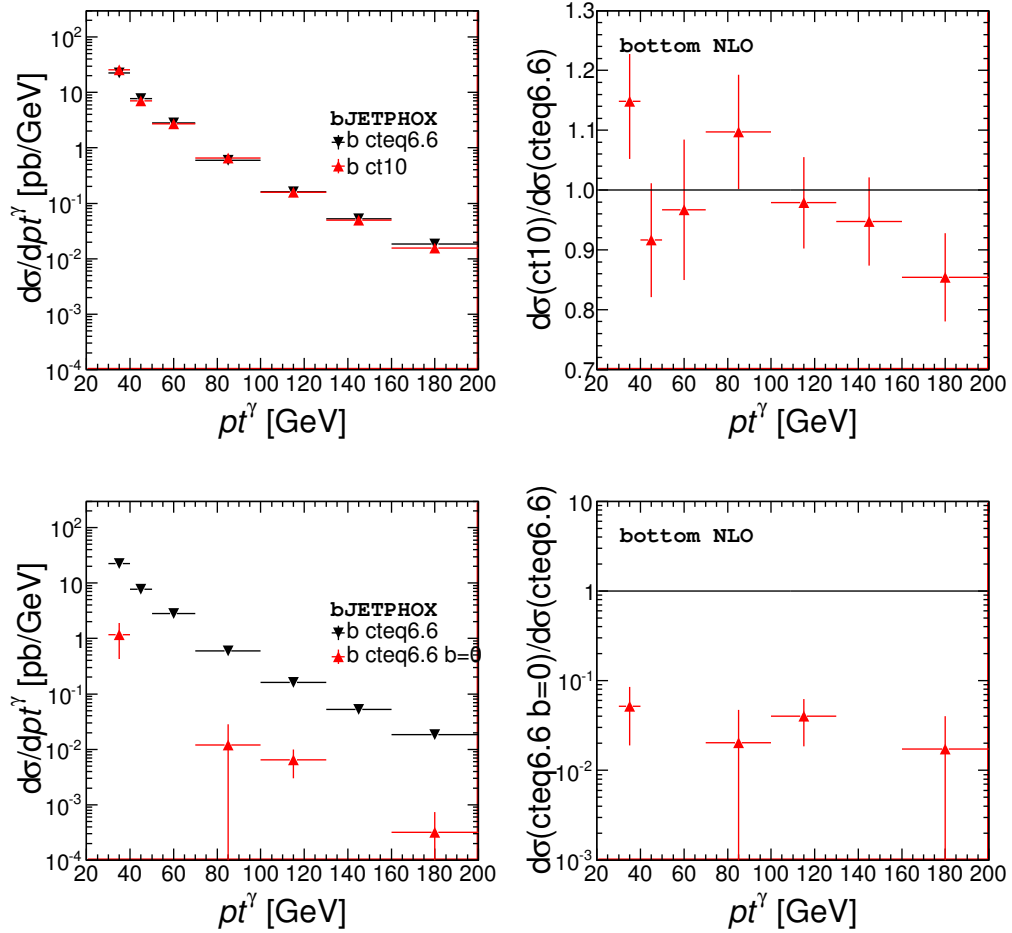


Figure 4.29: Top: Comparison between CTEQ6.6, CTEQ6.6 with b 's PDF =0, and CT10. Bottom: An example for direct subprocess contributions with bottom PDF equal zero (in pp collisions at $\sqrt{s} = 14$ TeV.)

this case is $Qg \rightarrow Q\gamma g$ for all p_{\perp}^{γ} and therefore the corresponding results strongly depend if the heavy-quark PDF is set to zero. Unfortunately, the behavior of the differential cross section with respect to p_{\perp}^{γ} , putting bottom PDF equal zero, is irregular. We want to emphasize that the fact of putting the bottom density equal to zero completely suppresses the $Qg \rightarrow Q\gamma g$ subprocess (see in Figs. 4.20) but does not affect much the other subprocesses such as $q\bar{q} \rightarrow Q\gamma\bar{Q}$ (see the left plots in Figs. 4.20)⁹ and leaves $gg \rightarrow Q\gamma\bar{Q}$ untouched. On the bottom plots of Fig. 4.29, for the histogram where the b -PDF is set to zero some bins do not show up because they are negative due to the fact that $gg \rightarrow Q\gamma\bar{Q}$ contributes negatively to the direct NLO calculation and has the highest magnitude in absolute value for almost every bins when p_{\perp}^{γ} ranges from 30–200 GeV. So the irregular effect on the NLO calculation for zero bottom PDF comes from this subprocess.

9. This result is consistent with the fact that the PDF of heavy-quark is much smaller than the PDF of light-quarks.

To discuss about the bad behavior of the $gg \rightarrow Q\gamma\bar{Q}$ for zero bottom PDF, let us come back to the analytic calculation which contains the collinear divergence when the heavy-quark is collinear to the initial gluon, i.e. diagram (a) in Figs 4.30.¹⁰ This singularity is factored into a redefined PDF of the heavy-quark. As the results, this configuration contributes like $Qg \rightarrow Q\gamma$ subprocess, and therefore it contributes for the LO distribution. For convenience let us call this subprocess is quasi $Qg \rightarrow Q\gamma$. The fact of the LO and quasi LO differential cross sections vanish leads to the non compensation among the collinear cuts (p_{Tm}) which were introduced in the procedure for subtracting this collinear divergence. This is the reason one gets the behavior for full NLO distribution when the bottom PDF is put to zero.

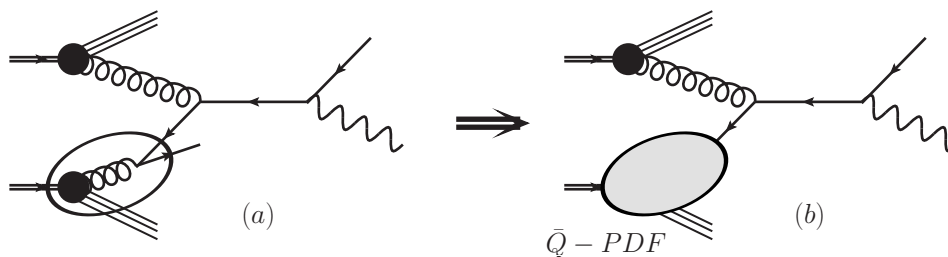


Figure 4.30: (a) An illustration for the heavy-quark collinear to initial gluon; (b) The collinear divergence part is factored out and is absorbed in the redefined PDF for heavy-quark.

In short, we want to emphasize that the two approaches used in this subsection are either too naive because we cannot set brutally the b-PDF to zero at NLO without having some troubles or too simplistic because we do not take into account the correlations between the b-PDF and the other PDFs. A full study would involve global fit analysis of proton data which is beyond the scope of this thesis. Despite these negative results, the process $\gamma + Q$ -jets at hadron colliders is worthwhile to study. It will bring, with other processes, information on the b content inside the proton.

10. This is the possible case for the diagram (b) in Fig. 4.5.

Chapter 5

Conclusion

In the previous two chapters, we have mainly discussed two aspects: the potential to set further constraints on FF sets, given the precise data at LHC ($\sqrt{s} = 8$ TeV), in chapter 3, and the production of photon plus heavy-quark jet in hadrons colliders at Tevatron and LHC in chapter 4.

The former study is based on the calculation of hadron plus jet cross section in p - p collisions at LHC at $\sqrt{s} = 8$ TeV. In completing the study, we have improved `JETPHOX` in order to have a suitable tool for performing this study: `HJETX`.

We find that the predictions using scales (renormalization and factorization) of the order of the transverse momentum of the hadron (p_{\perp}^h) are not stable, even the differential cross section becomes irregular at small momentum correlation z_h (z_3). As discussed in section 3.2.3, the reason is that this choice leads to large terms, $\sim \log(1/z)$, in the perturbative expansion. The suitable choice for this study is that some scales be of order of p_{\perp}^{jet} . Precisely, we choose for the renormalization, initial factorization, and final factorization scales, respectively, $\mu p_{\perp}^{\text{jet}}$, $\mu p_{\perp}^{\text{jet}}$, and $\mu R p_{\perp}^{\text{jet}}$, where R is the size of the jet and $\mu = 0.5, 1$, or 2 .

Using inclusive charged hadron FFs from various sets, i.e. AKK08, BFGW, DSS, HKNS, and Kretzer, the differential cross sections with respect to momentum correlation are compared. The results show that the predictions of AKK08/Kretzer sets at large z region differ from those of BFGW/HNKS/DSS and they are even out of the scale dependence band of DSS. Given the data at LHC allows to measure those observables precisely, further constraints on available FF sets can be set. The momentum correlation analyses are performed for both hadron plus same-side jet and hadron plus away-side jet productions. We also construct observables which can help discriminate between the FF sets. The results show that the same-side one offers tighter constraints on FFs than the away-side one. In addition, we find that the away-side study allows to disentangle between predictions using AKK08 and Kretzer. The identified hadrons, i.e. kaon and hadron, spectra inside jets even provide predictions using HKNS much higher from the DSS scale dependence band.

The latest study is based on the cross section of prompt photon production in association with heavy-quark jet in hadron collisions at Tevatron and LHC. Since the current version of JETPHOX did not allow to access to the flavor information of final partons in the partonic processes, we introduce and discuss a pick-up-process technique which is compatible with Monte Carlo simulation and apply it to improve JETPHOX into bJETPHOX.

Using the same b -jet definition which was used in previous calculations [117], we re-obtain successfully the result presented in the corresponding reference (see section 4.2.1). Besides, we give the comparison for those predictions using different assumptions on invariant mass cuts, i.e. m_Q^2 , $4m_Q^2$, and $8m_Q^2$. The results show that the predictions is not so sensitive on these invariant mass cuts.

We discuss also the calculation using flavor- kt algorithm [17] in section 4.2.2. We find that the photon spectrum of partonic process $gQ \rightarrow \gamma Qg$, in $p\text{-}\bar{p}$ collisions, is dominant at low $p_\perp^\gamma \lesssim 70$ GeV, while at larger p_\perp^γ the dominant one is $q\bar{q} \rightarrow \gamma Q\bar{Q}$ when using flavor- kt algorithm, this is the same behavior obtained by using the previous approach. Moreover, the flavor- kt strongly affects the contribution from $\gamma Q\bar{Q}$ production, this leads to the different predictions between two the approaches. This is not the case in $p\text{-}p$ collisions at LHC, where $gQ \rightarrow \gamma Qg$ is dominant for whole range of p_\perp^γ . The prediction using flavor- kt approach is new in studying prompt photon production in association with heavy-quark jet in hadron collisions either in theoretical calculation or experimental measurement. In order to compare between theory and data, this jet algorithm has to be used as well in the experimental measurements. In particular, the flavor of clusters are required to be known: heavy-flavor or heavy-flavorless.

The striking predictions come from using the charm-meson FF approach (as discussed in section 4.2.3). We perform the calculation of $\gamma + c + X$ by using DIPHOX, where the c can be produced in the partonic subprocess or can come from the fragmentation of a light parton. The ratio of the prediction using this approach to the one using the invariant mass approach behaves the same way, in shape and in magnitude, as the ratio of data to previous prediction using the invariant mass approach. This shows that the contribution from FF of partons into charm-meson is dominant at large p_\perp^γ , where the previous prediction is much lower than data [8, 9, 10, 11]. Our predictions for $\gamma + c + X$ production are compared to current precise measurements of D0 and CDF Collaborations using data at Tevatron at $\sqrt{s} = 1.96$ TeV [8, 9]. With the following assumptions: at low transverse momentum, the charm-mesons are carrying most of the momentum of the jet. A good agreement within the scale uncertainties is obtained. The predictions for $p\text{-}p$ collisions at LHC at $\sqrt{s} = 8$ TeV are performed.

We end this chapter with the outlook on the determination of the bottom non-perturbative input inside the proton. With a naive approach, setting the b PDF to zero, it shows that there is a problem. This suggests that the full study should be included into a PDF global fit analysis, which is out of the scope of the thesis. In general, given the b -jets are detected, the processes such as measurements of photon plus b -jet production will bring with other processes, a further knowledge on b PDF.

Appendix A

Analytical calculation

Contents

A.1	Invariant mass of two partons	132
A.2	The finite (factors) terms in parton differential cross section	134

A.1 Invariant mass of two partons

Let us consider the CMS of initial hadrons. In general, the 4-momenta of parton 1 and 2 are specified by

$$\begin{aligned} p_1 &= (E_1, |\mathbf{p}_1| \sin \theta_1 \cos \phi_1, |\mathbf{p}_1| \sin \theta_1 \sin \phi_1, |\mathbf{p}_1| \cos \theta_1) \\ p_2 &= (E_2, |\mathbf{p}_2| \sin \theta_2 \cos \phi_2, |\mathbf{p}_2| \sin \theta_2 \sin \phi_2, |\mathbf{p}_2| \cos \theta_2) \end{aligned} \quad (\text{A.1})$$

where E , $|\mathbf{p}|$, θ , and ϕ are the energy, length of 3-momentum, polar angle, and azimuthal angle of parton, respectively. In the massless limit, one has

$$\begin{aligned} p_1^2 &= E_1^2 - |\mathbf{p}_1|^2 = 0 \\ p_2^2 &= E_2^2 - |\mathbf{p}_2|^2 = 0 \end{aligned} \quad (\text{A.2})$$

Then the invariant mass of partons 1 and 2 can be estimated by

$$\begin{aligned} (p_1 + p_2)^2 &\approx 2 p_1 \cdot p_2 \\ &= 2(E_1 E_2 - \mathbf{p}_1 \cdot \mathbf{p}_2) \\ &= 2(E_1 E_2 - |\mathbf{p}_1| |\mathbf{p}_2| \cos \theta_{12}) \\ &= 2E_1 E_2 (1 - \cos \theta_{12}) \end{aligned} \quad (\text{A.3})$$

In p–p collision, instead of using θ , it is convenient to use the pseudo-rapidity, which transforms in an additive way under a boost along the beam direction and is defined as follows

$$\eta = -\frac{1}{2} \ln \left[\tan \left(\frac{\theta}{2} \right) \right] \quad (\text{A.4})$$

Using the formula

$$\tan \left(\frac{\theta}{2} \right) = \frac{1 - \cos \theta}{1 + \cos \theta} \quad (\text{A.5})$$

one can write the pseudo-rapidity in terms of momentum as follows

$$\eta = \frac{1}{2} \ln \left[\frac{|\mathbf{p}| + p_z}{|\mathbf{p}| - p_z} \right] \quad (\text{A.6})$$

where $p_z = |\mathbf{p}| \cos \theta$ is the longitudinal component of 4-momentum. From the Eq. (A.2), one sees that the pseudo-rapidity, for massless particle, is an approximation of the experimental rapidity

$$y = \frac{1}{2} \ln \left[\frac{E + p_z}{E - p_z} \right] \quad (\text{A.7})$$

where the particle can be parton 1 or 2.

From Eq. (A.4), (A.5), one has

$$e^{-2\eta} = \frac{1 - \cos \theta}{1 + \cos \theta} \quad (\text{A.8})$$

Then

$$\sin \theta = \frac{1}{\cosh \eta} \approx \frac{1}{\cosh y} \quad (\text{A.9a})$$

$$\text{and } \tan \theta = \sinh \eta \approx \sinh y \quad (\text{A.9b})$$

Thanks to Eqs. (A.2) and (A.9), one can write the 4-momentum which is given by Eq. A.1 in terms of "longitudinal invariant" parameters as follows

$$\begin{aligned} p_1 &= p_{\perp 1}(\cosh y_1, \cos \phi_1, \sin \phi_1, \sinh y_1) \\ p_2 &= p_{\perp 2}(\cosh y_2, \cos \phi_2, \sin \phi_2, \sinh y_2) \end{aligned} \quad (\text{A.10})$$

where $p_{\perp} = |\mathbf{p}| \sin \theta = E \sin \theta$ is the transverse momentum of the parton.

From Eq. A.10, the invariant mass of two partons can be, also, estimated by

$$\begin{aligned} (p_1 + p_2)^2 &\approx 2p_{\perp 1}p_{\perp 2} \\ &\times (\cosh y_1 \cosh y_2 - \cos \phi_1 \cos \phi_2 - \sin \phi_1 \sin \phi_2 - \sinh y_1 \sinh y_2) \quad (\text{A.11}) \\ &= 2p_{\perp 1}p_{\perp 2}(\cosh(y_1 - y_2) - \cos(\phi_1 - \phi_2)) \end{aligned}$$

Identifying Eqs. A.3 and A.11, one has

$$2E_1(1 - \cos \theta_{12}) = 2p_{\perp 1} \sin \theta_2 (\cosh(y_1 - y_2) - \cos(\phi_1 - \phi_2)) \quad (\text{A.12})$$

In the limit of $\theta_{12} \approx 0$ and therefore $\sin \theta_1 \approx \sin \theta_2$, the Eq. A.12 is equivalent to

$$\begin{aligned} E_1^2 \theta_{12}^2 &\approx p_{\perp 1} \sin \theta_1 E_1 ((y_1 - y_2)^2 + (\phi_1 - \phi_2)^2) \\ &\approx p_{\perp 1}^2 ((y_1 - y_2)^2 + (\phi_1 - \phi_2)^2) \end{aligned} \quad (\text{A.13})$$

where we use

$$\begin{aligned} \cos \theta &\approx 1 - \frac{\theta^2}{2}, \quad (\theta \ll 1), \\ \cosh y &\approx 1 + \frac{y^2}{2}, \quad (y \ll 1). \end{aligned} \quad (\text{A.14})$$

A.2 The finite (factors) terms in parton differential cross section

Conventionally, we denote N, n_f the number of colors, flavors. The QCD color factors are defined by

$$C_F = \frac{N^2 - 1}{2N} \quad (\text{A.15})$$

$$T_R = \frac{1}{2} \quad (\text{A.16})$$

The LO splitting functions are

$$P_{qq}(z) = C_F \left(\frac{1+z^2}{(1-z)_+} + \frac{3}{2} \delta(1-z) \right) \quad (\text{A.17})$$

$$P_{qg}(z) = T_R [z^2 + (1-z)^2] \quad (\text{A.18})$$

$$P_{gq}(z) = C_F \left[\frac{1+(1-z)^2}{z} \right] \quad (\text{A.19})$$

$$P_{gg}(z) = 2N \left(\frac{z}{(1-z)_+} + \frac{1-z}{z} + z(1-z) \right) + \delta(1-z) \left(\frac{11N - 2n_f}{6} \right) \quad (\text{A.20})$$

where the plus distribution is defined as

$$\int_0^1 dz \frac{f(z)}{(1-z)_+} = \int_0^1 dz \frac{f(z) - f(1)}{(1-z)} \quad (\text{A.21})$$

with $f(z)$ is a smooth function.

The finite factors obtained when computing the NLO corrections to DIS, section 1.2.3, are given by

$$\tilde{c}_{qq}(z) = \frac{4}{3} \left[(1+z^2) \left(\frac{\ln(1-z)}{1-z} \right)_+ - \frac{3}{2} \frac{1}{(1-z)_+} - \frac{1+z^2}{1-z} \ln z + 3 + 2z - \left(\frac{9}{2} + \frac{1}{3} \pi^2 \right) \delta(1-z) \right] \quad (\text{A.22})$$

$$\tilde{c}_{qg}(z) = (z^2 + (1-z)^2) \ln \frac{1-z}{z} + 6z(1-z) \quad (\text{A.23})$$

The gamma function defined by:

$$\Gamma(z) = \int_0^\infty dt t^{z-1} e^{-t} \quad (\text{A.24})$$

where z is different from a negative integer or 0.

The finite factor in parton differential cross section, section 1.3, is given by

$$K(\epsilon_{ir}) = \frac{\Gamma(1 - \epsilon_{ir}) \Gamma^2(1 + \epsilon_{ir})}{\Gamma(1 + 2 \epsilon_{ir})} \left(\frac{4\pi\mu^2}{M_F^2} \right)^{-\epsilon_{ir}} \quad (\text{A.25})$$

where $\Gamma(z)$, ϵ_{ir} , and μ are explained after Eq. (1.85) and M_F is an arbitrarily scale. It is clear that

$$K(\epsilon_{ir}) \xrightarrow{\epsilon_{ir} \rightarrow 0} 1 \quad (\text{A.26})$$

The finite terms obtained when computing the NLO corrections to the parton differential cross section, section 1.3, are

$$b_{qq}(z) = P_{qq}(z) \ln\left(\frac{q^2}{M_F^2}\right) + \left[2 \frac{1+z^2}{(1-z)_+} \ln(z) - \frac{3}{2} \frac{1}{(1-z)_+} + (1+z^2) \left(\frac{\ln(1-z)}{1-z} \right)_+ + \frac{5}{2} - \frac{3}{2} z + \delta(1-z) \left(\frac{2\pi^2}{3} - \frac{9}{2} \right) \right] \quad (\text{A.27})$$

and

$$b_{gq}(z) = P_{gq}(z) \ln\left(\frac{q^2}{M_F^2}\right) + P_{gq}(z) [\ln(1-z) + 2 \ln(z)] \quad (\text{A.28})$$

where $P_{qq}(z)$ and $P_{gq}(z)$ are given by Eqs. (A.17) and (A.19), respectively. Note that $b_{qq}(z)$, and $b_{gq}(z)$ are finite quantities when $z \rightarrow 0$.

Appendix B

Event analysis

Contents

B.1	List of chanel <code>j0</code>	138
B.2	Demo loading JETPHOX events with <code>read_tree.C</code>	140
B.3	HJETX: an upgrading from JETPHOX	144
B.3.1	Usage	144
B.3.2	Demo analyse HJETX events with <code>ahjetx</code> class	144
B.4	Demo analyse bJETPHOX events with <code>ajetphox</code> class	147

B.1 List of chanelns j0

Since the photon coupling is proportional to the electric charge of the quark, we have to distinguish up-type quark and down-type quark.

List of (D) (direct) contributions:

```

qi + qk -> jet + ph
1 : d + u -> jet + ph
2 : d + dp -> jet + ph
3 : u + up -> jet + ph
qi + qbk -> jet + ph
4 : d + ub -> jet + ph
5 : d + dpb -> jet + ph
6 : u + upb -> jet + ph
7 : qi + qi -> jet + ph
qi + qbi -> jet + ph
8 : d + db -> jet + ph
9 : u + ub -> jet + ph

10 : qi + g -> jet + ph
11 : g + g -> jet + ph

```

where u (up) is a up-type quark, d (dp) is a down-type quark, with $up \neq u$, $dp \neq d$. The jet is superposition of possible states, such as $|q\rangle$, $|g\rangle$, $|qq\rangle$, $|qg\rangle$

List of (F) (fragmentation) contributions:

```

1 : qi + qk -> jet + qk
2 : qi + qk -> jet + g
3 : qi + qbk -> jet + qbk
4 : qi + qbk -> jet + g
5 : qi + qi -> jet + qi
6 : qi + qi -> jet + g
7 : qi + qbi -> jet + qbk
8 : qi + qbi -> jet + qbi
9 : qi + qbi -> jet + g
10 : qi + g -> jet + qk
11 : qi + g -> jet + qbk
12 : qi + g -> jet + qbi
13 : qi + g -> jet + g
14 : qi + g -> jet + qi
15 : g + g -> jet + qi

```

16 : g + g -> jet + g

B.2 Demo loading JETPHOX events with read_tree.C

Assuming that the ntuple is written in the file `ggdtest_a.root`, after the run of a JETPHOX program, the following script loads the events from that ntuple, then constructs the variables $p_{\perp}^{h/\gamma}$, $y^{h/\gamma}$, x_1 , and x_2 . Event by event, the histograms corresponding to those variables are filled and then drawn.

`read_tree.C`:

```
{
#include "Riostream.h"

TFile *f = new TFile("ggdtest_a.root");
TTree *t2 = (TTree*)f->Get("t2");

t2->Print();

Int_t improv,ntrack;
Double_t e[3],px[3],py[3],pz[3];
Double_t x3;
Double_t pt[3],y[3];
Double_t x1,x2;
Float_t pdf_weight[1000];
Float_t weight;
// we get the value stored into the header for the normalisation
TList* list = t2->GetUserInfo();
list->Print();
TVectorT<float> &v = *(list->At(0));
float& nb_evt = v[0];
float& xsec = v[1];
float& sqrt_s = v[2];
float norma = xsec/nb_evt;

t2->SetBranchAddress("improv",&improv);
t2->SetBranchAddress("ntrack",&ntrack);
t2->SetBranchAddress("x3",&x3);
t2->SetBranchAddress("energy",e);
t2->SetBranchAddress("px",px);
t2->SetBranchAddress("py",py);
t2->SetBranchAddress("pz",pz);
t2->SetBranchAddress("pdf_weight",pdf_weight);

Int_t bin_pt = 40;
Int_t bin_y = 40;
```

```

Double_t pt_min = 30.;
Double_t pt_max = 200.;
Double_t y_min = -10.;
Double_t y_max = 10.;
Double_t bin_size_pt,bin_size_y;
bin_size_pt = (pt_max-pt_min)/(Double_t) bin_pt;
bin_size_y = (y_max-y_min)/(Double_t) bin_y;

TH1D *hpt = new TH1D("pt","essai",bin_pt,pt_min,pt_max);
TH1D *hy = new TH1D("y","essai",bin_y,y_min,y_max);
TH1F *hx1 = new TH1F("x1","essai",100,0.,1.);
TH1F *hx2 = new TH1F("x2","essai",100,0.,1.);
int nbin = 21;
float xbin[nbin];
float xmin = 1.e-8;
float xmax = 1.;
float temp;
int j;
for (j=0;j<nbin;j++) {
temp = log(xmin) + j*(log(xmax)-log(xmin))/float(nbin);
xbin[j] = exp(temp);
}
xbin[nbin] = xmax;
TH1F *hx1 = new TH1F("x1","essai",nbin-1,xbin);
TH1F *hx2 = new TH1F("x2","essai",nbin-1,xbin);

Int_t entries = (Int_t)t2->GetEntries();

for (Int_t i=0;i<entries;i++) {
t2->GetEntry(i);
// Pt and y are built, 0 is the photon, 1 is the hard parton and 2 is the
soft one
for (Int_t j=0;j<ntrack;j++) {
pt[j] = sqrt(px[j]*px[j]+py[j]*py[j]);
y[j] = log( (e[j]+pz[j])/(e[j]-pz[j]) ) * 0.5;
}
weight = pdf_weight[0];
// we build now x1 and x2
// for the 2 -> 3 case
if ( (iprover == 33) || (iprover == 44) )
x1 = (pt[0]/x3*exp(y[0])+pt[1]*exp(y[1])+pt[2]*exp(y[2]))/sqrt_s;
x2 = (pt[0]/x3*exp(-y[0])+pt[1]*exp(-y[1])+pt[2]*exp(-y[2]))/sqrt_s;

// for the other cases : 1 is the recoiling particle against the photon

```

```

else
x1 = pt[1]*(exp(y[0])+exp(y[1]))/sqrt_s;
x2 = pt[1]*(exp(-y[0])+exp(-y[1]))/sqrt_s;

hpt->Fill(pt[0],weight);
hy->Fill(y[0],weight);
hx1->Fill(x1,weight);
hx2->Fill(x2,weight);
}
// normalisation of the histograms
hpt->Scale(norma/bin_size_pt);
hy->Scale(norma/bin_size_y);
hy->Print();

TCanvas *c1 = new TCanvas("c1","Graph Draw Options",205,47,600,400);
c1->SetFillColor(0);

c1->Divide(2,2);
c1->cd(1);
gPad->SetLogy();
// pour eviter le titre
hy->SetTitle("");
// les titres des axes
hy->GetXaxis()->SetTitle("y");
hy->GetYaxis()->SetTitle("d #sigma/d y");

hy->Draw("AXIS");
hy->Draw("");
c1->cd(2);
gPad->SetLogy();
// pour eviter le titre
hpt->SetTitle("");
hpt->SetMaximum(200000);
hpt->SetMinimum(5.);
// les titres des axes
hpt->GetXaxis()->SetTitle("P_t #gamma");
hpt->GetYaxis()->SetTitle("d #sigma/d P_t #gamma");

hpt->Draw("AXIS");
hpt->Draw("");
c1->cd(3);
gPad->SetLogy();
// pour eviter le titre

```

```
hx1->SetTitle("");
// les titres des axes
hx1->GetXaxis()->SetTitle("x_2");
hx1->GetYaxis()->SetTitle("d #sigma/d x_2");

hx1->Draw("AXIS");
hx1->Draw("");
c1->cd(4);
gPad->SetLogy();
// pour eviter le titre
hx2->SetTitle("");
// les titres des axes
hx2->GetXaxis()->SetTitle("x_2");
hx2->GetYaxis()->SetTitle("d #sigma/d x_2");

hx2->Draw("AXIS");
hx2->Draw("");
}
```

End of demo scripts read_tree.C.

B.3 HJETX: an upgrading from JETPHOX

B.3.1 Usage

As discussed in chapter 3, we choose a scale of order of p_{\perp}^{jet} , which was not allowed by the current version of JETPHOX. Moreover, in this study, beside the away-side jet, we also construct the same-side jet which was not supported by JETPHOX. In order to perform the study, we modify JETPHOX into HJETX.

We emphasize the different properties between JETPHOX and HJETX as in the Table B.1.

Table B.1: The differences in using HJETX versus JETPHOX.

running option	HJETX	JETPHOX
production	jet+h/ γ	jet+h/ γ and inclusive h/ γ
jet	away-side or same-side with hadron	away-side with hadron
scale choice	order of p_{\perp}^{jet}	order of $p_{\perp}^{\text{h}/\gamma}$

B.3.2 Demo analyse HJETX events with ahjetx class

The following script creates the histograms for p_{\perp}^{h} and p_{\perp}^{jet} , and z_{h} distributions.
demo_analyse_hjetx.cxx:

```
#include "Riostream.h"
#include "TH1.h"
#include <math.h>
#include "ahjetx.h"

int main()
{
double cut_tot;
double ptjet3, ptjeth, pth;
double zjet3, zjeth, zx3;
double ptjet3_min, ptjet3_max, yjet3_min, yjet3_max;
double ptjeth_min, ptjeth_max, yjeth_min, yjeth_max;
double r_kt, r_c, r_sep;
char *algorithm, *merging, *acceptance, *file_ntuple;
// FILE which STORES NTUPLE (*)
file_ntuple = "ggobfgw_4e7_4ntmu1_hpt30t200y1_j4pt30.root";
// INPUT the OPTION FOR DEFINING JET (*)
r_kt = 0.5;
r_c = 0.7;
r_sep = 1.4;
```

```

merging = "ho";
acceptance = "gp";
algorithm = "kt";//use kt algorithm to define the jet.
// algorithm = "d0";//use mid point algorithm to define the jet.
// jet kinematic
ptjeth_min = 30.;
ptjeth_max = 4000.;
yjeth_min = -6.;
yjeth_max = 6.;
ptjet3_min = 0.;
ptjet3_max = 4000.;
yjet3_min = -6.;
yjet3_max = 6.;
// BOOK the HISTOGRAM (*)
int nbins_uqb_z = 9;
double z_bins[] = {0.1, 0.2, 0.3, 0.4, 0.5, 0.6, 0.7, 0.8, 0.9, 1.};
int nbins_uqb_ptj = 6;
double pth_bins[] = {15., 30., 40., 50., 70., 100., 190.};
int nbins_uqb_ptj = 7; double ptj_bins[] = {15., 30., 40., 50, 70, 100.,
140, 250.};
int numh = 5;
TH1D *h[numh];
h[0] = new TH1D("pt_hadron_uqb", "hjetx",nbins_uqb_ptj, pth_bins);
h[1] = new TH1D("pt_LLjet3_uqb", "hjetx",nbins_uqb_ptj, ptj_bins);
h[2] = new TH1D("pt_LLjeth_uqb", "hjetx",nbins_uqb_ptj, ptj_bins);
h[3] = new TH1D("zjet3_uqb", "hjetx",nbins_uqb_z, z_bins);
h[4] = new TH1D("zjeth_uqb", "hjetx",nbins_uqb_z, z_bins);
h[5] = new TH1D("zx3_uqb", "hjetx",nbins_uqb_z, z_bins);
// ACTIVATE the TOOL (hard code)
ahjetx *ajp = new ahjetx();
ajp->ajetalg(r_kt, r_c, r_sep, algorithm, merging, acceptance);
ajp->ajethcuts(ptjeth_min, ptjeth_max, yjeth_min, yjeth_max);
ajp->ajethcuts(ptjet3_min, ptjet3_max, yjet3_min, yjet3_max);
ajp->loadtree(file_ntuple);
ajp->aprintjet();
double norma = ajp->norma;

for (Int_t i=0;i<ajp->entries;i++) {
    // ANALYSIS (hard code)
    ajp->getentry(i);
    ajp->printtrack();
    ajp->analyse();
    // Take out the cut_flag
    bool cut_jet3 = ajp->cut_jet3;

```

```
bool cut_jeth = ajp->cut_jet_45;
cut_tot = cut_jet3&&cut_jeth;
double weight = ajp->weight;
// CONSTRUCT the OBSERVABLE (*)
ajp->azjet();
ptjet3 = ajp->ptjet3;//pt of jet which goes against photon
ptjeth = ajp->ptjeth;//pt of jet besiding photon
zjet3 = ajp->zjet3;//jet goes against photon
zjeth = ajp->zjeth;//jet besides photon
pth = ajp->pt[0]);// pt of hadron
// FILL the HISTOGRAM (*)
if (cut_tot) {
    h[0]->Fill(pth,weight);
    h[1]->Fill(ptjet3,weight);
    h[2]->Fill(ptjeth,weight);
    h[3]->Fill(zjet3,weight);
    h[4]->Fill(zjeth,weight);
}
}
// BUILD the DISTRIBUTION (*)
for (int k=0;k<numh;k++) h[k]->Scale(norma,"width");
// WRITE the HISTOGRAM TO FILE (*)
TFile fwrite("demo_histo_hjetx.root","recreate");
for (int k=0;k<numh;k++) h[k]->Write();
fwrite.Close();
return 0;
}
```

End of demo scripts demo_analyse_hjetx.cxx.

B.4 Demo analyse бJETPHOX events with ajetphox class

We want to emphasize that if one does not specify the flavor of the jet, бJETPHOX plays the same role as JETPHOX.

The following script creates the histograms for p_{\perp}^{jet} and p_{\perp}^{bjet} distributions, respectively, the transverse momentum of a flavorless jet and a b-jet.

demo_analyse.cxx:

```
#include "Riostream.h"
#include "TH1.h"
#include <math.h>
#include "ajetphox.h"

int main()
{
double ptjet, ptjetsubl, pth;
double ptjet3_min, ptjet3_max, yjet3_min, yjet3_max;
double r_kt, r_c, r_sep;
char *algorithm, *merging, *acceptance, *file_ntuple;
// FILE which STORES NTUPLE (*)
file_ntuple =
"../../lhc8/ggdbfg02_lhc8_4e6_4mu1_isl_gpt30t200y1.root";
// INPUT the OPTION FOR DEFINING JET (*)
r_kt = 0.5;
r_c = 0.7;
r_sep = 1.4;
merging = "ho";
acceptance = "gp";
// algorithm = "kt";//use kt algorithm to define the jet
// default: Q is bottom or anti-bottom.
// algorithm = "kt_Ccfl";// use flavour-kt to define c-quark jet
algorithm = "kt_Bbfl";// use flavour-kt to define b-quark jet
// jet kinematic
ptjet3_min = 15.;
ptjet3_max = 7000.;
yjet3_min = -.8;
yjet3_max = .8;
// BOOK the HISTOGRAM (*)
int nbins_uqb_ptj = 7;
double ptj_bins[] = {15., 20.,35., 50, 70, 100., 140, 250.};
int numh = 2;
TH1D *h[numh];
h[0] = new TH1D("pt_LLjet_uqb", "bjetphox",nbins_uqb_ptj, ptj_bins);
```

```

h[1] = new TH1D("pt_Qjet_uqb", "bjetphox",nbins_uqb_ptj, ptj_bins);
// ACTIVATE the TOOL (hard code)
ajetphox *ajp = new ajetphox();
ajp->ajetalg(r_kt, r_c, r_sep, algorithm, merging, acceptance);
ajp->ajetcuts(ptjet3_min, ptjet3_max, yjet3_min, yjet3_max);
ajp->loadtree(file_ntuple);
ajp->aprintjet();
double norma = ajp->norma;

for (Int_t i=0;i<ajp->entries;i++) {
    // ANALYSIS (hard code)
    ajp->getentry(i);
    ajp->printtrack();
    ajp->analyse();
    // Take out the cut_flag
    bool cut_jet = ajp->cut_jet[0];
    bool cut_jetsubl = ajp->cut_jet[1];
    bool Qh_flavour = ajp->Qh_flavour;// support LL Qjet (bar Q)
    bool Ql_flavour = ajp->Ql_flavour;// be false whenever LL is Q (or
bar Q)
    bool Qlp_flavour = ajp->Qlp_flavour;// not depend on LL jet.
    double weight = ajp->weight;
    // CONSTRUCT the OBSERVABLE (*)
    ptjet = ajp->ptj[0];//pt of jet which goes against photon
    ptjetsubl = ajp->ptj[1];//pt of sub LL jet
    pth = ajp->pt[0];// pt of hadron/photon
    // FILL the HISTOGRAM (*)
    if (cut_jet) {
        h[0]->Fill(ptjet,weight);
        if (Qh_flavour) {
            h[1]->Fill(ptjet,weight);
        }
    }
    if (cut_jetsubl) {
        if (Ql_flavour) {
            h[1]->Fill(ptjetsubl,weight);
        }
    }
}
ajp->aend();// (hard code)
// BUILD the DISTRIBUTION (*)
for (int k=0;k<numh;k++) h[k]->Scale(norma,"width");
// WRITE the HISTOGRAM TO FILE (*)
TFile fwrite("demo_histo.root","recreate");

```

```
for (int k=0;k<numh;k++) h[k]->Write();  
fwrite.Close();  
return 0;  
}
```

End of demo scripts demo_analyse.cxx.

Bibliography

- [1] P. Aurenche, R. Baier, M. Fontannaz, and D. Schiff, *Prompt Photon Production at Large $p(T)$ Scheme Invariant QCD Predictions and Comparison with Experiment*, *Nucl.Phys.* **B297** (1988) 661.
- [2] P. Aurenche, R. Baier, M. Fontannaz, J. Owens, and M. Werlen, *The Gluon Contents of the Nucleon Probed with Real and Virtual Photons*, *Phys.Rev.* **D39** (1989) 3275.
- [3] **CMS Collaboration** Collaboration, S. Chatrchyan et al., *Measurement of the Differential Cross Section for Isolated Prompt Photon Production in pp Collisions at 7 TeV*, *Phys.Rev.* **D84** (2011) 052011, [[arXiv:1108.2044](#)].
- [4] **ATLAS Collaboration** Collaboration, G. Aad et al., *Measurement of the inclusive isolated prompt photon cross-section in pp collisions at $\sqrt{s} = 7$ TeV using 35 pb^{-1} of ATLAS data*, *Phys.Lett.* **B706** (2011) 150–167, [[arXiv:1108.0253](#)].
- [5] **ATLAS Collaboration** Collaboration, G. Aad et al., *Measurement of the inclusive isolated prompt photon cross section in pp collisions at $\sqrt{s} = 7$ TeV with the ATLAS detector using 4.6 fb^{-1}* , [arXiv:1311.1440](#).
- [6] **ATLAS Collaboration** Collaboration, G. Aad et al., *Measurement of the production cross section of an isolated photon associated with jets in proton-proton collisions at $\sqrt{s} = 7$ TeV with the ATLAS detector*, *Phys.Rev.* **D85** (2012) 092014, [[arXiv:1203.3161](#)].
- [7] **CMS Collaboration** Collaboration, S. Chatrchyan et al., *Measurement of the triple-differential cross section for photon+jets production in proton-proton collisions at $\sqrt{s}=7$ TeV*, [arXiv:1311.6141](#).
- [8] **D0 Collaboration** Collaboration, V. M. Abazov et al., *Measurement of the differential photon + c -jet cross section and the ratio of differential photon+ c and photon+ b cross sections in proton-antiproton collisions at $\sqrt{s} = 1.96$ TeV*, *Phys.Lett.* **B719** (2013) 354–361, [[arXiv:1210.5033](#)].
- [9] **CDF Collaboration** Collaboration, T. Aaltonen et al., *Measurement of the cross section for direct-photon production in association with a heavy quark in $p\bar{p}$*

- collisions at $\sqrt{s} = 1.96$ TeV*, *Phys.Rev.Lett.* **111** (2013) 042003, [arXiv:1303.6136].
- [10] **D0 Collaboration** Collaboration, V. Abazov et al., *Measurement of gamma + b + X and gamma + c + X production cross sections in p anti-p collisions at $s^{*(1/2)} = 1.96$ -TeV*, *Phys.Rev.Lett.* **102** (2009) 192002, [arXiv:0901.0739].
- [11] **CDF Collaboration** Collaboration, T. Aaltonen et al., *A Study of the associated production of photons and b-quark jets in p p-bar collisions at $s^{*(1/2)} = 1.96$ -TeV*, *Phys.Rev.* **D81** (2010) 052006, [arXiv:0912.3453].
- [12] **CDF Collaboration** Collaboration, A. Abulencia et al., *Measurement of the Inclusive Jet Cross Section using the k_T algorithm in $p\bar{p}$ Collisions at $\sqrt{s} = 1.96$ TeV with the CDF II Detector*, *Phys.Rev.* **D75** (2007) 092006, [hep-ex/0701051].
- [13] **CMS Collaboration** Collaboration, S. Chatrchyan et al., *Measurement of the differential dijet production cross section in proton-proton collisions at $\sqrt{s} = 7$ TeV*, *Phys.Lett.* **B700** (2011) 187–206, [arXiv:1104.1693].
- [14] **ATLAS Collaboration** Collaboration, *Measurement of inclusive jet and dijet cross sections in proton-proton collision data at 7 TeV centre-of-mass energy using the ATLAS detector*, .
- [15] T. Binoth, J.-P. Guillet, E. Pilon, and M. Werlen, *A Full next-to-leading order study of direct photon pair production in hadronic collisions*, *Eur.Phys.J.* **C16** (2000) 311–330, [hep-ph/9911340].
- [16] S. Catani, Y. L. Dokshitzer, M. Olsson, G. Turnock, and B. Webber, *New clustering algorithm for multi - jet cross-sections in e+ e- annihilation*, *Phys.Lett.* **B269** (1991) 432–438.
- [17] A. Banfi, G. P. Salam, and G. Zanderighi, *Infrared safe definition of jet flavor*, *Eur.Phys.J.* **C47** (2006) 113–124, [hep-ph/0601139].
- [18] F. Arleo, M. Fontannaz, J.-P. Guillet, and C. L. Nguyen, *Probing fragmentation functions from same-side hadron-jet momentum correlations in p-p collisions*, arXiv:1311.7356.
- [19] **Particle Data Group** Collaboration, J. Beringer et al., *Review of Particle Physics (RPP)*, *Phys.Rev.* **D86** (2012) 010001.
- [20] S. Bethke, *World Summary of α_s (2012)*, *Nucl.Phys.Proc.Suppl.* **234** (2013) 229–234, [arXiv:1210.0325].

- [21] S. Bethke, *Experimental tests of asymptotic freedom*, *Prog.Part.Nucl.Phys.* **58** (2007) 351–386, [hep-ex/0606035].
- [22] F. Halzen and A. Martin, *QUARK & LEPTONS: AN INTRODUCTORY COURSE IN MODERN PARTICLE PHYSICS*. Wiley India Pvt. Limited, 2008.
- [23] G. Altarelli, R. K. Ellis, G. Martinelli, and S.-Y. Pi, *Processes Involving Fragmentation Functions Beyond the Leading Order in QCD*, *Nucl.Phys.* **B160** (1979) 301.
- [24] G. Altarelli, R. K. Ellis, and G. Martinelli, *Large Perturbative Corrections to the Drell-Yan Process in QCD*, *Nucl.Phys.* **B157** (1979) 461.
- [25] J.-P. Guillet, *Habilitation à diriger des recherches, Universite de Provence (Aix-Marseille I), 1991, .*
- [26] G. Altarelli and G. Parisi, *Asymptotic Freedom in Parton Language*, *Nucl.Phys.* **B126** (1977) 298.
- [27] W. Furmanski and R. Petronzio, *Singlet Parton Densities Beyond Leading Order*, *Phys.Lett.* **B97** (1980) 437.
- [28] G. Curci, W. Furmanski, and R. Petronzio, *Evolution of Parton Densities Beyond Leading Order: The Nonsinglet Case*, *Nucl.Phys.* **B175** (1980) 27.
- [29] A. Martin, W. Stirling, R. Thorne, and G. Watt, *Parton distributions for the LHC*, *Eur.Phys.J.* **C63** (2009) 189–285, [arXiv:0901.0002].
- [30] D. Duke and J. Owens, *Q^{*2} Dependent Parametrizations of Parton Distribution Functions*, *Phys.Rev.* **D30** (1984) 49–54.
- [31] H. Abramowicz, J. de Groot, J. Knobloch, J. May, P. Palazzi, et al., *Neutrino and anti-neutrinos Charged Current Inclusive Scattering in Iron in the Energy Range $20\text{-GeV} < \text{Neutrino Energy} < 300\text{-GeV}$* , *Z.Phys.* **C17** (1983) 283.
- [32] **European Muon Collaboration** Collaboration, J. Aubert et al., *Measurement of the proton structure function F_2 in muon - hydrogen interactions at 120-GeV and 280-GeV*, *Phys.Lett.* **B105** (1981) 315.
- [33] A. Bodek, M. Breidenbach, D. Dubin, J. Elias, J. I. Friedman, et al., *Experimental Studies of the Neutron and Proton Electromagnetic Structure Functions*, *Phys.Rev.* **D20** (1979) 1471–1552.
- [34] A. Ito, R. Fisk, H. Jostlein, D. Kaplan, S. Herb, et al., *Measurement of the Continuum of Dimuons Produced in High-Energy Proton - Nucleus Collisions*, *Phys.Rev.* **D23** (1981) 604.

- [35] J. Branson, G. Sanders, A. Smith, J. Thaler, K. Anderson, et al., *Production of the J/ψ and ψ -prime (3.7) by $225\text{-GeV}/c$ π^+ - and Proton Beams on C and SN Targets.*, *Phys.Rev.Lett.* **38** (1977) 1331–1334.
- [36] A. D. Martin, R. Roberts, and W. J. Stirling, *Structure Function Analysis and ψ , Jet, W, Z Production: Pinning Down the Gluon*, *Phys.Rev.* **D37** (1988) 1161.
- [37] **CTEQ Collaboration** Collaboration, H. Lai et al., *Global QCD analysis of parton structure of the nucleon: CTEQ5 parton distributions*, *Eur.Phys.J.* **C12** (2000) 375–392, [hep-ph/9903282].
- [38] **H1 Collaboration** Collaboration, C. Adloff et al., *A Measurement of the proton structure function $f_2(x, q^2)$ at low x and low q^2 at HERA*, *Nucl.Phys.* **B497** (1997) 3–30, [hep-ex/9703012].
- [39] **ZEUS Collaboration** Collaboration, M. Derrick et al., *Measurement of the proton structure function F_2 at low x and low q^2 at HERA*, *Z.Phys.* **C69** (1996) 607–620, [hep-ex/9510009].
- [40] A. D. Martin, R. Roberts, W. Stirling, and R. Thorne, *MRST2001: Partons and α_s from precise deep inelastic scattering and Tevatron jet data*, *Eur.Phys.J.* **C23** (2002) 73–87, [hep-ph/0110215].
- [41] **H1 Collaboration** Collaboration, C. Adloff et al., *Deep inelastic inclusive $e p$ scattering at low x and a determination of $\alpha(s)$* , *Eur.Phys.J.* **C21** (2001) 33–61, [hep-ex/0012053].
- [42] **ZEUS Collaboration** Collaboration, S. Chekanov et al., *Measurement of the neutral current cross-section and F_2 structure function for deep inelastic $e + p$ scattering at HERA*, *Eur.Phys.J.* **C21** (2001) 443–471, [hep-ex/0105090].
- [43] **D0 Collaboration** Collaboration, B. Abbott et al., *The inclusive jet cross section in $\bar{p}p$ collisions at $\sqrt{s} = 1.8\text{ TeV}$* , *Phys.Rev.Lett.* **82** (1999) 2451–2456, [hep-ex/9807018].
- [44] **CDF Collaboration** Collaboration, F. Abe et al., *Measurement of the lepton charge asymmetry in W boson decays produced in $\bar{p}p$ collisions*, *Phys.Rev.Lett.* **81** (1998) 5754–5759, [hep-ex/9809001].
- [45] **D0 Collaboration** Collaboration, B. Abbott et al., *Inclusive jet production in $\bar{p}p$ collisions*, *Phys.Rev.Lett.* **86** (2001) 1707–1712, [hep-ex/0011036].
- [46] **CDF Collaboration** Collaboration, T. Affolder et al., *Measurement of the inclusive jet cross section in $\bar{p}p$ collisions at $\sqrt{s} = 1.8\text{ TeV}$* , *Phys.Rev.* **D64** (2001) 032001, [hep-ph/0102074].

- [47] **LHAPDF** the Les Houches Accord PDF Interface, “<https://lhpdf.hepforge.org/>.”
- [48] P. M. Nadolsky, H.-L. Lai, Q.-H. Cao, J. Huston, J. Pumplin, et al., *Implications of CTEQ global analysis for collider observables*, *Phys.Rev.* **D78** (2008) 013004, [arXiv:0802.0007].
- [49] H.-L. Lai, M. Guzzi, J. Huston, Z. Li, P. M. Nadolsky, et al., *New parton distributions for collider physics*, *Phys.Rev.* **D82** (2010) 074024, [arXiv:1007.2241].
- [50] R. D. Ball, L. Del Debbio, S. Forte, A. Guffanti, J. I. Latorre, et al., *A first unbiased global NLO determination of parton distributions and their uncertainties*, *Nucl.Phys.* **B838** (2010) 136–206, [arXiv:1002.4407].
- [51] E. Perez and E. Rizvi, *The Quark and Gluon Structure of the Proton*, *Rep.Prog.Phys.* **76** (2013) 046201, [arXiv:1208.1178].
- [52] S. Forte and G. Watt, *Progress in the Determination of the Partonic Structure of the Proton*, *Ann.Rev.Nucl.Part.Sci.* **63** (2013) 291–328, [arXiv:1301.6754].
- [53] R. D. Ball, V. Bertone, F. Cerutti, L. Del Debbio, S. Forte, et al., *Impact of Heavy Quark Masses on Parton Distributions and LHC Phenomenology*, *Nucl.Phys.* **B849** (2011) 296–363, [arXiv:1101.1300].
- [54] P. Duinker, *Review of Electron - Positron Physics at PETRA*, *Rev.Mod.Phys.* **54** (1982) 325.
- [55] R. Field, *Applications of perturbative QCD*. Frontiers in physics. Addison-Wesley, The Advanced Book Program, 1989.
- [56] **ALEPH Collaboration** Collaboration, D. Buskulic et al., *Measurement of alpha-s from scaling violations in fragmentation functions in e+ e- annihilation*, *Phys.Lett.* **B357** (1995) 487–499. Erratum-ibid. B364:247-248, 1995.
- [57] L. Bourhis, M. Fontannaz, J.-P. Guillet, and M. Werlen, *Next-to-leading order determination of fragmentation functions*, *Eur.Phys.J.* **C19** (2001) 89–98, [hep-ph/0009101].
- [58] **OPAL Collaboration** Collaboration, K. Ackerstaff et al., *Measurements of flavor dependent fragmentation functions in Z0 ->q anti-q events*, *Eur.Phys.J.* **C7** (1999) 369–381, [hep-ex/9807004].
- [59] **SLD Collaboration** Collaboration, K. Abe et al., *Production of pi+, K+, K0, K*0, phi, p and Lambda0 in hadronic Z0 decays*, *Phys.Rev.* **D59** (1999) 052001, [hep-ex/9805029].

- [60] S. Kretzer, *Fragmentation functions from flavor inclusive and flavor tagged e^+e^- annihilations*, *Phys.Rev.* **D62** (2000) 054001, [hep-ph/0003177].
- [61] B. A. Kniehl, G. Kramer, and B. Potter, *Fragmentation functions for pions, kaons, and protons at next-to-leading order*, *Nucl.Phys.* **B582** (2000) 514–536, [hep-ph/0010289].
- [62] S. Abachi, M. Derrick, P. Kooijman, B. Musgrave, L. Price, et al., *Study of Vector Meson Production in e^+e^- Annihilation at $\sqrt{s} = 29\text{-GeV}$* , *Phys.Rev.* **D40** (1989) 706.
- [63] **ALEPH Collaboration** Collaboration, D. Buskulic et al., *Inclusive production of neutral vector mesons in hadronic Z decays*, *Z.Phys.* **C69** (1996) 379–392.
- [64] L. Bourhis, M. Fontannaz, and J.-P. Guillet, *Quarks and gluon fragmentation functions into photons*, *Eur.Phys.J.* **C2** (1998) 529–537, [hep-ph/9704447].
- [65] S. Albino, B. Kniehl, and G. Kramer, *Fragmentation functions for light charged hadrons with complete quark flavor separation*, *Nucl.Phys.* **B725** (2005) 181–206, [hep-ph/0502188].
- [66] **OPAL Collaboration** Collaboration, G. Abbiendi et al., *Leading particle production in light flavor jets*, *Eur.Phys.J.* **C16** (2000) 407–421, [hep-ex/0001054].
- [67] B. A. Kniehl, G. Kramer, and B. Potter, *Testing the universality of fragmentation functions*, *Nucl.Phys.* **B597** (2001) 337–369, [hep-ph/0011155].
- [68] **H1 Collaboration** Collaboration, C. Adloff et al., *Evolution of $e p$ fragmentation and multiplicity distributions in the Breit frame*, *Nucl.Phys.* **B504** (1997) 3–23, [hep-ex/9707005].
- [69] **ZEUS Collaboration** Collaboration, M. Derrick et al., *Inclusive charged particle distributions in deep inelastic scattering events at HERA*, *Z.Phys.* **C70** (1996) 1–16, [hep-ex/9511010].
- [70] **ZEUS Collaboration** Collaboration, J. Breitweg et al., *Observation of scaling violations in scaled momentum distributions at HERA*, *Phys.Lett.* **B414** (1997) 428–443, [hep-ex/9710011].
- [71] S. Albino, B. Kniehl, G. Kramer, and C. Sandoval, *Confronting fragmentation function universality with single hadron inclusive production at HERA and e^+e^- colliders*, *Phys.Rev.* **D75** (2007) 034018, [hep-ph/0611029].
- [72] **H1 Collaboration** Collaboration, F. Aaron et al., *Charged Particle Production in High Q^2 Deep-Inelastic Scattering at HERA*, *Phys.Lett.* **B654** (2007) 148–159, [arXiv:0706.2456].

- [73] M. Hirai, S. Kumano, T.-H. Nagai, and K. Sudoh, *Determination of fragmentation functions and their uncertainties*, *Phys.Rev.* **D75** (2007) 094009, [hep-ph/0702250].
- [74] **BaBar Collaboration** Collaboration, B. Aubert et al., *Measurement of D_s^+ and D_s^{*+} production in B meson decays and from continuum e^+e^- annihilation at $\sqrt{s} = 10.6$ GeV*, *Phys.Rev.* **D65** (2002) 091104, [hep-ex/0201041].
- [75] **CLEO Collaboration** Collaboration, M. Artuso et al., *Charm meson spectra in e^+e^- annihilation at 10.5-GeV c.m.e.*, *Phys.Rev.* **D70** (2004) 112001, [hep-ex/0402040].
- [76] **Belle Collaboration** Collaboration, R. Seuster et al., *Charm hadrons from fragmentation and B decays in e^+e^- annihilation at $s^{*(1/2)} = 10.6$ -GeV*, *Phys.Rev.* **D73** (2006) 032002, [hep-ex/0506068].
- [77] **ALEPH Collaboration** Collaboration, R. Barate et al., *Study of charm production in Z decays*, *Eur.Phys.J.* **C16** (2000) 597–611, [hep-ex/9909032].
- [78] M. Cacciari, P. Nason, and C. Oleari, *A Study of heavy flavored meson fragmentation functions in e^+e^- annihilation*, *JHEP* **0604** (2006) 006, [hep-ph/0510032].
- [79] T. Kneesch, B. Kniehl, G. Kramer, and I. Schienbein, *Charmed-meson fragmentation functions with finite-mass corrections*, *Nucl.Phys.* **B799** (2008) 34–59, [arXiv:0712.0481].
- [80] **OPAL Collaboration** Collaboration, K. Ackerstaff et al., *Measurement of $f(c \rightarrow D^{*+} X)$, $f(b \rightarrow D^{*+} X)$ and $\Gamma(c \text{ anti-}c) / \Gamma(\text{hadronic})$ using D^{*+} -mesons*, *Eur.Phys.J.* **C1** (1998) 439–459, [hep-ex/9708021].
- [81] **PHENIX Collaboration** Collaboration, S. Adler et al., *Mid-rapidity neutral pion production in proton proton collisions at $\sqrt{s} = 200$ -GeV*, *Phys.Rev.Lett.* **91** (2003) 241803, [hep-ex/0304038].
- [82] **STAR Collaboration** Collaboration, B. Abelev et al., *Strange particle production in $p+p$ collisions at $s^{*(1/2)} = 200$ -GeV*, *Phys.Rev.* **C75** (2007) 064901, [nucl-ex/0607033].
- [83] **BRAHMS Collaboration** Collaboration, I. Arsene et al., *Production of mesons and baryons at high rapidity and high $P(T)$ in proton-proton collisions at $s^{*(1/2)} = 200$ -GeV*, *Phys.Rev.Lett.* **98** (2007) 252001, [hep-ex/0701041].
- [84] **CDF Collaboration** Collaboration, D. Acosta et al., *K_S^0 and Λ^0 production studies in $p\bar{p}$ collisions at $\sqrt{s} = 1800$ -GeV and 630-GeV*, *Phys.Rev.* **D72** (2005) 052001, [hep-ex/0504048].

- [85] D. de Florian, R. Sassot, and M. Stratmann, *Global analysis of fragmentation functions for protons and charged hadrons*, *Phys.Rev.* **D76** (2007) 074033, [arXiv:0707.1506].
- [86] D. de Florian, R. Sassot, and M. Stratmann, *Global analysis of fragmentation functions for pions and kaons and their uncertainties*, *Phys.Rev.* **D75** (2007) 114010, [hep-ph/0703242].
- [87] S. Albino, B. Kniehl, and G. Kramer, *AKK Update: Improvements from New Theoretical Input and Experimental Data*, *Nucl.Phys.* **B803** (2008) 42–104, [arXiv:0803.2768].
- [88] F. Arleo and J.-P. Guillet, “<http://lapth.cnrs.fr/generators/>”
- [89] S. Catani, Y. L. Dokshitzer, M. Seymour, and B. Webber, *Longitudinally invariant K_t clustering algorithms for hadron hadron collisions*, *Nucl.Phys.* **B406** (1993) 187–224.
- [90] S. D. Ellis and D. E. Soper, *Successive combination jet algorithm for hadron collisions*, *Phys.Rev.* **D48** (1993) 3160–3166, [hep-ph/9305266].
- [91] A. Banfi, G. P. Salam, and G. Zanderighi, *Accurate QCD predictions for heavy-quark jets at the Tevatron and LHC*, *JHEP* **0707** (2007) 026, [arXiv:0704.2999].
- [92] **D0 Collaboration** Collaboration, V. Abazov et al., *Measurement of the inclusive jet cross-section in $p\bar{p}$ collisions at $s^{91/2} = 1.96$ -TeV*, *Phys.Rev.Lett.* **101** (2008) 062001, [arXiv:0802.2400].
- [93] M. Cacciari, G. P. Salam, and G. Soyez, *The Anti- $k(t)$ jet clustering algorithm*, *JHEP* **0804** (2008) 063, [arXiv:0802.1189].
- [94] P. Chiappetta, R. Fergani, and J.-P. Guillet, *Double prompt photon production from hadronic collisions*, *Phys.Lett.* **B348** (1995) 646–656.
- [95] P. Chiappetta, R. Fergani, and J.-P. Guillet, *Production of two large $p(T)$ hadrons from hadronic collisions*, *Z.Phys.* **C69** (1996) 443–457.
- [96] R. K. Ellis, D. Ross, and A. Terrano, *The Perturbative Calculation of Jet Structure in $e^+ e^-$ Annihilation*, *Nucl.Phys.* **B178** (1981) 421.
- [97] S. Frixione, Z. Kunszt, and A. Signer, *Three jet cross-sections to next-to-leading order*, *Nucl.Phys.* **B467** (1996) 399–442, [hep-ph/9512328].
- [98] S. Catani and M. Seymour, *A General algorithm for calculating jet cross-sections in NLO QCD*, *Nucl.Phys.* **B485** (1997) 291–419, [hep-ph/9605323].

- [99] S. Catani, M. Fontannaz, J.-P. Guillet, and E. Pilon, *Cross-section of isolated prompt photons in hadron hadron collisions*, *JHEP* **0205** (2002) 028, [hep-ph/0204023].
- [100] P. Aurenche, M. Fontannaz, J.-P. Guillet, E. Pilon, and M. Werlen, *A New critical study of photon production in hadronic collisions*, *Phys.Rev.* **D73** (2006) 094007, [hep-ph/0602133].
- [101] S. Kawabata, *A New Monte Carlo Event Generator for High-Energy Physics*, *Comput.Phys.Commun.* **41** (1986) 127.
- [102] G. P. Lepage, *A New Algorithm for Adaptive Multidimensional Integration*, *J.Comput.Phys.* **27** (1978) 192.
- [103] D. d’Enterria and J. Rojo, *Quantitative constraints on the gluon distribution function in the proton from collider isolated-photon data*, *Nucl.Phys.* **B860** (2012) 311–338, [arXiv:1202.1762].
- [104] **D0 and CDF Collaboration** Collaboration, S. Soldner-Rembold, *Prompt photon production at the Tevatron*, *Acta Phys.Polon.* **B37** (2006) 733–738, [hep-ex/0511051].
- [105] **CDF Collaboration** Collaboration, T. Aaltonen et al., *Measurement of the Inclusive Isolated Prompt Photon Cross Section in p anti- p Collisions at $s^{*(1/2)} = 1.96$ -TeV using the CDF Detector*, *Phys.Rev.* **D80** (2009) 111106, [arXiv:0910.3623].
- [106] A. Mas, *Mesure de la production des photons isolés dans les collisions p - p à $\sqrt{s} = 7$ TeV avec le détecteur ALICE, thèse de doctorat, Ecole des Mines, Nantes (2013), .*
- [107] F. Arleo, *(Medium-modified) Fragmentation Functions*, *Eur.Phys.J.* **C61** (2009) 603–627, [arXiv:0810.1193].
- [108] D. d’Enterria, K. J. Eskola, I. Helenius, and H. Paukkunen, *Confronting current NLO parton fragmentation functions with inclusive charged-particle spectra at hadron colliders*, arXiv:1311.1415.
- [109] Z. Belghobsi, M. Fontannaz, J.-P. Guillet, G. Heinrich, E. Pilon, et al., *Photon - Jet Correlations and Constraints on Fragmentation Functions*, *Phys.Rev.* **D79** (2009) 114024, [arXiv:0903.4834].
- [110] D. de Florian and G. F. Sborlini, *Hadron plus photon production in polarized hadronic collisions at next-to-leading order accuracy*, *Phys.Rev.* **D83** (2011) 074022, [arXiv:1011.0486].

- [111] **CMS Collaboration** Collaboration, S. Chatrchyan et al., *Measurement of jet fragmentation into charged particles in pp and PbPb collisions at $\sqrt{s_{NN}} = 2.76$ TeV*, *JHEP* **1210** (2012) 087, [arXiv:1205.5872].
- [112] S. Catani, M. Fontannaz, J. P. Guillet, and E. Pilon, *Isolating Prompt Photons with Narrow Cones*, *JHEP* **1309** (2013) 007, [arXiv:1306.6498].
- [113] F. Arleo, D. d’Enterria, and A. S. Yoon, *Single-inclusive production of large- p_T charged particles in hadronic collisions at TeV energies and perturbative QCD predictions*, *JHEP* **1006** (2010) 035, [arXiv:1003.2963].
- [114] **ATLAS** collaboration, “
<https://twiki.cern.ch/twiki/bin/view/AtlasPublic/LuminosityPublicResults>.”
- [115] **CMS** collaboration, “
<https://twiki.cern.ch/twiki/bin/view/CMSPublic/LumiPublicResults>.”
- [116] **CDF Collaboration** Collaboration, D. Acosta et al., *Measurement of the $t\bar{t}$ production cross section in $p\bar{p}$ collisions at $\sqrt{s} = 1.96$ TeV using lepton + jets events with secondary vertex b -tagging*, *Phys.Rev.* **D71** (2005) 052003, [hep-ex/0410041].
- [117] T. Stavreva and J. Owens, *Direct Photon Production in Association With A Heavy Quark At Hadron Colliders*, *Phys.Rev.* **D79** (2009) 054017, [arXiv:0901.3791].
- [118] B. Mele and P. Nason, *The Fragmentation function for heavy quarks in QCD*, *Nucl.Phys.* **B361** (1991) 626–644.
- [119] B. Bailey, E. L. Berger, and L. Gordon, *Production of a prompt photon in association with charm at next-to-leading order in QCD*, *Phys.Rev.* **D54** (1996) 1896–1907, [hep-ph/9602373].

Abstract

The LHC at CERN, which is the most powerful collider in the world, was designed to search for the Higgs boson and new physics signals. But besides these discoveries, the LHC experiments have collected (and will collect) a large amount of data that can be used to improve our knowledge about Quantum ChromoDynamics (QCD). This thesis is in this former line of research. It contains two parts which use correlation variables to constrain non perturbative inputs.

The first part concerns the constraints which can be put on fragmentation functions (FFs) using momentum correlation variables in hadron+jet production. The non perturbative inputs for the recent FFs were extracted from the LEP e^+e^- collision data. These LEP data put constraints on the FFs at low fragmentation variable x ($x < 0.7$), but do not give constraints at larger x . Because of that, the behaviors of the FF-sets at high x differ strongly from one another. A next-to-leading order (NLO) analysis of hadron-jet momentum correlations in p-p collisions at the LHC is carried out. We consider two cases: the correlation between a hadron and an away-side jet, and the correlation between a hadron and the jet to whom the hadron belongs. These two cases give complementary results. We show that the inclusive charged hadron momentum distribution inside jets is a very sensitive observable which allows one to disentangle among various fragmentation function sets presently available. Correlations using identified hadrons (kaons, protons) are investigated as well.

The second part concerns the study of the associated production of photon + heavy-flavor tagging in hadronic collisions at the Tevatron and the LHC. This cross section is used to constrain the heavy-flavor partonic densities inside the proton. A previous theoretical calculation showed a large discrepancy between the predictions and the experimental measurements for associated production of photon + charm at the Tevatron. We present three ways to compute this cross section depending on how the heavy flavor is tagged in experiments. The first way, called the invariant mass approach, has been used to recover the previous results, the second one, called the flavor- k_t algorithm, uses a flavor jet algorithm which leads to an infra-red safe observable. The third way, called FF approach, uses fragmentation functions of partons into heavy-flavor hadrons, the jet size being taken into account in the final state factorization scale. The predictions for the three ways are given in the NLO approximation of perturbative QCD. They have been implemented into a code which has been built from the `JETPHOX` program. By using the invariant mass approach, the results of the previous theoretical calculation have been re-obtained. These results are comparable with the one using flavor- k_t algorithm. These two approaches give theoretical predictions which are too low for the charm flavor compared to Tevatron results. The charm hadron FF approach predicts a differential cross section with respect to the photon transverse momentum (p_\perp) about 1.8–2.7 times greater than the one obtained using the invariant mass approach when $p_\perp \sim 80\text{--}110$ (GeV) at the Tevatron. This result agrees well with the experimental data. Predictions are given at LHC energy using the different ways for charm flavor and bottom flavor.

Résumé

Le LHC au CERN, qui est le collisionneur le plus puissant au monde, a été construit pour découvrir le boson de Higgs ainsi que des signaux de nouvelle physique. Mais au-delà de ces découvertes, les expériences auprès du LHC ont accumulé (et vont continuer à accumuler) une grande quantité de données qui pourront être utilisées pour accroître notre connaissance de la ChromoDynamique Quantique (QCD). Cette thèse est dans cette dernière ligne, elle contient deux parties qui utilisent des variables de corrélations pour contraindre les différentes entrées non perturbatives.

La première partie concerne les contraintes pouvant être mises sur les fonctions de fragmentation (FF) en utilisant des variables de corrélation dans la production de hadron + jet. Les entrées non perturbatives pour les récentes FF ont été extraites des données e^+e^- de LEP. Ces données mettent des contraintes sur les FF à petites valeurs de la variable de fragmentation x ($x < 0.7$), mais n'en donnent pas pour des grandes valeurs de x . Pour cette raison, le comportement des jeux de FF diffère de façon importante pour des grandes valeurs de x . Une analyse à l'approximation au-delà de l'ordre dominant (NLO) des corrélations hadron-jet dans les collisions p-p au LHC a été menée. Nous avons considéré deux cas : la corrélation entre un hadron et le jet de recul, et la corrélation entre un hadron et le jet qui le contient. Ces deux cas donnent des résultats complets. Nous montrons que la production inclusive de hadrons chargés à l'intérieur d'un jet est une observable discriminante qui permet de différencier les différents jeux de FF disponibles. Nous étudions aussi le cas où l'on utilise des hadrons identifiés (kaons, protons).

La deuxième partie concerne l'étude de la production associée de photon + jet de saveur lourde dans les collisions hadroniques au LHC et au Tevatron. Cette section efficace peut être utilisée pour contraindre les densités partoniques de saveurs lourdes dans le proton. Une étude antérieure avait montré qu'il y avait un grand désaccord entre les prédictions théoriques et les données expérimentales dans le cas de la production associée d'un photon et un jet de saveur charmée au Tevatron. Nous présentons trois façons de calculer cette section efficace dépendant de la manière dont est détecté le jet de saveur lourde. La première façon, appelée méthode de la masse invariante, a été utilisée pour retrouver les précédents résultats, la deuxième, appelée algorithme en kt avec saveur, utilise un algorithme de jet avec saveur qui permet de reconstruire des observables qui sont insensibles au domaine infrarouge. La troisième façon, appelée approche FF, utilise des fonctions de fragmentation de partons en hadrons de saveur lourde, la taille du jet est prise en compte à travers l'échelle de factorisation de l'état final. Les prédictions utilisant les trois façons sont données à l'approximation NLO en QCD perturbative. Elles ont été implémentées dans un programme construit à partir de JETPHOX. En utilisant l'approche masse invariante, nous retrouvons les résultats précédents. Ces résultats sont comparables à ceux obtenus en utilisant l'approche algorithme en kt avec saveur. Ces deux méthodes donnent des résultats théoriques qui sont trop bas comparés aux données expérimentales du Tevatron pour une saveur charmée. L'approche FF prédit une section efficace différentielle par rapport à l'impulsion transverse du photon (p_\perp) d'environ 1,8 à 2,7 fois plus grande que celle obtenue en utilisant l'approche masse invariante pour des p_t de 80 à 110 GeV au Tevatron. Ce résultat est en bon accord avec les données expérimentales. Des prédictions sont aussi présentées pour l'énergie du LHC utilisant les trois façons de calculer pour une saveur charmée ou belle.